Airfoil turbulence-impingement noise reduction by porous cells or wavy leading-edge design

Georgios Bampanis


N° d'ordre NNT: 2021LYSEC03

THÈSE de DOCTORAT DE L'UNIVERSITÉ DE LYON
opérée au sein de l'École Centrale de Lyon

École Doctorale N° 162
Mécanique Énergétique Génie Civil Acoustique

Spécialité de doctorat : Acoustique

Soutenue publiquement le 20/01/2021, par

Georgios Bampanis

Airfoil Turbulence-Impingement Noise Reduction by Porous Cells or Wavy Leading-Edge Design

---

Devant le jury composé de:

AZARPEYVAND, Mahdi	Professeur	Université de Bristol	Rapporteur
GERVAIS, Yves	Professeur	Université de Poitiers	Rapporteur
MOREAU, Stéphane	Professeur	Université de Sherbrooke	Examinateur
HERR, Michaela	Docteure	DLR	Examinatrice
AYTON, Lorna	Docteure	University of Cambridge	Examinatrice
SCHRAM, Christophe	Professeur	von Kármán Institute	Co-directeur de thèse
ROGER, Michel	Professeur	École Centrale de Lyon	Directeur de thèse

Laboratoire de Mécanique des Fluides et d'Acoustique, URM CNRS 5509
École Centrale de Lyon

Abstract

Broadband noise radiated from airfoils has been considered as a generic problem of primary engineering and research interest along the last decades. Noise emission from turbofan engines, drones, ventilation systems and other industrial and domestic applications could be mainly characterized as broadband and airfoil turbulence-impingement noise (TIN) is its dominating contributing mechanism. This thesis investigates the TIN mitigation by wavy leading-edge designs or porous inclusions. Experimental techniques and analytical models for the noise predictions are the main tools used for these investigations. The first three chapters are dedicated to investigating experimentally the three-dimensional features of the TIN of flat plates and NACA-0012 airfoils and its reduction by leading-edge serrations. A combination of far-field (single microphone) and near-field (spiral antenna) measurements showed consistent results with previous studies and highlighted the trailing edge noise (TEN) detrimental effect on the airfoil noise reduction performances. Results have shown that TIN reductions extend linearly for flat plates and exponentially for thick airfoils over a wider low-and-middle frequency range after subtracting TEN. In chapter 4, noise prediction tools for TIN have been validated both for straight and wavy leading edges by making use of the obtained experimental results. Chapters 5 deals with a basic flow analysis around the wavy leading edge performing tomographic and stereoscopic PIV measurements. Results showed consistency with previous works by validating computational simulations similar to the present experiments. Considering simple serration designs on leading edge and trailing edge, an optimization strategy is proposed for minimizing the total airfoil noise in chapter 6. The last chapter is dedicated to the acoustic and aerodynamic exploration of porous airfoils. The observed noise reductions vary between 4 and 6 dB, which makes porosity a promising technique for the noise mitigation of thick airfoils, with potentiality similar to that of leading-edge serrations for fans and other industrial applications.

Keywords: aeroacoustics, airfoil noise, turbulence, leading-edge serrations, microphone array, experimental techniques, wind tunnel, porous airfoil

Résumé

Au cours des dernières décennies, le bruit à large bande émis par les profils aérodynamiques a été considéré comme un problème générique d'un intérêt primordial pour l'ingénierie et la recherche. Les émissions sonores des turboréacteurs, des drones, des systèmes de ventilation et d'autres applications industrielles et domestiques pourraient être principalement caractérisées comme du bruit à large bande, dont le mécanisme dominant est le bruit d'impact de turbulence (BIT). Cette thèse étudie l'atténuation du BIT par des ondulations au bord d'attaque ou des inclusions poreuses. L'utilisation de techniques expérimentales et de modèles analytiques pour la prévision du bruit sont les principaux outils de ces recherches. Les trois premiers chapitres sont consacrés à l'étude expérimentale des caractéristiques tridimensionnelles du BIT de plaques planes et de profils aérodynamiques NACA-0012, et à sa réduction par des dentelures au bord d'attaque. Une combinaison de mesures en champ lointain (microphone unique) et en champ proche (antenne en spirale) a montré des résultats cohérents avec les études précédentes et a mis en évidence l'effet contaminant du bruit de bord de fuite (BBF), qui réduit les performances des dentelures en matière de réduction du bruit des profils. Les résultats montrent que les réductions du BIT varient quasi linéairement avec la fréquence pour des plaques planes et exponentiellement pour des profils épais, sur une plus large gamme de basses et moyennes fréquences après soustraction du BBF. Dans le chapitre 4, les outils de prédiction du BIT ont été validés pour des bords d'attaque à la fois droits et ondulés en utilisant les résultats expérimentaux obtenus. Le chapitre 5 porte sur l'analyse fondamentale de l'écoulement autour du bord d'attaque ondulé par des mesures de PIV tomographiques et stéréoscopiques. Les résultats corroborent des travaux précédents en validant des simulations numériques similaires aux expériences actuelles. En considérant des géométries simples de dentelures sur le bord d'attaque et le bord de fuite, une stratégie d'optimisation a été proposée dans le chapitre 6 pour minimiser le bruit total d'un profil tout en préservant ses performances. Le dernier chapitre est consacré à l'exploration acoustique et aérodynamique des profils poreux. Les réductions de bruit observées varient entre 4 et 6 dB, ce qui fait de la porosité une technique prometteuse pour l'atténuation du bruit des profils aérodynamiques épais, avec une potentialité similaire à celle des dentelures de bord d'attaque pour les ventilateurs et autres applications industrielles.

Mots clés: aéroacoustique, profil aérodynamique, bruit des profils, turbulence, dentelures au bord d'attaque, antenne microphonique, techniques expérimentales, soufflerie, profil aérodynamique poreux

To my family,

Acknowledgements

I am very grateful to the acoustic group of Acoustique du Laboratoire de Mécanique des Fluides et d'Acoustique (LMFA) from l'École Centrale de Lyon, where this doctoral thesis has been carried out (from September 2017 to January 2021). The high-level experimental facilities as well as the academic and technical support of the laboratory had been provided to me generously at any time it was needed. Apart from their valuable scientific contribution in aeroacoustic community, the laboratory spirit involves strong elements of creativity, fellowship, solidarity and social life. This pleasant atmosphere allowed Denis Ricot in 1999 to work at the same laboratory on the physical modeling of accordion reeds under the supervision of Dr. René Causse and Professor Michel Roger. My passion with music and accordion brought me face to face with their study that I discovered in 2012. The accordion sound is a matter of aeroacoustics thus from that point my motivation for this research field started growing up.

I would like to express my deepest gratitude to Professor Michel Roger, my thesis director. Michel, thank you for trusting me to deal with such a complicated topic and helping me to offer a small contribution to science. Thank you for the valuable knowledge you disseminated to me, the fruitful discussions about science and music, the music moments and for reminding to me to retain a balance in my life between work and personal life. As you have said, life is not only aeroacoustics. Many thanks to my thesis advisor Professor Stéphane Moreau who helped to consolidate a spherical background and obtain a better overview of my thesis topic. His always judicious remarks, nourished by an impressive knowledge of literature, has greatly helped me clarify my work. Stéphane, thank you for your endless and excellent humor, your positive attitude, our long midnight discussions and your surprising welcoming in Greek.

I am very thankful to the directors of the SmartAnswer project I was involved in, my advisor Professor Christophe Schram and Dr. Julien Christophe. They provided an excellent supervision of the project with professionalism, plenty of innovative ideas and rich knowledge. Thank you as well for your kind attitude and your smart humor. I feel honored to continue working with you as a postdoctoral researcher.

I would like to thank the Associate Professor Daniele Ragni and Assistant Professor Francesco Avallone for hosting me in their lab during my secondment in TU Delft in Netherlands. It was a unique experience for me to be part of your excellent team and work together. Dani and Fra, thank you for everything. I am particularly grateful to Professor Kyriakos Giannakoglou and Dr. Varvara Assouti for hosting me in their lab in NTUA in Athens for two months. Thank you for the interest you showed for my work, the

priceless knowledge you provided to me in optimization techniques and your availability.

I could not omit to express my biggest appreciation to the permanent staff of LMFA. Thanks to Marie-Gabrielle Perriaux and Benedict Martin for the continuous administrative service and help they provided to me, Marie Curie project kept them quite busy. I am very grateful to Dr. Pascal Souchotte and Dr. Emmanuel Jondeau for their priceless technical support and their patience to my crazy manufacturing ideas. Pierre Roland, Laurent Pouilloux, Bernard Barbier, my poor laptop apologies to all of you for its numerous crash problems. Thank you for solving them rapidly, efficiently and always with a positive smile. Ahmed Telali, Bruno Poirel and Horacio Correia merci beaucoup pour votre support technique. Ce fut très agréable de travailler avec vous.

Research life would not be interesting and efficient enough without developing a nice atmosphere in the office. I would like to thank all of my colleagues, doctorates and postdocs for helping to build a pleasant and friendly relationship among each other as well as for their support. Étienne Spieser, thank you for making me a better person. Your big heart had enough space for all of us. Nacho Zurbano-Fernandez (Nachoulis), thank you for staying always on a helping mode for me. Delivering the shovel in the middle of the night makes you always the best friend. Yuanyuan Deng, the night office guardian who kept our fellowship alive, thank you for being so kind. Yann Martelet, magka mou and king of the cakes, thank you for correcting patiently my French accent (chaussures). Thomas Lechat, the Lord of Matlab, I hope in the future to share the same stage apart from the same desk. Léo Girier, thank you for bringing tones of humor in our lab. Danny Lewis, thank you for reminding me always my dark side. Élina Cros, the skiing star, thank you for bringing brightness in our office. Miguel Pestana, thank you so much for renting me your mics. I was expecting finally from you to donate them to me but unfortunately you never did it. Emanuele de Bono, fratemo, thank you for your calm energy which spreads joy all around. Cristina Vidali, my italian sister with the bright smile and the golden heart. Andrea Maffioli, ela reee. Pierre Pineau, thank you so much for your unlimited kindness and positiveness. Gabriele Grasso, thank you for motivating us to participate in the cake and yoga events. Vianney Masson and Marion Capuano, I was always excited with your scientific and musical strengths. Thank you for motivating me through our discussions. Mathieu Varé, thank you so much for your kindness and your huge spirit. Ariane Emmanuelli, thank you for your positiveness and your enthusiasm. Many thanks to Justine Giez, Gyuzel Yakhina, Paul Laffay, Livia Grandoni, Fabio Feraco, David Lamidel, Raphaël Da Mota, Simon Bouley, Maria Karzova, Petr Yuldashev and Courtney Ford, Igor Kurek and Daher Diab. Thanks to our interns Achraf Radi, Loic Berger and Javier Beltran. I would like to thank as well Professor Christophe Bailly and Dr. Sebastien Ollivier for approving and supporting the proposal I had written on musical acoustics for the accordion reed project. I am grateful to my students who worked hard for this project, with dedication and enthusiasm: Arnaud Cimolino, Jérémi Bernard and Benjamin Etchebarne. I would not forget to thank my colleagues (ESRs) from the SmartAnswer

team for sharing together so many unique moments, either personal or scientific. Many thanks to Riccardo Zamponi, Alessandro Zarri, Niloofar Sayyad Khodashenas, Massimo Emiliano d'Elia, Thanushree Suresh, Christopher Teruna, Lourenço Tércio Lima Pereira, Sergi Pallejà Cabré, Felipe Alves Pires, Morteza Monfaredi, Chaitanya Sanghavi, Simone Tamaro, Mohd Javed Ayyubi, Thomas Laurence.

An integral part of this journey is my life in Lyon and all the people and friends who became part of it. Thank you all from the bottom of my heart. Your warm welcoming and your company made my life very interesting and full of memories. I dedicate this thesis to my family, thank you for your long term support. Your spirit accompanied me till now giving me strength and motivation to go ahead in my life.

This study has received funding from the European Union's Horizon 2020 research and innovation programme under the Marie Skłodowska Curie, grant agreement No 722401.

> "We must have perseverance and above all confidence in ourselves. We must believe that we are gifted for something and that this thing must be attained"

Marie Skłodowska Curie

Contents

Nomenclature

Acronyms

AoA	Angle Of Attack	[deg]
BGN	BackGround Noise	[dB]
LBL	Laminar Boundary Layer	
LEN	Leading Edge Noise	[dB]
LE	Leading Edge	
OAPWL	OverAll sound PoWer Level	[dB]
PSD	Power Spectral Density	[dB.Hz^{-1}]
PWL	Sound PoWer Level	[dB.Hz^{-1}]
SPL	Sound Pressure Level	[dB.Hz^{-1}]
TEN	Trailing Edge Noise	[dB]
TE	Trailing Edge	
TIN	Turbulence-Interaction Noise	[dB]

Greek characters

α	Speed of sound	[ms^{-1}]
Λ	Turbulence integral length scale	[m]
λ	Serration wavelength	[m]
λ_a	Acoustic wavelength	[m]
λ_h	Hydrodynamic wavelength	[m]
ω	Angular frequency	[Hz^{-1}]
ϕ	Polar angle	[deg]

ρ	Air density	[kg.m^{-3}]
ρ_{man}	The liquid (water) density inside the manometer	[kg.m^{-3}]
Θ	Graham's parameter	
θ	Azimuthal angle	[deg]

Latin characters

$2b$	Chord of the theoretical flat plate	[m]
$2d$	Span of the theoretical flat plate	[m]
$2h$	Serration depth	[m]
$< u'u' >$	Streamwise time-averaged velocity fluctuations	[s^{-1}]
$< v'v' >$	Spanwise time-averaged velocity fluctuations	[s^{-1}]
$< w'w' >$	Vertical time-averaged velocity fluctuations	[s^{-1}]
$\boldsymbol{x_0}$	Coordinates vector of a position on the flat plate	[m]
$\boldsymbol{x}$	Observer's coordinates vector	[m]
$\mathcal{L}$	Acoustic transfer function	
ω'_x	Instantaneous streamwise vorticity	[s^{-1}]
ω'_y	Instantaneous spanwise vorticity	[s^{-1}]
ω_x	Mean streamwise vorticity	[s^{-1}]
ω_y	Mean spanwise vorticity	[s^{-1}]
c	Airfoil chord	[m]
c_0	Airfoil mean chord	[m]
C_D	Drag coefficient	
C_L	Lift coefficient	
D	The dimension of the array	[m]
E_n	General expansion coefficient	
F_s	Shape function of the leading-edge geometry	
g	Transfer function	
i	Angle of attack	[deg]

k	Acoustic wavenumber	[m^{-1}]
k_1^*	Non-dimensional chordwise aerodynamic wavenumber	
k_1	Chordwise aerodynamic wavenumber of the incident fluctuation	[m^{-1}]
k_2	Span-wise aerodynamic wavenumber of the incident fluctuation	[m^{-1}]
kc	Helmholtz number	
L	The typical distance between the center of the array and the mid plane of the measured area	[m]
L_s	The overall scan map extent	[m]
M	Mach number	
P_{ref}	Reference pressure	[Pa]
R	Distance between observer and sound source	[m]
R	The microphone distance to the airfoil leading-edge center point	[m]
R_B	Beamforming spatial resolution	[m]
S_0	Corrected distance accounting for sound convection by the surrounding flow	
S_{pp}	Far-field sound pressure	[$dB.Hz^{-1}$]
St_h	Strouhal number based on serration depth	
T_{ref}	Reference temperature	[°C]
TI	Turbulence Intensity	
U, V, W	Streamwise, spanwise and vertical averaged velocities	[ms^{-1}]
U_0	Free-stream velocity	[ms^{-1}]
U_c	Convection speed	[ms^{-1}]
u_{rms}	Root mean square velocity u	[ms^{-1}]
W	Sound Power	[dB]
w_n	Spanwise eigenmode	
x	Chordwise/streamwise direction measuring from the airfoil leading edge	[m]
y	Spanwise direction	[m]
z	Wall-normal direction	[m]

List of Figures

List of Tables

Introduction

Motivation

URBAN noise exists in our lives since many years but has never been so intense and pervasive as in the last decades. The high concentration of citizens in cities of developing countries increased dramatically the frequent use of transportation (including road, rail and air-traffic), construction and public work, ventilation systems, office machines and home appliances. According to World Health Organization in 1995, about 40% of the European population is exposed to road traffic noise with an equivalent sound pressure level exceeding 55 dB(A) daytime, and 20% are exposed to levels exceeding 65 dB(A) [1]. Latest recommendations (strong or conditional) have been published for road traffic noise, aircraft noise, wind turbine noise and railway noise [2]. ACARE has set targets with high expectations within Flightpath 2050 to improve air travel by 2050. Specifically, the perceived noise emission from aircraft should be reduced by 65% by 2050 relative to 2000 [5].

The aforementioned engineering domains partly meet the origin of their noise source nature in flow-generated sound. Specifically low-speed fans in engine cooling units, in ventilation systems, wind turbines as well as propulsive rotating-blade technologies for aeronautical transport, drones and others include these sound sources. Turbulent flows interacting with solid surfaces are efficient sources of broadband noise. In particular the turbulence-impingement noise (TIN) generated at the leading edge of an airfoil placed in a highly disturbed flow is considered a generic problem of primary engineering and research interest. Typically, a protection grid or a heat exchanger upsteam of a cooling fan, the rotor wakes of the fan of a turbofan engine impinging on outlet guide vanes or just atmospheric turbulence are sources of broadband noise for rotating blades or stationary vanes that cannot be easily mitigated without affecting the design parameters of the geometries. Sketch 1-(a) illustrates the existence and the interaction of vortices with the inner rigid structure components of a turbofan engine. In pictures 1-(b) and (c) turbulent structures are visualized with the Q-criterion for an axial fan and a centrifugal fan used for cooling and ventilation applications respectively. In both cases vortices interact with the rigid nearby surroundings (shroud, heating grid and backplate etc.) generating broadband noise.

Most often, the turbulence is an unavoidable component of the flow. Therefore, alter-

native sound-reduction strategies must be sought in modifications of the blades or vanes that remain compatible with the aerodynamic performances. In recent years several studies have been carried out on TIN reduction by modifying the material and mainly the geometry of the leading edge [128, 116, 40].

The work described in this thesis is part of the SmartAnswer [4] research program which aims at mitigating flow-induced acoustic radiation and transmission for reduced aircraft, surface transport, workplaces and wind energy noise. The present thesis addresses two different techniques for reducing the Turbulence-Interaction Noise (TIN) on airfoils or blades. The strategy followed is to modify the geometry and/or the structure of the blades so as to reduce their acoustic response to this turbulence. In summary, the proposed structural and geometrical modifications that will be investigated are: the airfoils with a sinusoidal leading edge and the use of a partially porous material in place of the conventional rigid structure of airfoils. It is the continuation of a preliminary study in which both technologies have been compared [126], with promising results in terms of noise reduction even with non-optimized implementation.

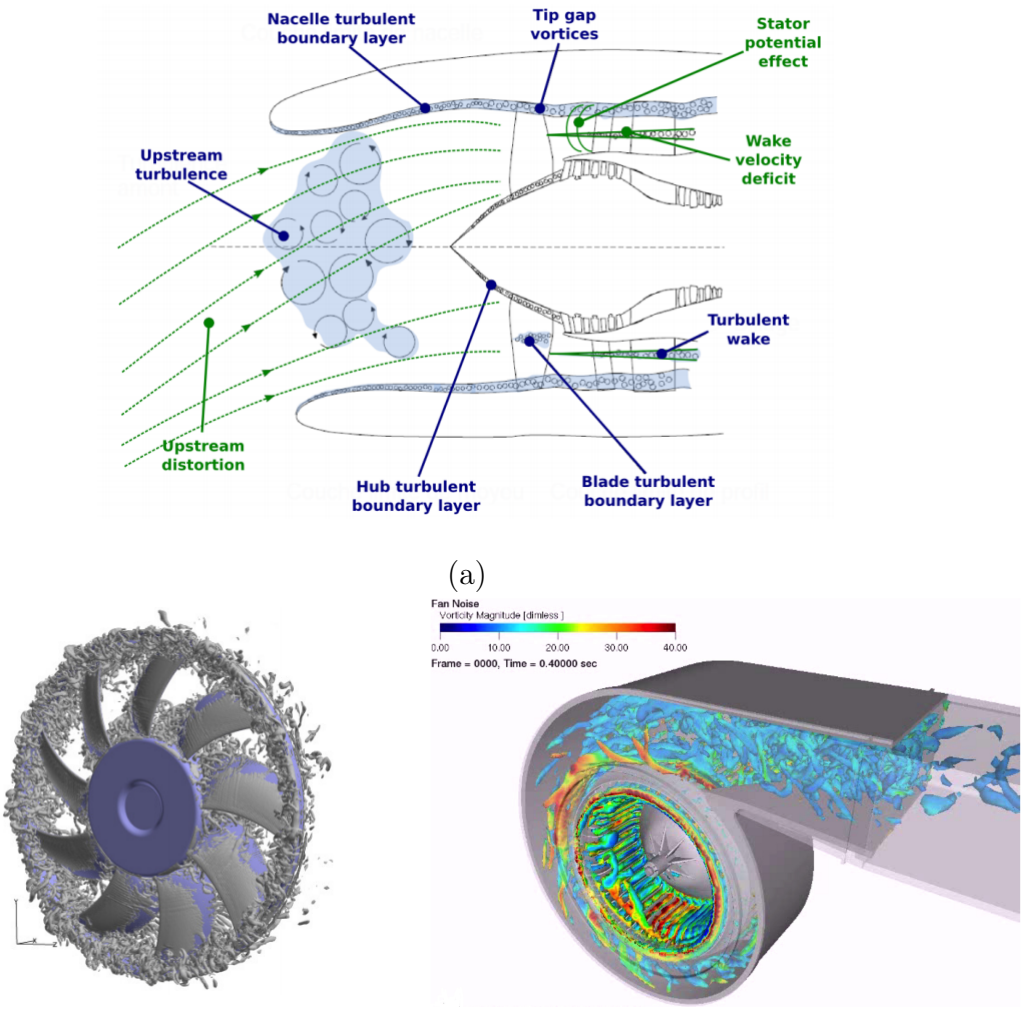

Figure 1: (a) Sketch of turbofan noise sources (taken from Moreau [96]), Q-criterion around (b) a cooling axial fan (taken from San-josé *et al.* [132]) and a centrifugal fan (from ExaCorporation [7]).

Objectives and tools

The experimental approach is the main tool chosen in this work to investigate the effects of leading-edge serrations (or tubercles) and of porosity. Theoretical models are also used to strengthen the results investigating the three-dimensional features of the radiated sound in the far-field. The applied techniques and the objectives in detail are as follows:

- The sinuous cut of the leading edge of airfoils or blades is already thoroughly reported in the recent literature, in terms of aerodynamics and acoustics. Yet reported experiments only rely on measurements performed in the mid-span plane. Furthermore, some conclusions need to be confirmed. The present work investigates the three-dimensionality of the radiated sound generated by these airfoils. The acoustic field is explored by using microphone arrays in the near-field and in the far-field. Existing theoretical models are compared with the experimental data base. The flow characteristics around the serrations are also explored with the time-resolved tomographic PIV technique.

- The benefits of the use of porous inclusions in place of the conventional rigid structure of a NACA-12 airfoil are assessed. The empirical optimization of this technology aims at qualifying the porosity properties ensuring good acoustic performance without degrading the aerodynamic performance.

- An optimization study on the sound radiation minimization with the use of leading-edge and trailing-edge serrations, preserving a good aerodynamic performance is attempted. Noise prediction tools for modified and baseline airfoils are the key tools for this survey.

In all cases, systematic anechoic wind tunnel tests are performed to generate the required experimental database. Far-field noise measurements with a rotating arc antenna, noise-source localization technique with a spiral microphone array, Hot Wire Anemometry (HWA) technique, acoustic impedance measurements and PIV measurements are the tools used for the whole experimental campaign. TIN reduction is estimated by developing relevant subtraction procedures of other contributions, such as trailing-edge noise and background noise.

Serrations inspiration

Bio-inspired periodic leading-edge shapes of airfoils in the spanwise direction, referred to as tubercles or serrations, have been studied extensively in engineering sciences for both their aerodynamic and acoustic effects. The secrets for the noise reduction technology (serrations) stem from the owl wings. Owls are known for their characteristic silent flight, capable of flying just inches from their prey without being detected. A particular example between different species of owls is the barn owl in Fig. 2. Birds biomimetics inspired Graham [62] in 1934 to study the peculiarities of barn owls' feathers anatomy, proposing their technology for future aircraft application. The stiff comb-like fringe on the front margin of every feather functions as a leading edge of varying length and size depending on the bird size. In the seventies Kroeger [77] investigated the aerodynamic and the aeroacoustic effects of owl's feathers whereas in the last five decades other researchers continued studying the wing structure and its aeroacoustic benefits on real owl feathers [41, 51, 84, 24, 76].

Figure 2: Photograph of a barn owl (Tyto alba). From Wikipedia [6].

A clear distinction must be made depending on the size of one serration period with respect to the chord length, expecting different main physical mechanisms. Three special characteristics of owl's wings have been recognized as noise mitigation devices; the comb-like geometry in the leading edge, the fluffy surface at the bottom side of the wings and the fringes on the trailing edge of the wing. The leading edge of owls' wings features spike-like serrations of very small size which control the boundary-layer growth over the wings by generating streamwise micro-vortices. This, with the additional effect of the fluffy structure of the wing surface, has the effect of indirectly reducing trailing-edge noise. Serrations are also found at the trailing edge, now directly contributing to the trailing-edge noise reduction. Detailed pictures of the feathers structure of a barn owl (Fig. 3-(b)) and of a pigeon (Fig. 4-(b)) are provided by Bachmann [24]. The differences of both structures are obvious; the former looks comb-like at the LE and fluffy at the TE whereas the latter looks straight-edged and rigid.

(a)

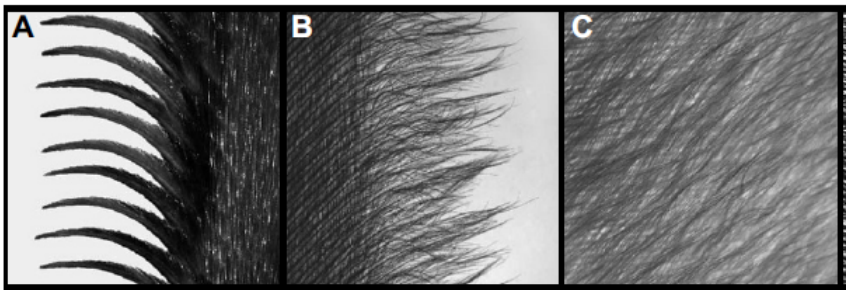

(b)

Figure 3: Pictures of: (a) the feather of a barn owl emphasized with the leading-edge comb and trailing edge fringes and (b) the feather details that correspond to the leading edge comb (A), the trailing-edge fringes (B) and the velvet-like dorsal surface (C) of the inner feather vane. Pictures from Bachmann [24] and Geyer [51].

(a)

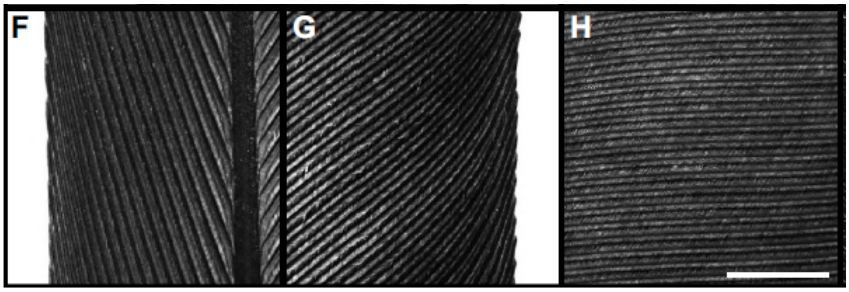

(b)

Figure 4: Pictures of: (a) the feather of a pigeon and (b) its details that correspond to the leading edge (F), the trailing edge (G) and the surface (H) downstream the shaft. Pictures are taken from Bachmann [24] and Treeclimber-Stock on DeviantArt [9].

In contrast, the foreflippers of humpback whales have leading-edge tubercles of much larger characteristic length when compared to the chord, featuring a sinuous pattern. The tubercles are known to be very efficient for hydrodynamical reasons [47, 48]. Unlike other species, these whales use their foreflippers to move forward nearly in the same way as birds their wings to fly, and not only their tail, typically in acceleration bursts. One aerodynamic effect of the turbercles is delaying stall at transient high angles of attack [93], thus increasing manoeuvrability.

Figure 5: Photographs of humpback whales' flippers showing the tubercles at the leading edge position. From Fish *et al.* [48]

In both cases the aerodynamic effects and their acoustic consequences are intricate. They are at the origin of bio-inspired technologies for noise control. These characteristics inspired and guided the whole aeroacoustic community for the last twenty years in the domain of noise mitigation strategies on airfoils with the application of serrated edges and porous materials. A detailed description of the advantageous applications of these devices is given in Chapter 3.

Publications

The content of this thesis has been partially published at the conferences mentioned below. The author's contribution for each publication involves the experiments conduction, the data post-processing, the application of the theoretical models and the writing where the author appears as first. Also, the author contributed at the work of Palleja-Cabre [111] for performing the experimental techniques. Some parts of this thesis is an ongoing work which is included in journals that are going to be submitted in the near future.

Journal papers

1. Bampanis, G., Roger, M. and Moreau, S. "On a three-dimensional investigation of airfoil turbulence-impingement noise and its reduction by leading-edge tubercles". Journal of Sound and Vibration, p.116635, 2021.

2. Palleja-Cabre, S., Tester, B.J., Jeremy Astley, R. and Bampanis, G., 2021. "Aeroacoustic Assessment of Performance of Overtip Liners in Reducing Airfoil Noise". AIAA Journal, 59(9), pp.3622-3637, 2021.

Conference papers

1. Bampanis, Georgios, and Michel Roger. "Three-dimensional effects in the reduction of turbulence-impingement noise of aerofoils by wavy leading edges." Euronoise 2018 Crete (2018): 97-104, 2018.

2. Bampanis, Georgios, Michel Roger, Daniele Ragni, Francesco Avallone, and Christopher Teruna. "Airfoil-Turbulence Interaction Noise Source Identification and its Reduction by Means of Leading Edge Serrations." In 25th AIAA/CEAS Aeroacoustics Conference, p. 2741, 2019.

3. Bampanis, Georgios, and Michel Roger. "On the Turbulence-Impingement Noise of a NACA-12 Airfoil with Porous Inclusions." In AIAA AVIATION 2020 FORUM, p. 2577, 2020.

4. Moreau, Stephane, Georgios Bampanis, and Michel Roger. "Analytical and experimental investigation of leading-edge noise reduction on a flat plate with serrations." In AIAA AVIATION 2020 FORUM, p. 2542, 2020.

5. Palleja-Cabre, S., Tester, B.J., Astley, J. and Bampanis, G. "Aeroacoustic assessment of the performance of Over-Tip liners in reducing noise of an aerofoil over a flat surface". In AIAA AVIATION 2020 FORUM, p. 2608, 2020.

1 Literature Review on Airfoil TIN

Contents

Summary

This Section explains briefly the TIN mechanism for flat-plates and airfoils through a literature review. A history of the studies conducted on TIN prediction describes the theoretical tools that have been developed (theories and models) for flat plates and airfoils including the effects of thickness and loading.

1.1 Turbulence Interaction Noise (TIN)

Broadband noise radiated from airfoil-like bodies embedded in a disturbed or turbulent flow is the result of the interaction between the turbulence and the solid surface. The unsteadiness of the interaction is the necessary condition, leading to the development of pressure fluctuations on the airfoil surface, acting as acoustic sources. More precisely, turbulent interaction noise includes two noise mechanisms called Leading-Edge Noise (LEN), or equivalently turbulence-interaction or turbulence-impignement noise (TIN) and Trailing-Edge Noise (TEN). Both sound sources result from the same process described above and their nature differs on the way of generation. Trailing-edge noise is a part of what is called airfoil self-noise. It is generated due to the interaction between an airfoil and the turbulence produced in its own boundary layer and near wake as a consequence of the Kutta condition. Brooks [29] described five different self-noise mechanisms listed below which were defined and characterized through an extensive experimental campaign.

- Trailing-edge noise generated by turbulent boundary layer
- So-called vortex shedding noise generated by laminar boundary layer

- Stall noise due to flow separation
- Vortex shedding noise due to trailing-edge bluntness
- Tip vortex formation noise

TIN is due to the interaction with upstream turbulence, carried by the mean flow independently of the presence of the airfoil. The name 'leading-edge' noise can be considered equivalent to TIN because the scattering of impinging turbulence as sound is a very fast and concentrated mechanism. Going into details, the response of the airfoil to upstream turbulence involves the entire chord at low frequencies for which the chord is compact. In that sense, TIN is not only 'leading-edge' noise. As frequency increases, the response involves dominantly the leading-edge area and both names are equivalent. In any case, with or without upstream turbulence, the developing boundary layers as source of trailing-edge noise exist, and they are not correlated to TIN. Fig. 1.1 visualizes LEN and TEN as a consequence of airfoil-turbulence interaction.

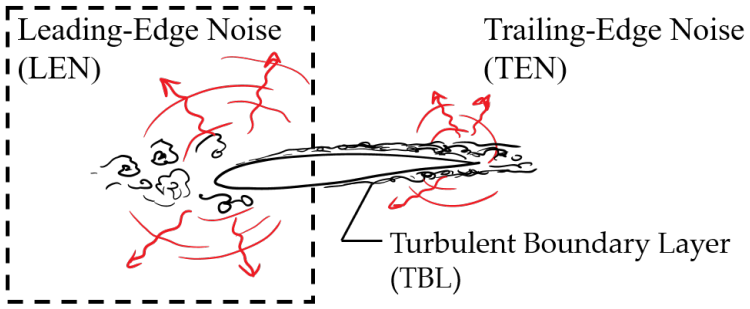

Figure 1.1: Leading-Edge Noise (LEN) and Trailing-Edge Noise (TEN) sources as a consequence of airfoil-turbulence interaction.

1.1.1 TIN Prediction for Flat Plates

Turbulence-impingement noise is strongly related to the generic topic of unsteady aerodynamic airfoil theory. Von Kármán and Sears [150, 139, 140], based on the circulation theory of airfoils, derived expressions that predict the unsteady lift and the moment of an oscillating thin airfoil in 2D. The forces induced on an airfoil by upwashes were also given. The most important contribution is the solution for a harmonic sinusoidal gust that has been fundamentally used by next researchers for predicting unsteady lift forces and developing noise prediction models [54, 145]. All prediction models assimilate the airfoil to a zero-thickness flat plate for mathematical tractability.

First dealing with unsteady-lift studies, Graham [61] derived similarities rules that relate the generic three-parameter problem of a compressible oblique gust impinging on a leading edge to two simplified two-parameter problems, depending on the Mach number and the impingement angle between the gust front and the edge. Hence, an incompressible oblique gust is considered as similarity basis for subcritical flows and a compressible

two-dimensional gust parallel to the leading edge for supercritical flows. The rules are a way of deriving solutions for the difficult mathematical three-parameters problem. The notion of sub- and supercritical gusts will be detailed in Chapter 4.

Adamczyk [10] overcame the difficulty of compressibility and three-dimensionality effects by developing a high-frequency analysis that yields to approximate closed-form expressions for the unsteady aerodynamic response of an infinite swept to an arbitrary gust in a compressible flow.

A theoretical expression for the sound radiation in the far-field by an airfoil placed in a subsonic turbulent stream that could be considereed as the acoustic continuation of previous works is given by Amiet [12]. Initially, analytical expressions [11] are derived for the pressure, lift and moment on a thin airfoil encountering a sinusoidal gust in compressible subsonic stream, based on Osborne [109] and Miles [94] solutions. Then, extending the work of Graham [61], Adamczyk [10] and based also on the acoustic analogies [83, 43, 46], Amiet derived closed-form approximate solutions [13] for the high-frequency thin airfoil impingement noise using an iterative procedure based on Schwarzschild's technique [138] cited by Landahl. Amiet [14] and Brooks & Hodgson [30] studied also the airfoil self-noise, taking as an input the convecting surface pressure statistics upstream of the trailing edge. Few years later, Brooks *et al.* [29] contributed to this study by experimental evidence.

One decade later, Moreau *et al.* [100] studied the airfoil turbulence-impingement noise as a function of the effect of airfoil shape and the angle of attack. Roger & Moreau [124] and Moreau & Roger [99] extended Amiet's trailing-edge noise model, showed its asymptotic compatibility with Howe's theory, and validated it against experimental databases. Roger [129, 121] also studied both theoretically and experimentally the turbulence impingement noise of a thin rigid ring placed in the mixing layer of a subsonic circular jet. An analytical model was derived as a direct extension of existing Amiet's formulations in cylindrical coordinates. The circular geometry has advantages, such as the minimization of the background noise, the absence of tip effects (no end plates unlike with rectangular airfoils) and the possibility of measuring the noise for all the radiation angles from the surface in the far-field. The very good agreement between the experimental and theoretical results was found to indirectly validate the transfer function for a rectangular airfoil at oblique radiation angles, which is not easily achievable in a set-up involving side plates and a rectangular nozzle. Yet the explicit validation of TIN radiation models off the mid-span plane remains an unanswered question, which partly motivated the present work.

An important limitation in linearized thin-airfoil unsteady aerodynamic theories is that the true cross-section shape is ignored, the airfoil being assimilated to a thin rigid plate. In fact, the mean angle of attack the camber and the thickness are all assumed zero in the analysis. The effects of airfoil shape and loading have been addressed by several authors, but often at the price of necessary numerical implementation, or much more cumbersome analytical developments.

1.1.2 Effects of Airfoil Shape and Loading

Goldstein & Atassi [58] proposed an analytical work for calculating the unsteady incompressible flow that results of a 2D airfoil interacting with a periodic gust. Overcoming the weaknesses of primarily theories based on a flat plate assumption with zero thickness and zero angle of attack [140, 79] which miss some of the coupling effects are missing [68, 106], they considered jointly the parameter of unsteady incident disturbances and small values of angle of attack, camber or thickness by developing second-order expansions. Based on the rapid distortion theory, the effect of distortion of the impinging gust due to the steady-state potential flow about the airfoil is included, causing changes in the incident vorticity wavelength. Results showed that when both the axial and the transverse aerodynamic wavenumbers approach infinity the fluctuating lift is affected significantly by the steady-state potential flow at higher frequencies. Atassi [16] based on the same approach showed that the unsteady lift created by the gust can be constructed by linear superposition of the classical lift of Sears' theory and of three independent components taking into account separately the effects of airfoil thickness, airfoil camber and non-zero angle of attack.

Tsai [146] based on Goldstein [58] rapid distortion theory studied the effect of thickness on the sound from the interaction of high-frequency convecting single gust with a symmetric airfoil at zero angle of attack. He concluded that the airfoil nose radius expressed in Strouhal number $St = \omega r_n/U_0$ acts as a sensitivity parameter to the total power level for different airfoil shapes. His work has been extended by Myers and Kerschen [103] by considering a cambered airfoil at non-zero angle of attack interacting with convected disturbances. A parametric analysis has shown that the mean-flow airfoil incidence angle affects significantly the TIN.

Moreau *et al.* [100] investigated the airfoil turbulence-impingement noise on three different geometries: a flat plate of 3% relative thickness, an industrial cambered airfoil of 4% relative thickness and a symmetric NACA0012 airfoil. Results showed that in the tested range the angle of attack plays no dominant role, whereas the increase of the airfoil's thickness is found to be proportional to the reduction of the turbulence-interaction noise. Based on their experimental results, they proposed semi-empirical analytical corrections based on geometrical modifications of the radiation integral and spectral predictions obtained by the rapid distortion theory (first order effect) around a bluff body. Eventually, these corrections account for the effect of camber and thickness of a slightly cambered thick airfoil on the far field sound. Their previous extended model [127, 123] for three-dimensional supercritical and subcritical gusts is shown to agree well with the experimental results for the two bodies in the midspan plane ($x_2 = 0$, spanwise wavenumber $K_2 = 0$) and the 3D subcritical gusts are also found to be significant off the midspan plane.

Glegg & Devenport [56] used the generalized form of Blasius theorem and proved that

the unsteady loading resulting from a blade vortex interaction depends on the passage of the vortex relative to the leading edge singularity in a transformed plane by conformal mapping. This analysis involves the thickness, the airfoil angle of attack and the vortex position and showed that by increasing the airfoil thickness the unsteady loading pulse is getting smoother. Considering a step gust, the unsteady loading is not affected by angle of attack, but its direction of action rotates forward by an angle equal to the angle of attack.

Panel methods have been used to predict interaction noise for airfoils with thickness. Grace [60], Glegg & Devenport [57], Santana *et al.* [134] used panel methods concluding that blade response unsteadiness decreases with increasing thickness and that the TIN is weakly dependent on the angle of attack. A supportive experimental work by Devenport *et al.* [44] has shown that the angle of attack has a strong effect on the noise for a single gust Fourier component of turbulence, but this effect considerably weakens because of the averaging effect of the isotropic turbulence spectrum. It is also observed that thicker airfoils generate significant noise reduction at high frequencies. Previous airfoil-shape effects, as well as others, are hard to include in simple analytical prediction schemes for extensive use. This motivated the development of corrections. Various correction factors have been proposed to capture the thickness effect of an airfoil response to impinging vortical gusts. Kucukcoskun *et al.* [78] also derived a semi-analytical model based on Amiet's theory implementing a geometrical near-field correction with the strip method. The scattered acoustic field was computed with a Boundary Element Method approach and was validated experimentally providing a good agreement. Lysak *et al.* [86, 85] developed a simple correction factor to account for the airfoil thickness effect in the gust response. An exact solution was addressed for the gust distortion by the mean flow only for high frequency gusts. The gust response model was validated successfully performing experiments.

Gershfeld [49] accessed to the airfoil turbulence interaction noise accounting for the effects of the airfoil thickness and the leading edge shape. A rigid surface Green's function estimates these effects as well as the trailing edge acoustic back scattering. He provided a correction factor of $e^{-k_1 h_1/2}$ to account for the dipole sound difference between an airfoil with thickness h_1 and a flat plate. This correction is supported by a comparison between theoretical and existing experimental measurements.

Moriarty *et al.* [102] provided prediction models for the inflow turbulence noise reduction and the trailing-edge noise. A numerical model based on boundary element method has been simplified accounting for the airfoil thickness effect on interaction noise reduction. It relates geometric quantities of an airfoil shape such as the thickness to chord ratio to the sound spectrum. Results have shown that "blunt" nose airfoils generate weaker turbulence interaction noise than airfoils with sharp leading edge. Oerlemans & Migliore [91] quantified the noise radiation from airfoils in turbulent and clean flows. In turbulent upstream conditions, it is observed that interaction noise increase with increasing sharpness of the airfoil leading edge while it follows a scaling with U^6.

Santana *et al.* [133] studied TIN by verifying experimentally existed semi-analytical developments [100, 44, 91, 95] on the gust-airfoil interaction accounting non-rectangular linearized airfoil shapes or blade tip effects. The distortion of turbulence that occurs in the vicinity of the airfoil leading edge has been investigated compared with Rapid Distortion Theory and supported experimentally with hot wire anemometry and stereo-PIV measurements. It has been shown that the distortion effects are concentrated in a narrow region close to the stagnation point of the leading edge, with dimension of the order of its radius of curvature, and that the turbulence intensity grows significantly as the flow approaches the airfoil leading edge. Results have shown that the modified von Karman spectrum [73, 36] which used as an input to Amiet's model reached a good agreement with the measured sound fields.

Paruchuri *et al.* [113] performed an extensive experimental study on the influence of airfoil geometry on TIN. A sensitivity analysis on the airfoil sound power level reduction ΔPWL by varying the airfoil thickness and leading-edge nose radius has been done, comparing the results to a flat plate case. It is concluded that small modifications on the leading-edge profile (nose radius, maximum thickness etc) act significantly on the gust distortion in the vicinity of the nose radius. The noise prediction due to the gust distortion can not be fully captured only by accounting for thickness, nose radius and position of maximum thickness. The use of empirical models for applying thickness correction factors to Amiet's theory has been made as well as CAA predictions.

In the present work, in view of experimental evidence for broadband noise from impinging turbulence, the effects of airfoil shape and angle of attack are all ignored, except the relative thickness. Indeed the latter causes a strong reduction of TIN, which leads to reconsider the balance between TIN and TEN. This point has to be included in discussions in order to properly extract the TIN reduction by LE serrations. However, attempting sound predictions including the effect of thickness are beyond the scope of this work.

2 Experimental Setup and Instrumentation

Contents

Summary

The biggest part of this thesis consists of experimental techniques performed in the anechoic open jet wind tunnel of E6 building at ECL. Thus, this chapter describes the experimental setup both for the acoustic and the aerodynamic measurements performed in E6. An overview of the theoretical and the practical background of the experimental techniques is presented; the acoustic far-field spectra, the noise localization technique, the hot wire anemometry and the turbulence noise prediction.

2.1 Experimental Setup and Instrumentation

All acoustic measurements have been conducted in the low-speed anechoic open-jet wind tunnel of Ecole Centrale de Lyon (ECL). Successive layers of rectangular glass wool panels are used as acoustic treatment on the chamber walls. The overall dimensions of the open space in the anechoic chamber are 6.4 m (length), 4.6 m (width), 3.8 m (height) and the lowest cut-off frequency threshold where deviations from the decay law $p \sim 1/r$ start to appear is in the region of 80 Hz. Six axial-flow fan stages deliver the flow from an external environmental inlet to the outlet in the anechoic chamber. Fan noise is absorbed by liners embedded in the duct in the streamwise direction and upstream the outlet nozzle. Considering fan stages operation independence while installing various cross-section nozzles the outlet flow speed can range up to 60 m/s (for a round jet of about 10 cm diameter). A top view sketch of the wind tunnel installation is presented in Fig. 2.1.

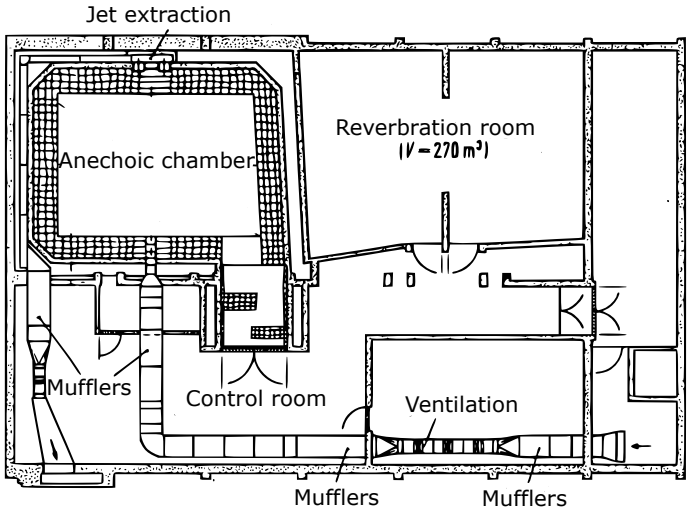

Figure 2.1: Top view schematic of the 'low-speed anechoic open-jet' wind tunnel installation at ECL.

In the present experiment, a rectangular nozzle with a vertical outlet cross-section of 15 cm x 30 cm is used for delivering a uniform flow into the anechoic chamber with a speed ranging from 19 m/s to 32 m/s. In all tested configurations the contraction ratio of the nozzle is 2:1 (from an initial section of 30 cm x 30 cm) and the turbulent flow is generated by a grid placed upstream the contraction. The grid is made of thin flat bars of 10 mm width and 2 mm thickness, and it has a mesh size of 5 cm (Fig. 2.2). The grid produces nearly homogeneous and isotropic turbulence, as confirmed by hot-wire measurements performed in absence of the airfoil at the location of the leading edge. A single hot-wire probe was used to this end. The turbulent intensity and the integral length scale have been found of 4.5% and 9 mm, respectively by fitting a von Kármán spectrum model on the measured streamwise velocity spectrum. Details on the turbulence characterization are given in the next section.

All measurements have been performed at flow speeds 19, 27 and 32 m/s. A micro-

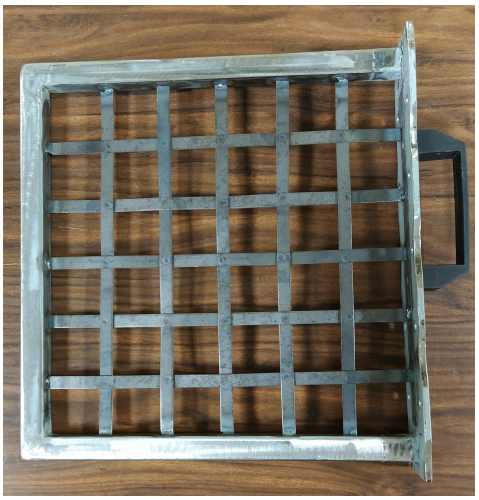

Figure 2.2: Metal grid for turbulence generation with perimeter dimensions 30 cm x 30 cm .

Table 2.1: Main flow conditions used for the present experimental campaign.

Flow condition	U_0 (m/s)	Temperature (°C)	Water height (mmH_20)	P_{atm} (hPa)	Fan (No)
Clean flow	U=19	T=23	$\Delta h = 21$	101700	n^o6(10')
Clean flow	U=27	T=23	$\Delta h = 45$	101700	n^o1+n^o6(9')
Clean flow	U=32	T=21	$\Delta h = 62$	101700	n^o1+n^o2+n^o6(8')
Turbulent flow	U=19	T=13	$\Delta h = 22.3$	99100	n^o1
Turbulent flow	U=27	T=15	$\Delta h = 45$	99575	n^o1+n^o2
Turbulent flow	U=32	T=15	$\Delta h = 63.8$	99985	n^o1+n^o2+n^o3

manometer type FCO510, a pitot tube and a thermocouple were used for calculating the free stream velocity at the nozzle outlet according to

$$U_0 = \sqrt{\frac{2\rho_{man} g \Delta h}{\rho}} \tag{2.1}$$

ρ_{man} is the liquid (water) density inside the manometer, ρ is the air density, g is the gravity standard acceleration and Δh the manometric height. As mentioned before, the velocity speed varies according to the selected fans. Fans n^o 1 to 5 have imposed, fixed rotational speeds. The rotational speed of fan n^o 6 is controlled by a potentiometer providing the desired flow speed adjustment. It is essential to keep the same flow speed in tests performed with and without turbulence grid. The main flow conditions used for the present experimental study are summarized in Table 2.1.

All tested airfoils were held between two narrow supports which minimize sound reflection or masking and allow for far-field measurements in a wide range of oblique directions off the mid-span plane (Fig. 2.3). A rotating vertical arc of six microphones $B\&K$ 1/2" type 4189 with preamplifiers of type 2671 is used to scan the three-dimensional radiating pattern of TIN on a portion of sphere, the measuring point being defined by its spherical coordinates (R, θ, ϕ), with origin at the mid-span leading edge of the baseline airfoil. A

calibration has been applied on each microphone of the arc antenna before every experimental campaign. All recorded signals have been corrected with the sensitivity factors given by the calibration for each microphone.

The microphones are equally distributed along the arc from $\phi = 0°$ (mid-span plane) to 75° by steps of 15°. The arc is attached to one end of a horizontal bar, the other end of which is fixed on a vertical pylon aligned with the airfoil leading edge. The pylon is fixed on a rotating table, so that the angle θ of the meridian plane of the arc from the streamwise direction is varied between 20° and 110°. The microphone distance to the airfoil leading-edge center point taken as origin is $R = 1.25\ m$. x is the horizontal, streamwise/chordwise coordinate and y the spanwise coordinate. The azimuthal angle θ is varied by making the horizontal support of microphones move in the (x, z) plane and the polar angle ϕ is explored along the vertical arc of the support. The whole setup is shown in Fig. 2.3.

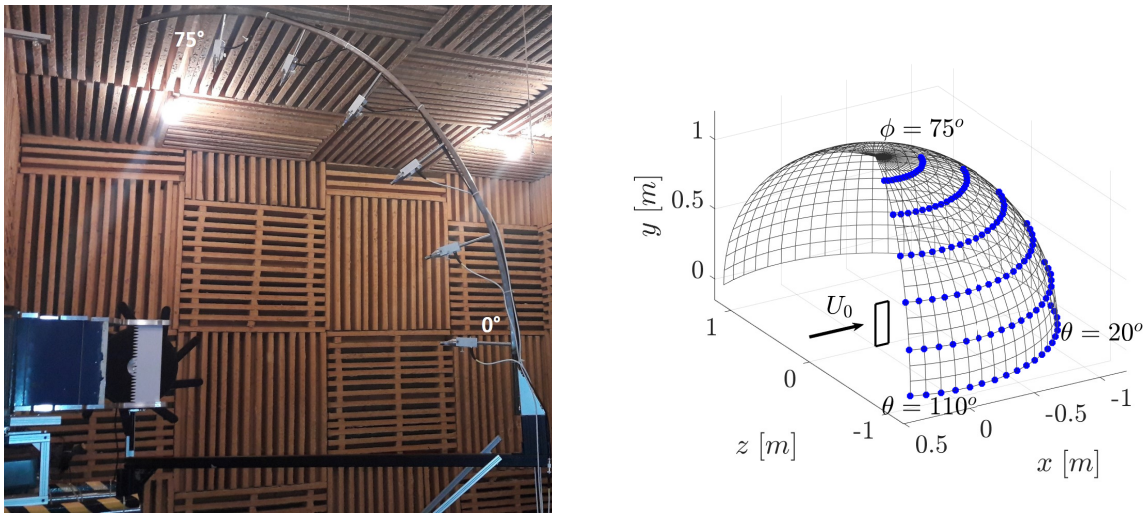

(a) (b)

Figure 2.3: (a) Photograph of the setup showing the nozzle on the left, the installed airfoil (white rectangle) and the circular arc of microphones in the ECL anechoic chamber. The black multi-branched structure behind the airfoil is the microphone array used for source localization. (b) Corresponding schematic of the measuring points over the whole surface of the explored spherical area.

The acquisition of the acoustic pressure has been made for the six microphones connected to an external unit $PXI - 1036$ averaging on 30 samples of 1 second, with the sampling frequency 51.2 kHz and a frequency resolution of 1 Hz. When making spectra subtractions, the resolution has been reduced to 16 Hz in order to avoid the large high-frequency scatter due to statistical errors. Fig. 2.4 displays the measured noises spectra for the microphone in the mid-span plane. The Fig. 2.4-(a) shows the frequency resolution modification from 1 Hz to 16 Hz. A comparison between TIN and background noise with the installed turbulence grid is shown in Fig. 2.4-(b).

The design of the upper and lower narrow support plates has been done empirically to

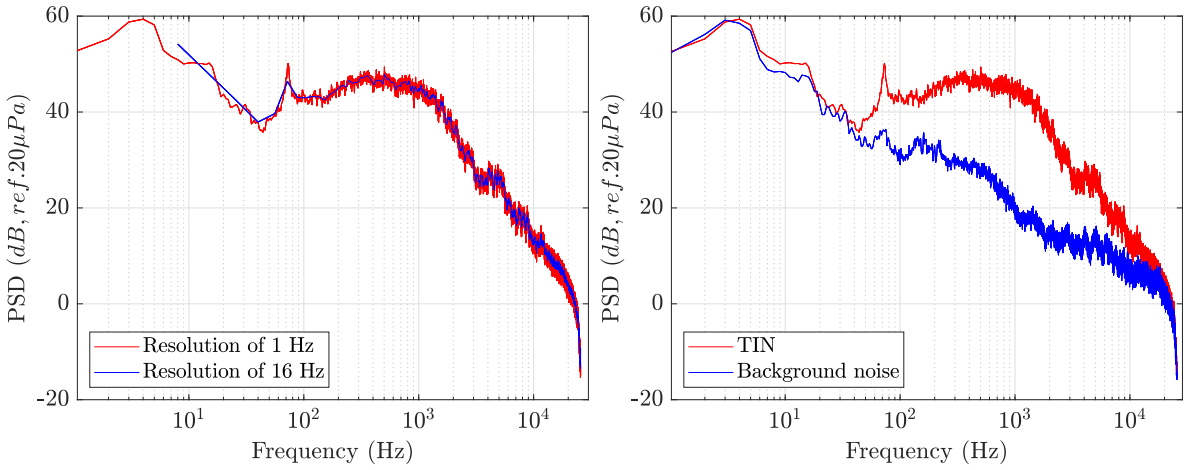

(a) (b)

Figure 2.4: TIN measured in the far-field at 90° in the mid-span plane for the baseline flat plate with (a) two different frequency resolutions of 1 Hz and 16 Hz. (b) TIN and background noise spectra with the installed turbulence grid.

expectedly minimize their aerodynamic and acoustic influence on the measured acoustic signature in the far-field (see Fig 2.5). The progressive reduction of the end-plates width ensures a nearly smooth development of the jet shear layers and acoustic visibility in all directions of radiation avoiding masking effects. However, the interaction of the shear-layer oscillations with the narrow supports generates different background noise sources, when compared to the case of extended plates more currently used.

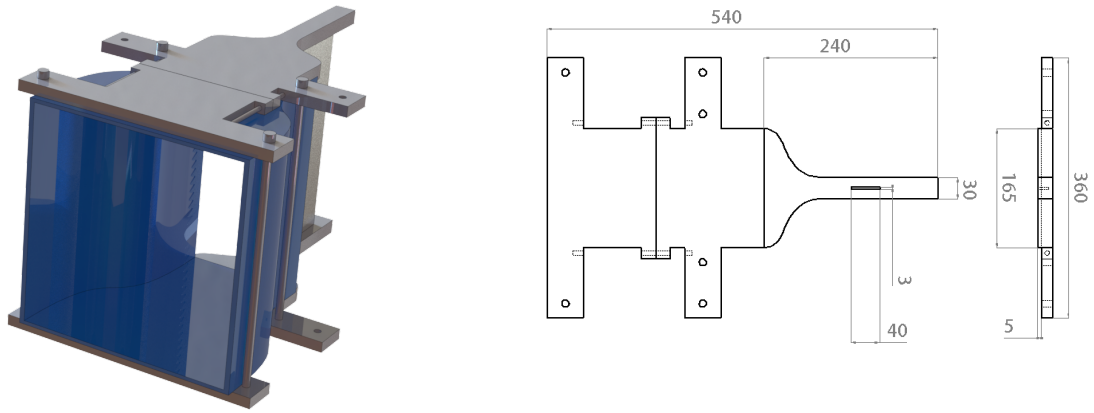

(a) b)

Figure 2.5: (a) Narrow support plates installed on the outlet nozzle in gray and (b) their corresponding dimensions in *mm*.

2.2 Turbulence Spectrum Characterization and Hot-Wire Instrumentation

Hot-wire anemometry has been used for getting access to the boundary layer parameters as well as to the near wake losses at the trailing-edge position. Measurements have been done with various airfoils in different configurations. The spectrum of the turbulence is measured for the streamwise velocity component. The whole setup is shown in Fig. 2.6-(a) with the installation of the large end-plates that must be used for complementary assessment of the effect of angle of incidence. The hot-wire probe and a Pitot tube are placed on a rigid motorized support measuring simultaneously the velocity fluctuations and the mean velocity at the same location respectively. The motorized supporting system allowed to move the probe normal to the incident flow direction with an accuracy of $0.0005\,mm$, thus nearly normal to the wall of flat-plate airfoils. The instrumentation communicates with the recording software by an acquisition system and provides simultaneously indications of the airflow temperature, the ambient temperature, the mean velocity, the instantaneous velocity and the position of the probe. These indications are provided by a thermocouple, a Pitot tube and the probe which are placed in the flow. A single-wire small-size sensor Dantec DYNAMICS, probe-type 55 P01, with a sensor resistance of 3.15 Ω was used for the HWA.

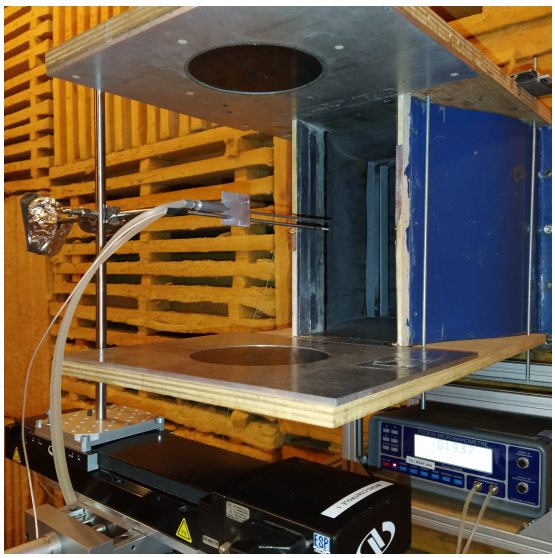

(a)

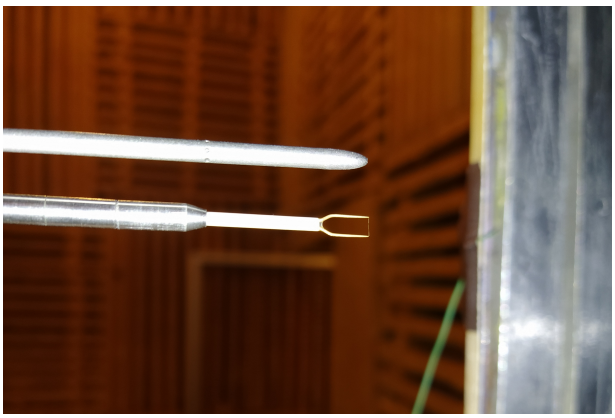

(b)

Figure 2.6: Hot-wire anemometry calibration setup: (a) Measurement of the turbulent streamwise velocity component at the center of the nozzle outlet. The larger end-plates are installed instead of the narrow supports. (b) Zoom on the hot-wire probe and Pitot tube.

2.2.1 Calibration

All the series of measurements are followed by a velocity calibration of the system linked to atmospheric temperature and reference pressure. The calibration curve is obtained in clean air flow for different flow speeds. One example of the performed calibrations is shown in Fig. 3.37. The offset temperature of the probe is set to $T = 200$ °C and the probe activated only when the airflow is on to avoid overheating.

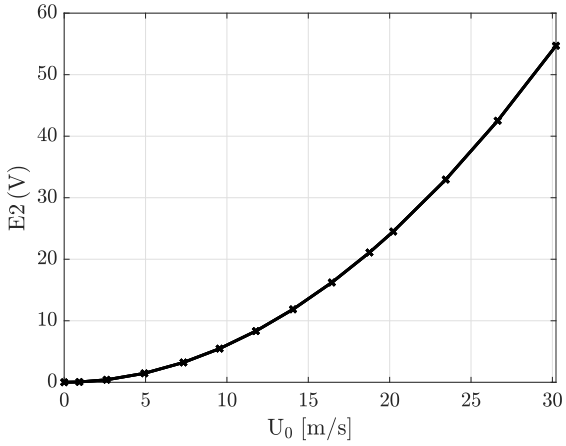

Figure 2.7: Hot-wire calibration curve. The probe is located at the center of the nozzle in a clean flow at $P_{ref} = 98090\,Pa$ and $T_{ref} = 18$ °C.

2.2.2 Free-Stream Measurements

The free-stream velocities in different positions along the steamwise direction have been measured under different conditions. Only the streamwise velocity component has been measured for the flow characterization in both clean and turbulent conditions. The clean flow was ensured by removing the grid from the nozzle. Table 2.2 shows the measured velocities with and without grid, as well as the different positioning of the HW probe (parallel/vertically to the flow). The value $x = 0$ was considered as the nozzle outlet position as shown in Fig. 2.8.

2.2.3 Turbulence Spectrum

The stream-wise velocity spectra are measured at the nozzle outlet by a single probe placed at the center of the cross-section. Therefore, the mean velocity profile and turbulent intensity is computed for clean and turbulent flows. The time history of the velocity field is measured for 120 seconds and the spectrum is calculated on an acquisition time of 20 seconds. The sampling frequency is set at 102400 Hz.

The statistics of the upwash turbulent component, normal to the airfoil surface, is needed for the modeling of the radiated noise. It would require a cross-wire two-dimensional anemometry. In our case, the Power Spectral Density (PSD) is provided only for the streamwise velocity component because of the single hot-wire probe. Therefore, the w_{rms}

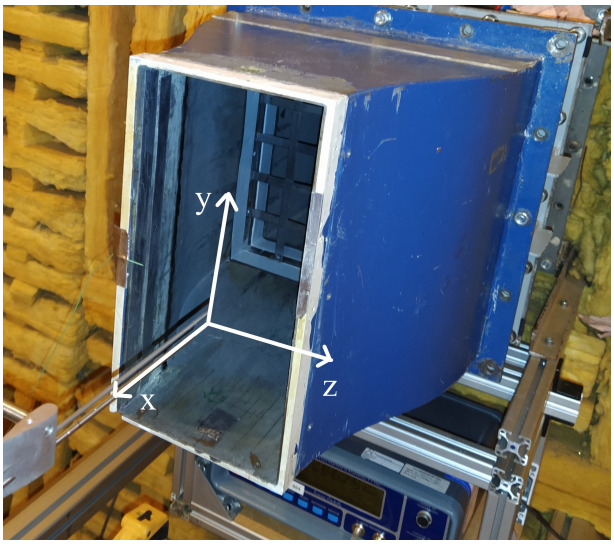

Figure 2.8: Measurement of the turbulent streamwise velocity component at the position $x = 0$ that is considered as the center of the nozzle outlet. The probe is placed parallel to the flow.

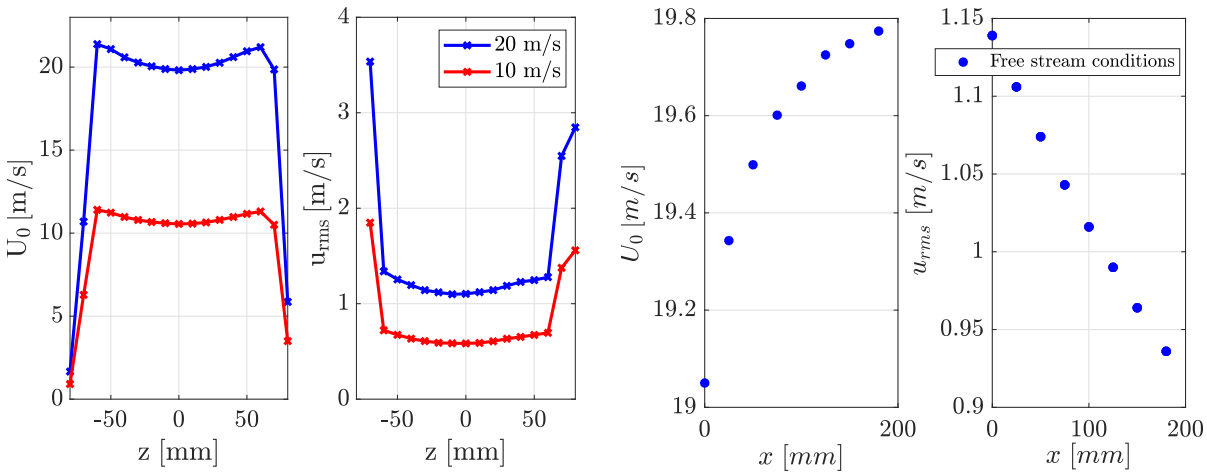

(a) (b)

Figure 2.9: (a) Streamwise mean velocity (left) and Root Mean Square (RMS) velocity (right) measured along the nozzle width (z-axis) for a turbulent flow at $P_{ref} = 96673\,\text{Pa}$ and $T_{ref} = 18,3\ ^\circ\text{C}$. (b) Velocities in different positions in streamwise direction (x-axis) on the center line at free stream conditions, $P_{ref} = 99078\,\text{Pa}$ and $T_{ref} = 14.5\ ^\circ\text{C}$.

is fitted by u_{rms} reconstructing S_{uu} spectra instead of S_{ww} using the von Kármán spectrum model [31] for the parameters (u_{rms}, Λ). The turbulence integral length scale is calculated by fitting the theoretical curve to the experimental as shown in Fig. 2.10. It has to be noted that the experimental fitting on the von Kármán spectrum model includes an uncertainty due to a possible anisotropy of the turbulence. Here, this uncertainty has not be considered.

When made dimensionless by the Strouhal number based on the inlet velocity U_0 and

Flow condition	Position (mm)	U_0 (m/s)	u_{rms} (m/s)
Probe parallel to the flow			
Clean flow	$x = 50$	$U = 21.5$	$u_{rms} = 0.061$
Turbulent flow	$x = 0$	$U = 18.9$	$u_{rms} = 1.102$
Turbulent flow	$x = 50$	$U = 19.3$	$u_{rms} = 1.030$
Turbulent flow	$x = 50$	$U = 19.3$	$u_{rms} = 1.030$
Turbulent flow	$x = 100$	$U = 19.5$	$u_{rms} = 0.939$
Turbulent flow	$x = 130$	$U = 20.0$	$u_{rms} = 0.957$
Turbulent flow	$x = 180$	$U = 19.6$	$u_{rms} = 0.898$
Probe transversal to the flow			
Turbulent flow	$x = 50$	$U = 19.9$	$u_{rms} = 1.010$
Turbulent flow	$x = 100$	$U = 20.1$	$u_{rms} = 0.957$
Turbulent flow	$x = 180$	$U = 20.2$	$u_{rms} = 0.886$

Table 2.2: Free-stream velocities measured in different positions along the steamwise direction. Two different positions of the HW probe have been used (parallel/vertically to the flow.)

the turbulence integral scale Λ, $St_\Lambda = f\Lambda/U_0$, the measured dimensionless streamwise spectra, S_{uu}/U_0, collapse at all speeds. This allows deducing the spectrum for the complementary crosswise or upwash velocity component that is used as input for subsequent analytical predictions. Λ has been found to be 9 mm and the turbulent intensity to be 4.5%. As shown by Moreau & Roger [98], a better agreement with measurements can be obtained at all frequencies, if an exponential correction factor is added [112], as Eq. 2.2. The resulting high frequency exponential correction β_1 is 8×10^{-4}.

$$S_{uu}(\omega) = \frac{\frac{u_{rms}^2 \Lambda}{\pi U_0}}{[1 + (\frac{k_1}{k_e})^2]^{5/6}} e^{-\beta_1 (\frac{k_1}{k_e})^2}, \qquad k_e = \frac{\sqrt{\pi}}{\Lambda} \frac{\Gamma(5/6)}{\Gamma(1/3)} \tag{2.2}$$

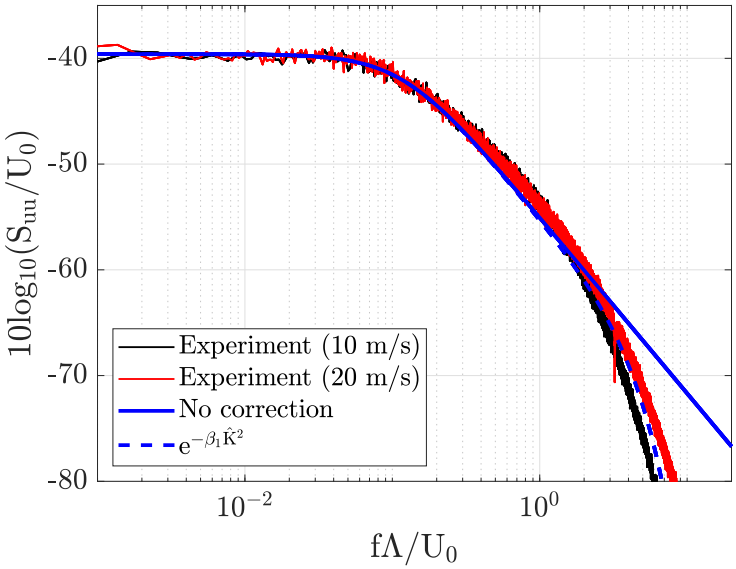

Figure 2.10: Streamwise velocity spectra measured 5 cm downstream of the nozzle exit. Flow speed 10 m/s (black), 20 m/s (red). Blue curves corresponding to the predicted turbulence spectrum by von Kármán spectrum model. $P_{ref} = 96673$ Pa and $T_{ref} = 18.3$ °C.

2.3 Airfoil Self-noise

Airfoil self-noise has been measured for all the isolated airfoils with and without serrations, by removing the turbulence grid from upstream the nozzle to obtain a clean flow. Therefore, the flow speed was adjusted properly at the flow speeds 19, 27 and 32 m/s. A medicine tape of 1 mm thickness was used as a tripping device for energizing airfoil boundary layers in turbulent condition. This acts destructively to the Kelvin–Helmholtz instabilities in the LBL region. DNS studies have shown that the observed generated tones stem from the Kelvin–Helmholtz instabilities which are much more amplified than that of the Tollmien-Schlichting boundary layer instabilities [143]. Different tripping devices were tested either with high or small thickness placed at the maximum airfoil thickness position. The following plot indicates that the two medicine tapes with slightly different thicknesses that were used cancel properly the undesired tone at 5 kHz without modifying the spectrum in the broadband zone.

The turbulence spectrum has been also evaluated for the clean flow condition 5 cm downstream the nozzle exit. The spectra for both turbulent and clean flows are presented in Fig. 2.12.

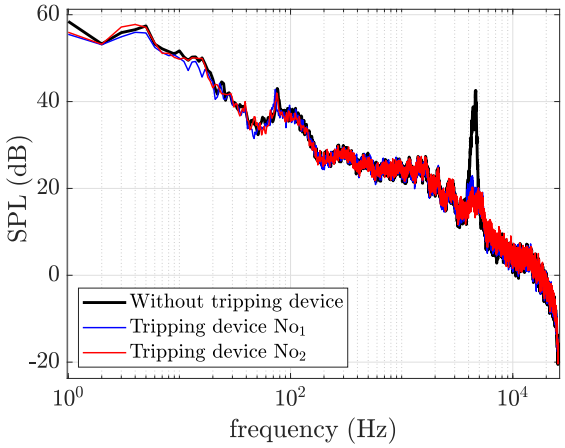

Figure 2.11: Self-noise measured in the far-field at 90° at 32 m/s for a baseline flat plate. Black line represents the LBL noise without the use of tripping device whereas the red and the blue lines correspond to two tripping devices with slight differences on their thickness. The resolution is 1 Hz and the background noise is not subtracted.

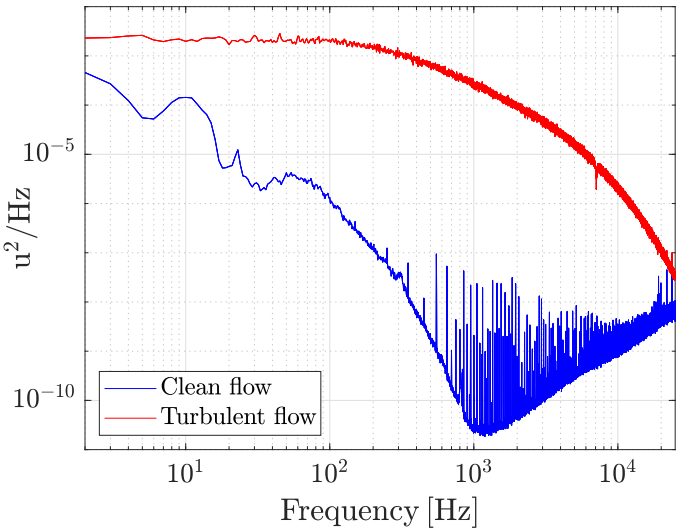

Figure 2.12: Stream-wise velocity spectra measured 5 cm downstream the nozzle exit for clean (blue) and turbulent flow (red). U_0 =20 m/s. The residual turbulence in clean flow measured beyond 1 kHz is explained as electrical noise effect due to the low amplitude signal.

2.4 Source Localization Technique

A spiral microphone array consisting of 81 sensors (MEMS) placed 0.5 m away from the airfoil and parallel to the flow direction is used for source localization (Fig. 2.13). The sampling frequency of the recorded signals is set by the LMS software either at 25.6 kHz or at 51.2 kHz depending on the frequency range of interest. The measurements have been performed on one airfoil side only, since all the measured airfoils have symmetrical profiles.

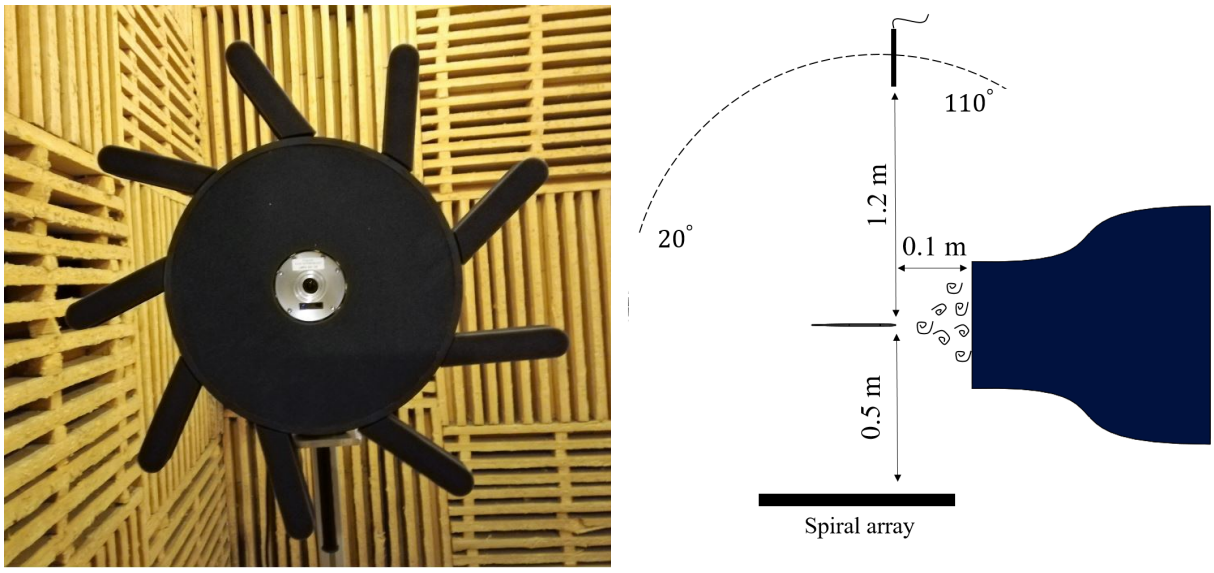

(a) (b)

Figure 2.13: (a) Photograph of the spiral microphone array as viewed from the airfoil and (b) the schematic of the whole setup (nozzle, the airfoil and the microphone antennas locations) from a top view.

Advanced post-processing techniques of microphone arrays that extend the capabilities of conventional beamforming (CBF) can be used to extract and quantify the acoustic signature of one source from a total sound field in which several sources contribute. They have been recognized as a crucial need in the present work to solve the high-frequency issues in the TIN studies associated with trailing-edge noise. Here the deconvolution algorithm called CIRA operated by LMS software has been used. It has been developed by ONERA in 1994 and is based on classical beamforming. A detailed description of the method is given by Piet *et al.* [118]. Only the main aspects are outlined here. CIRA denotes a branch of advanced sound source localization algorithms which overcomes some of the significant drawbacks of conventional beamforming. The spatial resolution limits have been broadened, improving the performance at low frequencies. Therefore, the source identification and separation in case of several sources is made possible, as well as a relevant estimate of power-level spectra for each source.

The CIRA method extends beamforming algorithm calculating the pressure signals $p_m(\omega)$, as the integration of the contribution of N multiple sources for sensors numbered by m:

$$p_m(\omega) = \sum_{i}^{N} p_{mi}(\omega) = \sum_{i}^{N} h_{mi} A_i(\omega) \tag{2.3}$$

where $h_{mi}(\omega)$ is a steering acoustic propagation function for sensor m and source i and $A_i(\omega)$ is the source i amplitude. Similar to the beamforming technique, an averaged cross-spectrum between sensors m and n is calculated, then the beamforming result reads

$$P_j^2(\omega) = \frac{\sum_m^M \sum_n^M \sum_i^N h_{mj}(\omega) h_{mi}^*(\omega) h_{ni}(\omega) h_{nj}^*(\omega) |A_i(\omega)|^2}{\sum_m^M \sum_n^M |h_{mj}(\omega)|^2 |h_{nj}(\omega)|^2} = \sum_i^N H_{ij} |A_i(\omega)|^2 \tag{2.4}$$

or, in matrix form,

$$\mathbf{B}{=}\mathbf{H}.\mathbf{S} \tag{2.5}$$

The solution of the above problem is calculated using an iterative optimization algorithm called steepest gradient descent. Finally, for each iteration the solution will be updated by the computed residual. The column vector $\mathbf{B}$ contains the beamforming results $B_j = P_j^2$, where $(1 \leqslant j \leqslant N)$, the array $\mathbf{H}$ is the array response matrix of elements H_{ij}, where $(1 \leqslant i \leqslant N, 1 \leqslant j \leqslant N)$ and $\mathbf{S}$ is the column vector that gives the squared amplitudes of i sources $S_i = |A_i|^2$, where $(1 \leqslant i \leqslant N)$.

In particular the low-frequency spatial resolution limit is evaluated from the condition $R_B/L_s \lesssim 0.5$, where $R_B \backsim L\lambda_\alpha/D$ is the beamforming spatial resolution, L_s the overall scan map extent, D the dimension of the array, L the typical distance between the center of the array and the mid plane of the measured area and λ_α the acoustic wavelength. So the lowest frequency that this method could evaluate is 572 Hz according to the condition

$$f \gtrsim \frac{2\alpha L}{D L_s} \tag{2.6}$$

A correction must also be provided to account for the apparent source displacement caused by the flow-convection effect. The apparent displacement is estimated as

$$\Delta = \frac{edU}{\alpha L} \tag{2.7}$$

where d is the geometric distance between the microphone and the noise source and e is the thickness of flow crossed by the acoustic ray.

Again the reader will find details of the algorithms in the references. The technique is used as a tool in the present work and only practical implementation points are discussed. A previous application of the same method, using the same microphone array, and the comparison with other localisation techniques for airfoil-noise extraction is already described by Yakhina *et al.* [153].

2.4.1 Experimental Uncertainty

In all experiments, certain quantities are measured and then other quantities are determined from the measured data. The determination of the reliability of experiments is to evaluate the measurement uncertainties associated with the measured quantities. These uncertainties equal to a positive or negative deviation from the true value and the causes of the deviation can exist because of instrumentation, data acquisition, environmental conditions and others.

In the present experiments, the possible sources of uncertainties can be found in initial parameters such as flow velocity related to temperature, atmospheric pressure and the microphone positioning. Changes of the angle of attack is also an important parameter that noise emissions are sensitive. Nevertheless, it has been proved that small changes of AOA does not affect TIN, the main interest of this study. Additionally, the narrow support plates used for the acoustic measurements do not include any rotation motion.

The flow velocity was determined by a Pitot tube and a micro-manometer Furness FCO510 (see Sec. 2.1), which has the accuracy of calibration to 0.25 % of readings. The Pitot tube was aligned along the streamwise direction fixed with a rigid support. In fact, the water height (mmH_2O) was extracted from the manometer display having a deviation of ± 0.5 mm every 0.3 second approximately. The thermocouple wire located at the nozzle lips in the flow measured the temperature that was stable for a long period of time compared to the duration of the measurement at a constant speed. The atmospheric pressure was provided from a meteorological station located nearby and outside the wind tunnel while the pressure changes were also stable compared to the duration of one set of measurements. Nevertheless, considering uncertainties of $\Delta H = \pm 0.5$ mm, $T = \pm 1°C$ and $P_{atm} = \pm 10$ Pa the resulting velocity deviation is about of 0,3 m/s. Finally, the deviation of 0.3 m/s corresponds to $\pm$ 0.5 dB of difference in the far-field after the background noise subtraction. The microphone positioning was controlled remotely using a motor with an uncertainty of 0.5° to 1° degrees. According to Fig. 4.5 the directivity lobes in high frequencies appeared every 30° at least meaning that the variation of 1° is significantly small. Uncertainties on the PIV experiments are quantified from the errors on the instantaneous velocity fields which amount to less than 1% U_0 in the free stream-region and less than 3% U_0 in the boundary layer. The overall level of uncertainty reaches to 0.05% U_0 on the mean velocity and to the 2% $\sqrt{< u'u' >}$ on the time-averaged turbulent-intensity fluctuations. A detailed description for a similar tomographic PIV experiment is given by Ragni *et al* [119].

2.4.2 Concluding Remarks

In this chapter the experimental setup and the measurement techniques were described. A new setup of two narrow support plates and a rotating microphone array have been designed and used successfully for accessing to the directivity in three 3D space. The main flow conditions used for the present experiments have been listed by performing hot wire anemometry measurements. Using the same technique, the spectrum of the incoming turbulence has been estimated and also predicted using von Karman spectrum with a Pao's Gaussian high frequency correction. The jet has been also characterized by measuring the velocity profile at the exit of the nozzle as well as the mean velocity and the turbulent intensity at different streamwise positions. Procedures of noise spectra subtraction and frequency resolution reduction were used for all signals giving an example for each case. The airfoil self-noise measuring procedure has been described and the suppression of the tone generated by the Kelvin–Helmholtz instability waves has been performed.

3 Airfoils With and Without Sinusoidal Serrations

Contents

Summary

A detailed literature review on turbulence impingement noise reduction by means of serrations and its identification with experimental techniques is presented. The design and the use of the flat plates and the NACA-0012 airfoils with and without serrations are basic elements that the whole study is based on. The determination of the acoustic signature in the far-field for all the aforementioned airfoils is considered essential for estimating the TIN reduction by the serrations application. All the investigations in the far-field have been done in three-dimensional aspects using the rotating microphone antenna. At a second stage, TIN reductions have been explored deeper with the noise localization technique using the spiral microphone antenna. The identification, estimation and extraction of the leading- and trailing-edge sources are described as a second step procedures for evaluating the real performance of the wavy leading-edge serrations as a noise reduction device. Noise evaluations in PWL gives an integrated information of the acoustic source content, taken as a whole. The aerodynamic efficiency of each airfoil has been also estimated by measuring the drag coefficient at the wake of the trailing edge. Finally, all the blades have been compared each other in terms of acoustic and aerodynamic efficiency.

3.1 Noise Reductions Mechanisms Description

Taking into account only two-dimensional aspects of the unsteady flow and only intuitive time-delays or phase-shifts, one basic noise reduction mechanism can be related to the interference of two correlated sources at a given frequency. Within framework the distance from each other as well as the their propagation-path lengths to the observer yield to a possible partial cancellation of the two sounds depending the phase opposition. For the flat plate case, this can be easily estimated by inspection of the involved acoustic and geometrical parameters; hydrodynamic wavelength $\lambda_h = 2\pi U_0/\omega$, the acoustic wavelength λ_a, where $\lambda_h = M\lambda_a$, and the serration pitch λ and depth $2h$, Fig 3.1. At low Mach number, λ_h is much smaller than λ_a, whereas both have the same order of magnitude as M approaches 1. A key parameter for obtaining noise reductions is to ensure, or not, aerodynamic and acoustic compactness. If the pair of point sources is not aerodynamically compact, both point sources partly cancel each other, with nearly no propagation-path difference as long as acoustic compactness is ensured, $\lambda \ll \lambda_a$ or $h \ll \lambda_a$. As a result, serrations are able to produce a significant sound reduction. In addition, the reduction is expected an increasing function of frequency, as resulting from an increasing phase shift. In the very-high frequency range for which the serrations are no longer acoustically compact, individual serrations tend to decouple, and considering the edges of each serration as swept airfoils of limited span makes sense. The sound reduction becomes a pure effect of sweep

in this case.

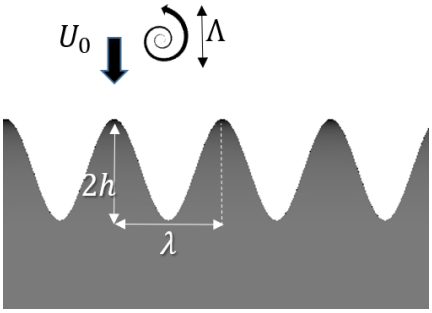

Figure 3.1: Schematic representation of leading-edge serrations parameters.

The noise reduction mechanism of serrations is activated by matching properly the integral length scale Λ of the impinging turbulence with the half of the serration wavelength. In that way, both serration peak and root are excited. Paruchuri *et al.* [32] proved the existence of an optimum serration wavelength that noise reduction maximized, $\lambda/\Lambda \approx 4$. Serrations tuned following this condition should provide noise reduction that follows the proposed empirical trend of $10\log_{10}(St_h)+10$ [32] as shown in Fig. 3.2. Below this number the adjacent valleys are excited coherently leading to constructive interference in the far-field whereas below this limit incoherently. This mechanism is different from the destructive interference mechanism existing at the peak-to-hill regions of the crest as it was named by Narayanan [105]. Additionally, the above relationship has been explained theoretically considering it as a problem of distributed compact sources over the airfoil span located at the valley positions. separated one wavelength λ apart. It is based on the finding of Kim *et al.* [75] that the noise sources at the valleys are dominant due to compactness. Also the condition $\lambda/\Lambda \leq 4$ uses the assumption of uncorrelated sources in all the spectrum.

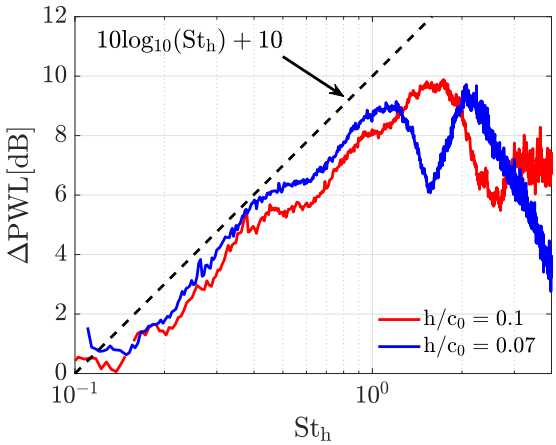

Figure 3.2: (a) Total sound power level reductions ΔPWL for the serrated flat plates $h/c_0 = 0.1$, $\lambda/\Lambda = 1.4$ (red) and $h/c_0 = 0.07$, $\lambda/\Lambda = 1.7$ (blue) at $U_0 = 32$ m/s. Comparison with $\Delta PWL = 10\log_{10}(St_h)+10$ (dashed) validates its use according to [32], where $St_h = fh/U_0$ is the Strouhal number.

Therefore, after the proper excitation of the serrated leading edge by the impinging turbulence, distributed sources are generated along the wavy edge (Fig. 3.3). Mean square surface pressure fluctuations at the peak and at the root have been found in strength similar as at the straight-edge counterpart. The hill region presents a reduced level of surface pressure fluctuations translated as a weak source of sound. Kim [75] characterized it as a source 'cut-off' effect. Noise reductions at the hill region could be expressed with $\overline{p_0'} \propto \cos\theta$ due to the sweep angle close to center of the hill (Roger & Carazo [122]). In addition, the increase of the serration amplitude (obliqueness) decreases the correlation along the serration arc with reference the peak position. It is observed that the correlation length scale along the arc is decreasing linearly with the increase of h, diversely to the increasing trend of the empirical expression $10\log_{10}(St_h)$ [32].

This leads to degraded noise emissions in the far-field (Fig. 3.3). Auto-spectra of surface pressure correlation have shown that low-frequency components are stronger at the trough whereas high-frequency components are stronger at the peak. The existence of dominant high-frequency components at the peak confirms also the functionality of the destructive interference in high frequencies at this region. Indeed, Cross-spectra have shown a reduction in mid-high frequencies from the peak position to the hill center along the serration arc whereas an increase of low-frequency components occurs approaching the trough [147]. The region between the peak and the hill shows an increased level of phase interference, they are fully out-of-phase (destructive interference) at mid-high frequencies. Comparing to the far-field noise reductions, the frequencies at which high phase-shifts occur compare to the straight edge, the maximum noise reductions achieved in the far-field.

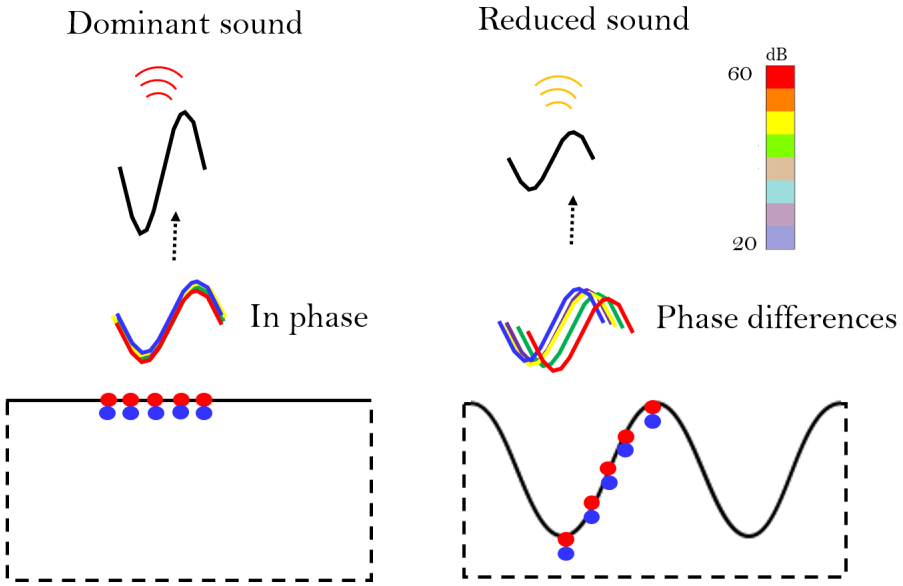

Figure 3.3: A schematic of the 'cut-off' effect due to the obliqueness of the serration arc compared to the straight edge.

Since the flow is guided in the serration trough, it is expected to be a significant source of sound as shown in Fig. 3.4. Indeed, the source strength at the root maintained at the level as at the straight edge counterpart and does not seems to change much in function to the serration depth. Despite this fact, the velocity perturbations at the root appear to be double in strength that the straight-edge counterpart. The source at the peak is weaker due to the reduced level of vertical velocity perturbation stem from the counteracting effect of streamwise vortices [147].

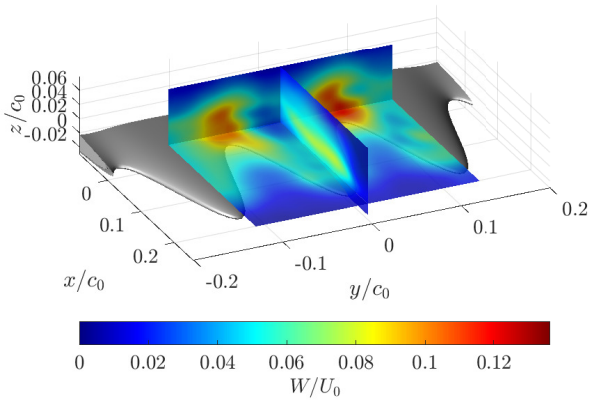

Figure 3.4: Planes of the mean vertical velocity component for the serrated flat plate.

In the far-field, although the surface pressure fluctuations at the trough and peak seem to have similar strength, the two-point correlation between observer (far-field) and the surface pressure fluctuations has shown that the source at the peak is less correlated than those at the root. In addition, the coherence level in low-frequency range is reduced, $St_h < 0.5$, where noise reductions in the far-field do not exist [147].

3.2 Bibliographical Review

Experimental investigations on the aerodynamic effect of airfoils with leading-edge serrations (LE) have been done by Soderman [141]. Flow field visualization showed that serrations introduce vortices that prevent stall at higher angles of attack maintaining the flow attached down to the trailing-edge. He observed that larger serrations block the flow at higher angles of attack causing flow separation sooner and decreasing lift. Inversely, smaller serrations caused increased lift by providing higher energy air to the boudary layer, reducing drag and delaying stall at higher angles of attack. Some years later Collins [42] observed also that introducing serrations on the leading edge of wings could improve lift and stall performances at low-speeds of aircraft during take-off and landing. Soderman [142] also studied the acoustic effects of airfoil leading-edge serrations applying them on rotors. Results have shown overall noise reductions between 4 and 8 dB and 3 to 17 dB in the high frequency ranges on a small-scale rotor and overall noise reductions up to 4 dB on a large-scale rotor at 800 and 1000 rpm. LE serrations applied on NACA 0012 and

NACA 0015 were tested at various blade angles and rotating speeds.

Hersh [65, 66], studied the effectiveness of LE serrations in mitigating the aerodynamic noise radiated by stationary and rotating airfoils (NACA 0012) in both clean and turbulent inflows. It is shown that properly placed serrations on the LE decrease the tonal noise generated by the fluctuating periodic motion near the TE by changing the vortex shedding of the wake from periodic to broadband. A successful comparison between a theoretical model and an experiment showed that the main source of the radiated sound is produced by the time-derivative of the fluctuating lift due to the incoming turbulence.

Miklosovic *et al.* [93], studied the aerodynamic effectiveness of humpback whale flippers with and without the presence of leading-edge tubercles. The idealized models of humpback whale flippers demonstrated that tubercles delay the stall dominantly in higher angles of attack till 20° by approximately 40%, presenting an increase of lift and a decrease of drag. The experiments have been done for Reynolds numbers $5.05 \times 10^5 - 5.20 \times 10^5$. Additionally, the authors tested aerodynamically two wings with finite (semi-span) and infinite-like span (full-span) [92]. Results for a full-span wing with scallops have shown decrease in lift and increase in drag conversely to the semi-span wing. Authors expect that scallops applied in semi-span wing operate beneficially in post-stall conditions, as the serrated leading-edge showed increasing lift and moment and decreasing drag at higher angles of attack.

Wang *et al.* [151] performed a numerical study on the aerodynamic performance of static and pitching NACA 0010-12 airfoils with and without leading-edge protuberances. The models are tested under laminar and turbulent flows by solving unsteady Reynolds Averaged Navier-Stokes equations with the k -ω SST turbulent model. Their results verify previous indications for serrated wings that they cause a delayed stall and an increased lift over the baseline case in the post-stall range. It is observed that surface-normal vorticity and stream-wise vorticity delay the stall, energizing the boundary layer to be longer attached to the surface.

The aerodynamic influence of undulating leading-edge modifications on a NACA 0021 airfoil was studied by Rostamzadeh [130]. Two wing cases were considered, a spanwise sinusoidally varried surface airfoil (wavy model) and a serrated airfoil with sinusoidal chord variations (tubercles model). Similar drag and lift characteristics were obtained in both cases using the circulation variable by applying Prandtl's nonlinear lifting-line theory. Experimental results showed that wavy airfoils yielded a gradual stall behavior whereas the airfoil with the highest peak-to-peak angular amplitude and smallest wavelength presented the most significant post-stall behaviour. CFD simulations have shown that a stronger adverse pressure gradient exists in the trough of the wavy airfoil close to the leading-edge region which forces flow to separation. Additionally, low pressure zone yielded at the same aforementioned region is responsible for the delay and the extended stall features as well as

the pairs of strong counter-rotating streamwise vortices in the airfoil wake. Similar aerodynamic characteristics have been observed on a serrated airfoil root-trough region. In general, wavy airfoils ensure higher maximum lift in a reduced angle at pre-stall conditions but present superior lift performance at higher angles at post-stall conditions compared to the unmodified wing.

Favier [45] performed a parametric study on wavy leading-edge geometrical variables in terms of aerodynamics using a three-dimensional incompressible Navier–Stokes solver. It has been found that a certain pair of the two leading-edge parameters (wavelength: $\lambda \simeq 1c$, amplitude: $A = 0.07c$ if c denotes the chord length) modifies significantly the wake topology for which a 35% reduction in drag occurs. For these geometrical values the flow is driven by the streamwise vortices caused by the bumps and the boundary layer is nearly attached to the surface downstream the serration peaks. The local flow reattachment seems to be caused by a Kelvin-Helmholtz-like instability driven by the spanwise modulation of the streamwise velocity profile.

Roger *et al.* [128] studied the sound reduction mechanisms of LE serrations in incoming turbulent flow, conducting experiments on a NACA 0012 and proposing an analytical noise prediction model of the response of a serrated LE in the limit of arbitrary large chord. This formulation was based on the generalized Amiet's theory and on a simplified strip-theory statement according to which the serrations are interpreted as a periodically varying sweep. It is discussed that the noise reduction efficiency is linked with the incident gusts sub-critical or supercritical character and of their inclination angle. Serrations reduce the response to supercritical gusts that carry the higher energy. Additionally, it is suggested that serrations effectiveness is connected with the Mach number. This experimental work was extended investigating airfoil turbulence-impingement noise reduction using NACA 0012 with wavy leading-edge and porosity [126]. Both technologies were compared giving promising results. Serrated flat-plates and NACA 0012 with $10cm$ and $12cm$ mean chord showed up to 10dB reduction at a chord-based Strouhal number of about 5-6 and the porous treatments up to 6dB in a slightly different frequency range. Noise reductions in high frequencies were decreased but also hardly discriminated because of the trailing-edge noise contamination.

Clair *et al.* [39, 40], in the framework of European Project FLOCON, studied experimentally and numerically the turbulence-impingement noise of a serrated airfoil. Noise reductions of 3-4 dB at high frequencies were observed at different flow speeds for a NACA65 airfoil with 0.15 m chord. RANS simulations and CAA nonlinear Euler approaches were used to predict the radiated sound. A mismatch on the sound power level (PWL) attenuation due to the serrations between experiments and CAA results has been found beyond 3.5 kHz, where the contribution of the oblique gusts ($k_y \neq 0$) was ignored. The effect of leading-edge serrations on aerodynamics and noise was emphasized using Amiet's thin airfoil theory as well as RANS solutions.

Lau *et al.* [81] performed numerical simulations of high-order accuracy on the effect of wavy leading-edge on airfoil-gust interaction noise. A suitable relation (ratio) between the geometrical parameters of the wavy leading-edge shape and the incident gust longitudinal (streamwise) wavelength (λ_g) is proposed for giving highest noise reductions. The noise reduction variation according to the leading-edge peak-to-peak amplitude (LEA) was defined by the ratio $0.3 \leq LEA/\lambda_g \leq 1$ for a constant serration wavelength in a wide range of propagation angles, whereas the less effective on the noise modifications is the serration wavelength which could varried between $1.0 \leq LEW/\lambda_g \leq 1.5$. Surface pressure time series along the serration tooth in the spanwise directions have shown a phase shift of the pressure fluctuations as well as weaker amplitudes compared to the baseline. Potentially, this leads to the acoustic destructive interference ([105, 75]) in the far-field sound radiation. Lastly, the acoustic efficiency of the wavy leading-edge is maintained for a variety of flow speeds and radiation angles particularly in high frequency ranges, and the large-amplitude serrations are the most effective.

A preliminary parametric study on the noise reduction effect from serrated leading edges has been carried out by Narayanan *et al.* [104]. The experimental investigations have been carried out for a flat plate with five different sets of leading-edge wavy pattern shapes and a NACA-65. Results confirmed the higher sensitivity of the teeth depth in terms of noise reduction compared to the teeth wavelength. It is observed that the serrated flat plate and airfoil reduce the noise by up to 8 dB and 4 dB at non-dimensional frequencies fc/α of 1.2 and 0.95 respectively. The flat-plate configuration was found to exhibit two humps of noise reduction at 1.9 and 2.5 non-dimensional frequencies compared to the one of the NACA-65. Visualizing the dependence between noise reductions and velocity in frequency domain, an increasing linear relation on the noise reduction efficiency is observed while the flow speed is increasing. In an extended work by the authors [105], it is confirmed that maximum noise reductions are obtained for the highest serration amplitude and large serration wavelength. The reduction is explained as a destructive interference phenomenon because of the wavy leading-edge pattern which creates incoherent sound sources along the span and chord length. Self-noise is mentioned as a reason for non-observable noise reduction at high frequencies where the trailing-edge noise is dominating. Significant noise reductions (above 3 dB) as a function of velocity and the serration depth $2h$ follow the linear relation $f_0 = \frac{\kappa U}{2h}$, where the parameter κ is determined by the lower frequency band (dashed line) that reductions take place. Narayanan *et al.* [105] defined this threshold with the expression $hf_0/U = 1/4$ after performing a parameterization analysis on the serration amplitude. Therefore, NR occur when the serration amplitude $2h$ is greater than the half aerodynamic wavelength $2h > \frac{U}{2f_0}$. Lastly, a successful interaction noise prediction with Amiet's theory has been implemented for the baseline flat plate whereas a computational simulation has shown a nearly good agreement in terms of PWL reduction till mid-range frequencies.

Paruchuri *et al.* [116] kept on investigating experimentally the sensitivity of the sound reduction with respect to the serration parameters and parameterised the sinusoidal serrated leading-edge geometries on the noise reduction by realistic airfoil geometries. They found that the optimum 'tuning' (noise minimization) is achieved by matching the half serration wavelength to the turbulence's integral-length scale. In addition, the existence of an optimum inclination angle of the teeth edge is observed, 70°-80°- approximately. Coherence spectra along the teeth have shown significant drops between the peak and valley positions, leading to the above matching observation. Additionally, the higher the serration amplitude, the wider are the frequency bands in which noise reduction occurs as the Strouhal number increases. Aerodynamic measurements have shown a drop in lift and increase of drag with angle the NACA65 airfoils. PIV measurements have shown that the overall aerodynamics performance is not degraded substantially.

An additional investigation on the noise reduction mechanisms [32] found the existence of an optimum serration wavelength λ_0 where the sound power is minimized. Equalizing the serration wavelength to nearly four times the turbulence integral length scale, the compact sources [75] at the adjacent valleys are excited incoherently. Inversely, sources with smaller adjacent distances interfere with each other constructively. At the optimum serration wavelength, the reduction in sound power level follows the trend $\Delta PWL(f) = 10\log_{10}(St_h) + 10$ where $St_h = fh/U$ and h is the serration amplitude that is proposed by Paruchuri *et al.* [116]. Thus, geometric similarities have shown that the sound power ratio between the serrated shape to the straight edge is found to be inversely proportional to St_h for $St_h \geq 0.2$. The inverse dependence suggests that the sources 'length' along the leading edge should be scaled linearly with the hydrodynamic wavelength $\lambda_h = U/f$. Despite the fact that serration valleys create thicker boundary layer profiles along the streamwise direction, serrations also cause a decrease on airfoil self-noise.

Identifying the interference significance of adjacent sources located at the serration roots, Paruchuri *et al.* [115] introduced three innovative leading-edge geometries that enhance noise reduction performances compared to conventional single-wavelength serrations. The general objective of these designs is to superimpose an additional source of sound at a secondary serration valley which is displaced in the streamwise direction. The proper distances h_{tt} (streamwise) and λ_{tt} (spanwise) between the root sources created a sound destructive interference by phase shifting. The geometries of double-wavelength serrations, slitted-root serrations and slitted-V-root serrations provided noise reductions up to 13 dB of sound power with one optimum hump whereas double-wavelength serrations broaden the efficiency in the frequency domain enhancing two maximum regions. A noise reduction sensitivity study on the h_{tt} and λ_{tt} parameters has been completed [114]. The streamwise distance between the adjacent roots h_{tt} affects the noise reduction efficiency in low frequencies due to their interference and the spanwise distance λ_{tt} the coherence degree of both sources. Maintaining the ratio $\lambda/\Lambda \leq 4$ as an optimum wavelength case for single-wavelength serration, both root sources ensure higher noise reductions than the

upper limit of $10\log_{10}(St_h)+10$ [32]. The ratio limit of 4 means that the spanwise distance between the adjacent roots should be less than twice the turbulence integral length scale, enhancing the noise reduction by at least 3 dB. Therefore, an analytical form based on sources interference is derived to express the total noise reduction as a sum of each root source contribution. The parametric study is applied on flat plates while representative 3D airfoils are tested giving similar acoustic performances.

Kim *et al.* [75] performed high-accuracy compressible Euler simulations on flat plates with wavy protuberances, investigating the underlying noise mechanisms of TIN. Setting-up a computational experimental configuration they combined near- and far-field spectrum data performing advanced spatial correlation, coherence and phase analysis along the arc length of the sinuous profile. It was shown that the linear increase of noise reductions with the serration amplitude is linked partially to the serration obliqueness (hill region) where the surface pressure fluctuations present a weaker level compared to the peak and the root. This is characterized as a source cut-off effect. Rapid decorrelation of surface pressure perturbations for high serration amplitudes is found to be the origin of noise reduction along all the frequencies whereas the peak and root local areas sustained their source energy comparable to that of the straight leading-edge counterpart. Observing similarities both in far-field noise reduction spectra and in relative difference in phase spectra from both profiles, the phase interference effect is identified as one of the TIN reduction mechanisms.

Turner *et al.* [147], based on a computational experiment similar to Kim *et al.* [75], described the link between the vortex-induced velocity perturbation time history and the corresponding wall pressure fluctuation on the wavy leading-edge profile. Imposing a prescribed spanwise vortex interacting with the flat-plate wavy geometry, it is observed that horseshoe-like secondary vortices are created stemming from the tooth peak area. Despite the fact that the horseshoe vortices (HV) enhance the vertical velocity perturbation around the valley by increasing the tooth amplitude, the source strength at the same position remains similar to that of the straight leading-edge counterpart. It is shown that the spanwise vorticity along the HV reduces the source strength at the peak by attenuating the vertical velocity fluctuations. This is also confirmed by using a semi-analytical expression based on Biot-Savart's law indicating that the HV-induced upwash and downwash vertical velocity components cancel each other as the tooth amplitude increases and finally converge to the upstream free-stream conditions.

3.2.1 Turbulence-Impingement Noise Investigation

Background-noise subtraction in the far-field provides an estimate of the noise radiated by the airfoil but it still combines TIN and TEN sources, the latter possibly masking the former at high frequencies. Therefore, additional efforts based on more advanced techniques are needed to isolate TIN and better understand the underlying physics. Nevertheless, even the background-noise is subtracted, the experimental investigation of specific noise sources like turbulence-impingement noise necessitates other methods that access to the near acoustic field and extract the right desired information. Some of these techniques are beamforming methods or similar based on the use of a microphone array. The first issue is to isolate TIN in order to produce convincing reduction spectra over an extended frequency range by subtracting far-field sound spectra measured with and without the modifications. It is addressed in Subsection 3.4.1. Refined estimates produced by an innovative use of microphone-array measurements are presented in Section 7.4.2. The identification of the background-noise sources is a necessary preliminary step when resorting to far-field measurements. In the present installation, contributions to the background noise are the noise coming from the inserted grid upstream of the contraction inside the nozzle, the mixing noise of the jet and the noise produced by the flow on the edges of the nozzle and on the narrow supports. In principle all background-noise contributions can be eliminated by subtracting the sound measured without the airfoil from the total noise measured with the airfoil. Yet at very low frequencies the oscillations of the nozzle-jet shear layers can interact with the airfoil surface even without direct impingement. This leads to equivalently consider that part of the background noise is modified when the airfoil is installed, which makes the subtraction questionable. This effect is only suspected at very low frequencies which do not enter the range of the presently investigated TIN. In addition, the interaction between large scale vortices coming from the free-jet shear layers with the airfoil wake generates a mixing noise that enters the very low frequency range. Numerical simulations of isolated into non-isolated airfoils overcome these obstacles and give an insight of their frequency range origin

Once the aforementioned background-noise sources are eliminated the measured noise still includes the TIN of interest and the undesirable TEN. A second subtraction procedure could be defined to eliminate TEN, typically by repeating the measurements without turbulence grid in the nozzle to estimate TEN separately. However the boundary layers may develop differently in both tests, therefore this part of the procedure becomes questionable.

3.3 Flat-Plates Design

Investigating turbulence-impingement noise, there is a need for creating a database for airfoils with and without serrations which will be easily considered as references and be comparable with analytical models which predict the broadband noise. Hence, two flat plates with wavy leading edges and one with straight edge as baseline have been manufactured with a three-dimensional printer. All flat plates have a thickness of 3 mm, a span of 30 cm and a mean chord length of 10 cm, see Fig. 3.7. The cross-section profile of the flat plates is designed creating a smooth round geometry at the leading edge and a sharp trailing edge. Similarly, the serration corners have been rounded to avoid artificial flow separation at the leading edge and a gradual decrease of thickness at the trailing edge has been done to avoid is vortex-shedding mechanism.

The cross-section is designed following the formula for a symmetrical 4-digit NACA profile, which is given below:

$$y_t = \pm 5t[0.2969\sqrt{x} - 0.1260x - 0.3516x^2 + 0.2843x^3 - 0.1015x^4] \tag{3.1}$$

where y_t is the thickness distribution above (+) and below (-) the mean line, t is the maximum thickness of the airfoil in percentage of the chord and x is the coordinate along the chord.

For the design of the assembly, a standard symmetric NACA-0004 shape has been split into two parts at its maximum thickness point and extended by adding a flat-plate portion in between. In this way, the flat plate of 3 mm thickness is merged smoothly with the serrations root and with the trailing edge. This transition is shown in Fig. 3.5

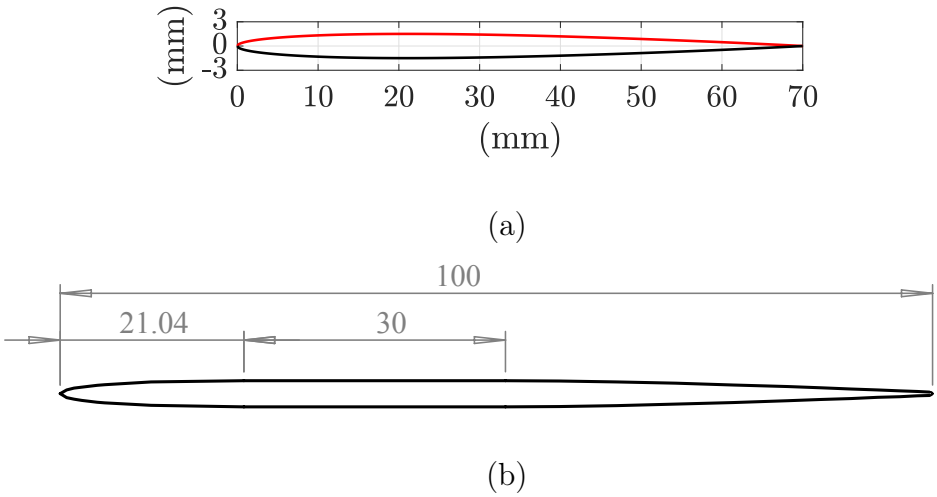

Figure 3.5: (a) Profile of a NACA-0004 with chord of 70 mm and (b) profile of the flat-plate (baseline) with thickness of 3 mm and chord of 100 mm merged by the NACA-0004 and a flat section of 30 mm. The dimensions in both profiles are in mm.

The parameters of the two serrated versions are defined according to the integral length scale $'\Lambda'$ of the incident turbulence which is 9 mm and the observations of Paruchuri *et al.* [116] about most efficient inclination angle and amplitude of the sinusoidal serrations for noise reduction. The airfoil with the bigger serrations is expected to be optimum in noise reduction whereas the smaller serrations are also tested to assess the sensitivity of the results. The results are compared with the baseline mock-up which is considered as reference. So taking into account the corresponding dimensionless parameters of amplitude $h/c_0 = 0.167$ and inclination angle $\theta = 76^\circ$ a first mock-up was printed, as well as a second one with a smaller depth of serrations. The parameters of both flat plates are summarized in the table of Fig 3.6-(a).

Parameters	Type 1	Type 2
Λ	9	9
λ	12.5	15
Λ/λ	0.72	0.6
h	10	7
c_o	100	100
c	110	107
h/c_o	0.1	0.07
λ/c_o	0.125	0.15

(a)

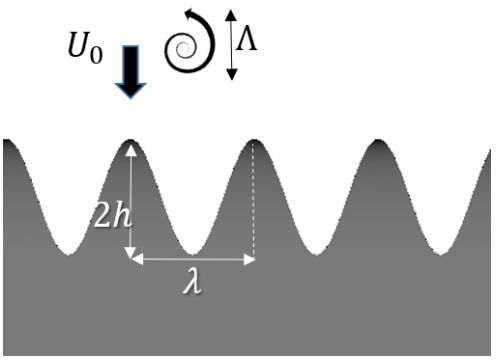

(b)

Figure 3.6: (a) Table with the leading-edge serration parameters (mm) and (b) the corresponding schematic representation.

Hence, two flat-plate based airfoils with wavy leading edges and a baseline one with straight edge, used as reference for comparisons, have been manufactured using a three-dimensional printer (see Fig. 3.7).

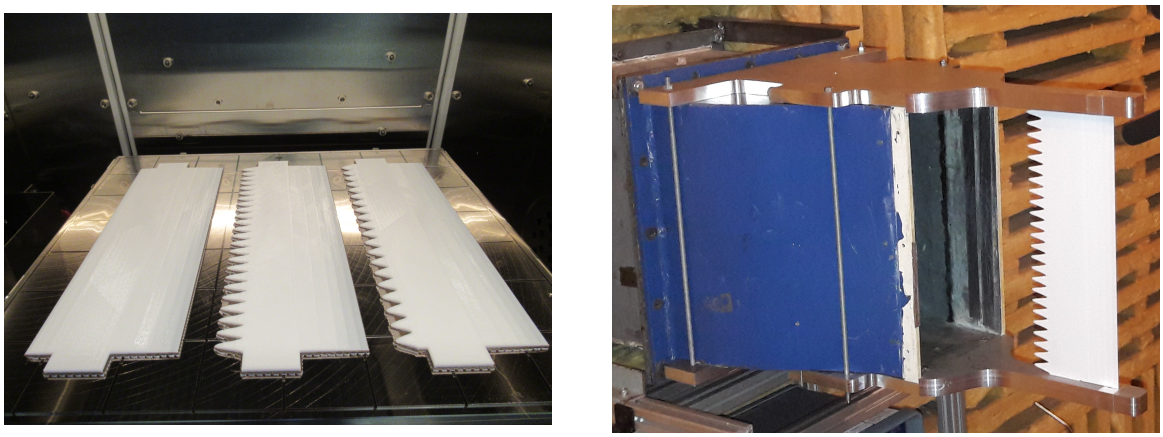

(a) (b)

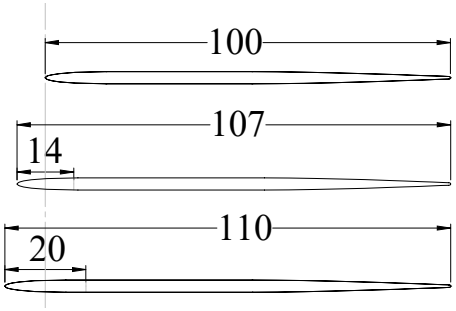

(c)

Figure 3.7: Photographs of (a) the 3D printed flat plates and (b) the narrow support plates installed at the nozzle. (c) Airfoil cross-sections selected for the study with maximum chord-wise dimensions given in [mm]. Same average chord length for all the flat-plates.

A concern about the 3D printed flat plates is their rigidity in terms of vibroacoustic phenomena after being embedded in the flow. A small vibration activity has been observed during the experiments. Therefore, a metal plate as a baseline, similar to the 3D printed, has been manufactured and tested for acoustic comparisons purposes. Finally, measuring the both baseline flat plates, a good superposition of between their spectra has been achieved as shown in Fig. 3.8. The appearance of a tone at 72 Hz in the spectrum of the 3D printed version can be a possible eigenfrequency which can be verified by solving analytically an eigenvalue problem for flat plates. Same behavior has been notified in other radiation angles. Thus, the 3D printed flat plates can be considered as reliable samples for performing acoustic measurements.

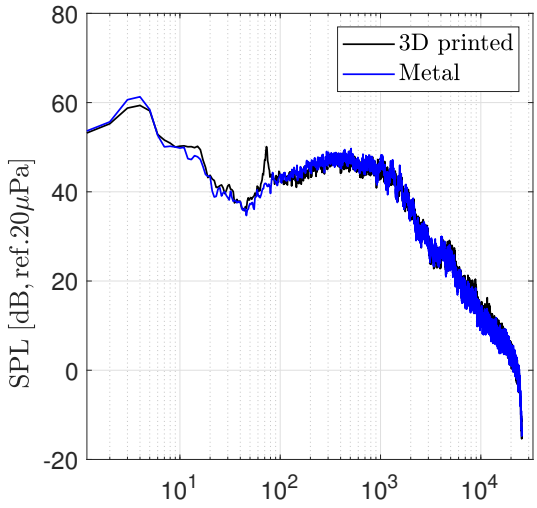

Figure 3.8: Far-field spectra measured at 90° in the mid-span plane at 32 m/s for the metal (–) and 3D printed (–) baseline flat plates.

3.4 Far-Field Single-Microphone Results

The first assessment of the effect of LE serrations on TIN relies on single-microphone measurements performed in the acoustic far field. The noise reduction is obtained by simply making spectral differences between the PSD (Power Spectral Densities) of the sound pressure measured separately with the baseline, straight-edge airfoil and with the serrated airfoil. If the results must be used for the validation of prediction methods, only TIN reduction must be characterized. Therefore the procedure is only valid as long as TIN dominates enough, so that other sources give a negligible contribution in terms of decibels. Two issues make this condition questionable. The first issue is that the background noise, made of the noise generated by the nozzle flow and the turbulence grid in absence of airfoil, must be subtracted in a first step from both mesurements made with the airfoils. This pinpoints the high-frequency and low-frequency limits. The former results from the drop of TIN beyond a 'cut-off' frequency imposed by the parameters of the turbulence grid. The latter results from undesired interaction between the jet shear-layer oscillations and the installed airfoil, leading to questionable measurements, because of the limited jet width. An extended but limited frequency range is therefore identified in the experiment. The second issue is that airfoil noise also includes trailing-edge noise (TEN) and that both TIN and TEN cannot be separated in far-field measurements. The reduction achieved by serrations can therefore be determined by spectral subtraction only if TEN remains much lower than TIN. Now the LE serrations induce a strong reduction of TIN, so that the TEN contamination is more pronounced when characterizing the serrated airfoil. Furthermore they also have an indirect effect on TEN. As a result the reduction cannot be assessed properly at high frequencies. The observed effect is that, based on far-field measurements, the reduction is first found to increase with frequency below a threshold and then to decrease beyond this threshold. This has been recognized as misleading by

several investigators [104, 116, 126, 27]. The measurements made with the arc antenna are considered as 'single-microphone' because no cross-spectral analysis is performed on the six microphones.

An alternative approach *a priori* free of these drawbacks is to rely on a planar microphone-array and an appropriate post-processing technique to generate a source map in the plane of the airfoil. Integrating the areas obviously corresponding to the leading and trailing edges on the map allows extracting each source of interest. Once this is performed for the LE area and for both the baseline and serrated airfoils, the reduction is unambiguously determined. Again attention must be paid to two aspects. Firstly, the reduction is now estimated on integrated equivalent source powers, thus on the source itself, instead of being estimated from the received SPL (Sound Pressure Level). Secondly, the technique is only possible if the map exhibits two clearly separate LE and TE areas, so that the integration is relevant. This resolution is only possible beyond some frequency, whereas TE and LE sources cannot be discriminated at lower frequencies.

In view of the aforementioned arguments the present study associates two experimental approaches. Spectral differences from the arc of far-field microphones are selected for the low and middle frequencies. A microphone-array post-processing is preferred for the middle-and-high frequencies. Merging both sets of experimental results produces an estimate of the reduction over the entire frequency range.

3.4.1 Far-Field Sound Spectra for Baseline and Serrated Airfoils

The present section quantifies the TIN from the far-field sound pressure PSD (power spectral densities) $S_{pp}(f)$ measured with the baseline and serrated airfoils, including the effect of directivity both in and off the mid-span plane. The Sound Pressure Level (SPL) is defined as

$$SPL(f) = 10\log_{10}(S_{pp}(f)/p_{ref}^2), \tag{3.2}$$

and measured for all ϕ_i angles simultaneously at each θ_j angle, p_{ref} is being the acoustic reference pressure 20×10^{-6} Pa, in the frequency range between 40 Hz and 14 kHz. Sound spectra are measured both with and without the airfoil to suppress the contribution of the background noise by simple spectral subtraction. However the noise observed below 40 Hz is attributed to some modification of the background noise sources associated with the free-jet oscillations, which cannot be suppressed by the subtraction procedure. At very high frequencies airfoil noise decreases below the background noise level, no longer allowing further investigation from simple far-field measurements. Self-noise, reduced to trailing-edge noise in the present case, also contributes to the total airfoil noise at high frequencies, as emphasized later on, which makes the assessment of TIN reduction more questionable. The threshold beyond which TEN takes over TIN is estimated below by means of dedicated measurements without turbulence grid. The alternative use of microphone-array measurements for the discrimination of sources will be addressed in the next section.

Far-field noise spectra for the three flat-plate airfoils are shown in Figs. 3.9-(a), (b)

and (c) for three flow-speeds 19, 27 and 32 m/s, respectively, and the measurement angles $\phi = 0°$ and $\theta = 90°$. The background noise has been subtracted from all measurements and the data are reliable up to the threshold of 15 kHz, beyond which a larger scatter appears with the present resolution of 1 Hz. Sound level and frequency increase with flow speed as expected. Furthermore, the spectra exhibit dips and humps attributed to the chordwise non-compactness beyond 3 kHz.

Yet, the roll-off starts earlier and the oscillations are slightly shifted, sign of a modification of the scattering at the leading edge induced by the sinusoidal shape. The spectra for the three airfoils are compared at the same speed at the same speed of 32 m/s in Fig. 3.9-(d) where the noise mitigation is clearly evidenced starting at 700 Hz, with an earlier noise level roll-off. No significant difference is observed between the two serration designs and we will therefore focus on the deepest case only from now on. For further treatment the bandwidth resolution will be decreased to 16 Hz (Fig. 3.9) or 64 Hz (Fig. 3.10-(a)) for better clarity. The reduction of TIN is defined as the quantity ΔSPL produced by the difference spectra. This quantity is plotted in Fig. 3.10-(a) for the three flow speeds. It exhibits different trends depending on the range of the Strouhal number based on the amplitude h. A regular increase with frequency is first seen up to $St = 1.5$; then the reduction seems to drop and starts increasing again beyond $St = 2.5$. The high-frequency behavior is an artifact of the procedure, as discussed later on. Higher noise reductions are observed for the lower speeds 19 and 27 m/s below the Strouhal number $St = 1$ and beyond $St_h = 2.5$, with reversed behavior between these two values. The flow speed dependence is shown beyond $St_h = 0.5$ where the noise reduction performance follows a different trend. Figure 3.10-(b) shows far-field spectra at various speeds for the serrated airfoil with deepest serrations in reduced variables. The PSD of the acoustic pressure divided by flow speed to the power 5 plotted as a function of the Strouhal number produces a clear collapse, except beyond $St_h = 0.5$ because of the non-compactness dips and humps. The trend below $St_h = 0.5$ is characteristic of TIN, also for straight-edge airfoils.

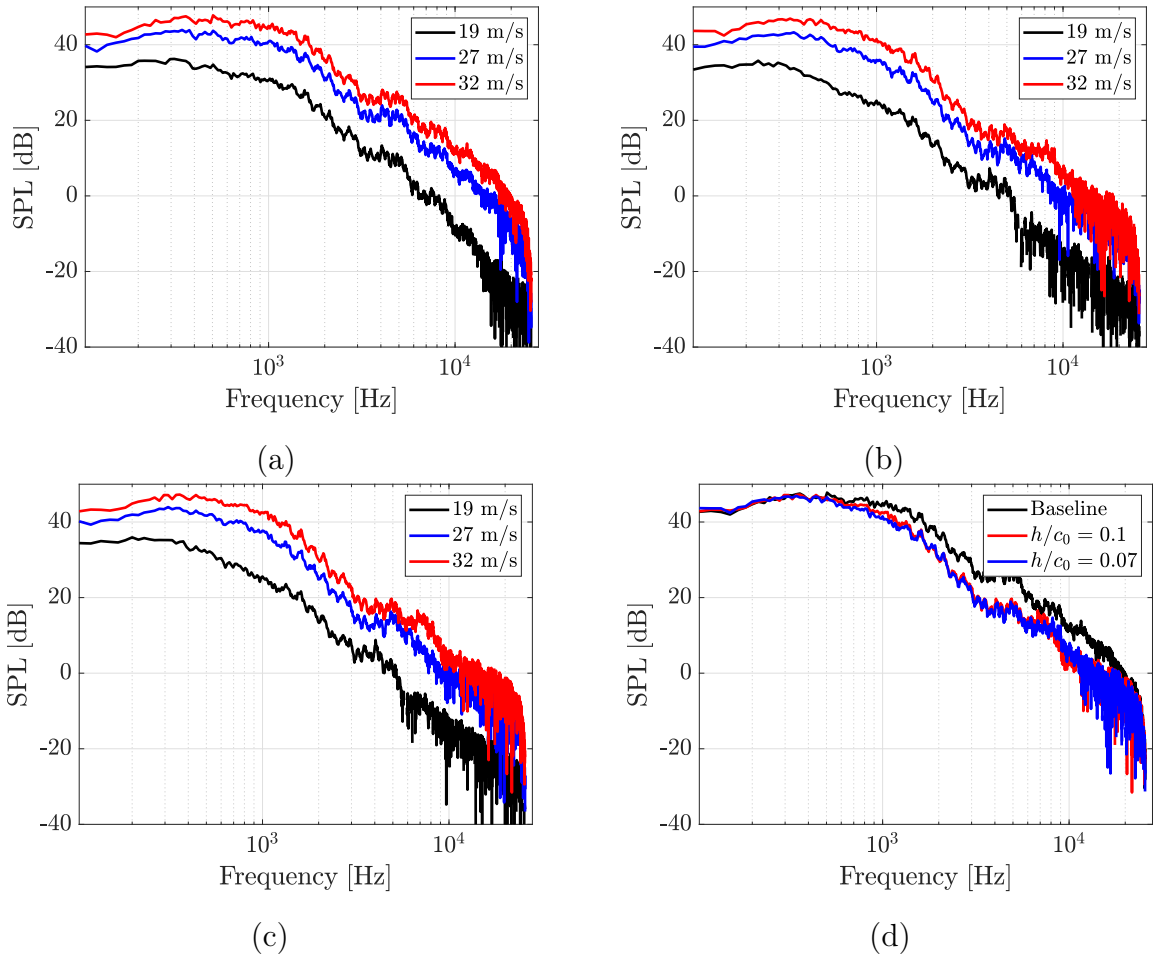

Figure 3.9: Far-field sound spectra at various flow speeds. Microphone angles $\phi = 0°$, $\theta = 90°$. (a) baseline airfoil, (b) serrations $h/c_0 = 0.07$, (c) serrations $h/c_0 = 0.1$. (d) Compared sound spectra of the three airfoils at $U_0 = 32$ m/s. Background noise subtracted.

A comparison between the serrated flat-plates and the baseline for all flow speeds in terms of directivity in the far-field in the mid-span plane is shown in Fig. 3.12. Polar diagrams at various frequencies present the evolution of radiation patterns at flow speeds 19 (blue), 27 (red) and 32 m/s (green) for all flat-plate cases. Each polar plot is divided into two parts, the serrated flat plate with $h/c_0 = 0.1$ (top) and with the $h/c_0 = 0.07$ (bottom) compared to the baseline (black) in both divisions. The airfoil is located at the center of the circular diagram and all the measurements were conducted at the same observer positions ($20° - 110°$). For clarity of the radiation patterns modifications, the diagrams of the serrated flat plates results have been displaced by a quantity Δ dB so as to be clearly comparable with the baseline directivity. The Δ dB is defined by the average sound level differences over all the interpolated radiation angles between the serrated flat plate and the baseline. The single value of Δ dB given in eq. (3.3) below is added to the serrated case SPL_{ser} to shift it without modifying its directivity pattern as in eq. (3.4). In addition, the averaged value is calculated by replacing NaN numbers produced by the

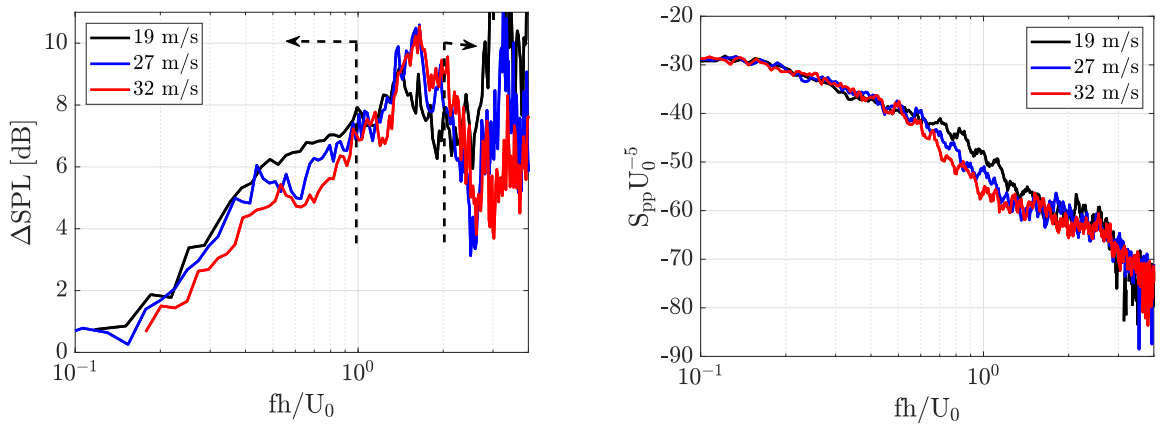

Figure 3.10: (a) Noise reduction from far-field inspection and bounds of the validity range as dotted lines. (b) Strouhal-number spectra scaling law with the 5^{th} power of the flow speed. Microphone angles $\phi = 0°$, $\theta = 90°$, serrated airfoil $h/c_0 = 0.1$.

subtraction procedure with zero so as to have a real-valued Δ dB.

$$\Delta SPL(f, \phi, U) = \frac{1}{2N-1} \sum_{i=1}^{2N-1} \Delta SPL_i(f, \theta, \phi, U) \tag{3.3}$$

$$DSPL_{ser}(f, \theta, \phi, U) = SPL_{ser}(f, \theta, \phi, U) + \Delta SPL(f, \phi, U) \tag{3.4}$$

Despite the fact that the sound level differences in Fig. 3.12 are discarded, the comparison of the radiation patterns is quite clear. At low-frequency regimes till the compactness limit of $kc_0 = 2\pi$ the patterns between the serrated cases and baseline superimpose very closely to each other. Beyond this threshold, the general radiation shape of serrated cases remains similar to the baseline but by increasing the frequency slightly more lobes appear. Additionally, the humps seen in the diagrams of serrated versions are shifted by 5° or 10° compared to the baseline. A shift or a change in patterns is also observed at different velocities for the serrated cases whereas the baseline maintains the same pattern without phase modification at all speeds. Similar analysis is presented in Fig. 3.13 where the directivity radiation is explored at the angle of $\phi = 75°$ off the mid-span plane. The radiation for all the airfoils is similar for all chosen wavenumbers and speeds. The sound level is substantially lower than in the mid-span plane and the directivity features a single, dipole-like lobe.

Three-dimensional directivity plots help to assess the sound radiation at various frequencies. A proper cubic interpolation between the measurements both in azimuth and elevation angles visualizes efficiently the radiation patterns without under/overestimate of the real perception of sound. The interpolated values have been obtained according to the corresponding grid of angles $\theta\epsilon[25° : 2.5° : 110°]$ and $\phi\epsilon[0° : 2.5° : 75°]$. Figure 3.11 shows

in black lines the mesh grid of the measurement points and the interpolated points by a fine grey mesh grid for a specific frequency $kc_0 = 3$.

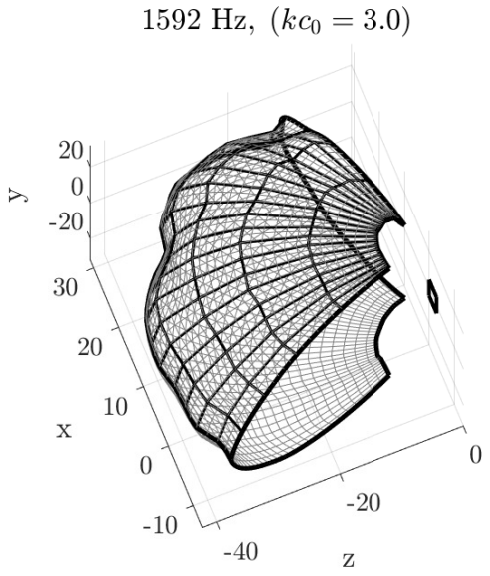

Figure 3.11: Three-dimensional directivity of the sound measurements corresponding to 1/8 of the sphere for $y \geq 0$. Values for $y \leq 0$ are an image of the measurement points for $y > 0$. The flow is along the positive X axis. Airfoil featured by the small parallelogram at the origin of coordinates.

Therefore, in Fig. 3.14 three-dimensional directivity plots for both baseline and serrated flat plate airfoils of h/c_0 are presented. Results are given for different Helmholtz numbers kc_0 corresponding to dimensionless acoustic wavenumbers $k\Lambda = 0.2,\ 0.7,\ 1.2,\ 1.6$ at $M = 0.09$ and $\Lambda = 0.009$. These frequencies are chosen for comparison reasons because the differences at mid-span plane are more obvious. At very low frequencies up to $kc_0 = 1.5$ noise reductions are negligible but they are increased as the frequency rises. The first chosen frequency for visualization in Fig. 3.14 is $kc_0 = 2$ at which the reduction differences between the two profiles reach up to 3 dB, becoming very noticeable to human ear perception. The uniform noise reduction (NR) along all the radiation angles is obvious and is following the NR trend according to Fig. 3.17 at 90° azimuthal angle, presented later on. Plot axis limits are not locked in terms of noise level so as to emphasize radiation pattern details. An artifact of this unblocked limits is the increasing scale view of the airfoil schematic as the sound level decreases. It is worth mentioning that the directivity with serrations remains similar to the baseline as already mentioned in Fig. 3.12 till the frequency where trailing edge starts dominating $kc_0 = 7.5$; finally some directivity changes appear above this threshold. Because these changes are attributed to trailing-edge noise contributions, far-field measurements could not clearly investigate that phenomenon but other means are suitable such as analytical models, surface pressure probes and beamforming technique. Some of them are used in the following sections. Despite the fact that the radiation above 110° close to leading edge was not measured, noise reductions are higher close to trailing edge than at 90°. This is also shown in Figs. 3.15 and 3.19 and

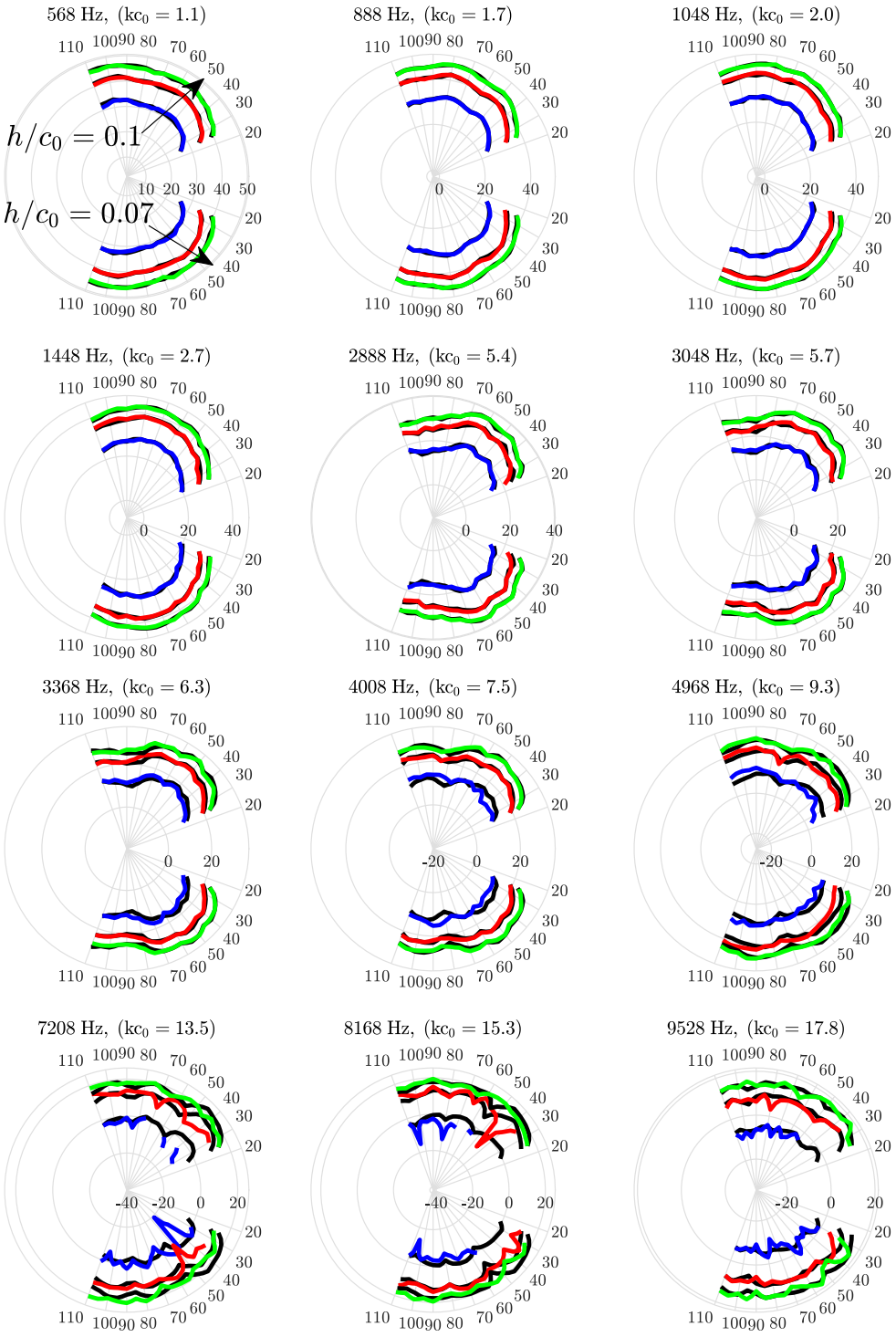

Figure 3.12: Far-field directivity polar diagrams measured at 19 (blue), 27 (red) and 32 m/s (green) in the mid-span plane ($\phi = 0°$) for all flat-plates. Each polar plot is divided into two parts corresponding to $h/c_0 = 0.1$ (top) and $h/c_0 = 0.07$ (bottom). Directivity of the serrated cases (blue, red, green) shifted from that of on the baseline (black) by the mean difference between all the directions for each frequency.

additionally observed by Lyu & Azarpeyvand [89] for nearly same speed, frequencies and serration wavelength.

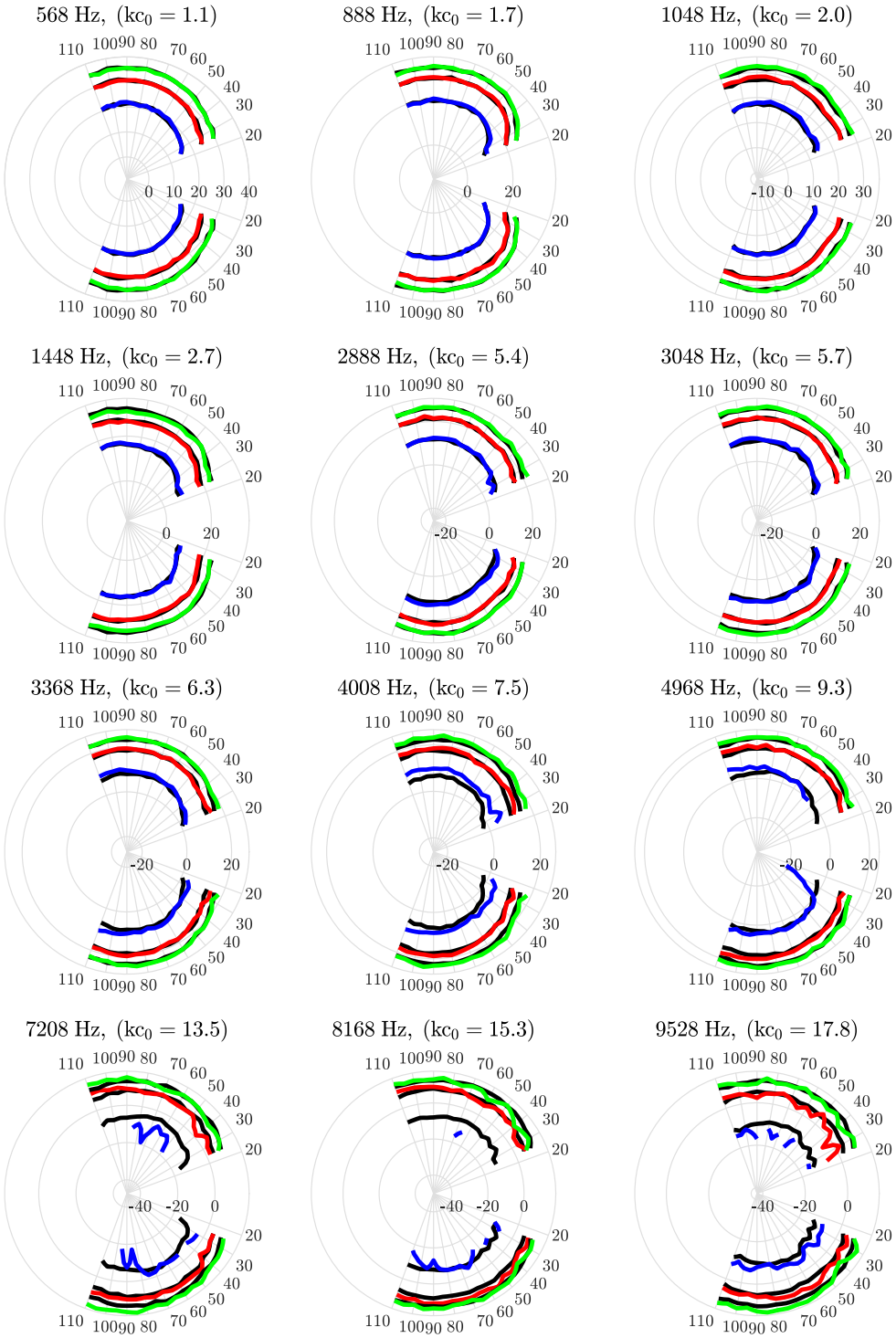

Figure 3.13: Off the mid-span plane ($\phi = 75°$) far-field directivity polar diagrams measured at 19 (blue), 27 (red) and 32 m/s (green) in the plane ($\theta = 90°$). Same conventions as in Fig. 3.12.

Noise reductions along the azimuthal θ and polar angles ϕ are explored in Figs. 3.15-(a), (b) and (c) as functions of non-dimensional frequencies. Identical NR patterns appear

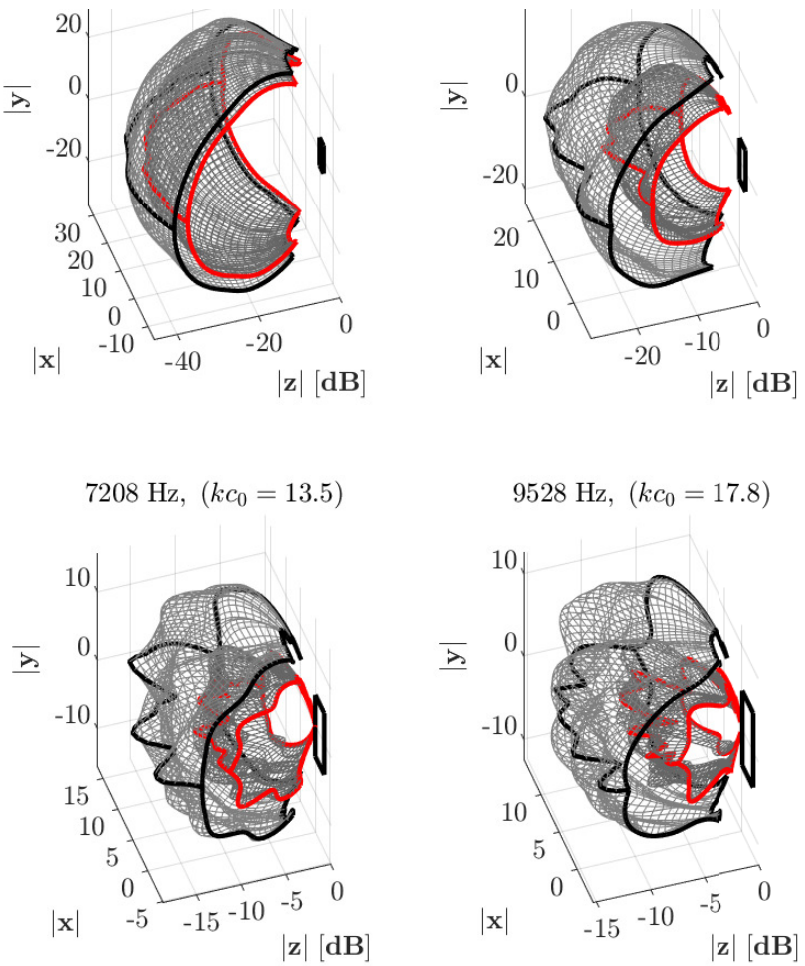

Figure 3.14: Experimental three-dimensional directivity plots corresponding to both baseline (black) and serrated flat-plate (red) of $h/c_0 = 0.1$ at Mach number $M = 0.09$. Results are presented at Helmholtz numbers of $kc_0 = 2,\ 7.5,\ 13.5$ and 17.8. The flow is delivered from negative to positive values along the x axis.

at different polar angles but displaced as the Strouhal flow dependence numbers are increased. An average efficiency of $8 - 10\ \Delta dB$ is observed along all azimuthal angles at non-dimensional frequencies $15,\ 10,\ 8$ for the speeds $19,\ 27,\ 32$ respectively. Additionally, maximum values of NR around $15\ dB$ appear between $30° - 60°$ azimuthal angles.

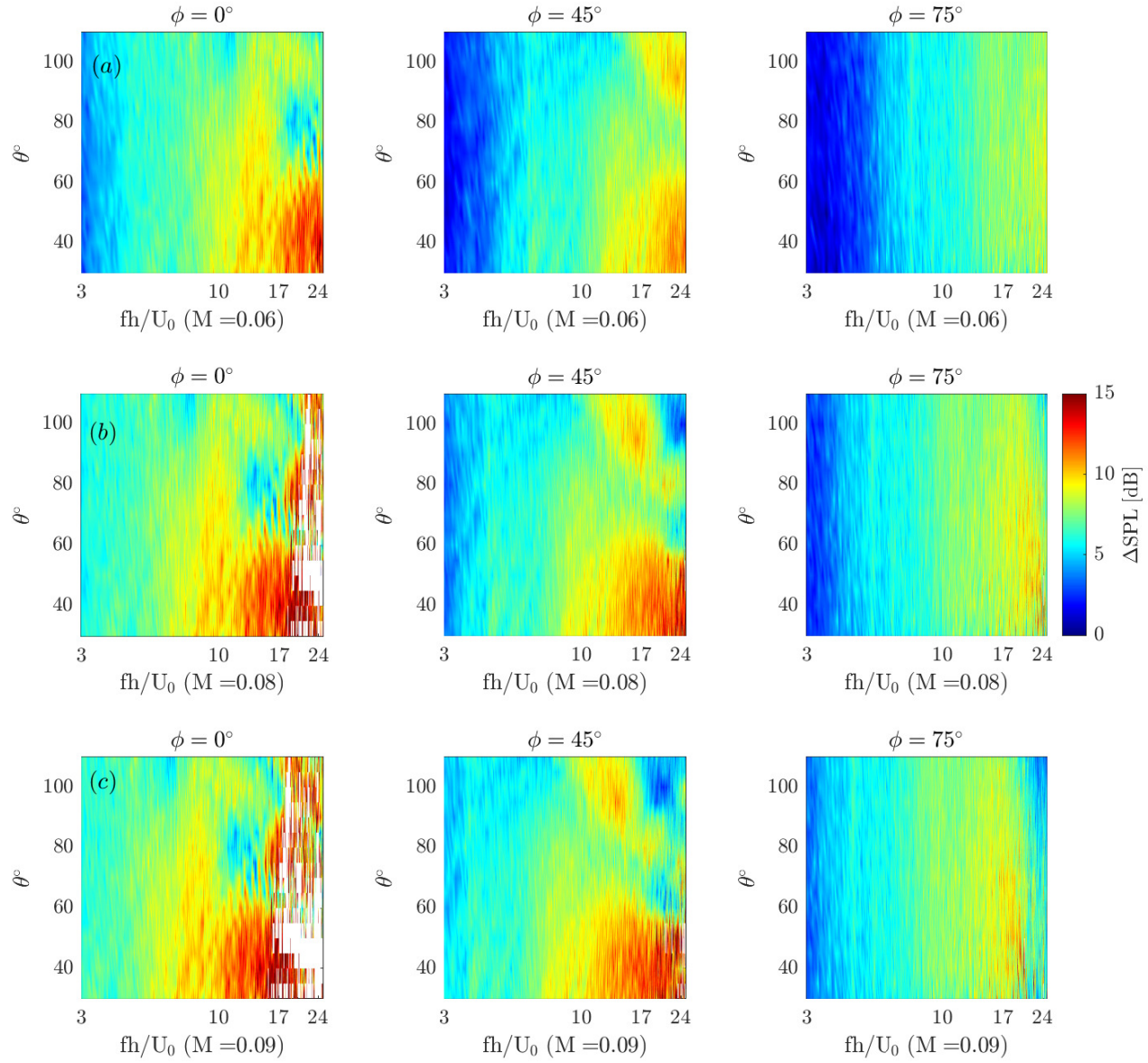

Figure 3.15: Sound pressure level reductions (ΔSPL) for the serrated flat-plate $h/c_0 = 0.1$ for all radiation angles at Mach numbers $M = 0.06,\ 0.08$ and 0.09.

3.4.2 Noise Reductions and Sound Power Level Spectrum Calculation

In this section an overview of the sound power reduction spectra for two serration amplitudes h is presented. Sound power spectrum $W_{ij}(f)$ defined in Eq. 3.7 is used for estimating the power level of a single surface segment in spherical coordinates system. The total power is calculated by the power integration between all segments A_{ij} on the sphere surface. A_J is the surface area delimited between the measured points in the far-field at distance 1.25 m from the airfoil leading edge. Each segment maintains its length along the z-axis (Fig. 3.16) and is changed along y-direction.

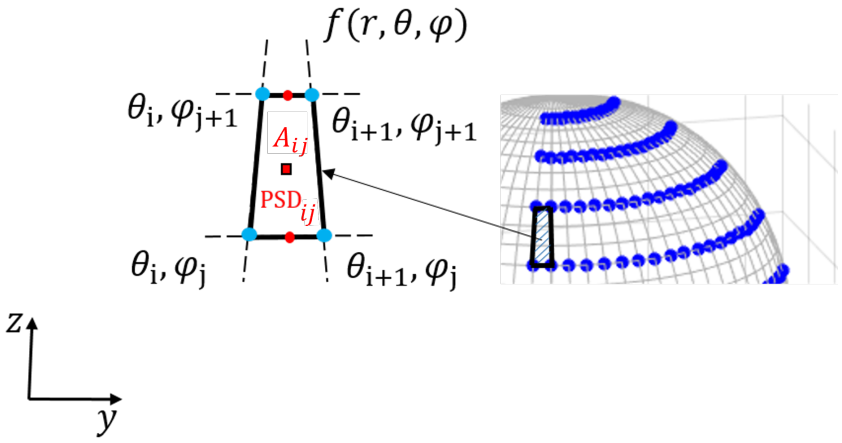

Figure 3.16: Surface segment delimited between the measured points on the portion of sphere in the far-field.

A sound-power estimate is used in this section to assess globally the effect of serrations in a three-dimensional context. For this, each measurement PSD_{ij} is multiplied by the area of the patch defined by the arcs at angles $\theta_i \pm \theta/2$ and $\phi_j \pm \phi/2$, thus

$$A_{ij} = r^2\,\Delta\theta\,(\sin[\phi_j + \Delta\phi/2] - \sin[\phi_j - \Delta\phi/2]),\ (\theta_{i+1} - \theta_i) = \Delta\theta \tag{3.5}$$

Therefore, total integration of all the segments for the angles $\theta\,\epsilon\,[20°\ 110°]$ and $\phi\,\epsilon\,[0°\ 75°]$ leads to the expression

$$PWL(f) = 10\log_{10}\,(\sum_{j=1}^{M}\sum_{i=1}^{N} W_{ij}(f)/W_{ref}) \tag{3.6}$$

with

$$W_{ij}(f) = \frac{A_{ij}}{\rho\alpha} \times PSD_{ij}(f) \times cos(\theta_r)^0 \tag{3.7}$$

N and M are the numbers of measurement points in θ and ϕ angles respectively, $W_{ref} = 10^{-12}W$ is the reference sound power and

$$PSD_{ij}(f) = \frac{PSD_{i,j} + PSD_{i+1,j} + PSD_{i,j+1} + PSD_{i+1,j+1}}{4} \tag{3.8}$$

As pointed in a previous study by Bampanis & Roger [25], making the difference in decibels between simple far-field sound spectra produces misleading reduction spectra at high frequencies. This is responsible for the artifact noted in Fig. 3.10-(a) and observed similarly in Fig. 3.17-(a) for a microphone at 90° in the mid-span plane (this location is chosen for further comparison with the microphone-array measurements of section 7.4.2). In this figure the two serrated airfoils are compared. The reduction is found to be an increasing function of frequency up to a maximum of about 8-10 dB in the range 4-6 kHz. At higher frequencies a dramatic drop of reduction is found, followed by another increase. This is better understood by inspecting also the sound spectra corresponding to the total

noise and to the selfnoise in Fig. 3.17-(b). Selfnoise is measured by removing the turbulence grid and forcing transition to turbulence in the boundary layers by tripping when needed. It is trailing-edge noise and takes over TIN for frequencies typically beyond 4 kHz. Indeed both spectra have levels close to each other and the same shape in this range. Furthermore subtracting the TEN spectrum (blue) from the total spectrum (red) would produce a PSD level lower than the TEN spectrum. This makes the simple subtraction procedure in Fig. 3.17-(a) inappropriate to evaluate the TIN reduction operating at the leading edge. Apart from these differences between the two serrated flat-plate airfoils in terms of noise reduction are observed in Fig. 3.17-(a). The $h/c_0 = 0.1$ configuration ensures a larger reduction in the low frequency range than the $h/c_0 = 0.07$ configuration with shorter teeth.

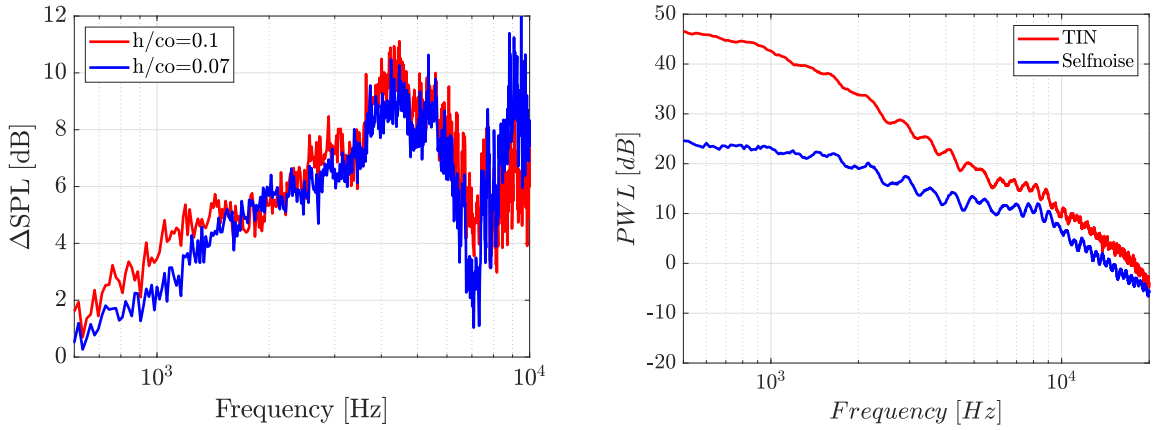

(a) (b)

Figure 3.17: (a) Noise-reduction spectra obtained for the serrated flat-plate airfoils by simple spectra subtraction and (b) typical far-field noise spectra comparing total noise (TIN+TEN) and TEN. Flow speed $U_0 = 32$ m/s, observation angle 90° in the mid-span plane.

As mentioned before, the parameter of the two serrated versions are *a priori* tuned to the integral length scale of the incident turbulence according to the observation by Paruchuri *et al.* [116] that efficient noise reduction depends on proper inclination angle and amplitude of the sinusoidal serrations. A global observation made by many studies [116, 75, 32, 18, 147, 28] prove that longer serration amplitude achieve higher noise reductions. The use of this optimum non-dimensional serration wavelength achieves noise reductions that follow the simple trend of $\Delta PWL = 10\log_{10}(\mathrm{St_h}) + 10$ [32], where St_h is the Strouhal amplitude dependence number. Reductions of total sound power in Fig. 3.18 nearly follow the above proposed NR trend in terms of non-dimensional frequencies $St_h = fh/U_0$. The ratio λ/Λ on both serration amplitudes is 1.3 and 1.67 with $h/c_0 = 0.1$ and 0.07 respectively. Fig. 3.18-(a) confirms also similar NR trend of an airfoil with same serration geometry used in [32]. Strouhal number scaling law of various flow speeds shows to follow the same motononic increase along frequency domain in Fig. 3.18-(b).

Overall sound pressure level reductions $\Delta OASPL$ are computed according to Eq. 3.9

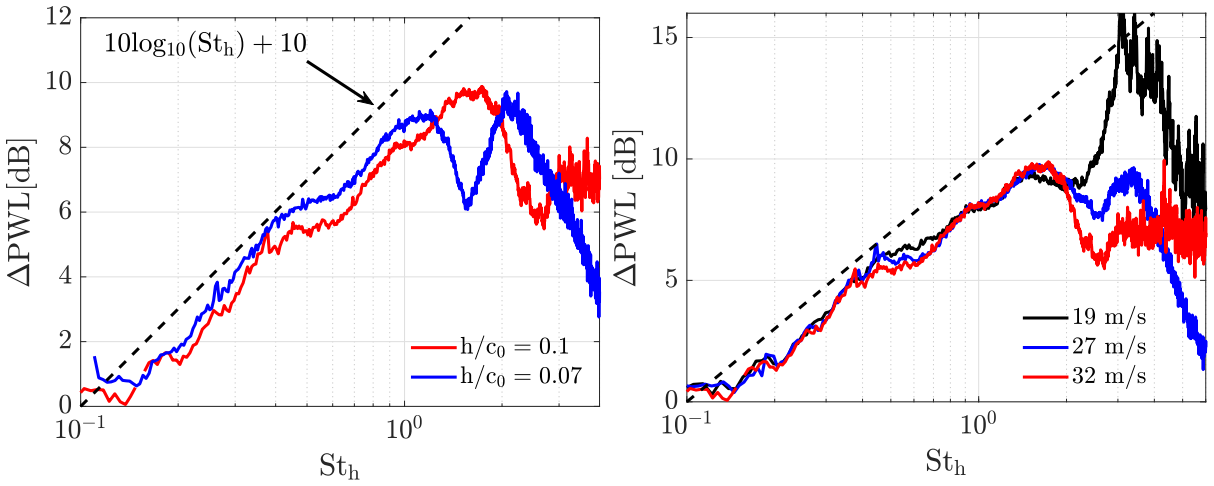

(a) (b)

Figure 3.18: (a) Total sound power level reductions ΔPWL for the serrated flat plates $h/c_0 = 0.1$ (red) and $h/c_0 = 0.07$ (blue) at $U = 32$ m/s. (b) ΔPWL for $h/c_0 = 0.1$ at different flow speeds. Comparison with $\Delta PWL = 10\log_{10}(St_h) + 10$ (dashed) validates its use according to [32], where $St_h = fh/U_0$ is the Strouhal number.

for both serrated flat plates for all the radiation angles at $M = 0.09$, see Fig. (3.19). Discarding some values that stand out from the average values of the histogram, the highest overall reduction occurs at the azimuthal angles 30° and 90° and the corresponding polar angles 45° and 60°. It is observed that overall noise reductions at the mid-span plane at $\theta = 90°$ are lower compared to the other angles. Most of the researchers conduct measurements at the mid-span plane. This can be considered as a safe procedure according to the above results where noise reductions are shown to be higher at swallow angles.

$$OA\Delta SPL_{ij} = 10\log_{10}\Big(\sum_{\mathrm{f=0.1kHz}}^{\mathrm{10kHz}} \mathrm{PSD_{ij}(f)/P_{ref}^2}\Big) \tag{3.9}$$

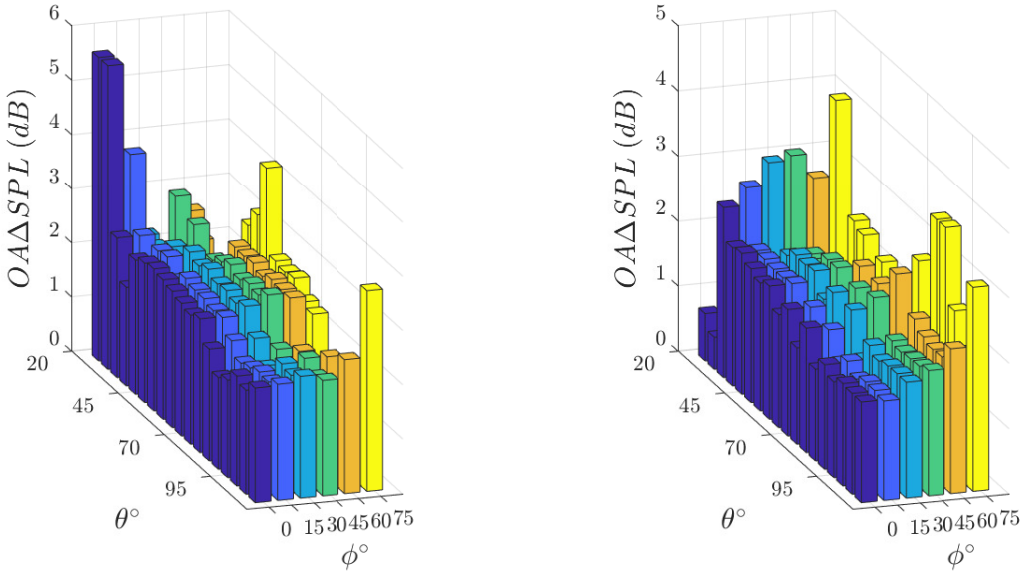

(a) (b)

Figure 3.19: Overall sound pressure level reductions $OA\Delta SPL$ for the serrated flat plates (a) $h/c_0 = 0.1$ and (b) $h/c_0 = 0.07$ for all the radiation angles at $M = 0.09$.

3.5 Self-Noise Influence on Turbulence Impingement Noise

Investigations on the effect of the trailing-edge noise (TEN) to the total radiated sound either on baseline or on serrated flat plates require the isolation and extraction of the TEN. Despite the fact that TEN can be measured with far-field noise measurements on a clean flow (without turbulence), this is impossible for TIN case where leading- and trailing-noise exist both in mid-high frequency ranges. Airfoil self-noise and TIN could be comparably close at high frequencies (8 kHz) in terms of sound level but this does not mean that both sound sources are equal. This should be clear from researchers who use this technique to evaluate the trailing-edge noise generated by TIN. The following figures evaluate the total radiated noise in terms of sound power comparing TIN and self-noise of flat plates with and without serrations. Fig. 3.20-a presents TIN (red) and self-noise (blue) of the serrated flat plate ($h/c_0 = 0.1$) in frequency domain and Fig. 3.20-b shows the same noise mechanisms for both baseline and serrated profile in non-dimensional frequencies fc_0/U. Self-noise starts dominate at 5 kHz where differences with TIN reduces to less than 10 dB and this is also occurs at non-dimensional frequency of 15 for the serrated case. Detailed comparisons between self-noise of both profiles show that at the serrated case is reduced compared with the baseline at all frequencies confirming the observation of Paruchuri that leading-edge serrations decrease also the airfoil-self noise [116].

Fig. 3.21 shows different combinations of sound power reductions in total sound power ΔPWL between TIN and self-noise for both profiles. Description of these noise reduction quantities are given in Eq. 3.10 and defined as TIN reduction (ΔTIN) between TIN of baseline (PWL_{TIbln}) and serrations (PWL_{TIser}), reduction of self-noise (ΔSN) between

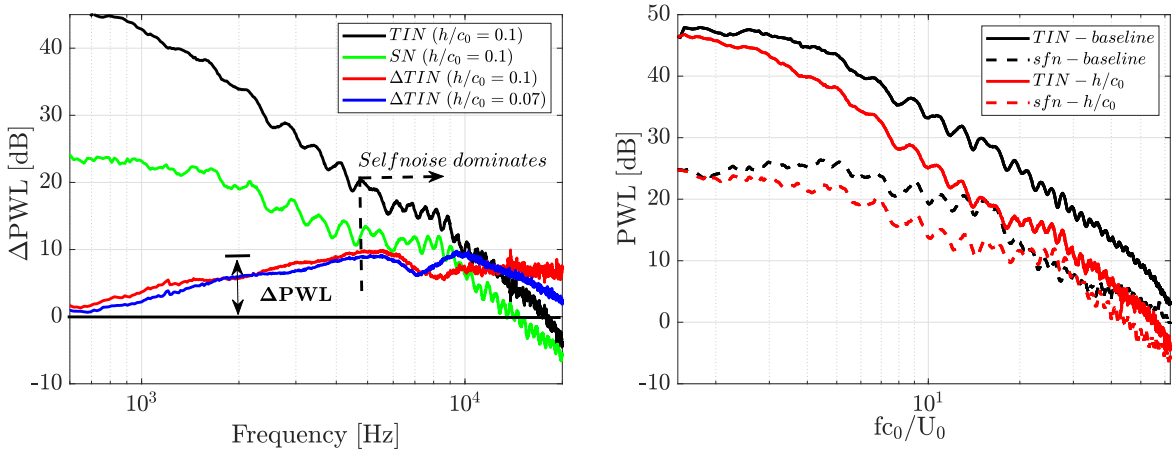

(a) (b)

Figure 3.20: Total sound power integrated over the 1/8 of the sphere: (a) TIN (black) vs self-noise (green) and noise-reduction spectra obtained for the serrated flat-plate airfoils by simple spectra subtraction at $M = 0.09$. (b) TIN of the baseline (black) and the serrated plate ($h/c_0 = 0.1$) (red) and their corresponding self-noise in dashed lines.

self-noise of baseline (PWL_{SNbln}) and serrations (PWL_{SNser}), differences (ΔSN_{bln}) between TIN (PWL_{TIbln}) and self-noise (PWL_{SNbln}) for baseline and differences (ΔSN_{ser}) between TIN and self-noise (PWL_{TIser}) for serrations (PWL_{SNser}).

$$\begin{aligned}
\Delta TIN(\omega) &= PWL_{TIbln}(\omega) - PWL_{TIser}(\omega) \\
\Delta SN(\omega) &= PWL_{SNbln}(\omega) - PWL_{SNser}(\omega) \\
\Delta SN_{bln}(\omega) &= PWL_{TIbln}(\omega) - PWL_{SNbln}(\omega) \\
\Delta SN_{ser}(\omega) &= PWL_{TIser}(\omega) - PWL_{SNser}(\omega)
\end{aligned} \tag{3.10}$$

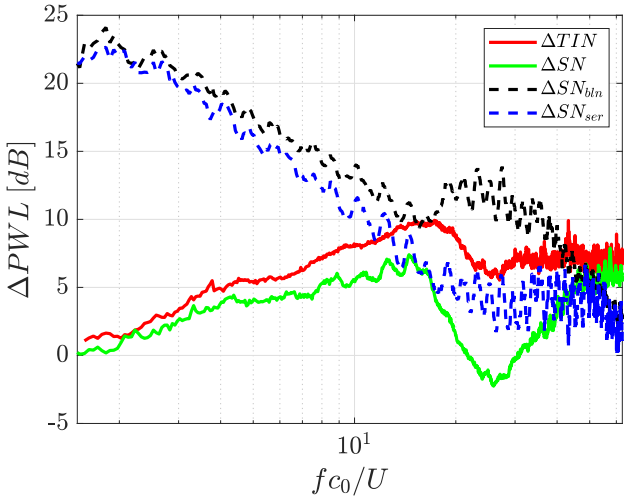

Figure 3.21: Total noise reductions between TIN and self-noise for baseline and serrated flat plate ($h/c_0 = 0.1$).

According to Fig. 3.21, TIN reduction reaches its threshold at $fc_0/U = 15$ (red) at

which the self-noise differences (ΔSN_{ser}) are decreased simultaneously under the limit of 10 dB. This shows that the serrations at the leading edge are modifying the BL development and consequently the TEN. Therefore, subtracting selfnoise measured separately on the reference configuration will not work.

Looking at the black and blue curves for Strouhal numbers over 15, the noise differences between them are different and not zero level. Taking the assumption that trailing-edge noise which stems from TIN and self-noise are equal each other, it is concluded as false. Self-noise differences ΔSN in Fig. 3.21 confirms additionally that self-noise due to serrations is decreased compared to baseline [116] (Figure 17). Considering that ΔTIN presents a monotonic increase as frequency increases, serrations self-noise destroy this tendency as self-noise approach TIN. Therefore, combining ΔTIN and ΔSN_{ser} curves, the ΔTIN begins again increase at those frequencies at which ΔSN_{ser} remains constant at 5 dB. According to the far-field measurements, we could conclude that self-noise of serrated profiles restricts the NR efficiency over $fc_0/U_0 = 15$ but that could be changed if self-noise could be decreased dominantly. In that case, noise reduction could present a motonotic increase trend (Fig.3.25) till higher frequencies. This can obtained by applying proper serration devices both on trailing and leading edges of the airfoil minimizing both noise sources.

Three-dimensional plots of self-noise radiation for both baseline and serrated flat plate can illustrate their differences at frequencies that are discussed above. Thus, Fig. 3.22 visualizes the self-noise radiation of both flat plates at Strouhal numbers 2.5, 15, 18.7 25 at which sound level of the serrated version firstly ($fc_0/U_0 = 2.5$) is close to the baseline and secondly ($fc_0/U_0 = 15$) decreases up to 8 dB.

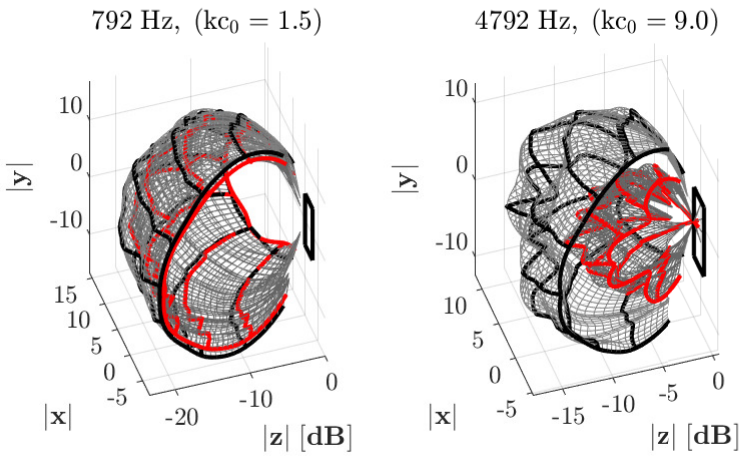

Figure 3.22: Experimental three-dimensional directivity plots corresponding to both baseline (black) and serrated flat plate (red) of $h/c_0 = 0.1$ at $M = 0.09$. The flow is going from negative to positive values along the x axis.

3.6 Source Localization and Extraction

The quantification and evaluation of the noise sources that stem from leading and trailing edges requires their isolation of the total radiation noise which is a demanding procedure experimentally. In this section, the beamforming technique is used for localizing and quantifying the aforementioned noise sources. Experimental results presented in this section will be used for validation with the corresponding noise predictions of the previous chapter. Furthermore, noise localization technique will provide an insight on the trailing-edge noise source compare to the self-noise that is studied in the previous chapter.

The results are based on equivalent sound-power source maps produced by the algorithm. Typical maps shown in Figs. 3.23 and 3.24 show quantified contributions of LE and TE noise sources for both the baseline airfoil and the serrated flat-plate airfoil with $h/c_0 = 0.1$, and for specified frequency ranges. Integrating the two selected areas at the leading and trailing edges (red and green rectangular boxes respectively in Fig. 3.23-(b)), the contribution of each source defined as its integrated power is extracted, keeping in mind that the needed assumption of uncorrelated equivalent monopoles is believed a reasonable interpretation. The separation and extraction of individual noise sources is made possible only if the airfoil chord is non-compact, so that the equivalent sources at the trailing edge and at the leading edge can be unambiguously separated. Here, compactness ends around $\sim 3.4\ kHz$, so the procedure is meaningful beyond this threshold. The main idea of the present work is to assess TIN reduction in the low-to-middle and the middle-to-high frequency ranges by complementary and totally different methods, namely spectra difference from far-field measurements for the former and source-power differences from microphone-array post-processing for the latter.

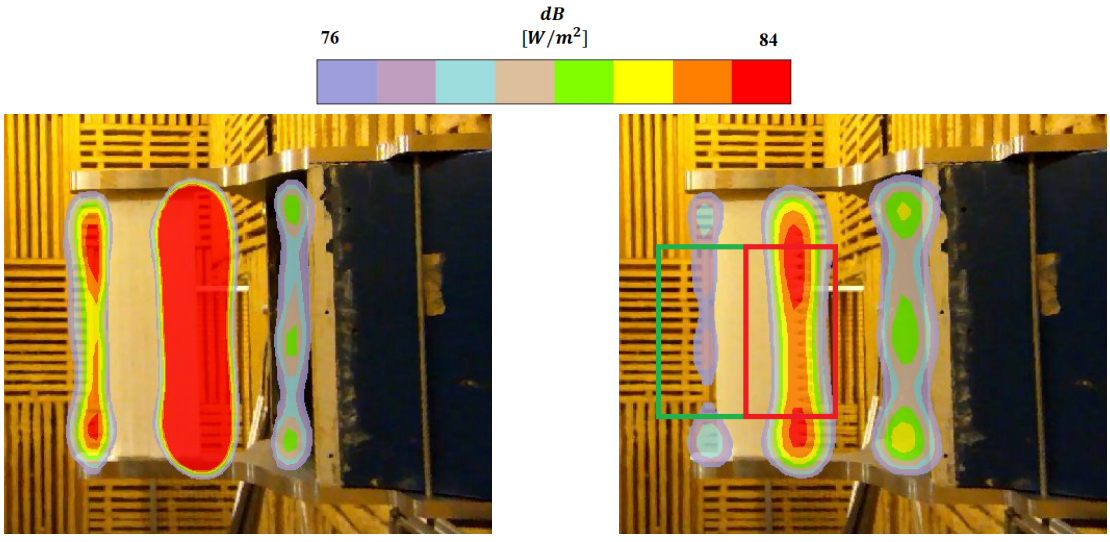

(a) (b)

Figure 3.23: Source localization color maps for the integrated frequency range 3.4−7.4 kHz at 32 m/s. (a) baseline airfoil, (b) serrated airfoil with $h/c_0 = 0.1$. The rengtangular boxes define the interogation areas for the noise source extraction. Flow from right to left.

The maps in Fig. 3.23 indicate three contributions obviously attributed to leading-edge (LE) noise (identified to TIN), trailing-edge (TE) noise and background noise originating from the nozzle lips. The slightly different background-noise signature is not significant in terms of decibels. In contrast the more substantially different trailing-edge noise signatures with and without leading-edge serrations suggest that the latter notably modify the developing boundary layers. Figure 3.23 evidences reduction for both LE and TE emissions despite the fact that the noise reduction as assessed from the far-field results decreases beyond 4 kHz as shown in Fig. 3.17-a. Complementary maps are provided in Fig. 3.24 for the frequency ranges $[4.5-6.7]$ kHz and $[6.7-10]$ kHz. They confirmed that the background noise from the nozzle is kept unchanged. With leading-edge serrations, TEN is reduced in the range $[4.5-6.7]$ kHz and increased in the range $[6.7-10]$ kHz. The interpretation of these results is that the serrations reduce the large-scale content of the near-wall turbulence and at the benefit of the small-scale content. Moreover, leading-edge serrations create secondary large scale vortices that can interact with the developed BL close to the trailing edge. This may leads to the modification of the internal turbulence in the BL but only at low frequencies. The internal turbulence sound sources remain unmodified at mid-high frequencies due to the protection of the BL.

The results of map integration over the leading edge (LE) and trailing edge (TE) rectangular areas are displayed in Fig. 3.25 in integrated source-power (ISP) levels. The LE and TE power spectra are plotted as red and blue lines in Fig. 3.25-a and b for the baseline airfoil and the serrated airfoil, respectively, and the sum of both as the black lines. TE noise is much lower than LE noise below 4 kHz, which corresponds to the range in which both traces cannot be separated, therefore the reconstructed source spectrum only starts from this frequency. It is clear that TEN dominates at high frequencies for the serrated airfoil. The LE noise reduction as deduced from the difference of source-power spectra is plotted in red in Fig. 3.25-c, where it is compared to the reduction deduced from the far-field measurements, in blue. A monotonic increase, nearly linear in terms of decibles on a log-frequency scale, is found, up to the investigated high-frequency limit, with a maximum of about 15 dB. The overall noise reduction trend follows closely the function $10\log_{10}(\mathrm{fh/U}) + 10$ [32] for the optimum serrations amplitude as already mentioned. Interestingly the blue and red reduction spectra coincide all along the validity range of the far-field subtraction procedure, which proves that both approaches produce estimates of the same quantity even though they totally differ in principle. The black line in Fig. 3.25-(c) attempts a reconstruction of the reduction that would be produced from the far-field data but taking the ISP levels as input, to test the consistency of the procedure. In other words a difference is made between the total spectra free of the background noise (combined TE and LE contributions) for both baseline and serrated airfoils. The discrepancies with the blue line are attributed to the background noise. The same black and blue spectra in Fig. 3.25-(c) are reproduced in Fig. 3.25-(d), in which the reduction spectrum of the trailing-edge noise only as deduced from the localization-map integration is added as the red line. The reduction remains positive up to a Strouhal number fh/U_0 of 2 and is negative for higher Strouhal numbers. This illustrates the

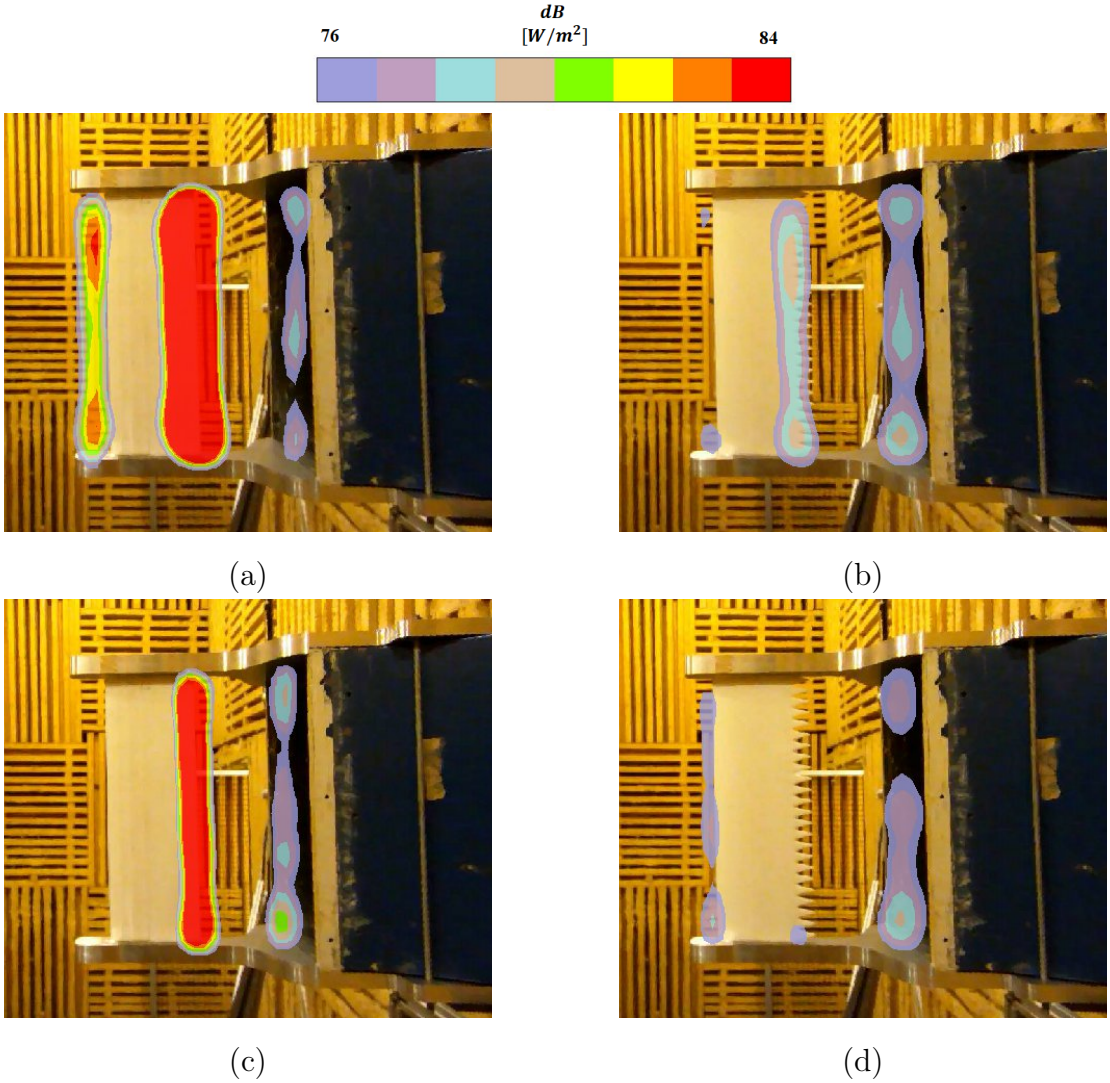

Figure 3.24: Source localization maps in the integrated ranges $4.5 - 6.7\,kHz$ (a,b) and $6.7 - 9\,\text{kHz}$ (c,d), at $U_0 = 32\,\text{m/s}$. (a,c): baseline airfoil; (b,d): serrated airfoil. Flow from right to left.

aforementioned increase and decrease in both frequency ranges in Fig. 3.24 and illustrates the different TE noise traces in Figs. 3.25-(a) and (b).

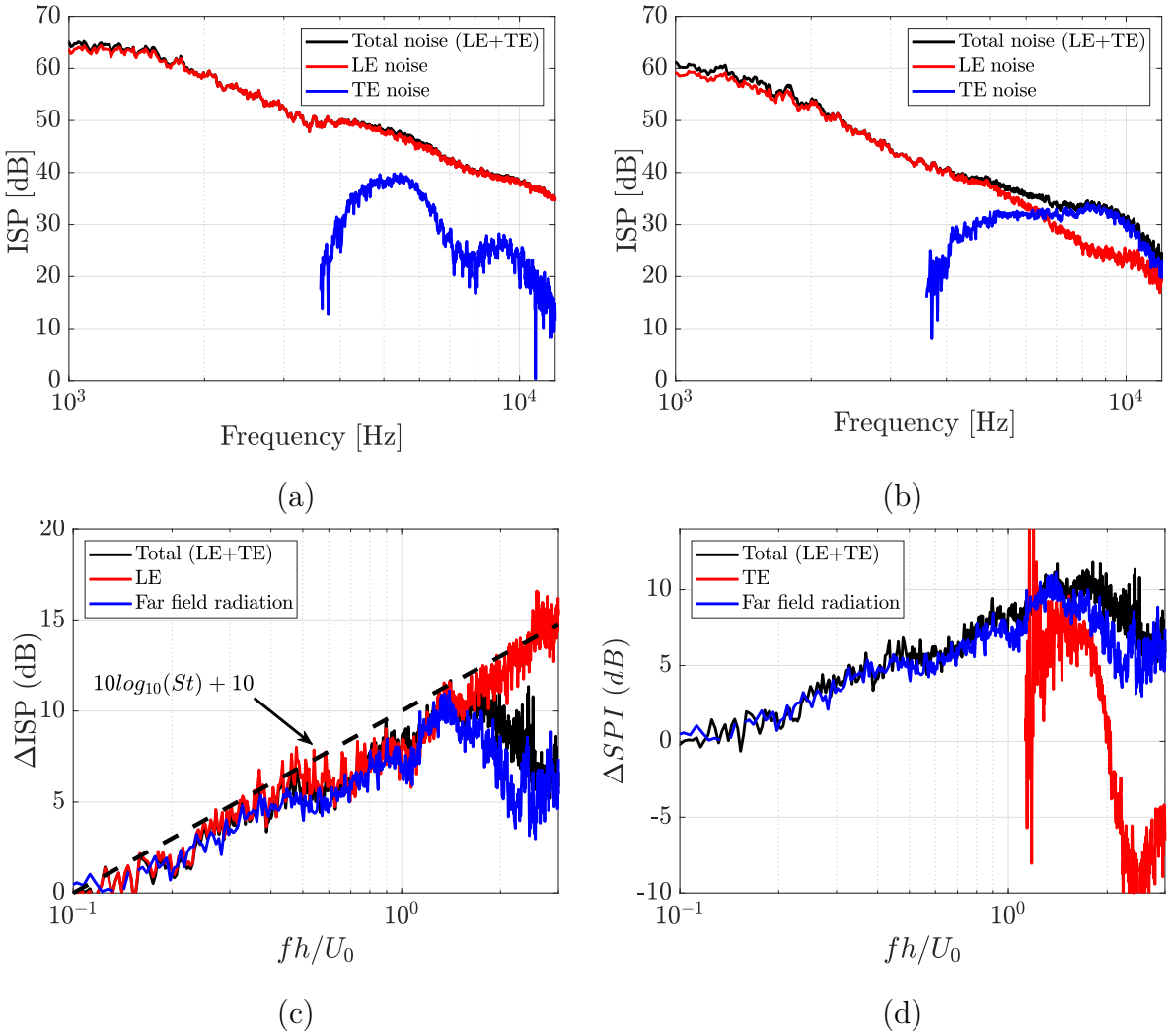

Figure 3.25: LE noise (TIN), TE noise and total noise extractions generated by the filtered array processing (see the red and green interogated windows respectively in Fig. 3.23-(b)). (a): baseline airfoil; (b): serrated airfoil with $h/c_0 = 0.1$. (c): LE noise reduction as estimated from far-field data (blue) or map integration (red) and reconstruction of the far-field data processing from the map integration (black). (d): TE noise reduction from map integration.

3.6.1 The Reconstruction Procedure

The above analysis is supported in detail by a reconstruction of all the noise sources by performing simple subtractions. Fig. 3.26 shows the integrated source-power of the rectangular areas displayed in Fig. 3.23-(b) as well the background noise of the corresponding areas in the absence of the airfoils but the existence of the support plates. Starting from the measured total noise source (Total noise) of the serrated profile ($h/c_0 = 0.1$) and subtracting the total background noise (Total BGN), the resulting subtracted total noise (Total noise (Sbtr)) starts to separate from the initial curve (Total noise) at 3 kHz where the differences between them become less than 10 dB. The subtracted total noise curve was used above for comparisons to the single microphone measurement results (Fig. 3.25-

(b), (c)). Then, the extraction of the leading edge (LEN (Sbtr)) and the trailing edge (TEN (Sbtr)) sources has clearly shown the reconstruction of the - LE+TE (Sbtr) - curve which corresponds to the summation of these two sources. The integrated power of the background noise of the corresponding rectangular areas of the aforementioned sources are subtracted without modifying the LEN and TEN sources as their background level is quite low (dashed lines).

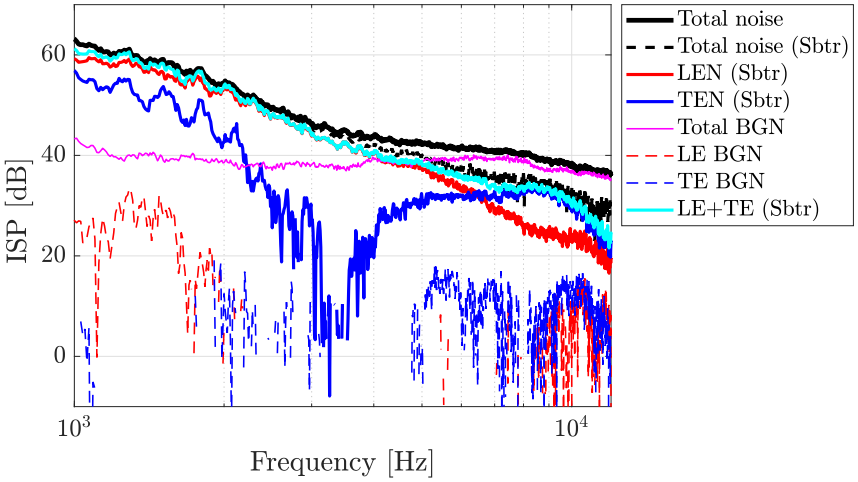

Figure 3.26: With the use of the spiral antenna, multiple noise sources generated of the serrated flat plate and the setup are plotted together for reconstructing the total radiated noise. Sources: Total noise, LEN, TEN and their corresponding subtraction for each integrated area.

3.6.2 Noise Sources Contributions to the Total Airfoil Noise

Noise reductions (ΔPWL) of leading- and trailing-edge noise sources extracted from the TIN between serrated and baseline airfoil are plotted in Fig. 3.27. The reduction of TIN (blue) and self-noise (green) measured at the far-field with the rotating antenna are presented again and are compared with the NR due to the leading- and trailing-edges that are measured with the spiral array. The level differences are calculated on integrated sound power for both techniques, the frequency resolution of the spiral array has decreased from 10 Hz to 40 Hz and the sampling frequency is set at 52.1 kHz. Essentially, this aggregate plot shows the TIN (blue) behavior that already presented in Fig. 3.25 according to LE and TE noise contributions. Observing the 8 dB of TIN deviation from the LEN (red) at Strouhal number around 28 and also the 8 dB of TEN (red dashed) deviation from zero level occuring at the same non-dimensional frequency, we conclude that TEN for the serrated case increases significantly compare to the LEN reduction giving modifying eventually the TIN in the far-field. This observation is also intersects with the TIN power difference (black) between the baseline and serrations that stems of the logarithmic summation of LE and TE noise as follows:

$$\Delta TIN_{LE+TE} = 10log10(\frac{10^{(BSL_{le}/10)} + 10^{(BSL_{te}/10)}}{10^{(SER_{le}/10)} + 10^{(SER_{te}/10)}}) \tag{3.11}$$

Self-noise reduction (green) matches closely to the TEN reduction but is still different in terms of level meaning that different boundary layers upstream the TE give different input for TEN generation. In higher frequency ranges where ΔTIN_{LE+TE} is increased compare to the total ΔTIN, the analytical sound prediction models described at the next section could provide an additional hint.

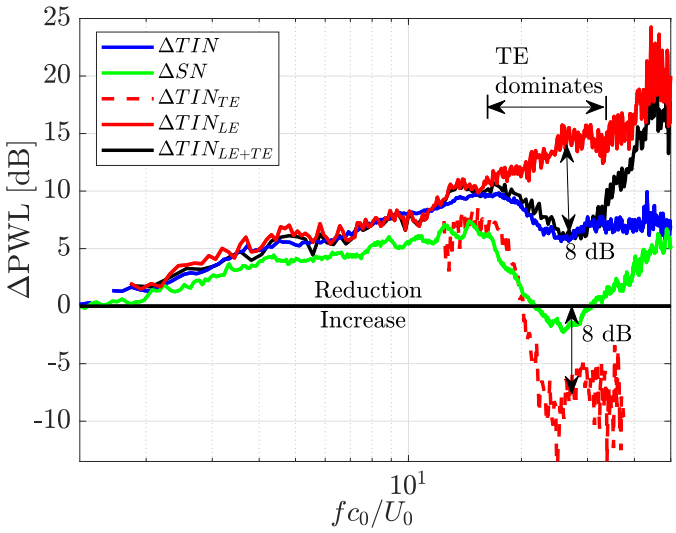

Figure 3.27: Nose reduction curves of TIN and self-noise with the use of the single microphone and the spiral antenna at $U_0 = 32$ m/s.

3.7 NACA-0012 Airfoil Investigations and Comparisons

In this section, the acoustic signature of the NACA-0012 airfoil with and without serrations is explored and is also compared with the correspondent flat plates at their most relevant performances. Following the same methodology as for the flat-plates configuration, NACA 0012 airfoils have been tested in the far-field and with the near-field microphone array. The LEN of the serrated airfoil has been evaluated and compared to the corresponding noise source predicted for a serrated NACA65 [116].

3.7.1 3D Airfoils

TIN is explored by performing sound level differences in the far-field between the serrated and the non-serrated airfoil. The symmetric NACA 0012 airfoil with 10 *cm* mean chord and 30 *cm* span has been manufactured with a three-dimensional printer and the design parameters (depth and wavelength) of the wavy leading edge are the same as for the serrated flat plate version ($h/c_0 = 0.1$). The selected design parameters are not the optimum in terms of noise reduction but they will be enough to investigate the contribution of each noise source independently, here is the LE and TE sources, after the serrations application. For simplifying the definition of geometrical parameters, the serrations pattern modifies the leading-edge shape till the position of maximum thickness following the chord function $x(y) = c_0 + h\sin(2\pi y/\lambda)$ and maintaining the same 4-digit profile downstream $0.7c_0$ without varying the thickness. Geometrical details of the serrated airfoil are shown in Fig. 3.28. The choice of NACA 0012 profile also ensures clearer observations because of its symmetric geometry and allows taking benefit from the extended literature. Setting as a starting point the acoustic measurements in the far-field, the noise reductions of the airfoil as a single component were evaluated, indicating the frequency ranges that the beamforming technique could be used for deeper analysis.

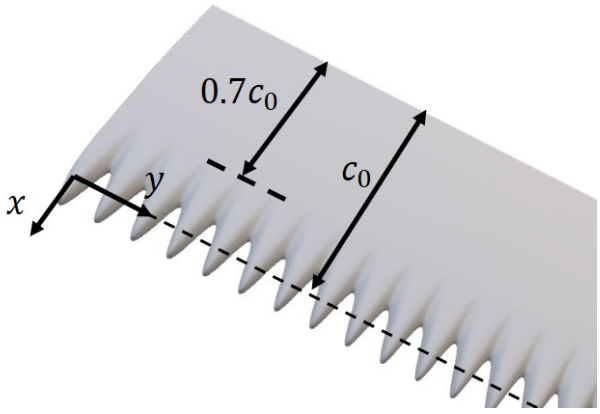

Figure 3.28: Three-dimensional printed NACA 0012 with serrated leading-edge and non dimensional amplitude $h/c_0 = 0.1$, c_0 is the mean chord.

3.7.2 Acoustic Performance in the Far-Field

Results from the TIN measured in the far-field have shown important reductions between the baseline and the serrated airfoil in a low non-dimensional frequency St_h range between $0.1 - 2$ ($500 - 3000$ Hz) whereas there is a small increase with the serrated profile approaching the very high frequency ranges close to 15 kHz, see Fig. 3.29-(a). The self-noise, plotted at the same figure, showed reduction up to 4 dB for the same frequency range as the TIN while it is approaching the background noise level quite close at high frequencies. Comparing the TIN and self-noise at high frequencies, TIN shows to be slightly higher but always following the self-noise trend in spectra. This highlights the noise source nature between them which is the trailing edge noise but due to the different upstream conditions the noise level is different. The noise differences are confirmed at Fig. 3.29-(b) for both TIN and SN where the maximum reduction appears at 7 dB while for St_h numbers $3.5 - 7$ stabilized at 6 dB. In addition the TIN reduction validates the empirical relation $10\log_{10} St_h + 10$ additionally to the flat-plates application. The plateau that the NR happens seems to be linked to the increase of self-noise similarly observed to the flat-plates NR performance. Here ((Fig. 3.29-(a))), for St_h equals to 0.8 (2.5 kHz) self-noise is approaching the levels of TIN for the serrations and finally collapses to it at $St_h = 0.93$ (3 kHz) where the NR (Fig. 3.29-(b)) is starting to decrease.

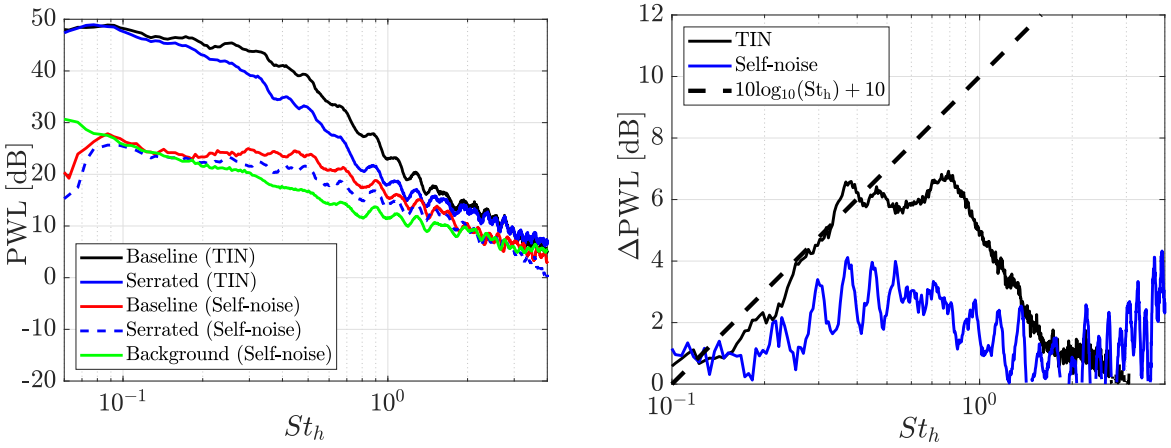

(a) (b)

Figure 3.29: (a) Sound radiation in the far-field measured with a single microphone at 90° radiation angle, serrated profile (red curve), baseline (black curve), (b) noise reductions between baseline and serrated airfoil using a single microphone in the far-field (blue curve) and the spiral antenna (black curve).

The beamforming technique was used also for the NACA-0012 airfoil for evaluating the LE and TE sources. Defining the same rectangular areas as in Fig. 3.23, the LE and TE sources were extracted and plotted in Fig. 3.30. Again, the background noise of each integrated area has been subtracted for each sound source. Surprisingly, the TEN sources for both airfoils overcome the total noise in the limit and apart from that the total noise appears an oscillatory behavior in high frequencies. The explanation is that the total noise

is masked by the background noise at high frequencies ($\geq$ 7 kHz) without equalizing the negative differences to NaN numbers. Thus, a clearer visualization of the sound sources is succeed. The most important outcome from Fig. 3.30 is the reduction of the LEN at $St_h = 0.7$ and the decrease of the total noise level to the limit of TEN. Fig. 3.31 confirms these observations by showing the noise reductions of the spiral (black curve) and the single microphone (blue curve) arrays. Additionally, LEN and TEN are plotted as well as the logarithmic empirical expression. The noise reduction curves found perfect agreement in terms of level and frequency till $St_h = 0.7$ and the same trend till high frequencies with a small overestimation due to the background noise differences. LEN reduction collapses also with the total noise till $St_h = 0.7$ where it dominates whereas beyond $St_h = 0.7$ increases steeply without following the empirical expression. Surprisingly, this trend follows closely the numerical predictions of the LEN reduction (green curve) [116] (Fig.35-(a)) of a flat plate with $h/c_0 = 0.1$ and $\lambda/c_0 = 0.066$ where the reconstructed noise does not involve the trailing-edge part. Both curves fit each other and the increasing trend after $St_h = 0.7$ is the same till 14 dB where the background noise level do not allow experiments access in lower sound levels. This simulation consists of 3D compressible Euler equations which still does not count for the full turbulence evolution at the LE. Thus high order simulations are needed for obtaining a more accurate prediction. Beyond $St_h = 0.7$, the TEN increases efficiency up to positive reduction values maintaining the NR level positive,around 2 dB, but still low at higher frequencies. This confirms the similar self-noise behavior of both baseline and serrations in Fig.3.29 where they nearly collapse each other above $St_h = 0.7$.

Many similarities have been observed between flat plates and NACA-0012 airfoils in terms of noise reductions and directivity. Next section 3.8 describes both performances in terms of aerodynamic and acoustic efficiency.

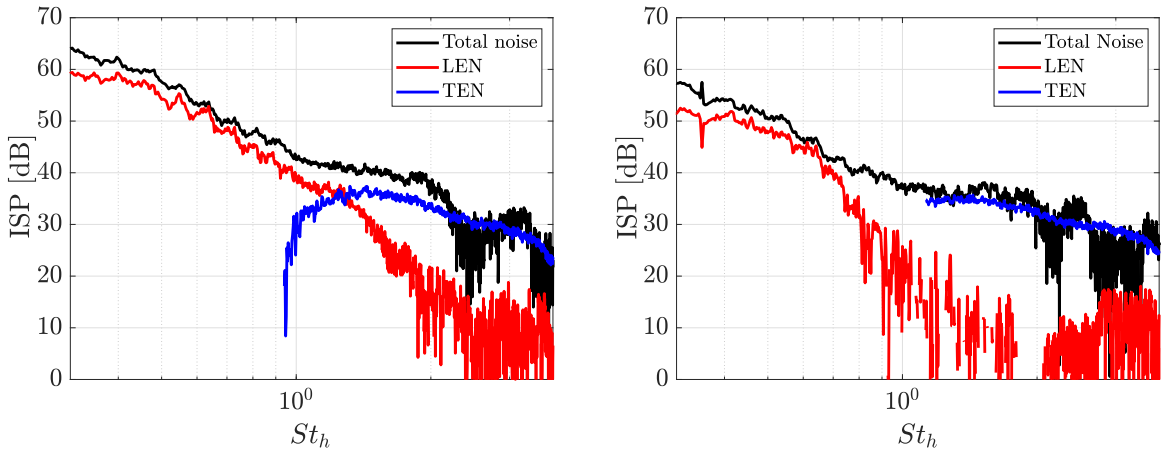

Figure 3.30: LE and TE noise measured with the spiral antenna for (a) the baseline and (b) the serrated airfoil in turbulent conditions. The total noise (black curve) equals to the radiated noise from the whole set-up. The background noise has been subtracted. $U_0 = 32$ m/s.

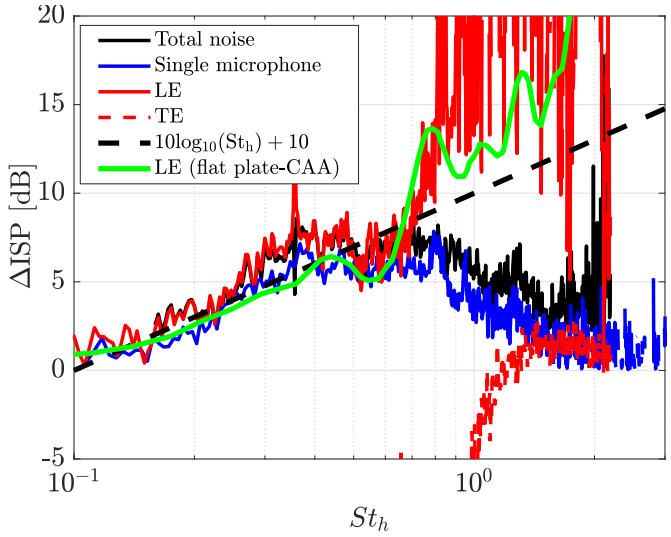

Figure 3.31: Noise reduction trends for LEN, TEN and total noise sources with the use of the spiral and single microphone antennas at 90°. $U_0 = 32$ m/s.

3.8 Comparisons between 2D and 3D Airfoils

The acoustic performance exploration of both flat plates and NACA-0012 airfoils can be extended further by making comparisons in terms of efficiency. Therefore, at this section both applications are compared in terms of acoustics and aerodynamics proposing possibly the best choice to be applied at a real engineering device. The answer of delivering the most efficient device will not be given in the present work, mostly due to the unknown conditions of the engineering or application environment such as the space, the speed, the lift, the durability, the allowed aerodynamic penalties and others. From the acoustic perspective the following figures show the sound emissions both in clean and turbulent flow conditions. The aerodynamics have been explored by measuring the drag force at near wake downstream the trailing edge.

TIN has been investigated in Fig. 3.32 comparing the baselines and the corresponding serrated ($h/c_0 = 0.1$) using both the spiral and the single microphone antennas. Fig. 3.32-(a) highlights the big PWL differences between the NACA12 and the flat plate. It is clear that the additional thickness of NACA12 reduces efficiently the TIN as the noise level of the serrated flat plate reaches the level of the NACA12 baseline. Apart from that, the baseline NACA12 yield reductions of about 3 dB than the serrated flat plate beyond $St_h = 1$. Complementary noise reductions were achieved with the serrated NACA12 at which the differences with the baseline flat plate reaches up to 16 dB while it generates less noise over all the frequency range. The correspondent noise reductions as well as their LEN sources extracted with the spiral antenna are compared in Fig. 3.32-(b). Flat plate reaches noise mitigation up to 10 dB over a large frequency range whereas NACA12 show lower reductions till 7 kHz for a narrower frequency range. Same performances are found by [116, 126] for thick airfoils in similar upstream conditions. Same measurements have been done by Roger and Moreau [126] for NACA-0012 airfoils with 10 and 12 cm

mean chord and they found higher noise reductions up to 10 dB for the 10 cm chord mock-up. It is worth to mention that the serrated pattern modifies the baseline profile at its thickness progressively till the wavy shape be merged smoothly with flat surface at the span-wise direction. This surface shape probably modifies the boundary layers development downstream the serrations resulting to a different scattering of the boundary layers to sound. Plotting again the empirical expression $10\log_{10}\mathrm{St_h}+10$, all the reductions trends follow the monotonic increase up to $St_h = 0.7$ while the flat plate even extends to higher frequencies. For a better interpretation, the resolution of the spiral antenna extractions has been reduced from 10 Hz to 40 Hz. Note that the NACA12 LEN reduction curve does not follow the empirical expression at higher frequencies highlighting a different behavior of serrations at thick airfoils.

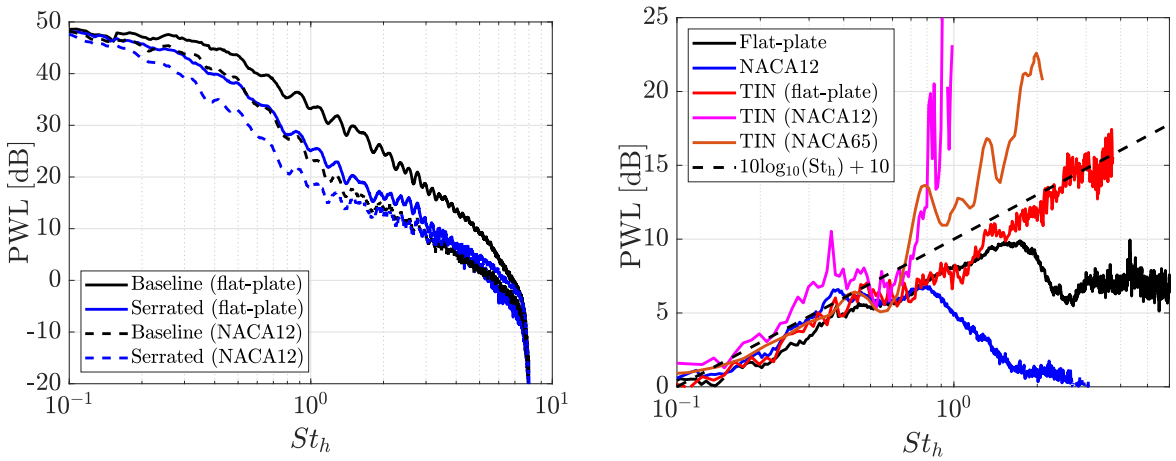

(a) (b)

Figure 3.32: (a) Sound Power level of TIN measured with the single microphone for flat plates and NACA12 airfoil and (b) the corresponding noise reductions making also the use of the spiral antenna. $U_0 = 32\ m/s$.

The influence of self-noise on the total TIN has been already discussed on the previous sections for each serrated airfoil while in Fig. 3.33 the self-noise and TEN are shown additionally in common. Significant noise reductions occur also in self-noise; flat plate shows 7 dB of maximum reduction and an increase of 2 dB between 1 and 2 Strouhal numbers (see Fig. 3.33-(a)). Beyond the non-dimensional frequency 7 both baselines approach the background noise level (green) while the both serrated fall under the background level after its subtraction. This is clear shown in Fig. 3.33-(a) where a second NR hump of about 6 dB appears above $St_h = 7$. This secondary NR humps are confirmed partially also with the TEN reduction curves extracted with the spiral antenna. Here, the curves of the integrated power of the rectangular areas correspond to the TEN generated from the TIN. Both differences and similarities are presented at their agreement with far-field measurements of self-noise, meaning that TEN stems from TIN is slightly different to the TEN due to the self-noise. This is already noted in Section 3.6.2. The above observation supports conversely the self-noise measured for a NACA65 airfoil by Paruchuri *et al.* [32].

According to this reference (Figure 10) the self-noise generated from serrated airfoil is higher compare to the baseline beyong the non-dimensional frequency $fc_0/U_0 = 30$. Beyond this frequency (13 kHz) noise is not clearly detected from human hearing especially at low Mach numbers. Additionally, the sound level is already quite low for detecting the differences, thus most of the results are out of interest beyond this frequency.

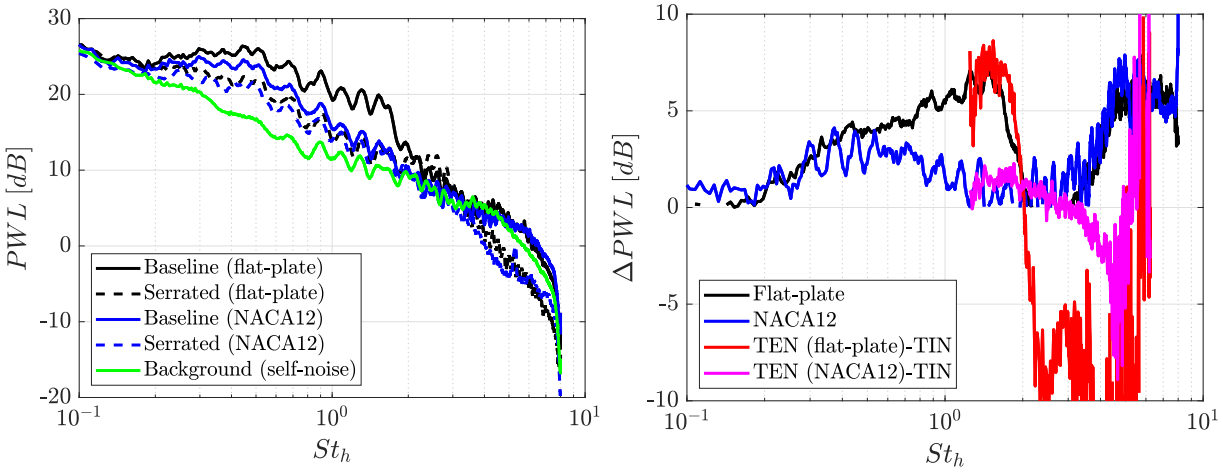

(a) (b)

Figure 3.33: (a) Sound Power level of self-noise measured with the single microphone for flat plates and NACA12 airfoil and (b) the corresponding noise reductions making also the use of the spiral antenna. $U_0 = 32$ m/s.

3.9 Aerodynamic Measurements

This section investigates the aerodynamic efficiency of the tested airfoils and flat plates used at the previous chapters. Although, acoustics are of primal interest of this work, the aerodynamics of the serrated airfoils have also to be considered for using them on industrial applications. According to previous studies mentioned in the literature 3.2 longer serrations achieve higher noise reductions and also delay stall. Conversely, longer teeth have aerodynamics penalties due to the reduced lift surface and the increased drag. The serration size at the present work has been chosen in a such way that the losses in aerodynamics could be acceptable. The aerodynamic effect of serrations has been estimated from Hot Wire Anemometry (HWA) with a traversing single-wire probe, by measuring the velocity deficit in the wake. The estimated distance to the airfoil trailing edge is ≤ 1 mm. The drag coefficient has been calculated for all the airfoils and flat plates while the effect of angle of attack has been explored for NACA12 airfoil. Additionally, the velocity profiles at the leading-edge position and downstream have been measured highlighting the differences in mean and turbulent components between the valley and the peak of the tooth. The present results will be the validation data for supporting the PIV and the numerical results provided by RANS for performing further the optimization study.

3.9.1 Wake Characterization

Measuring the temporal local velocities at the very vicinity of the airfoil surface, the local mean-flow speed and the root-mean-square of the streamwise velocity component were computed. The measurements have been done in high spatial resolution normal to the chordwise direction with different displacement steps from 0.25 mm to 1 mm depending the measured velocity gradient of the BL.

3.9.2 Flat Plates

The velocity profiles were measured on both sides of the flat-plate positioning the trailing edge at zero. All the wake measurements have been repeated for two different positions for validation reasons. Fig. 3.34 shows the stream-wise velocity profiles for both baseline and serrated flat plates. The baseline presents slightly wider wake profile than the serrations up to 1 mm far from the surface whereas serrations wake becomes broaden beyond this limit. The u_{rms} profile at the right plot shows higher kinetic energy for the baseline case linked to increased trailing-edge noise. This is consistent with the self-noise reduction at low-mid frequency range due to the serrations. A rough estimation of the wall-pressure spectrum can be achieved using the boundary layer thickness displacement δ^*, linked to the BL thickness making use of different wall-pressure models. An increased δ^* could give higher noise levels. An example of the the TEN prediction will be given in Chapter 6.

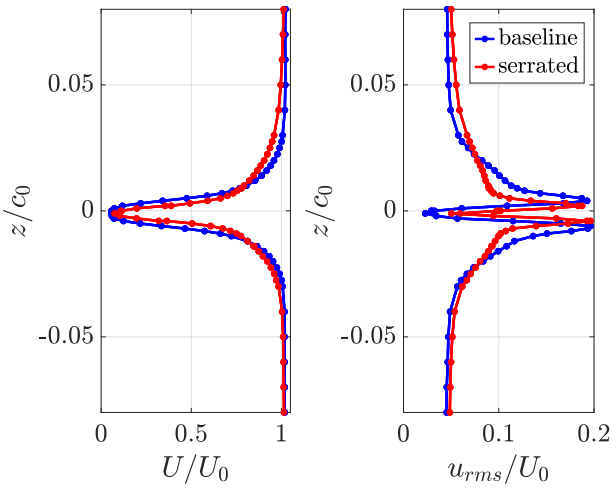

Figure 3.34: Velocity profiles in the wake for the flat plates measured at a distance less than 1 mm from the trailing edge and downstream the valley position for the serrated case. The velocity is $U_0 = 20\,\mathrm{m/s}$.

3.9.3 NACA-0012

The wake profile of the serrated NACA12 presents a clear increase of the BL thickness and a very small displacement on the one side. Nevertheless the drag coefficient has shown an increase of 15.5 % compared to the baseline (see Fig.3.35). This is also consistent with

Chaitanya's findings on a NACA65 airfoil [32]. Here, the u_{rms} profile for the serrations becomes wider while the maximum u_{rms} values close to the trailing edge appear smaller. A questionable issue that was already partially explored from other researchers is the wake influence after the serrations application. As mentioned before, wake measurements in two different positions at the trailing edge have been performed. This allows to estimate an average of the values needed for TEN prediction. The wake profiles plotted in Fig.3.36 correspond to positions downstream the the serrations valley and peak for the NACA12 baseline (top) and the serrated (bottom). No differences have been observed between the two positions meaning that the chord length and the size of the teeth are long enough for mixing the boundary layers generated of the peak and the valley. For longer teeth the result could be different as the valleys approaches more the trailing edge. Therefore, the data extraction for predicting the TEN could be done from any position at the trailing edge for the present serrated airfoil.

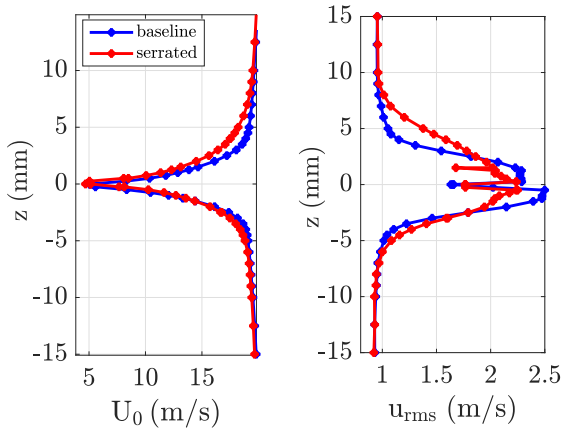

Figure 3.35: Velocity profiles in the wake for the NACA12 airfoil and the corresponding serrated at the spanwise positions z=122.5 mm and z=183.75 mm respectively. Free stream velocity: $U_0 = 20$ m/s.

3.9.4 Angle of Attack for NACA-0012 Airfoils

The aerodynamic degradation with the insert of leading-edge serrations has been explored by estimating the drag coefficient for different angles of attack (AoA). Thus, the velocity profiles at the wake have been measured for AoA $0°, 5°, 10°$ for NACA12 with and without serrations. The exploration of higher geometrical angles was not achievable because of the jet deflection of the open jet wind tunnel. Nevertheless, the angle of 10° is enough to estimate the aerodynamic signature of serrations. The momentum theorem has been used for estimating the drag coefficient for each airfoil at $U_0 = 20$ m/s as shown in Table 3.1. Comparing baseline and serrations for both flat plates and airfoils, the amount of increase in drag is quite similar while serrated flat plate seems to degrade more its aerodynamic efficiency. Also, the amount of losses of the serrated flat plate ($C_d = 0.0364$) shows to approach the baseline NACA12 ($C_d = 0.0383$). The angle of attack degrades additionally

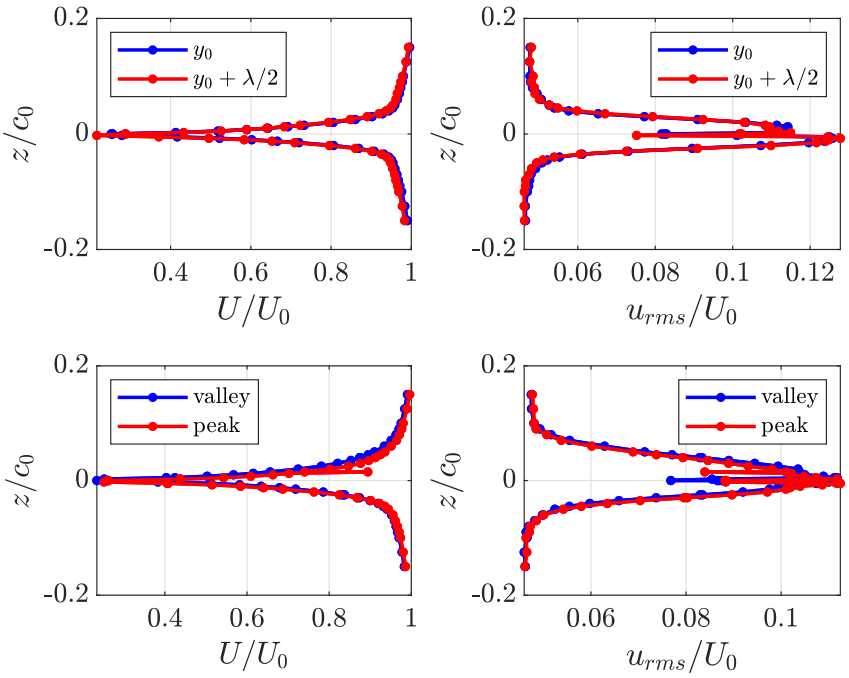

Figure 3.36: Mean velocity profiles U_0 (left) and u_{rms} (right) measured at the wake downstream at the very vicinity of the trailing edge of the baseline NACA12 (top) and the correspondent serrated (down). The two positions correspond to the serration valley and the serration peak. $U_0 = 20\,\mathrm{m/s}$.

Table 3.1: Drag coefficient estimation, C_d, for all the airfoils

AoA	Baseline (flat plate)	Serrations (flat plate)	Baseline (NACA12)	Serrations (NACA12)
0°	0.0257	0.0364	0.0383	0.0441
5°	-	-	0.0490	0.0528
10°	-	-	0.0565	0.1499

the drag of the airfoils while serrations increase the drag deeply for the big angle of 10°.

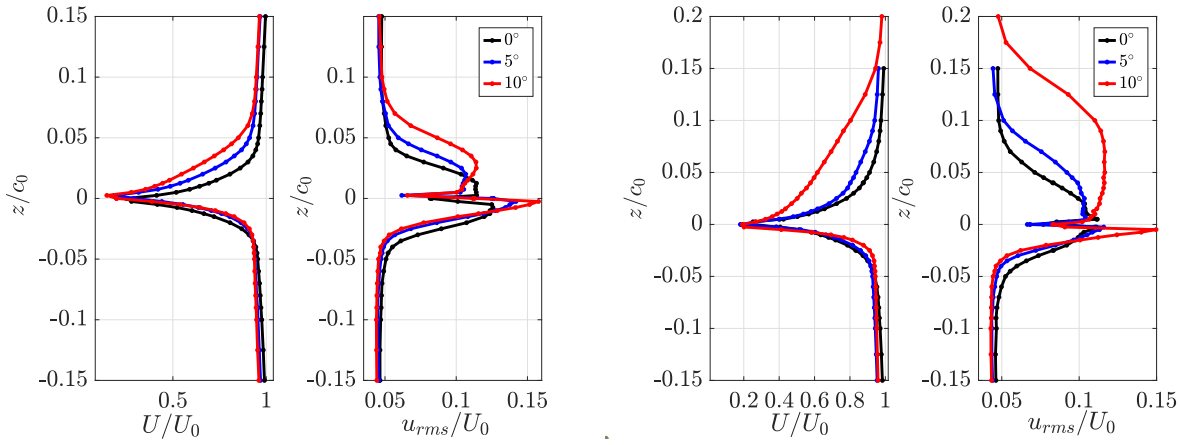

(a) (b)

Figure 3.37: Velocity profiles at the wake for the NACA12 airfoil (left) and the corresponding serrated (right). The velocity is $U_0 = 20\,\mathrm{m/s}$.

3.9.5 Boundary Layer Development along the Leading-Edge Serrations

In this section the effect of leading-edge serrations on the boundary-layer development has been investigated. The streamwise velocity component was measured in the very vicinity of the wall in different positions along the serration tooth and the corresponding positions for the baseline. The measured positions are shown in Figs. 3.38 and 3.40-(a) and corresponding boundary layers in Figs. 3.39 and 3.40-(b). The position 0 corresponds to the location of the tooth peak upstream the stagnation point at a distance $\leq$ 1mm. Other positions correspond to the hill and the root of the tooth as well as at the valley. The velocity profile measured at the position -1, 3mm upstream the leading edge, shows a small decrease to 19 m/s for the first 4 mm from the wall while the speed reached the freestream velocity at 6 mm. For all the other positions the velocity out of the boundary layer has been found $18 - 19$ m/s. Despite the fact that the boundary layer of the flat plates is quite small, the velocity needs more than 10 mm to recover its freestream conditions. This is shown clear for the position 3 that the velocity is stabilized at 18 m/s, Figs. 3.39. A slight increase of the velocity is appeared at the valley of the serration (position 4) where the speed tends to accelerate due to the narrow ending of the serration tooth. Conversely, the PIV results in Fig have shown a decrease of the streamwise component at the very close of the valley. More comparisons between the HWA and PIV techniques for the flat plates boundary-layers profiles will be presented in the Chapter 5. The development of the boundary layers for the baseline (Fig. 3.39)-(c)) shows a normal growth moving downstream the leading edge. Additionally, the thickness of the boundary layers seem to be smaller than 1 mm for the positions 1 and 2 that correspond to the hill and the root positions of the serration (Fig. 3.39)-(a)). Observing again the positions 1 and 2 for the baseline and the serrations, it seems that the boundary layer for the serrated case has been measured slightly more far from the wall than for the baseline. This argument is based

on the minimum values of the measured velocity. For example, at the position 1 serration shows minimum value of 15 m/s whereas the baseline shows 8 m/s as minimum measured velocity. These observations will be useful for further comparisons and validation of the PIV measured boundary layer profiles at the same positions.

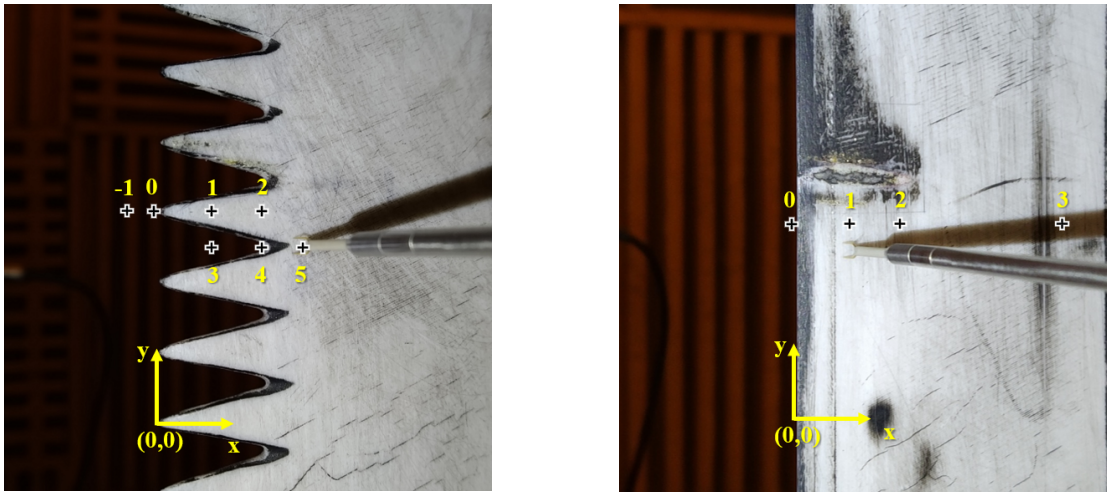

Figure 3.38: (a) Positions of the measured boundary layer profiles for the serrated (left) and the baseline (right) flat plates along the streamwise directions.

The corresponding u_{rms} velocity of the aforementioned positions are shown also in Fig. 3.39-(b). Here, the TI at the position of leading edge (-1) has been validated at ≈ 0.045 as measured in Chapter 2 with the difference that the flat plate here is installed. The u_{rms} at the position 5, $6-7$ mm downstream the valley, presents higher intensity than the positions along the teeth. This is consistent with the findings of Kim *et al.* [75] that higher turbulent intensity is concentrated at the valleys, thus the source of sound of the serrations is located at the valleys. Despite the fact that this finding is consistent with the vortical component of velocity, u_{rms} in the Figs. 5.19 obtained with the PIV show higher TI at the valleys than along the tooth. Apart from the above observations, positions that are before or after the point 5 for both straight and serrated leading edge present smaller TI than at position 5. Similar findings have been also found by Chaitanya [32] according to the development of BL downstream the serrations. The boundary layer development has been also measured for the serrated NACA12 airfoil along the streamwise direction of a tooth, see Fig. 3.40.

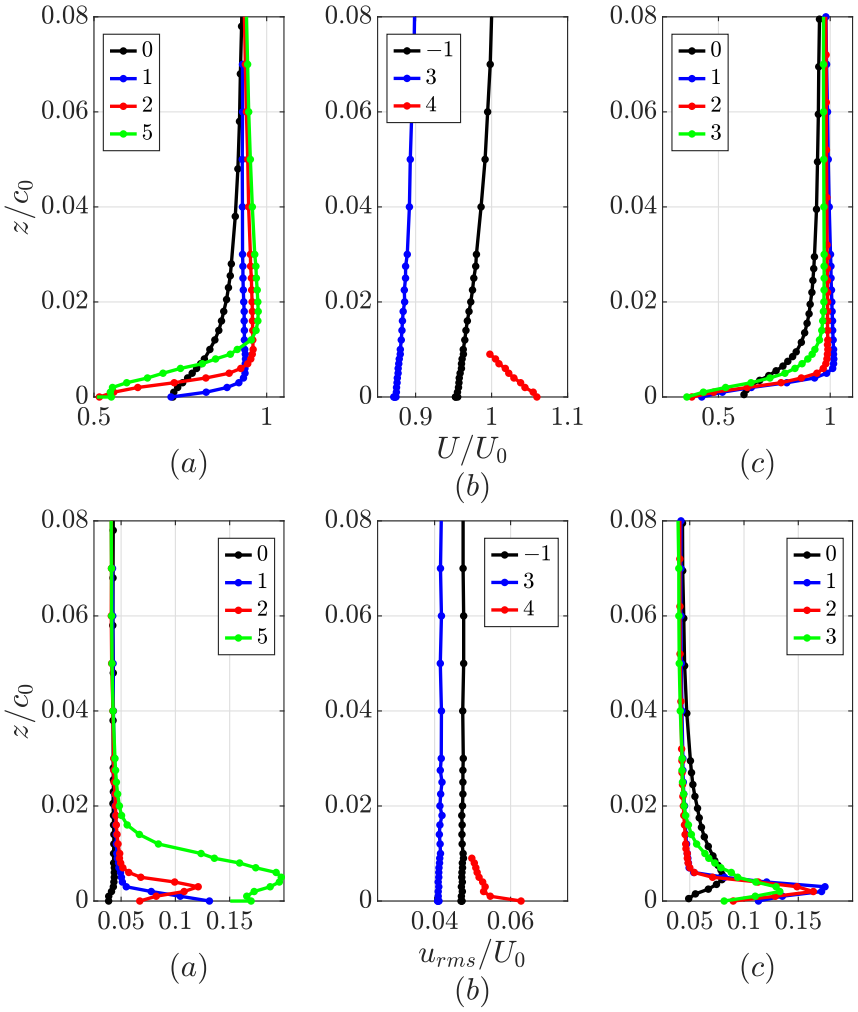

Figure 3.39: The boundary layers for the positions (a) and (b) of the serrated case (Fig. 3.38-(a)) and the boundary layer positions (c) for the baseline (Fig. 3.38-(b)). Free-stream velocity at $U_0 = 20$ m/s.

3.9.6 Concluding Remarks

Far-field and near-field acoustic measurements have been conducted on flat plates and NACA12 airfoils with and without serrations. Results have been found consistent with findings from different researchers, two wavy shaped leading edge serrations have shown substantial noise reductions over wide frequency range and flow speeds. Two noise reduction regimes have been identified for the serrated flat plates compared to a single one of the serrated NACA12. This observation has been highlighted in this study compared to previous works and a further exploration using the noise localization technique has been carried out. Using the rotating microphone antenna for accessing the noise emissions in the far-field and the localization technique for the near-field exploration, the most important outcomes are summarized below.

- The flow dependence and the non-compactness areas as a function of Strouhal number have been spotted while the threshold of non-compactness has been found at

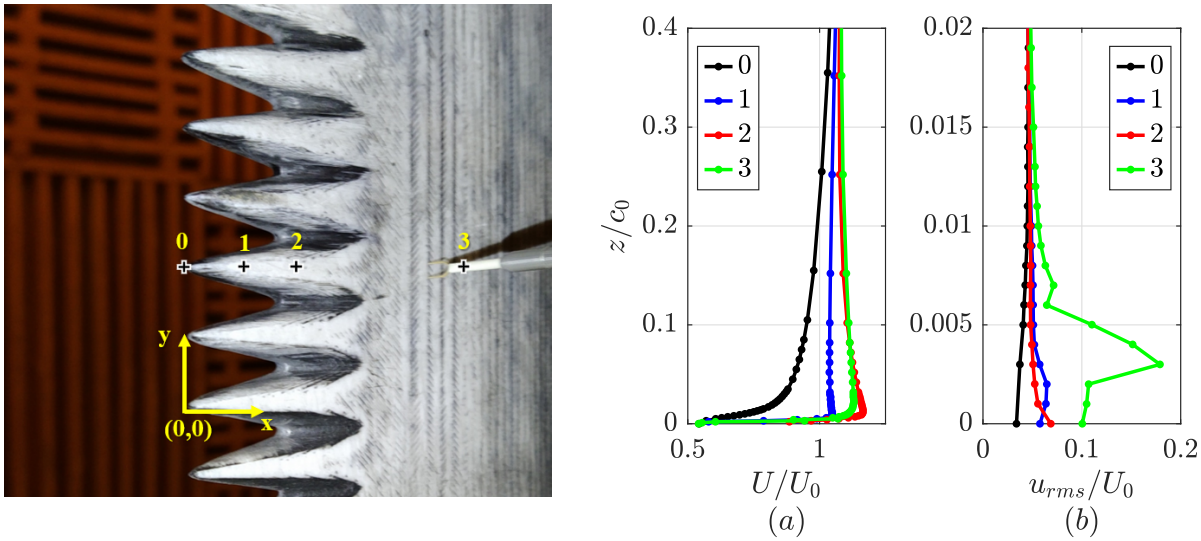

Figure 3.40: (a) Serrated NACA12 and the four measurement positions of the boundary layer profiles. (b) Boundary layer profiles that correspond to the four positions along the tooth. The velocity is $U_0 = 20$ m/s.

$St_h = 0.5$ for the serrated flat plate.

- Directivity patterns in 3D present the same directivity patterns at low-frequency regimes till the compactness limit of $kc_0 = 2\pi$ between the serrated case and the baseline flat plate. Beyond this threshold, the general radiation shape of serrated cases remains similar to the baseline but by increasing the frequency slightly more fringes appear while humps appeared in the diagrams of serrated versions are shifted by 5° or 10° compared to the baseline. The directivity radiation is explored also at the angle of $\phi = 75°$ off the mid-span plane where the radiation for all the airfoils is similar for all chosen wavenumbers and speeds. The sound level is substantially lower than in the mid-span plane and the directivity features a single, dipole-like lobe.

- The TIN spectra of the baseline aerofoil measured at $\theta = 90°$ have shown that the sound level decreases as the polar angle ϕ increases from 0° to 75°, according to the dipolar behaviour of the sources (about -12 dB at low frequencies, less at higher frequencies due to non-compactness).

- An average efficiency of $8 - 10$ ΔdB is observed along all azimuthal angles at non-dimensional frequencies 15, 10, 8 for the speeds 19, 27, 32 respectively. Additionally, maximum values of NR around 15 dB appear between $30° - 60°$ azimuthal angles. The highest overall reduction occurs at the azimuthal angles 30° and 90° and the corresponding polar angles 45° and 60°. It is observed that overall noise reductions at the mid-span plane at $\theta = 90°$ are lower compare to the other angles. This fact is positively considered as a safe threshold in terms of noise reductions

efficiency for conducting measurements at the mid-span plane as most of the studies do.

- Based on far-field measurements, serrated leading edges decrease the self-noise in a wide frequency range, even in high frequencies which is consistent with previous studies. This could be connected with the boundary layer thickness that has been measured closely downstream the trailing edge for both flat plates. Baseline flat plate has shown slightly smaller BL thickness, despite this fact the scattered turbulent BL at the trailing edge radiates higher noise than the serrated plate.

- Near-field measurements indicated that LEN reduction increases monotonically with Strouhal number while it validated the empirical relation $10\log_{10}(St_h)$ proposed by Chaitanya [116]. Additionally, LEN reduction stem from serrated NACA12 has shown an increase trend proportionally to Strouhal number but with a different increasing trend. Numerical NR predictions for a NACA65 shown the same NR trend have been also validated. Finally, a proper combination of far-field and near-field noise measurements propose that trailing edge noise is the most possible factor that degrade the TIN reduction efficiency at high frequencies.

- HWA performed at the wake of the airfoils have shown increase of the drag coefficient with the application of serrations of about 15.5 % and 41 % for the NACA12 and the flat plate at 0 angle of attack.

4 Analytical Predictions

Contents

Summary

The interest of research and development for industries in the last years is focused on the development and the use of noise prediction models. Even if they approach solutions in an approximate way, they provide fast and numerically cheap results. Of course, if the engineer is aware of the assumptions and the limitations that the model uses then solutions with good accuracy can be obtained. In this chapter, Amiet's theory and Lyu & Ayton's model have been used for predicting the TIN emitted by flat plates with straight and wavy leading edges respectively. A short description of Amiet's problem statement is presented for understanding the basic noise generation mechanisms. The three dimensional application of Amiet's model is presented and compared with the obtained experimental data base. Lyu & Ayton's model is applied in a 2D framework as a correction to Amiet's and compared with the experiments for both straight and wavy leading edge shape.

4.1 Analytical Modeling of Turbulence-Impingement Noise

4.1.1 Amiet's Problem Statement

The application of Amiet's theory is the most oftentimes used for predicting the noise radiated from turbulence interacting with thin airfoil edges in the field of unsteady aerodynamics. An airfoil embedded in a turbulent flow experiences an unsteady lift which should result in sound generation according to Curle's analogy [43]. By this principle, the unsteady aerodynamic field in a compressible context is linked to the acoustic field. Despite the fact that in aerodynamics the mean value of pressure or lift is of interest, in acoustics only the perturbation part p' is significant as it gives the sound information. The statement of the problem and the assumptions of Amiet's theory are given as follows.

It is assumed that the airfoil is an infinite strip (no tips or span ends) placed along the y axis with, a finite chord along the x axis (assumed to coincide with the flow direction) and z being the axis normal to the plate. The solution of the generic problem comes from the calculation of the fluctuating lift distributed all along the plate in a mean flow at zero angle of attack carrying velocity fluctuations normal to the plate. Von Kármán and Sears [150] showed that this is the limit case asymptotically reached with small parameters: camber, angle of attack, thickness and disturbances. By this geometrical approximation, it is indicated that only the mean lift depends on the shape of the airfoil according to the above characteristics, and the fluctuating forces (small perturbations) are not depending on the shape of the airfoil. There is a decoupling between steady-state aerodynamics and unsteady aerodynamics. But this is only valid in the case of small parameters. In case of impinging vortices on the LE, the fluctuating forces (induced by the velocity perturbations) generate dominant sound for a stationary airfoil. The interaction of the vortices

with the leading-edge (LE) is very fast, so the problem of the sound is a matter of inertia and not a matter of viscosity. This can justify the Euler approach both analytically and numerically. Also, the boundary layers and the trailing-edge (TE) noise are not essential for the description of this LE noise.

4.1.2 Frozen Turbulence Assumption and Helmholtz Decomposition

When formulating the problem of turbulence-airfoil interaction, the oncoming disturbances are assumed 'frozen' and purely convected by the mean flow. Indeed the time taken by the disturbances is very short when compared to the characteristic life-time of the turbulent eddies. This assumption of 'frozen turbulence' can be discussed in the general context of the modes of oscillation in a gas.

$$\frac{d}{dt}(\nabla \times V) = 0 \tag{4.1}$$

Based on Chu & Kovásznay [38] analysis, in a gas there are three kinds of oscillating motions; the vortical, the acoustic and the entropy modes, (associated with viscosity, compressibility and thermal conductivity, respectively). Turbulence impingement in our case is considered isotropic. Therefore, only the coupling of the vortical (vorticity) and acoustic (compressibility) modes of oscillation is taken into consideration. Helmholtz decomposition theorem [148] allows to express this coupling by expanding the velocity field as, $\vec{V} = \nabla\Phi + \nabla \times \vec{A}$, where the first and second terms are the potential and the rotational fields. The potentional part is rotational free ($\nabla \times \Phi = 0$) and the rotational part is divergence free ($\nabla\vec{A}$=0) by definition. The rotational part is named as vortical mode of oscillation in a gas and the divergence only involves the potential part.

$$\left.\begin{aligned} \nabla\cdot\vec{V} &= \nabla\cdot(\nabla\Phi + \nabla\times\vec{A}) = \nabla\cdot\nabla\Phi + \cancelto{0}{\nabla\cdot(\nabla\times\vec{A})} = \Delta\Phi \\ \nabla\times\vec{V} &= \cancelto{0}{\nabla\times\nabla\Phi} + \nabla\times(\nabla\times\vec{A}) = \nabla\times(\nabla\times\vec{A}) \end{aligned}\right\} \tag{4.2}$$

If a uniform and constant mean flow is considered and all the equations of gas dynamics are linearized, then both modes are decoupled. Therefore, considering no boundaries and no mean flow gradient (ideal conditions), there is no exchange of energy between the potential and the rotational parts. The unsteady compressible potential motion is associated with what is called acoustic mode. The compressibility is involved in the evolution of the potential part and viscosity is involved in the rotational part. In contrast if boundary conditions (a rigid body) are imposed then the two components of the velocity

are coupled because their sum has to go to the zero at the wall. Practically, adding an airfoil in a flow, potential motion is created while there is a transfer of energy from the vortical motion to a potential motion part of which propagates as sound.

4.1.3 Fourier Decomposition of the Impinging Gust

In Amiet's theory and Sears' problem, the boundary conditions are defined for the potential motion. The mechanisms of turbulence-impingement noise and trailing-edge noise (the BL eddies experience the suppression of a bounding wall) are seen as scattering problems, formulated on the additional potential field introduced by the airfoil singularity in the incident (vortical) disturbed flow.

The impinging disturbances, are decomposed by Fourier analysis [64] in space in both directions. In Sears' [140] problem , the variation of the disturbances in the direction normal to the blade is not essential. We assume that we have locally vertical velocity disturbances but we are interested in the vicinity of the plate. In fact, we assume that turbulence is expanded elementary components, called gust, a 2D wavy pattern described by two wavenumbers, one corresponds to the chordwise direction and the other to the direction of the span. The motion, along the z axis, corresponds to vertical velocity fluctuations w and it is representative for a three-dimensional space. A gust is said oblique because its hydrodynamic wave fronts have an angle with respect to the edge of the airfoil. Practically, Fourier tranform is performed in x and y directions along the span. This defines the 3D Sears' problem solved by linear superposition. Everything is solved in the frequency domain and everything is linearised. We need to use transfer functions. In this problem we use two transfer functions. The input is the velocity fluctuations (w-turbulence disturbances) assumed known.

Changing the inlet velocity at the airfoil leading edge, the response of the airfoil (dF) (Fig. 4.1), is not simultaneous. There is a time delay between the variations of velocity (incoming disturbances) and the response of the airfoil because vorticity is shed in the wake of the airfoil in order that the Kutta-condition [90] be fullfield at any time. The Kutta-condition is the key point of the models, allowing to introduce the effect of viscosity where it is needed, and stating that no flow goes around the trailing edge. We have at any time the flow goes downstream the TE and not around.

Combining the general lift expression, the random incident velocity fluctuations generated by the turbulent structures will cause time variations of both the magnitude and the angle of attack of the velocity vector experienced by the airfoil. Therefore, the velocity potential, $\vec{V} = \nabla\Phi'$ that coincides to the convected wave equation will be resulted from the airfoil lift. The problem analysis below is based on linearized unsteady aerodynamics theory. This theory corresponds to some assumptions, such as for subsonic thin airfoil conditions with small camber and angle of incidence (slightly aerodynamic loaded airfoils) and small velocity fluctuations. The two-dimensional sketch in Fig. 4.1. simply figures out the lift forces product because of the airfoil-velocity disturbances interaction. Summarizing

the above description, a linerized inviscid compressible equation for isentropic flows such as Euler equation is considered for describing this problem assuming small perturbations.

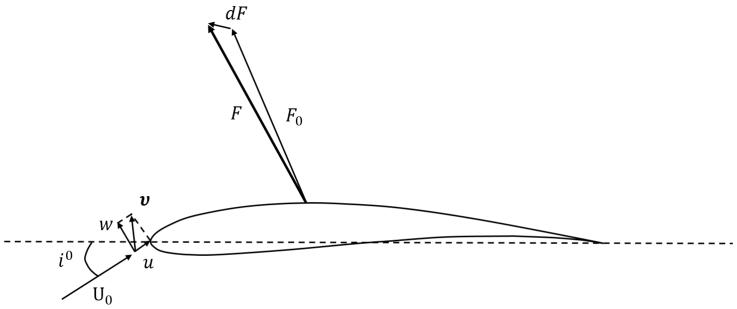

Figure 4.1: Velocity disturbances of the flow and the corresponding lift force vectors

Analyzing the temporal velocity $\boldsymbol{\upsilon} = (u, w)$ and applying it to the lift expression, the resulting expression read:

$$\begin{aligned} dF &= \frac{1}{2} C_L^{i_1} \rho c U^2 - \frac{1}{2} C_L^{i_0} \rho c U_0^2 \\ &= C_L^{i_0} \rho c U_0 u + \frac{1}{2} \frac{\partial C_L}{\partial i}|_{i_0} \rho c U_0 w \end{aligned} \tag{4.3}$$

where $\tilde{U}_0$ is the mean velocity. Expressing the above formulation with the linearized unsteady aerodynamic theory, some assumptions are considered. The airfoil is considered thin behaving like a flat plate with small camber and angle of attack. These conditions determine the steady lift without imposing significant changes on the unsteady load. Accounting that there is a spatial and magnitude homogeneity along the span of the incident perturbations, the normal to the airfoil disturbances consider to be mainly responsible for the unsteadiness. Therefore, for a slightly loaded Joukowski airfoil, the value C_L reads $C_L << 1$, $\partial C_L / \partial i_0 \approx 2\pi$ and Eq. (4.3) is simplified as

$$dF = \pi \rho c U_0 w \tag{4.4}$$

This quasi-steady approximation is known incomplete because it ignores the phase shift required to account for the convection of the shedding vorticity to infinity. Sears' theory is the first model accounting for that. The result is expressed as

$$F(\omega) = \pi \rho c U_0 w(\omega) S(\omega c / (2U_0)) \tag{4.5}$$

where S stands for the Sears' function. Transferring the problem to the 3D space, the origin of the coordinate system is placed at the center of the airfoil, where x is the axial, y is the spanwise and z the normal Cartesian co-ordinates, placed in a uniform flow of velocity U_0 along the chordwise direction and the coordinates on the airfoil surface are $\mathbf{x_0}= (x_0, y_0, z_0 = 0)$. The receiver's position given in Eq. (4.6) involves the corrected distance $S_0 = \left[((x - x_0)^2 + \beta^2((y - y_0)^2 + z^2)\right]^{1/2}$ where the sound-convection effect is taken into account.

$$\boldsymbol{x} = ((x - x_0) - MS_0/\beta^2; y - y_0; z - 0) \tag{4.6}$$

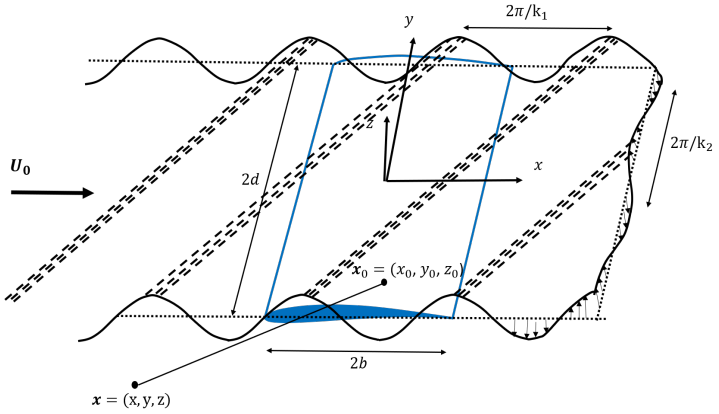

Figure 4.2: Airfoil impinged by a two-dimensional oblique gust in the streamwise direction with k_1, k_2 chordwise and spanwise wavenumbers respectively.

The transverse unsteady oncoming disturbances $\tilde{w}$ of the formulation (4.5) are expressed by considering a number of sinusoidal vertical gusts decomposed in Fourier series. Each gust parallel to the flow induces a certain load on the airfoil because of the convection speed U_0 at a corresponding reduced frequency. For the oblique oncoming gusts, spanwise aerodynamic wavenumbers k_2 are also considered, where the analysis is extended in three dimensions. Furthermore, taking into account the two-sided surface airfoil and the normal convected sinusoidal gust expression, the corresponding pressure jump of the lift force for a single oblique gust in a certain position x_0 is the vector summation of the pressures in both sides, the surface is written as

$$\Delta P(\boldsymbol{x}_0, t) = P - (-P) = 2\,P = 2dF(k_1, k_2) = 2\pi\rho U_0 w_0 g(x_0, k_1, k_2) e^{i(k_1 U_0 t - k_2 y_0)} \tag{4.7}$$

where $\tilde{w}$ is the vertical disturbances, $g(x_0, k_1, k_2)$ is the transfer function between the normal convected impinging gust and the variations of angle of attack.
The incident velocity perturbation for a single gust [11, 12] is defined as

$$\tilde{w}(x, y, t) = w_0 e^{i(k_1 U_0 t - k_1 x - k_2 y)} \tag{4.8}$$

Since the airfoil pressure jump of the lift force $\Delta P(\boldsymbol{x}_0, t)$ (4.7) has been defined in function to the incident velocity perturbation for a single gust $\tilde{w}(x, y, t)$ (4.8), thus both quantities will be expressed in frequency domain. A double spatial Fourier transform is performed in the incident disturbances ignoring the time variable as follows:

$$\hat{\tilde{w}}_R(k_1, k_2) = \frac{1}{(2\pi)^2} \iint_{-R}^{+R} w(x, y) e^{-i(k_1 x + k_2 y)} dx dy \tag{4.9}$$

where R is a large infinite number.

Integrating the pressure jump to all wavenumber components at a certain position, the normal convected sinusoidal gust impinging on the airfoil and the distribution of the pressure jump, ΔP, across a flat plate of infinite span reads

$$\Delta P(\boldsymbol{x}_0, t) = 2\pi\rho U \iint_{-\infty}^{\infty} \hat{\hat{w}}_R(k_1, k_2) g(x_0, k_1, k_2) e^{i(k_1 U_0 t - k_2 y_0)} dk_1 dk_2 \tag{4.10}$$

The frequency dependence will be formulated by performing Fourier transform to Eq. (4.10) and obtaining the pressure jump, ΔP, in frequency domain.

$$\begin{aligned} \Delta\hat{P}(\boldsymbol{x}_0, t) &= 2\pi\rho \iint_{-\infty}^{\infty} \hat{\hat{w}}_R(k_1, k_2) g(x_0, k_1, k_2) e^{-ik_2 y_0} \left(\frac{U}{2\pi} \int_{-\infty}^{\infty} e^{ik_1 U_0 t} e^{-i\omega t} dt \right) dk_1 dk_2 \Rightarrow \\ \Delta\hat{P}(\boldsymbol{x}_0, t) &= 2\pi\rho \int_{-\infty}^{+\infty} \hat{\hat{w}}_R(K_1, k_2) g(x_0, k_1, k_2) e^{-ik_2 y_0} dk_2 \end{aligned} \tag{4.11}$$

where K_1 is a given frequency component equal to ω/U_0 corresponds to the chordwise wavenumber.

The obtained pressure jump formulation is the junction between the aerodynamic and the acoustic part of the described theory. The description of the remaining part of Amiet's theory is summarized in Appendix A by highlighting the methodology, the main equations and the physics of the problem. The majority of the formulations have been taken from different references [12, 36, 31] and they have been used for presenting a robust description of the problem.

4.1.4 Amiet's Model for the Baseline Case

Analytical modeling of the TIN of a straight-edge airfoil is considered in this section following Amiet's theory [13] based on Schwarzschild's technique. The model is a high-frequency approximation valid as long as $M_0 K_1^*/\beta^2 > 0.4$, with $\beta = (1 - M_0^2)^{1/2}$, $M_0 = U_0/c_0$ being the Mach number and $K_1^* = \omega c/(2U_0)$ being the dimensionless aerodynamic chordwise wavenumber. It has been proved accurate when compared to various experimental databases. It provides closed-form expressions for the power spectral density of the far-field acoustic pressure $S_{pp}(\omega)$ radiated by a rectangular, rigid flat-plate airfoil.

For arbitrary aspect ratio L/c the PSD reads $\mathcal{L} = \mathcal{L}_1 + \mathcal{L}_2$, with

$$S_{pp}(\mathbf{x},\omega) \;=\; \left(\frac{k\,\rho_0\,c\,z}{2\,S_0^2}\right)^2 \pi\,U_0\,\frac{L}{2}\int_{-\infty}^{\infty}\left[\Phi_{ww}\left(\frac{\omega}{U_0},k_2\right)\right.$$

$$\left.\times\left|\mathcal{L}\left(x,\frac{\omega}{U_0},k_2\right)\right|^2\;\frac{\sin^2\left[\left(\dfrac{k\,y}{S_0}-k_2\right)\dfrac{L}{2}\right]}{\pi\,\dfrac{L}{2}\left(\dfrac{k\,y}{S_0}-k_2\right)^2}\right]\mathrm{d}k_2\,, \tag{4.12}$$

where Φ_{ww} is the two-dimensional wave-number spectrum of the turbulent velocity component normal to the airfoil, $\mathcal{L}$ a radiation integral accounting for chordwise non-compactness and $S_0 = [x^2 + \beta^2(y^2+z^2)]^{1/2}$ a corrected distance for flow-convection effects.

In the limit of large aspect ratio $L/c \to \infty$, an approximate expression follows from the equivalence of the sine-cardinal function with the Dirac delta function, as

$$S_{pp}(\mathbf{x},\omega) \;=\; \left(\frac{\rho_0\,k\,c\,z}{2\,S_0^2}\right)^2 \pi\,U_0\,\frac{L}{2}\,\Phi_{ww}\left(k_1,\frac{k\,y}{S_0}\right)\left|\mathcal{L}\left(x,k_1,\frac{k\,y}{S_0}\right)\right|^2\,. \tag{4.13}$$

This approximation selects the specific wavenumber $k_2 = k\,y/S_0$ and perfectly focuses the radiation in the corresponding oblique direction. It is acceptable for values of L/c of about 2.5 or 3, as suggested by tests reported in the similar problem of trailing-edge noise modeling [99].

Taylor's assumption of frozen incident turbulence is made. The turbulence is expanded by space Fourier analysis in oblique sinusoidal upwash components called gusts and defined by two wavenumbers $k_1,\ k_2$ in the chordwise and spanwise directions respectively. Its statistical properties are described by the two-dimensional wavenumber spectrum according to the Von Kármán model Φ_{ww}, expressed as

$$\Phi_{ww}(k_1,k_2) = \frac{4}{9\pi}\frac{\bar{u^2}}{k_e^2}\frac{\hat{k}_1^2+\hat{k}_2^2}{(1+\hat{k}_1^2+\hat{k}_2^2)^{7/3}}\,, \tag{4.14}$$

where

$$\hat{k}_{1,2} \;=\; \frac{k_{1,2}}{k_e}\,,\quad k_1 = \frac{\omega}{U_0},\quad k_2 = \frac{ky}{S_0}\,,\quad k_e \;=\; \frac{\sqrt{\pi}}{\Lambda}\frac{\Gamma(5/6)}{\Gamma(1/3)}\,,$$

Λ being the integral length scale and $\bar{u^2}$ the mean-square turbulent velocity, with

$$\sqrt{\bar{u^2}} = \frac{TI\cdot U_0}{100}$$

TI denoting the turbulent intensity.

The function $\mathcal{L}$ has different expressions for the sub-critical and supercritical gusts.

For supercritical gusts it reads [125]

$$\mathcal{L}_1 \;=\; -\frac{1}{\pi}\sqrt{\frac{2}{(k_1^* + \beta^2\,\kappa)\,\Theta_4}}\,\mathrm{e}^{-\mathrm{i}\,\Theta_2}\,\mathrm{E}\left[2\,\Theta_4\right]\,, \tag{4.15}$$

$$\mathcal{L}_2 \;=\; \frac{\mathrm{e}^{-\mathrm{i}\,\Theta_2}}{\pi\,\sqrt{2\,\pi\,(k_1^* + \beta^2\,\kappa)\,\Theta_4}} \tag{4.16}$$

$$\times\left\{\mathrm{i}\,(1-\mathrm{e}^{2\,\mathrm{i}\,\Theta_4}) \;-\; (1+\mathrm{i})\left[\mathrm{E}(4\,\kappa) \;-\; \mathrm{e}^{2\,\mathrm{i}\,\Theta_4}\sqrt{\frac{2\,\kappa}{\Theta_3}}\,\mathrm{E}\left[2\,\Theta_3\right]\right]\right\}\,,$$

with $\Theta_2 = \mu\,(M_0 - x_1/S_0) - \pi/4$, $\Theta_3 = \kappa + \mu\,x_1/S_0$, $\Theta_4 = \kappa - \mu\,x_1/S_0$. E is a combination of Fresnel integrals defined as

$$\mathrm{E}(\xi) \;=\; \int_0^{\xi}\frac{\mathrm{e}^{\mathrm{i}t}}{\sqrt{2\pi\,t}}\,\mathrm{d}t\,.$$

For sub-critical gusts κ is replaced by $\mathrm{i}\,\kappa'$ with $\kappa' = \sqrt{(k_2^{*\,2}/\beta^2) - \mu^2}$ and the term involving the function $(1+\mathrm{i})\,\mathrm{E}(4\kappa)$ by the error function $\mathrm{erf}(\sqrt{4\,\kappa'})$. However it is worth noting that all gusts involved in the large-aspect ratio approximation are supercritical.

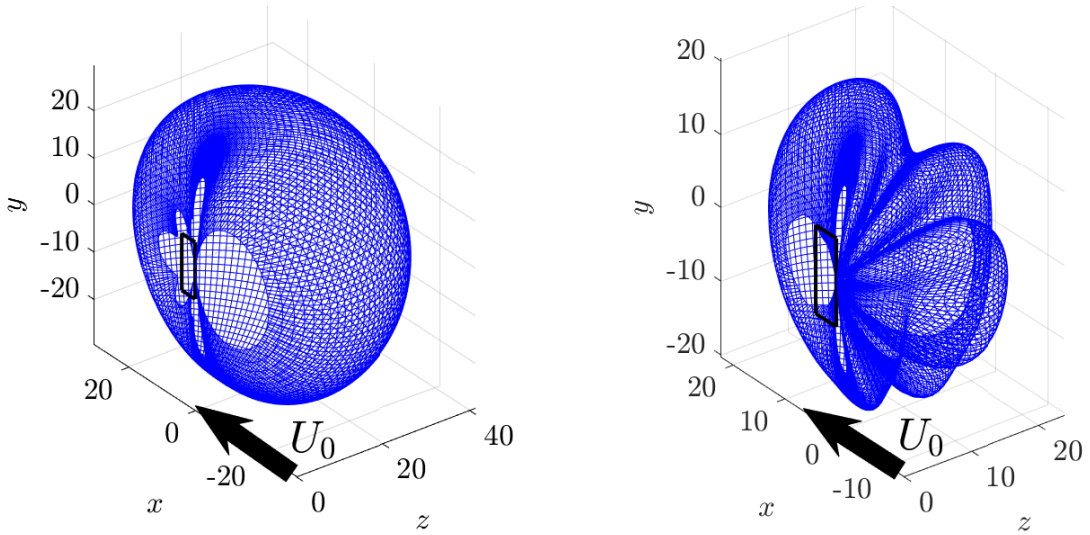

Figure 4.3: Predicted 3D directivity of the TIN of the straight leading-edge flat plate at Mach number $M = 0.09$ ($U_0 = 32\,\mathrm{m/s}$). Von Kármán model used as input with integral length scale $\Lambda = 0.009\,m$ and turbulent intensity 4.5 %. (a) $k\Lambda = 0.05$ and (b) $k\Lambda = 0.8$.

Typical three-dimensional directivity patterns of TIN [26] as predicted using Amiet's theory are plotted in Fig. 4.3 for two frequencies corresponding to the dimensionless wavenumbers $k\Lambda = 0.05$ and $k\Lambda = 0.8$ based on the integral length scale, or $kc_0 = 0.56$

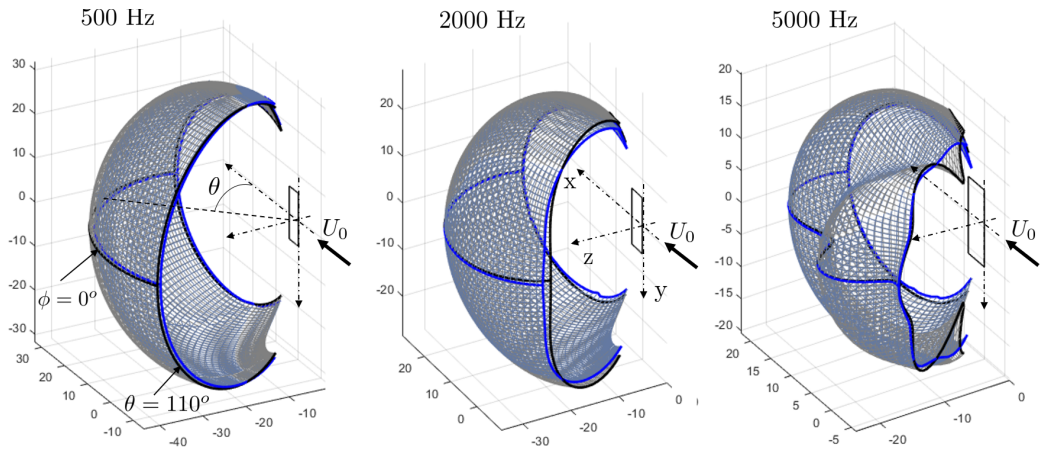

Figure 4.4: Single-frequency, three-dimensional directivity patterns of TIN as predicted by Amiet's model over the part of observation sphere covered by the rotating antenna (assuming up-and-down symmetry). Left-bank side only, same decibel scale on all plots. Exact formulation (blue) and large L/c approximation (black).

and $kc_0 = 8.9$ based on the chord length. At the lowest frequency the directivity is that of an equivalent compact dipole. At the highest frequency three lobes in the θ direction are identified, with increasing amplitude from upstream to downstream.

Sample directivity results are plotted in Fig. 4.4, for the three frequencies 500 Hz, 2 kHz and 5 kHz corresponding to Helmholtz numbers kc of 0.935, 3.74 and 9.35, respectively, at the Mach number $M_0 = 0.09$ ($U_0 = 30$ m/s). The bold lines feature the mid-span plane arc at $\phi = 0°$ and the extreme meridian arcs at $\theta = 25°$ and $\theta = 110°$. At the lowest frequency the total sound is about that of a dipole of axis **z**. The parameter kL is 2.8, which stresses that not only the chord but also the span is nearly compact. At the intermediate frequency a single main broad lobe is again seen, slightly flattened in the **z** direction with a maximum at oblique ϕ angles. At 5 kHz the airfoil chord is no longer compact and multiple lobes are observed, especially in the midspan plane $\phi = 0°$. The prediction with the large-aspect ratio approximation, in gray mesh and black lines, is close to the exact formulation in gray-blue mesh and blue lines, except at the higher frequency when approaching the plane of the airfoil (ϕ around 75° and beyond). This confirms the overall relevance of the approximation as L/c is equal to 3.

4.1.5 Directivity Patterns and Comparison with Analytical Predictions

The small thickness of the flat-plate airfoils was initially chosen in the experiment to ensure reliable comparisons with analytical models usually based on the zero-thickness assumption. Here, cuts of the three-dimensional directivity of TIN are plotted for the baseline airfoil and the serrated airfoil with $h/c_0 = 0.1$ in Fig. 4.5, for a set of frequencies between 0.5 and 7.2 kHz. The plots are projections of the cuts in the plane of angle θ. The solid lines represent the acoustic radiation in the mid-span plane and the dotted lines those in the plane of elevation angle $\phi = 75°$. The large difference between the former and the latter is expected from the dipolar nature of the sources. It nearly coincides with the point-dipole directivity pattern according to $20\log_{10}|\cos(\theta)|$ and indicates that the airfoil chord is acoustically compact. Indeed the single-lobe shape for both airfoils is maintained below a threshold of about 3 kHz, 3.4 kHz corresponding to the value 2π of the Helmholtz number kc_0. Beyond this limit the airfoil becomes substantially non-compact. In low-frequency regimes the acoustic effects of the wavy leading edge are minor, about 1 dB. The radiation at the highest measured angle $\phi = 75°$ seems to keep the same one-lobe trend at all frequencies.

Theoretical directivity plots are reported in Fig. 4.5 as the blue solid lines for the microphone at $\phi = 0°$ and as the blue dashed lines for the microphone at $\phi = 75°$. The validity of the model was proved in the past regarding its application in the mid-span plane but not off the mid-span plane. The present results indicate good performance in all directions, despite the fact that corrections were not implemented for the refraction of sound that occurs through the jet shear layers. These corrections are weak for the present experiment (see next section for estimates). Independently of these effects Amiet's model underestimates the sound radiation at low frequencies. This has been attributed to possible installation effects. Indeed the nozzle flow width is only 1.5 chord, therefore low-frequency interactions of the shear-layer oscillations of the jet with the airfoil are suspected.

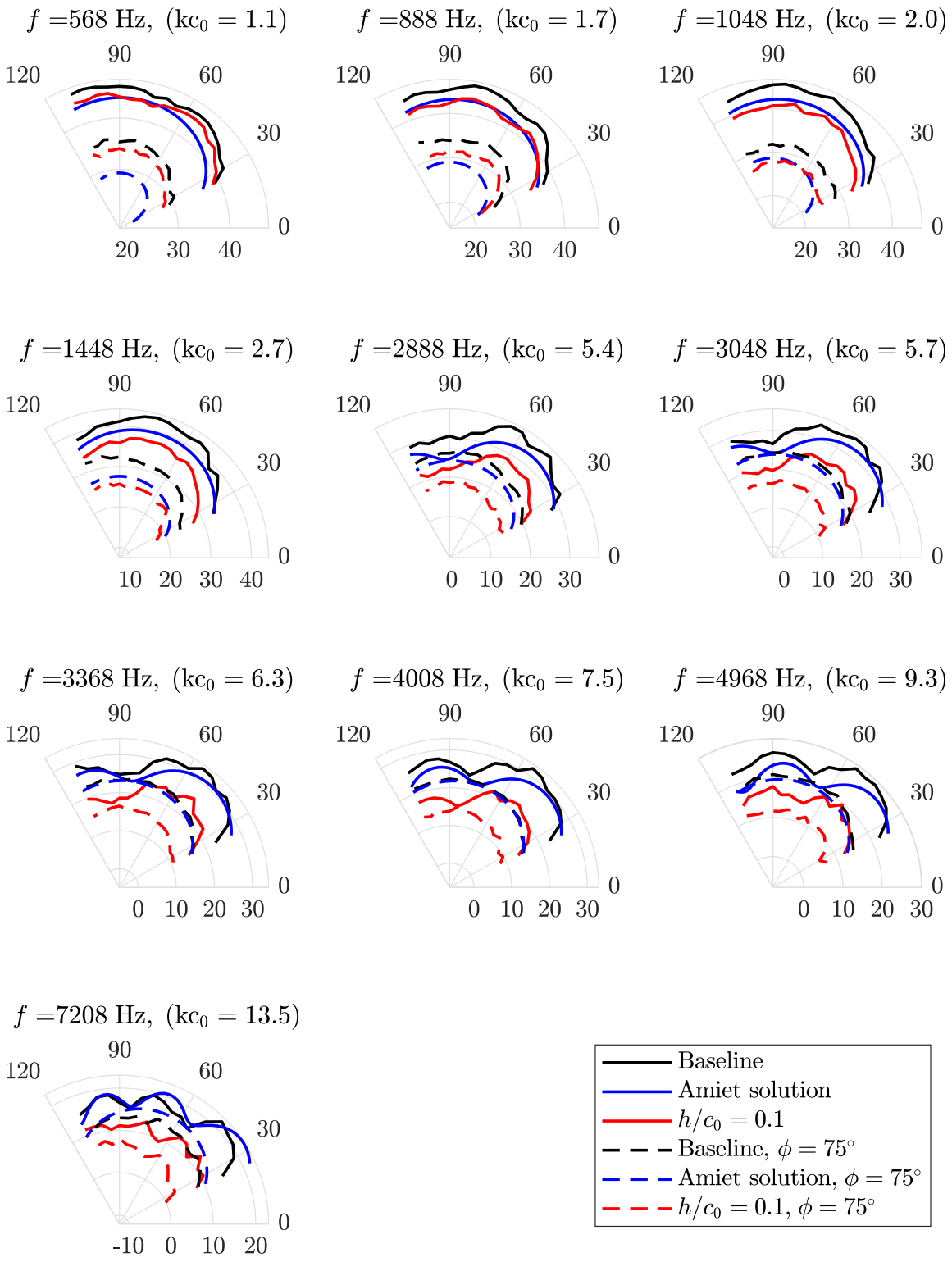

Figure 4.5: Far-field directivity polar diagrams measured at 32 m/s in the mid-span plane and in the horizontal plane corresponding to the last arc microphone. Frequencies in Hz and associated chord-based Helmholtz numbers kc_0. Red lines: serrated LE $h/c_0 = 0.1$, black lines: baseline, blue lines: predictions. Sound levels in dB scale.

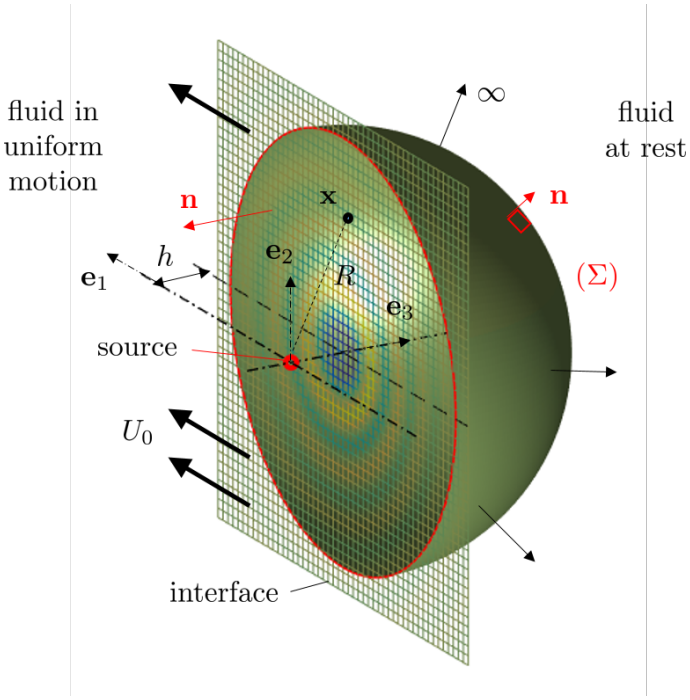

Figure 4.6: Control surface for Kirchhoff's integral calculation. Source and observer featured as red and black points. Instantaneous pressure wavefronts illustrated on the interface.

4.1.6 Corrections for Shear-Layer Refraction

Sound paths from the sources to a far-field microphone include sound convection inside the nozzle-jet flow and propagation in air at rest outside. The refraction through the jet shear layer is known to deviate sound propagation, so that the measurement angle does not coincide with neither the true emission angle nor the total angle combining propagation and convection. This is an issue when comparing the measurements to predictions based on a model assuming a flow of infinite extent, for which only the total angle is involved. This is why measurements performed in open-jet wind-tunnels are often corrected, typically to determine what would be the equivalent position where what is measured at a given microphone position would be found were the flow of infinite extent. The two-dimensional model proposed by Amiet [15] is often referred to for its easy implementation. Detailed considerations are also found in Glegg & W. Devenport [55].

Another way of assessing the shear-layer refraction by the lateral nozzle-jet shear layer is described in this section and in the recent study of Bampanis *et al.* [26]. It assimilates the shear-layer to a plane interface of arbitrary extent and is based on Kirchhoff's integral formulation. The latter states that the sound pressure at some frequency and at any point inside a volume of air ($\mathcal{V}$) free of sources is related to the pressure on the surface (Σ) enclosing ($\mathcal{V}$) by the surface integral

$$p(\mathbf{x}) = \int_{(\Sigma)} \left(\mathrm{G}_0(\mathbf{x},\mathbf{x}_0) \frac{\partial p(\mathbf{x}_0)}{\partial \mathbf{n}} - p(\mathbf{x}_0) \frac{\partial \mathrm{G}_0(\mathbf{x},\mathbf{x}_0)}{\partial \mathbf{n}} \right) \mathrm{d}\mathbf{x}_0 \,, \tag{4.17}$$

where $\partial/\partial\mathbf{n}$ stands for the normal derivative calculated with respect to the source coordinates and G_0 stands for the free-space Green's function for the Helmholtz equation in a medium at rest. In the present application the surface (Σ) is made of the interface completed by a large half-sphere in the quiescent-air region, as shown in Fig. 4.6. As the half-sphere is extended to infinity its contribution to the integral goes to zero by virtue of the Sommerfeld radiating condition and the only remaining part is the integral over the interface. This statement is only an approximation because the true shear-layer, of limited extent in the experiment, is modeled by an infinite plane separating two half-spaces, one with air at rest and the other one with air in uniform motion at the nozzle-exhaust flow speed U_0 and corresponding Mach number M. Furthermore the integral must be discretized and truncated for numerical implementation. Yet the formulation has the advantage of implicitly considering the exact wavefront structure of the incident sound on the interface. It is implemented as follows, for the sake of defining a simple correction procedure.

As first step a point dipole with axis in the direction of unit vector $\mathbf{e}_3$ normal to the lateral shear layer is assumed as source at the origin of coordinates. In a three-dimensional context, the sound field inside the nozzle-jet region and its trace on the interface, for a unit dipole strength, would be expressed expressed by the gradient of the free-field Green's function for the convected Helmholtz equation in the same direction, leading to the sound pressure

$$p_{in}(\mathbf{x}) \;=\; \frac{\partial \mathrm{G}}{\partial z}\,, \quad \text{with} \quad \mathrm{G}(\mathbf{x},\mathbf{x}_0) \;=\; \frac{1}{\beta}\,\mathrm{e}^{-\mathrm{i}kM_0\,(x-x_0)/\beta^2}\,\frac{\mathrm{e}^{\mathrm{i}k\,R_s/\beta^2}}{4\pi\,R_s}$$

and $R_s^2 \;=\; (x-x_0)^2 + \beta^2\,((y-y_0)^2+(z-z_0)^2)$. The normal derivative of the incident pressure in the right-hand side of Eq. (4.17) is defined as

$$\frac{\partial p_{in}}{\partial \mathbf{n}} \;=\; -\frac{\partial p_{in}}{\partial z} \;=\; -\frac{\partial^2 G}{\partial z^2}\,.$$

The second step, straightforward, is to derive G_0 and $\partial \mathrm{G}_0/\partial\mathbf{n}$ from the definition

$$\mathrm{G}_0(\mathbf{x},\mathbf{x}_0) \;=\; \frac{\mathrm{e}^{\mathrm{i}k\,R}}{4\pi\,R} \quad \text{with} \quad R = |\mathbf{x}-\mathbf{x}_0|\,,$$

now considering that the source point $\mathbf{x}_0$ is the field point of the first step on the interface. This makes the integrand in Eq. (4.17) known from the direct field of the source. The integral is computed by standard quadrature. It has been verified that typically integrating over a square of extent larger than 10 to 15 wavelengths ensures convergence. This general approach has been applied only in a two-dimensional context in this section, in order to assess its benefit when compared to classical Amiet's corrections. For this the two-dimensional Green's function for the Helmholtz equation has been used.

Fig. 4.7 shows the 2D sound pressure field that would be generated by a chordwise distribution of lift dipoles deduced from Amiet's theory in a stream of M=0.17. The source distribution corresponds to a parallel gust and the chord length is c=10 cm. Looking closely to the dipole source where symmetrical and instantaneous wavefronts are radiated

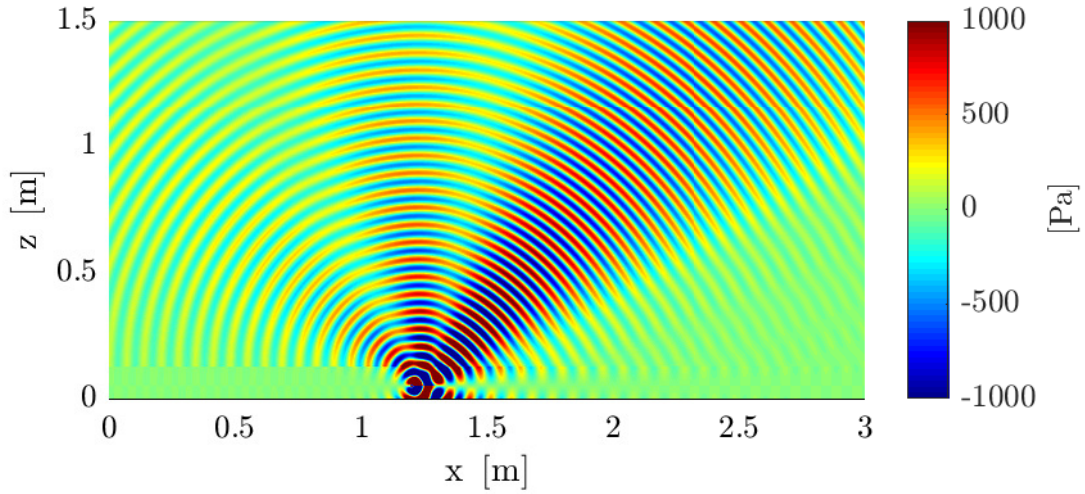

Figure 4.7: Typical 2D sound pressure field generated from Amiet's lift fluctuations applying convection and refraction effect using Kirchhoff's radiation integral at the boundary of the jet. U_0=60 m/s, f =4968 Hz and shear layer at z =0.125 m.

along both directions in z axis, the refraction effect can be distinguished at the jet limit (0.075 m far from the source) considering a jet with thickness of 0.15 m (same as in ECL experiment). The artificially high flow speed has been selected to better illustrate the refraction effect. The model has also been applied with the parameters of the present experiment. The results are given only for one indicative directivity diagram. Finally comparing the obtained sound pressure levels at the microphone locations to what is expected for the same lift distribution in an infinite stream at the same locations leads to the results in Fig. 4.8. Both Amiet's corrections extracted from the abacuses of Amiet [15] and Kirchhoff's integral implementation for the jet shear layer refraction have been used. The interest of the formulation is that it can be extended to a distribution of correlated sources, for instance in the present case a chordwise distribution of dipoles the stength of which is tuned on Amiet's TIN model.

The black rectangular marks show the same experimental directivity pattern at f = 4968 Hz as in Fig. 4.5 and the red circle marks correspond to Kirchhoff's radiation. The agreement is good enough and quite improved compared to Amiet's original formulation for infinite flow extent (blue pattern). Implementing Amiet's correction [15] then changes on the radiation angle (red dashed) and amplitude (red solid) are obvious. Indeed, the red dashed line is shifted of about 5° to higher angles and the red line obtains a small gain of about 0.5 dB or even more in lower angles. For the extreme angles around 20-to-30° the infinite-stream prediction is found to exceed the shear-layer corrected solution by about 5 dB, which is very significant in view of the quite small Mach number of 0.1 considered for the test and representative of the present study. Nevertheless, Amiet's corrections agree well enough with Kirchhoff's radiation proposing them as a tool of satisfactory fidelity. They suggest that the predicted directivity in Fig. 4.5 could be shifted uniformly by 5° as a simplified correction. The test also confirms that the Kirchhoff's integral could be

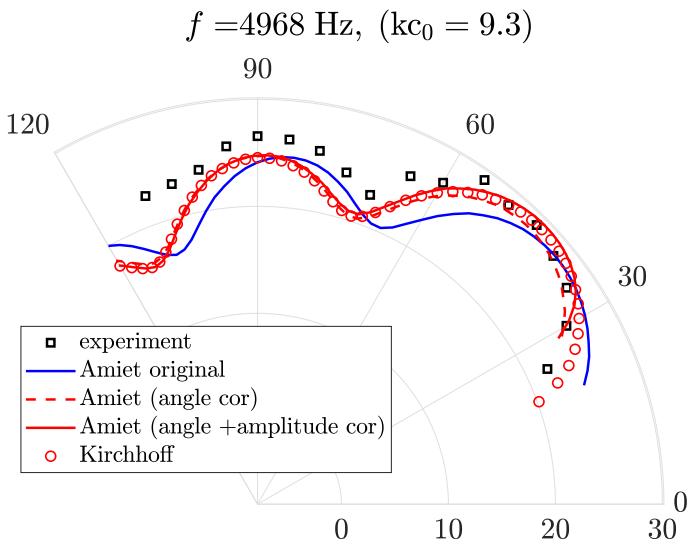

Figure 4.8: Directivity of Amiet's TIN prediction after applying Amiet and Kirchhoff's corrections counting for convection and refraction effects. U_0=32 m/s.

used systematically when some information is available on the source distribution. In particular, unlike Amiet's corrections, it provides information in the silent 'cone' that would be predicted at low angles according to geometrical ray-tracing. In this area the predicted wavefronts are those of an almost plane wave (see Fig. 4.7).

4.1.7 Comparison between Experiments and Analytical Predictions in Three-Dimensions

TIN radiation is rarely investigated in its three-dimensional form, therefore it is essential to compare the experimental sound radiation to analytical predictions on a portion of a sphere. Fig. 4.9 shows in dB scale the directivity shapes of TIN of experimental and analytical sound emissions corresponding to a flat plate with straight leading edge. As an analysis extension to Fig. 4.5, the 3D plots highlight the agreement between both data sets till the Helmholtz number of 2π. In this range, the trailing-edge noise (TEN) contribution is still weak. In contrast, a strong disagreement in terms of dB levels is found at $kc_0 = 13.5$ at which TEN dominates. The results prove that Amiet's model accurately reproduces TIN measurements, as long as TIN remains the dominant airfoil-noise contribution.

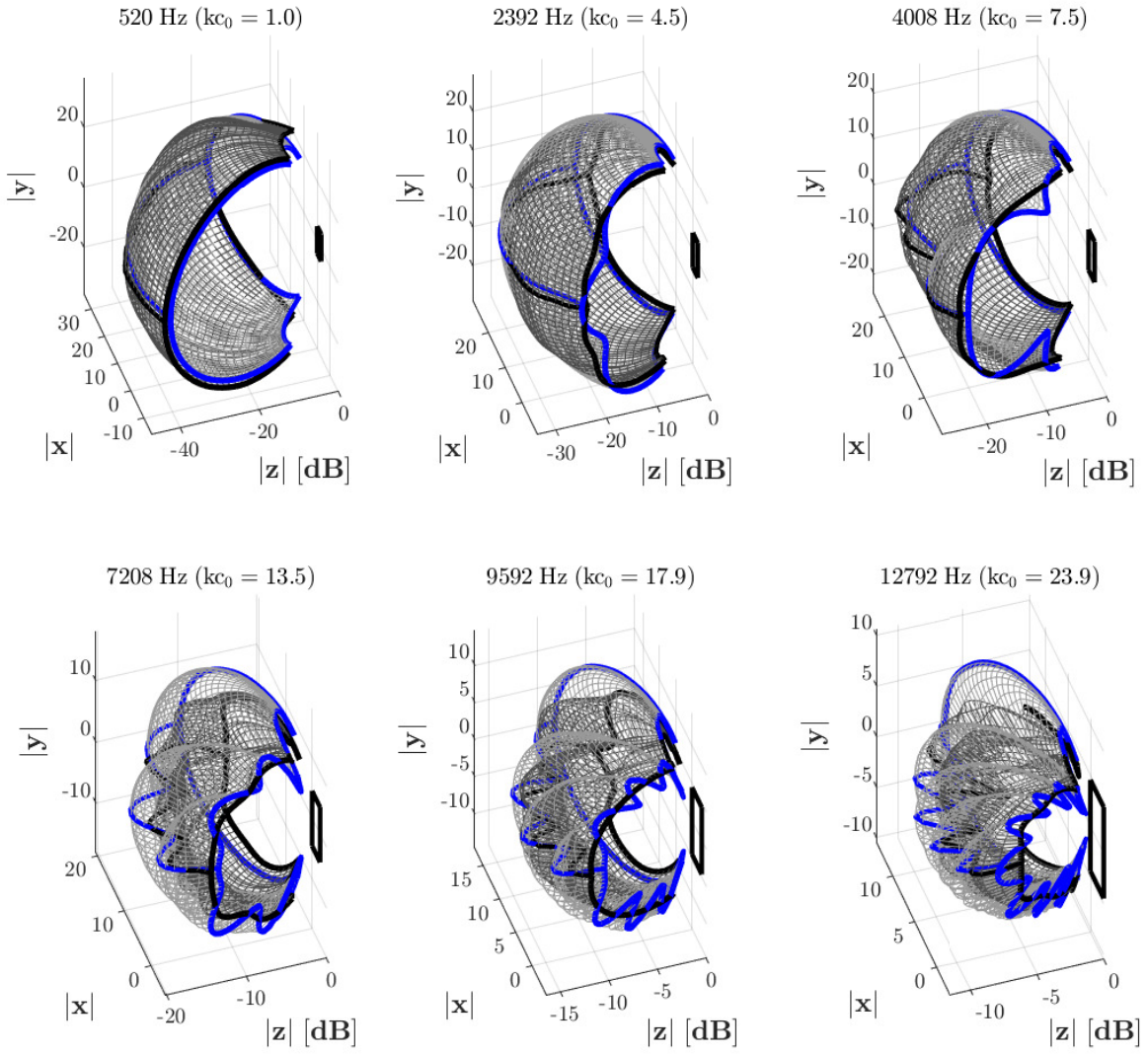

Figure 4.9: Three-dimensional experimental (black) and analytical (blue) sound directivity patterns of TIN at a single frequency for the straight leading-edge flat plate at Mach number $M = 0.09$. Again, it is assumed an up-and-down symmetry.

4.2 Analytical Models for Modified Leading Edges

4.2.1 Bibliographical Review

Noise prediction models for trailing-edge serrations have been already derived in the past but only recently theoretical models have been developed for the prediction of TIN radiated by airfoils with serrated leading edges. Initially, Roger *et al.* [128] proposed a dedicated stretching of variable to define a modified Amiet-Schwarzshild's problem, but with an approximation producing a too large amount of reduction.

Lyu & Azarpeyvand [89] proposed an analytical model for the prediction of the turbulence interaction noise radiated by a thin airfoil with triangular-shape leading-edge serrations. Amiet's theory [12] was extended to the case of serrated airfoils formulating a complex differential equation using Schwarzschild technique iteratively, including the spanwise geometrical parameter corresponding to the number of the teeth along the span. The model was validated with previous experimental data [105] showing good agreement. It has been shown that a small wavelength λ and a large root-to-tip amplitude $2h$ serration tooth compared to the streamwise hydrodynamic wavelength achieves an efficient noise reduction.

Ayton [19] derived an analytic solution that predicts the noise generated by the turbulence interaction with a semi-infinite flat plate with serrated edges. The solution is defined using the Wiener-Hopf technique, imposing as boundary conditions only the continuity of the upstream potential and the hard wall condition on the surface. An experimental validation has been performed [21, 22] for different leading-edge geometries. The sound prediction of a complete airfoil including leading- and trailing-edge noise was performed using Ayton's solution and Amiet's model [14] respectively. The good agreement with the experiments confirms the noise reduction mechanism due to the destructive interference between root and tip. Isolating analytically the leading-edge noise, it is observed that the noise reduction increases till high frequency ranges proportionally to the frequency. In addition, the airfoil surface pressure distribution due to the dominant modes has been investigated confirming the noise reduction efficiency because of the high tip-to-root ratio that leads to a destructive interference. The efficiency in terms of noise reduction of the different leading-edge shapes is also discussed.

Ayton & Kim [20] approached the same problem accounting for serrations as a periodic pattern and avoiding the lengthy procedure of a Fourier expansion. The solution is defined using Wiener-Hopf in conjunction with a non-orthogonal coordinate transformation technique accounting as boundary conditions only the continuity of the upstream potential and the slip condition on the surface. Therefore the formulation is used in the present work to estimate the response difference in the mid-span plane between a straight edge and a serrated edge. In view of the relevance of the large-aspect ratio approximation the same difference is believed to hold for the serrated airfoil of finite chord and in the mid-span plane. Thus, the formulation 4.18 [21, 22] is identical to the solution presented in Ayton & Kim [20] and reads

$$p(R,\theta,y) \sim i \sum_{n=-\infty}^{\infty} \frac{(\frac{k_1}{\beta^2} - w_n \cos\theta) e^{\pi i/4} G_n^+(-w_n \cos\theta)}{\sqrt{\pi R}} E_n(-w_n \cos\theta) \times \cos\left(\frac{\theta}{2}\right) Z_n(-w_n \cos\theta, y) e^{-i w_n \cos\theta c_s F_s(y)} \tag{4.18}$$

where $G_n^+(-w_n \cos\theta) = \frac{i}{-w_n \cos\theta + \kappa} \frac{1}{\sqrt{-\kappa - w_n}}$ is an analytic sub-term of the upper half-plane, $\kappa = k_1/\beta$, $w_n^2 = (k_1/\beta M)^2 - \chi_n^2$ the spanwise eigenmode with $\chi_n = \pm k_2 + 2n\pi$, k_1 is the reduced streamwise convective wavenumber and k_2 the spanwise convective wavenumber.

The general expansion coefficient E_n required for the far-field radiation formula is:

$$E_n(\lambda_p) = \int_0^1 e^{ik_1 c_s F_s(y) + ik_2 y} \overline{Z_n(\bar{\lambda}_p, y)} dy = \int_0^1 e^{ic_s(k_1+\lambda_p)F_s(y)} e^{-i2n\pi y} dy \tag{4.19}$$

where $Z_n(-w_n \cos\theta, y) = e^{-i(-w_n \cos\theta)c_s F(y)} e^{ik_2 z + i2n\pi y}$ is the spanwise basis function and the bar stands for the complex conjugate. $F_s(y)$ is the closed-form expression that defines the leading-edge shape pattern, i.e. triangles, sinusoidal, slitted $\upsilon -$ root, slitted u $-$ root, chopped peak and square wave. Ayton and Paruchuri [22] provide analytically all the aforementioned geometries apart from the sinusoidal. In this reference all the functions are normalized such that $\mathrm{max_y F_s(y)} - \mathrm{min_y F_s(y)} = 1/2$. An example of the radiation integral E_n for a triangular function for a serrated edge is given below:

$$E_n(\lambda_p) = \frac{4(-1)^n s}{s^2 - 4n^2\pi^2} \sin(\frac{1}{4}(s - 2n\pi)) \tag{4.20}$$

with $s = c_s(k_1 + \lambda_p)$. Here the parameter c_s stands for a 'tip-to-root' ratio ($c_s = 1, 2, 3$ etc.) and $\lambda_p = -\bar{k}\cos\theta$. The evaluation of the PSD of the acoustic pressure over all oblique gusts is defined by a total integration as

$$S_{pp}(\mathbf{x}, \omega) = \int_{-\infty}^{\infty} |p(R, \theta, y)|^2 \Phi_{ww}(\frac{\omega}{U_0}, k_2) dk_2 \tag{4.21}$$

In fact, the implementation of an infinite-interval integral (Eq. (4.21)) at the final results is complex and errors can easily appear. Therefore, Lyu & Ayton [87] readdressed this difficulty by replacing the infinite-interval integral with a simple sum for the case at which the serration wavelength is small compared to the transformed acoustic wavelength. The replacement is based on the weak coupling between expanded modes except at very high frequencies and that high-order modes are cut-off.

4.2.2 Lyu's and Ayton's Analytical Model

The present work makes use of this proposed model [88] for both leading- and trailing-edge noise prediction applications for serrated edges. The corresponding expression for the leading-edge case that computes the PSD of the radiated sound in the far-field is given as follows:

$$S_{pp}(R, \theta, y) \sim 2\bar{k}\frac{1}{\pi r} \cos^2\frac{\theta}{2} \frac{(\frac{k_1}{\beta^2} - \bar{k}\cos\theta)^2}{(\bar{k}_1 - \bar{k}\cos\theta)^2(\bar{k}_1 + \bar{k})} \sum_{n=-\infty}^{\infty} \Phi_{ww}(\omega, k_2)|E_n(-\bar{k}\cos\theta)|^2 \tag{4.22}$$

with

$$E_n(\lambda_p) = \int_0^1 e^{i(\bar{k}_1+\lambda_p)\bar{h}_s F_s(y)} e^{-i2n\pi y} dy \tag{4.23}$$

Here the parameter with $\bar{h}_s$ stands for a 'tip-to-root' ratio following a different dimensionalization compare to [22] such that $\max_y F_s(y) - \min_y F_s(y) = 2$. The Von Kármán turbulence spectrum model Φ_{ww} has been already presented in the section 4.1.4. The substitution of $k_1 = \omega/U_0$ and $k_2 = 2n\pi/\lambda$ the streamwise and spanwise convective wavenumbers respectively has been considered.

The application of both model versions [22, 87] in a dimensional form requires a change of coordinate system. Two different coordinate reference systems are used in both equations 4.18 and 6.1 for describing the scaling of the serration length, $[-\frac{1}{4}, \frac{1}{4}]$ and $[-1, 1]$ for the scaling factors c_s and h_s respectively [22, 87]. Then the shape function should be dimensionalized in a proper way that follows the coordinate system and the variables connect each other by the relation $c_s = 4h_s$.

The radiation integral E_n for the wavy leading-edge geometry $F_s(y) = h_s \sin(2\pi y)$ is obtained below (Eq. (4.24)) with maximum normalized amplitude of $h_s = 1$ and $s = \bar{h}_s(\bar{k}_1 + \lambda_p)$.

$$E_n(\lambda_p) = \frac{(-1)^n}{2\pi} \int_{-\pi}^{\pi} e^{i(-s)\sin y} dy = \; J_n(-s)(-1^n) \equiv J_{-n}(-s) \tag{4.24}$$

The parameters $\bar{k}_1$ and λ_p are defined as in reference [22] and J_n is the Bessel function of the first kind of order n.

Lyu and Ayton's model has been validated in the present work both in dimensional [88] and non-dimensional form [87] published results. The serration wavelength $\tilde{\lambda}$ is used to normalize the lengths i.e. h, Λ, x and the wavenumbers while the density $\tilde{\rho}$ and the velocity $\tilde{U}_0$ are used to non-dimensionalize other dynamic variables such as pressure and velocity potential, mainly in the trailing-edge case. Here, for the non-dimensional variables the notation ($\bar{}$) is used and the corresponding dimensional the notation ($\tilde{}$). Considering a non-dimensional speed of 1, the resulting variables are $\bar{\omega} = \tilde{\omega}\lambda/\tilde{U}_0$, $k_1 = \bar{\omega}$, $\bar{k} = \bar{\omega}M/\beta$, $\bar{k}_1 = k_1/\beta$, $\bar{h}_s = h_s/\beta$ and $k_2 = 2n\pi$.

The use of the model on an experimental data base requires its dimensionalization. Therefore, Eq. (6.1) will be used at its initial form while its variables will be dimensionalized as below

$$\begin{gathered} \tilde{\Lambda} = \bar{\Lambda}\lambda, \quad \tilde{u}_{rms} = \tilde{U}_0 TI, \quad \tilde{k}_1 = k_1/\lambda, \quad \tilde{k}_2 = 2n\pi/\lambda, \quad \tilde{k} = \bar{k}/\lambda, \\ \tilde{R} = R\lambda, \quad \tilde{x} = x\lambda, \quad \tilde{\omega} = \bar{\omega}U_0/\lambda = 2\pi f \end{gathered} \tag{4.25}$$

To validate the proper implementation of the latter model, one of the serration test cases proposed by Lyu & Ayton is selected [88] (Figure 8). It corresponds to the sawtooth serration with an aspect ratio $h/\lambda = 0.5$, the experimental results of which are reported in Ayton and Paruchuri [22]. Fig. 4.10 shows that the present results are similar to those obtained by Lyu & Ayton for both straight and serrated edges [97], and that the model reproduces the experimental results except at low and very high frequencies. Similar good

agreement is found with other serration cases.

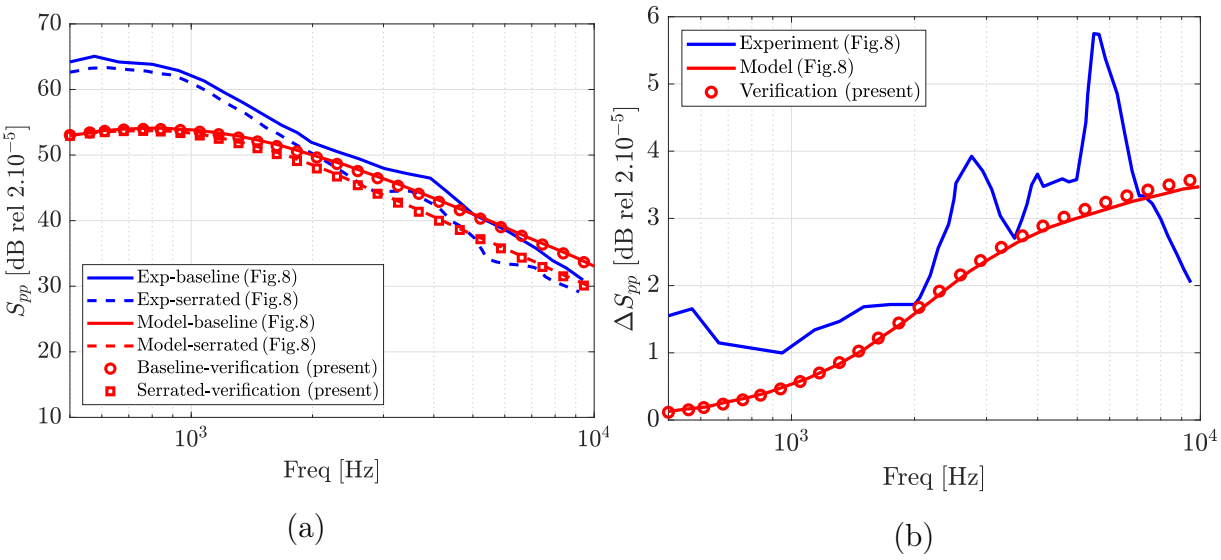

Figure 4.10: Validation of the code [97] used for the present experiment with the published results of Lyu & Ayton [88] (Figure 8). The serration parameters and the flow conditions have been scaled respectively.

4.2.3 Analytical Solutions and Comparison with Experimental Results for Serrated Flat Plates

In this section, sound predictions of analytical models will be presented and compared with the present experimental results in the mid-span plane. Since Amiet's theory is validated for the baseline case of the flat plates, a comparison with Lyu & Ayton's model is possible. Their model is expressed in cylindrical coordinates thus all radiation angles correspond to the mid-span plane. Initially, all the model implementations should be tested on straight edges for the measured flow speeds. This is all the more important for Lyu & Ayton's model as it must be calibrated on such a clean configuration to compensate for the two above assumptions of infinite span and two-dimensional radiation.

In Fig. 4.11 predictions of both models are plotted for all speeds at 90° and zero angle of attack. Three colors correspond to the three velocities, the thick continuous line to Amiet's predictions and the dashed line to Lyu & Ayton's model considering a very small serration amplitude $h = 0.001$ when properly rescaled on the SPL level of the measured baseline. Both model predictions capture the overall sound level on the spectra presenting an underestimated behavior at low frequencies where the airfoil becomes acoustically compact as already mentioned by the authors [25, 27]. A good agreement is found both in terms of spectral shape and levels over most of the frequency range for all flow conditions with Amiet's model till higher frequencies whereas Lyu & Ayton's model lacks in terms of accuracy missing the oscillating behavior of the curves. Taking into account that these oscillations stem from the backscattering and the chord-wise compactness effect which is neglected from the origin boundary conditions of Ayton's model [18]. Nevertheless, this is already commented by the authors [22] who validated Ayton's model with previous experimental findings of Chaitanya *et al.* [32]. Despite the fact that the present model predicts well the radiated sound for Mach numbers higher than $M = 0.1$ considering similar applications in literature [18, 22, 87], our present analytical results overestimate the measured sound at lower Mach numbers. Accurately, beyond 300 Hz Ayton's model for h = 0.001 (straight edge) follows the mean trend of Amiet's model, coincides with its high-frequency approximation, and consequently matches the experimental levels nicely. Then, beyond 3 kHz the airfoil being no longer compact, oscillations appear because of the scattering effect at the trailing edge. These oscillations are reproduced with Amiet's model by the Fresnel functions in Eq. (4.13). Only at low speed, the decay of the PSD at high frequencies is overestimated by the model. Recent measurements on a flat plate showed a similar over-prediction at low speeds [101]. This is most likely a Reynolds number effect and the flow is no longer fully turbulent as assumed in the analytical model (less small scale turbulence). For both wavy serrations sets (Figs. 3.9-(d)), the expected noise reduction is observed and a similar pattern for the spectra is found.

Fig. 4.11-(b) taken from Ref. [97] shows the same PSD of the far-field acoustic pressure at 90° above the airfoil leading edge but for 32 m/s only. Only predictions with Amiet's [12] and Lyu & Ayton's analytical models are shown here. Several variants of the former model as described in Amiet's original paper are presented. The low frequency model corresponds to Sears' incompressible model. The square symbol corresponding to

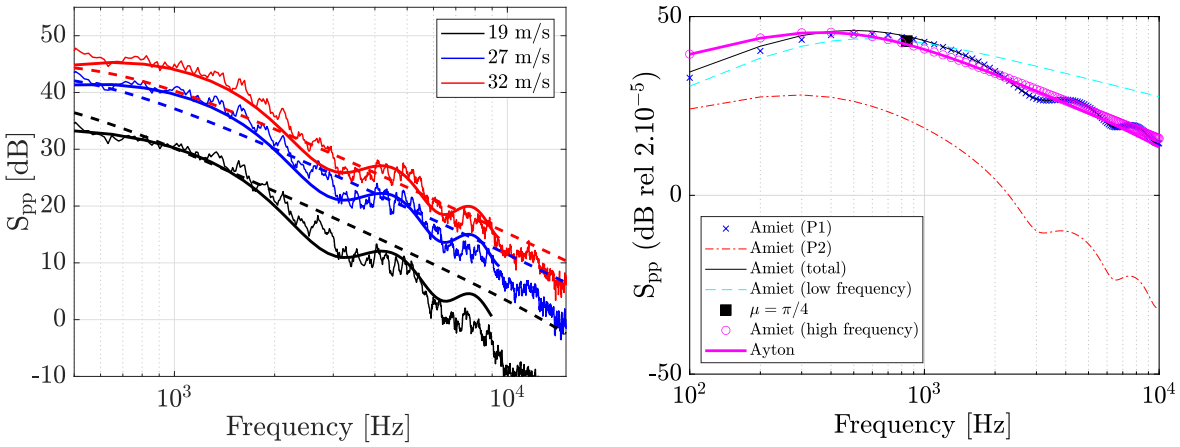

(a) (b)

Figure 4.11: Sound predictions of TIN for the baseline at M=0.06, 0.08, 0.09 at 90° and zero angle of attack obtained by (a) Amiet's model (thick solid), Lyu & Ayton's model (dashed) and compared with expreriments (light solid). (b) Comparison between Lyu & Ayton's and Amiet's model with and without trailing-edge back-scattering correction. M=0.09.

the reduced wave number 4 shows the frequency limit of this approximation. Amiet's model is also an iterative procedure between both edges of the airfoil. The P1 then corresponds to the main leading-edge scattering term and P2 to the trailing-edge back-scattering correction. The high-frequency approximation replaces the Fresnel integrals in Amiet's model with asymptotic expressions and represents the mean behavior of the full model beyond the reduced wave number 4. Amiet's full model that compares well with experiment in Fig. 4.11-(a) is then the reference. Amiet's low frequency model clearly overpredicts the sound over most of the frequency range. For this particular case, the main leading-edge scattering is also dominant and the back-scattering only contributes to the overall sound below 300 Hz. Thus, the finite chord effect should only be relevant for the present study on flat plates below this frequency. This is actually very similar to what was observed by Moreau & Roger [98] on the Controlled Diffusion airfoil at similar flow regimes. Ayton's model (the solid magenta line) is exactly matching the high frequency approximation when properly rescaled. This is very similar to what Moreau et al. [101] found for the trailing-edge noise. It can then be inferred that both asymptotic models are similar.

Fig. 4.12 illustrates the SPL calculated analytically for both serrated flat plates with $h/c_0 = 0.1$ and $h/c_0 = 0.07$ against the experimental measurements. The differences between the two versions of serrations are not significant (Fig. 3.18-(a)) as both designs correspond to nearly realistic airfoils with similar noise reductions. A good agreement is found for the serrated flat plates (Fig. 4.12) for a wide frequency range above 2 kHz. Both tests prove again the validity of Lyu & Ayton's model presenting the same sensitivity in terms of geometrical scaling and sound radiation compared to the experiments. Given the possible uncertainty on the serration geometry in the prototypes, some small variations

around the nominal values of Tab. 3.6-(a) have been studied numerically. This is easily feasible given the speed of the analytical model (a few seconds on a laptop). No significant variations are observed in this frequency range with a small variation of pitch or serration height h (10%). In addition, experimental verification of the model for other leading-edge geometries has shown its accuracy in terms of SPL for frequencies of about 1 kHz and higher [22].

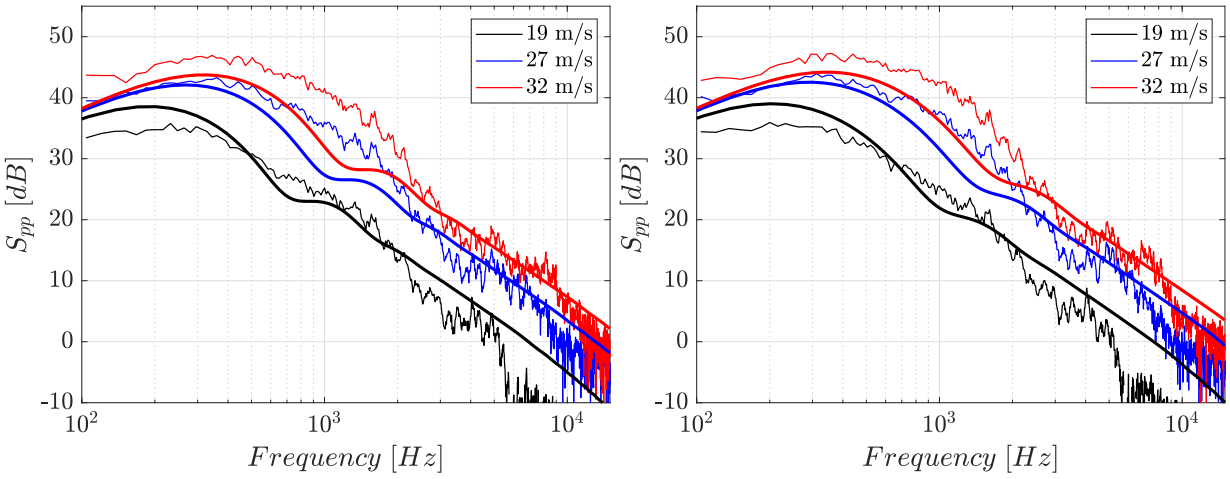

Figure 4.12: Sound predictions of TIN for two different serrated flat plates at $M = 0.06,\ 0.08,\ 0.09$ at 90° and zero angle of attack. The SPL of the radiated sound in the far-field measured at a distance of 1.2 m above the leading edge obtained by expreriments (light solid) Lyu's & Ayton's model (dashed). Serration dimensions: (a) $h/c_0 = 0.1$ & $\lambda/c_0 = 0.125$ and (b) $h/c_0 = 0.07$ & $\lambda/c_0 = 0.15$.

Fig. 4.13 compares the noise reduction achieved by the serrated flat plate $h/c_0 = 0.1$ for all speeds. As mentioned above only the deeper serrations are studied here as little differences are observed experimentally between the two designs (Fig. 3.9-(d)). The noise mitigation is also estimated by considering the difference of PSD, S_{pp}, between the straight and serrated edge and compared to the experimental trends shown in Fig. 4.13. In all these results, the convergence of the model predictions using Eq. (6.1) was achieved with only n=20 modes: this is consistent with what was observed for the trailing-edge noise by Moreau et al. [101].

Without any further scaling, Lyu & Ayton's model is able to capture most of the noise reduction observed with the long serrations. At 32 m/s below 500 Hz and beyond 2000 Hz, it again matches the experimental levels nicely. Only at mid-frequencies, around 1 kHz, the model overpredicts the noise reduction and presents a dip and a hump. Moreover, the finite chord effect and the trailing-edge back scattering can hardly be evoked as it was only found important below 300 Hz for the straight edge (Fig. 4.11). Yet, Fig. 4.13 shows that, even though the model shows a wide peak at about 1200 Hz (corresponding to the dip in the spectra), the overall noise gain shows the experimental trend nicely, and follows the empirical linear law (dashed line) representing the noise mitigation by

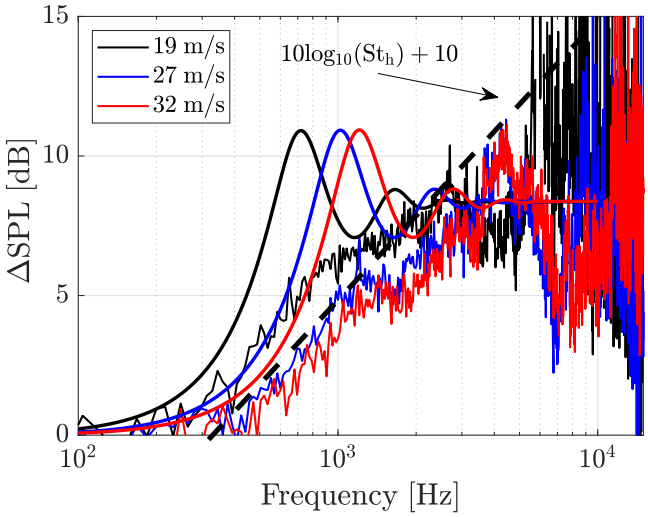

Figure 4.13: Noise reduction predictions of TIN for the serrated flat plate $h/c_0 = 0.1$ at three flow speeds in the mid-span plane and compared with experiments and the emprical linear law (dashed line).

serrations up to 3500 Hz. Note that the experimental data follow the same wavy pattern at the same frequencies, but with a smaller amplitude. At higher frequencies, the noise mitigation predicted by the model becomes constant, and deviates from the total noise gain measurements.

At 27 m/s the same trends in the spectra are shown as at high speed. The dip in the spectra in Fig. 4.12-(a) is, however, slightly shifted to lower frequency (centered around 1 kHz), spread over a slightly smaller frequency range. This is confirmed in Fig. 4.13, where the noise mitigation is very similar to the high speed case with a wide peak showing a $5-7$ dB overprediction shifted to 1 kHz. The overall trend again follows the empirical linear law (dashed line) representing the noise mitigation by serrations up to about 3000 Hz. The same overall trends are seen at the lower speed. Maintaining always the same dB scaling, here the overall sound level is overpredicted compare to other flow conditions (Fig. 4.12-(a)). The dip is shifted even more to lower frequencies and narrower. Fig. 4.13 confirms that the peak is now shifted to a lower frequency around 700 Hz. Its amplitude remains around 5 dB. The overall noise gain predicted by the model now follows the empirical linear law (dashed line) representing the noise mitigation by serrations up to about 2000 Hz. As in the other two cases, the predicted noise mitigation again becomes constant at higher frequencies following the trend of the total noise gain measurements.

Finally, it should be noticed that the low frequency underprediction by Lyu & Ayton's model in all the above cases has also been observed in all test cases considered by Lyu & Ayton [88] as illustrated in Fig. 4.10. However, in the ISVR experiment, the spurious jet noise might be the cause as it is also observed for the straight edge, at similar levels. In the present experiment, the jet noise is below 100 Hz for the present flow regimes and the lower frequency range is well predicted at all speeds. The amplitude and size of the dip in the modeled spectra and the position of its resonant trough depend on the flow regime.

Therefore, it cannot be a purely acoustic phenomenon, and should be related instead to the way the turbulent flow is distorted at the leading edge. At high frequencies, the noise mitigation predicted by Ayton's model is more consistent with the total raw measurement than with the leading noise only, obtained with the beamforming technique (see Fig. 3.25). However, as shown by Roger *et al.* [100, 125] beyond $St_\Lambda \simeq 1$ (corresponding to 3560 Hz at 32 m/s, 3000 Hz at 27 m/s and 2110 Hz at 19 m/s respectively), some further noise reduction could be achieved by the blade thickness not accounted for in the model.

A basic parametric evaluation of the predicted sound on a varying serration depth is presented in Fig. 4.14. Comparison between the straight edge (dashed) and three serrated cases (solid) shows the noise reduction efficiency and sensitivity against geometrical modifications. The serration depth increases from 7 to 13 mm with a step of 3 mm while the wavelength remains constant at 12.5 mm. Fig. 4.14-(a) shows the sound reduction trends as the serration depth increases for the widest frequency range. The peaks and the humps that were observed before (Fig. 4.12) show up also for all the cases and the oscillatory trend becomes now even more obvious with the increase of the serration depth. The observed oscillations are displaced to lower frequencies where at frequencies between 1 kHz and 2.2 kHz the noise reduction is misleading by reversing its better efficiency to the smaller teeth. Despite that fact the noise reduction level in obvious beyond 2 kHz as mentioned above. An interesting point is that keeping the same variation step of serration depth, the noise reduction difference appears to be slightly higher for h equal to 7 mm and 10 mm than 10 mm and 13 mm leading to a non-linear trend. Small variations of wavelength λ do not modify the SPL, however same variations of amplitude h has some significant impact around 1 kHz. This is consistent also with the case of sawtooth serrations [22].

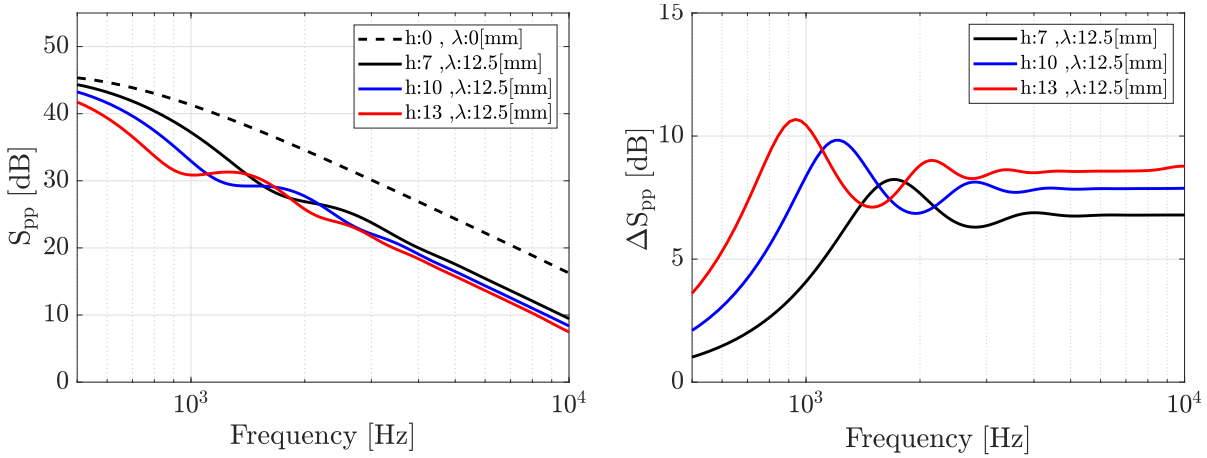

(a) (b)

Figure 4.14: (a) S_{pp} predictions for a varying serration depth (h = 7, 10, 13, solid) and the straight edge (dashed). (b) Difference of S_{pp} between the straight and wavy edges. Microphone angles $\phi = 0°$, $\theta = 0°$ and $U_0 = 32$ m/s.

A good attempt for illustrating more realistically the emitted sound of the serrated plate would be to calculate the predicted ΔdB (Lyu & Ayton's) between baseline and

serrated plates, see Fig. 4.15-(a) (blue curves) and finally subtract it from the baseline case using Amiet. Such a reconstruction is obtained in Fig. 4.15-(a) (solid red) where the prediction of the serrated plate is captured with higher accuracy.

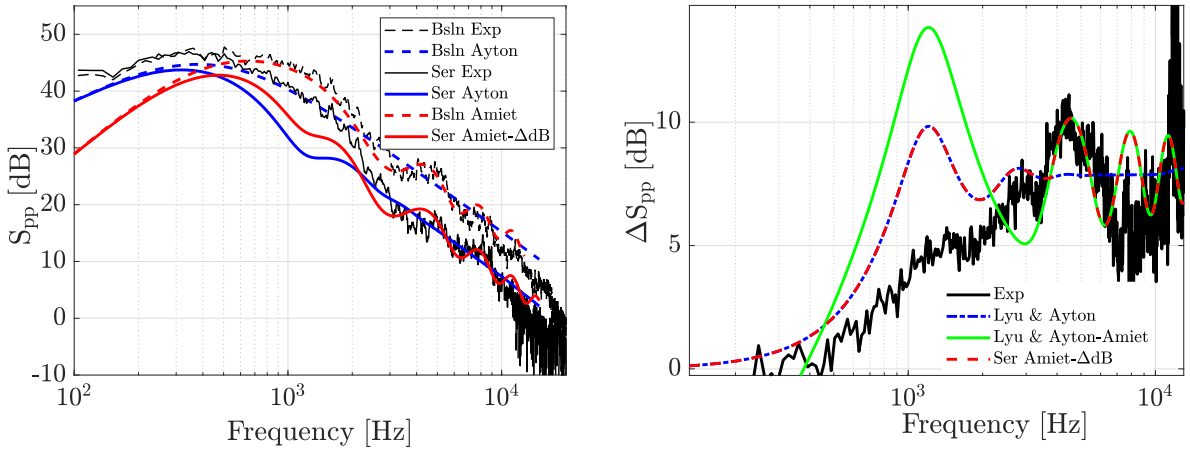

(a) (b)

Figure 4.15: (a) Reconstsructed serrated case curve. (b) NR using a mixed version of Amiet and Lyu & Ayton's model.

The reconstructed curve is used for evaluating the noise reduction (PSD) at 90° against the measurements at $M = 0.09$. Fig. 4.15-(b) shows the NR for different combinations of the model predictions. Starting from Lyu & Ayton's model (blue), the ΔdB of about 7.5 dB is predicted from 3kHz and above whereas an overestimation appears at 1.2 kHz. Now, subtracting Lyu's prediction for serrated case (dashed blue, Fig. 4.15-a) from Amiet's baseline prediction, the NR (green, Fig. 4.15-b) is evaluated. The oscillating part above 2.4 kHz is now illustrated better. A NR illustration combined by both aforementioned curves is given in dashed red. Here, we keep the ΔdB provided by Lyu's & Ayton's model till 2.8 kHz and the oscillating part for the higher frequencies. The last evaluation is made for reconstructing as much as better the experimental NR curve but this does not correspond totally to the NR behavior of the serrated LE performance. According to the finding in Fig. 3.27, the extended monotonic increase of LE noise reduction till 15 kHz is not captured by the analytical model but it remained stable (dashed blue, Fig. 4.15-b) till the higher frequencies. Nevertheless, using the reconstructed NR curve, the agreement between the model and the 'single-microphone' measurement is close capturing the oscillating behavior of the NR curve. Concluding, Lyu's & Ayton's model is a reliable tool for predicting the SPL reduction for sinusoidal shape serrations but it lacks of accuracy on the real performance of the leading-edge serrations.

4.2.4 Concluding Remarks

Amiet's theory has been successfully compared to the measurements in a complete three-dimensional context for the baseline/straight-edge airfoil. In particular, Amiet's model

is shown to faithfully reproduce the measured noise spectra, both in terms of levels and spectral shape, including the diffraction oscillations occuring when the airfoil chord becomes non compact (Helmholtz number based on the chord $\mathrm{He_c} = kc \geq 1$). Ayton's model, provided a correction in the levels to account for the fact that the model is purely two-dimensional and for an infinite span, is also seen to closely match the high-frequency approximation of Amiet's model and consequently can predict the absolute levels without the oscillations caused by the combined leading-edge and trailing-edge scattering.

For serrated edges, Ayton's model can then predict the noise spectra both in terms of levels and shapes for all test cases, without further calibration. The noise reduction levels are much more faithfully predicted than with previous models such as Howe's model. Even though an additional wide peak yields a 5 dB overprediction of the predicted noise reduction around a given frequency, the overall trend follows the empirical linear law found in the present and previous experiments, and so up to a certain frequency after which the predicted levels of noise mitigation become constant. The additional gain observed experimentally (especially after isolation of the leading-edge noise by beamforming) might be attributed to the additional effect of thickness on turbulence-interaction noise not accounted in the analytical model. The frequency of the peak is also shifting to lower frequencies with lower flow velocity, suggesting that this discrepancy could be attributed to some modification of the incoming turbulence induced by the serrations. Further investigation is needed to confirm these presumptions.

Eventhough the present formulation of Lyu & Ayton's model requires a calibration with experimental data to be compared with experimental spectra, its noise gains are already quantitative and can be used to predict the effect of different serration designs. For instance, a first possible development is to apply such a correction directly on Amiet's model for straight edges. Such a quantitative prediction could then be used in an optimization loop as proposed in Section 6 both for leading and trailing edges. A more physically-based improvement of the model could be to extend Amiet's model using Ayton's pressure jump for the serrated airfoil. Another possible extension to this model could be a trailing-edge back scattering to account for the airfoil finite chord length.

5 Particle Image Velocimetry

Contents

Summary

This chapter describes the investigation of the three-dimensional features of the turbulence and mean flow at the leading edge with the time-resolved tomographic particle image velocimetry (PIV) technique. Measurements are performed for flat-plate airfoils with both straight and wavy leading edges at zero angle of attack and the same geometrical parameters, mean chord and span. Comparisons between the stereoscopic PIV, the tomographic and the numerical results from literature and present simulations are performed.

5.1 Experimental Apparatus

The time series of the three velocity components were recorded in a rectangular fluid volume. The measurements were carried out in the low-speed wind-tunnel (W) at Delft University of Technology during a secondment of the SmartAnswer project. The technique is used a complementary aspect to other experimental methods in this work, therefore only key details are given. Smoke particles were injected into the flow and were illuminated by a laser sheet to allow the cameras to have a clear field of view in the flow field. The laser sheet is provided by a high speed *Continuum* Mesa PIV laser (Nd: YAG, 18 mJ/pulse given

maximum power at 22V x 32A). Laser optics such as mirrors, spherical and cylindrical focals are used for forming the laser sheet on its width and directivity, see Fig.5.3. Particle images were recorded by three high speed Photron Fastcam S5 cameras (1024 x 1024 pixels, 12 *bit*, 20 μm/px) used with a Nikon-Nikkor 200 mm focal length, focus range $1 - 40$ and $f^{\#} = 11$. For each measurement, 10000 images were recorded at an acquisition frequency of $f_c = 10$ kHz. Cameras and laser were both synchronized and triggered by a LaVision HighSpeed contoller (HSC). The recorded images were post-processed with the software LaVision DaVis 8.1. Figure 5.1-a shows the corresponding PIV set-up consisting of three high-speed cameras, two poly-carbonate support plates and the laser beam. A metal grid made of flat rods was placed at the nozzle contraction outlet, generating nearly the same turbulent conditions as in the anechoic wind tunnel of ECL. The nozzle outlet cross section is 40 x 40 cm^2. The free-stream mean velocity was measured to be around $U = 22$ m/s using a Pitot tube and subsequently verified by the PIV results after the velocity field reconstruction. The final reconstructed measurement volume for the serrated version is approximately 30 x 20 x 10 mm^3 having the longest side along the streamwise direction. The origin of the Cartesian coordinate system for each configuration is selected at the position of the mean chord at the mid-span plane of each model.

Tomographic, stereoscopic and planar PIV measurements are conducted using two different set-ups as shown in Fig. 5.1 and Fig. 5.2. The first set-up (Fig. 5.1) consists of two horizontal support plates that hold vertically the airfoils making the flow volume to be visible by the cameras. In the second set-up (Fig. 5.2) the support plates were rotated at a vertical position to hold the airfoils horizontally. In both configurations the airfoil is visible by the cameras view and the laser beam because of the transparent support plates made by plexiglas. Sketch photographs showing the set-ups in Fig. 5.3 and Fig. 5.4 provide a more detailed view of the equipment that is used as well as the laser sheet directivity and the optics. A description about each set-up is given at the bottom of the photographs.

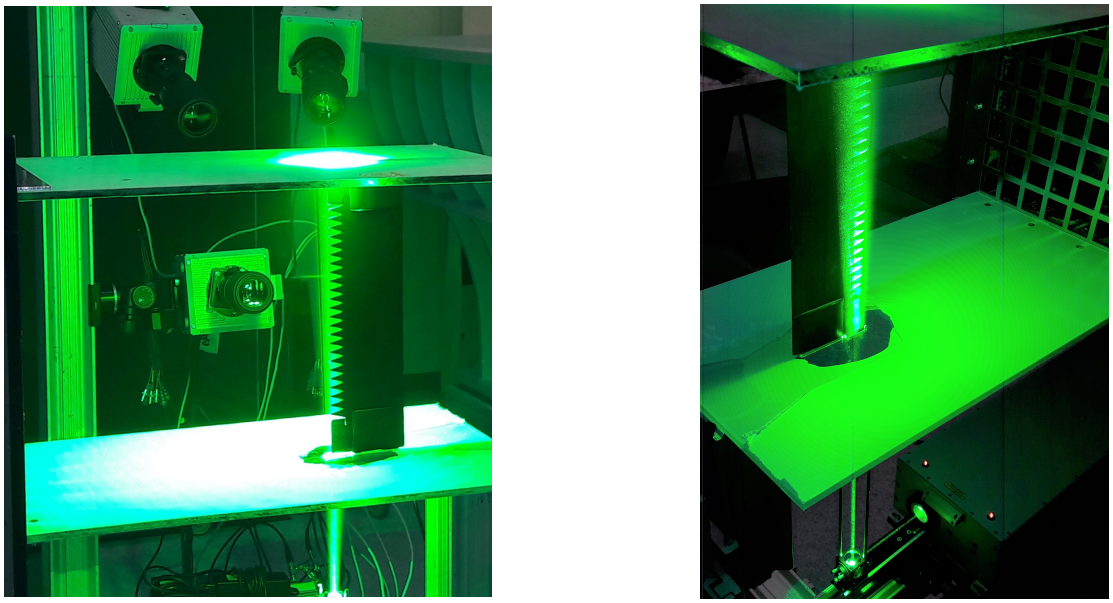

(a) (b)

Figure 5.1: Portside (a) and starboard (b) views of the tomographic PIV set-up, showing the serrated flat plate airfoil held vertically and the laser beam along the spanwise direction. Turbulence grid seen on the right in (b).

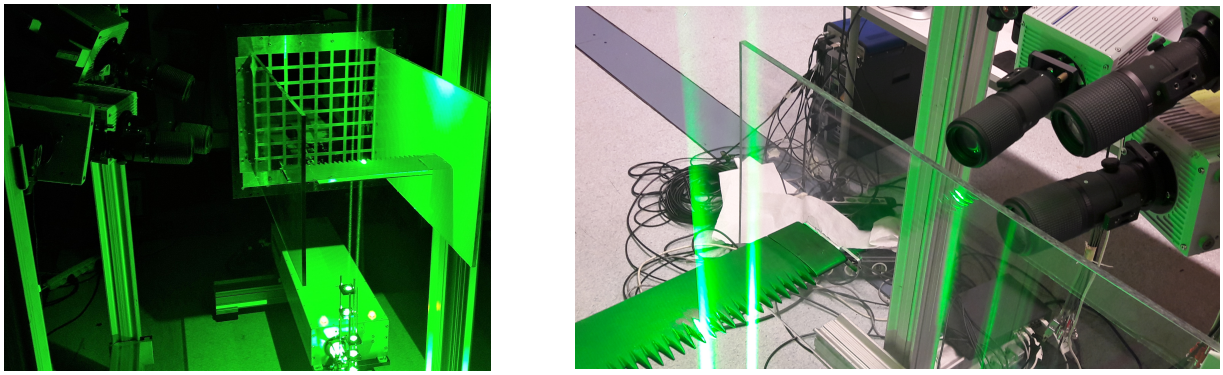

(a) (b)

Figure 5.2: Photographs of the second tomographic PIV set-up showing the serrated airfoil be held horizontally and the laser beam crossing vertically the airfoil at the leading-edge position. (b) The three cameras receive the instantaneous lighting through the transparent support plate made by plexiglass.

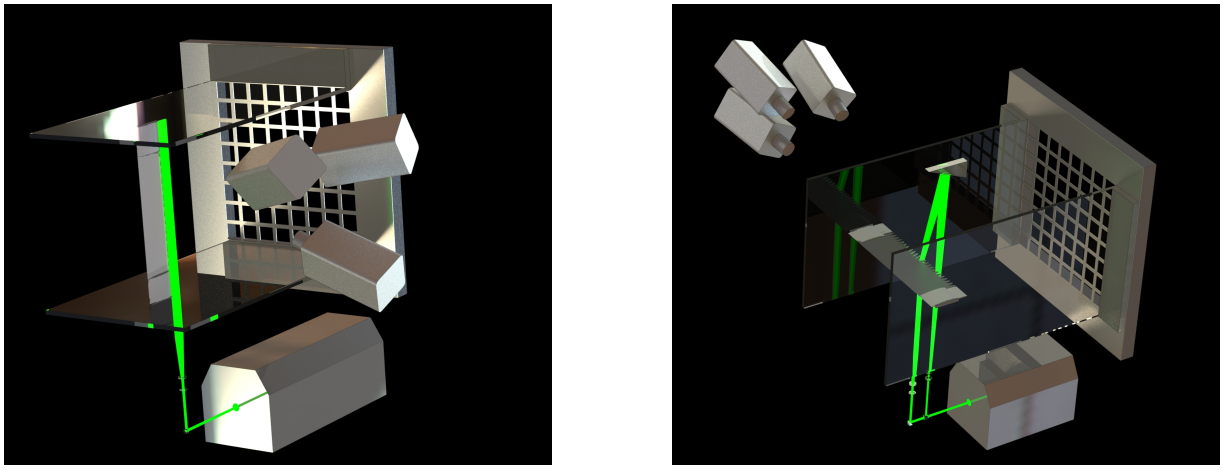

(a) (b)

Figure 5.3: Sketch photographs of the tomographic PIV set-ups: (a) the serrated flat plate is held vertically between support plates. (b) The system of the support plates and the serrated flat plate are reverted 90° compared to (a). The laser sheet crosses the flat plate vertically. Two corner mirrors, two spherical and two cylindrical focals and one spliter are used for directing the laser sheet.

(a) (b)

Figure 5.4: Sketch photographs of the laser beam direction and the optics that are used for the corresponding set-ups: (a) a corner mirror, a spherical focal and a cylindrical focal direct the laser sheet parallel to the leading edge (1st set-up). (b) The laser beam is split in two and finally two laser sheets cross the flat plate vertically. One corner mirror, one spherical, one cylindrical focal and one spliter are used for directing the laser sheet (2nd set-up).

5.2 Calibration Imaging

A calibration plate of "Type 7" is initially centered at the position on the desired recorded volume so that its surface is aligned to the center of the measured volume in the z direction. The center of the volume is set at the tooth tip position which also coincides with the baseline leading edge. The calibration system is set in DaVis84 software according to the right-handed coordinate system, the x-axis is aligned with the stream-wise direction and the z-axis with the spanwise direction facing the cameras. Fig. 5.5 shows the calibration procedure; the calibration plate is positioned at the center of the tooth peak surface (a) and the calibration has been conducted in the absence of the airfoil (b).

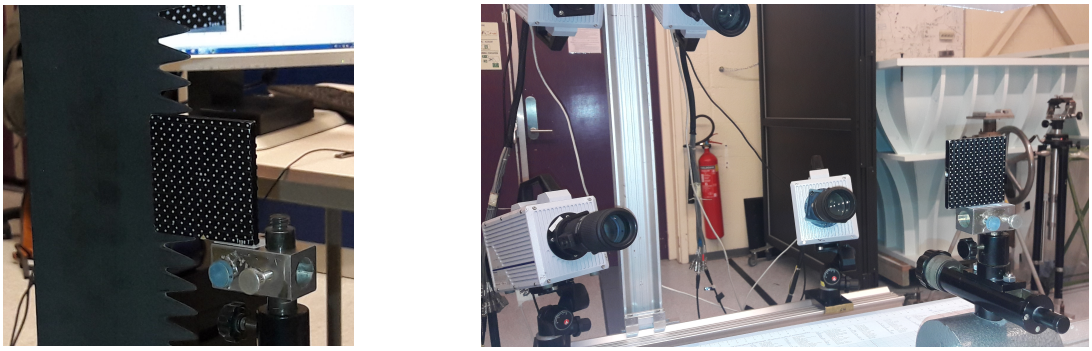

(a) (b)

Figure 5.5: Calibration plate imaging; (a) the calibration plate centered ($x-y$ axis) at the tooth peak of the vertical airfoil matching the correct height and (b) finally centered (z axis) to the volume origin in the absence of the airfoil. The fourth camera at the bottom right was not used.

5.3 Results

The illuminated volume for PIV interrogation is shown in Fig. 5.6 and the dimensionless time-averaged velocity is displayed in Fig. 5.7 by orthogonal plane views in the interrogation volume, with the bottom plane along the span of the serrated leading edge.

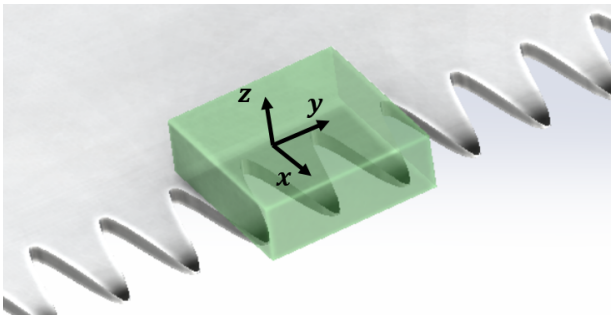

Figure 5.6: Illuminated volume of the tomographic PIV domain. The flow direction is along the negative x-axis.

Despite our best effort to reduce the contamination by light reflections on the wall, the very near-wall region remained inaccessible to the measurements. Eventually, the reconstructed volumes were located above the serrations parallel to the surface and the lowest recorded distance from the surface varies between 0.5 mm and 1 mm, which means that part of the boundary layer or whole is missing. The color map slices of the absolute velocity around the serrated leading edge (Fig. 5.7-(a)) indicates an asymmetric flow on both sides of a tooth. This asymmetry might stem from the wall irregularities generated during the smoothing procedure of the airfoil surface. The flow on the left-side part of the tooth decelerates whereas the velocity on the right-side remains closer to the free-stream velocity.

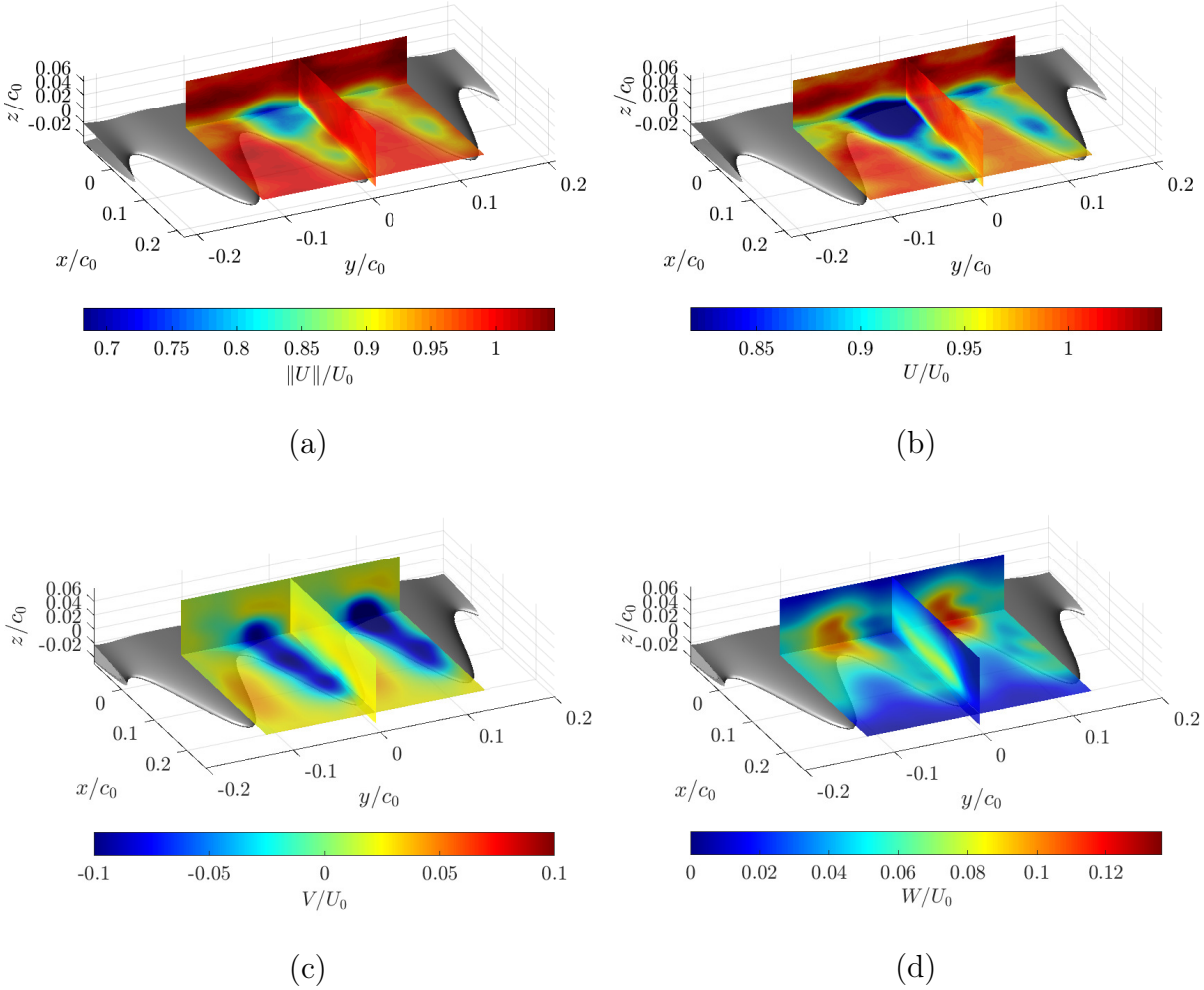

Figure 5.7: Planar views of the mean velocity components for the serrated airfoil flat plate. The bottom plane is located at $z/c_0 = 0.017$. $U_0 = 22$m/s is the free stream velocity

Fig. 5.8 shows horizontal planar cuts of the vertical velocity component W at different distances from the wall. The blockage of flow that would occur along the edge of a straight-edge airfoil appears mainly concentrated at the valleys of the serrations. Similar flow topology was observed by Avallone *et al.* [17] in the case of trailing-edge serrations.

The flow tends to move into the empty spaces between adjacent teeth and to accelerate at their tips. Observations in latest studies by Turner and Kim [147] and Chaitanya *et al.* [32] mention the importance of the stagnation-point region for leading-edge noise and the deflection of the flow between the teeth. This raises the interest of paying attention to the vertical velocity component linked to the deflection of the flow around a tooth. Additionally, the thickness at the root of a tooth is larger than at the valley nearby.

The vertical component upstream of the wavy leading edge and between teeth is nearly zero and goes to a maximum approaching the wall at a valley. This indicates that the vertical velocity component W is affected not only by the surface thickness but also by the local transfer of flow. The spanwise velocity components (Fig. 5.7-(c)) are maximized at one hill side of the teeth, again asymmetrically in terms of level, resulting probably to an counter-clockwise flow rotation.

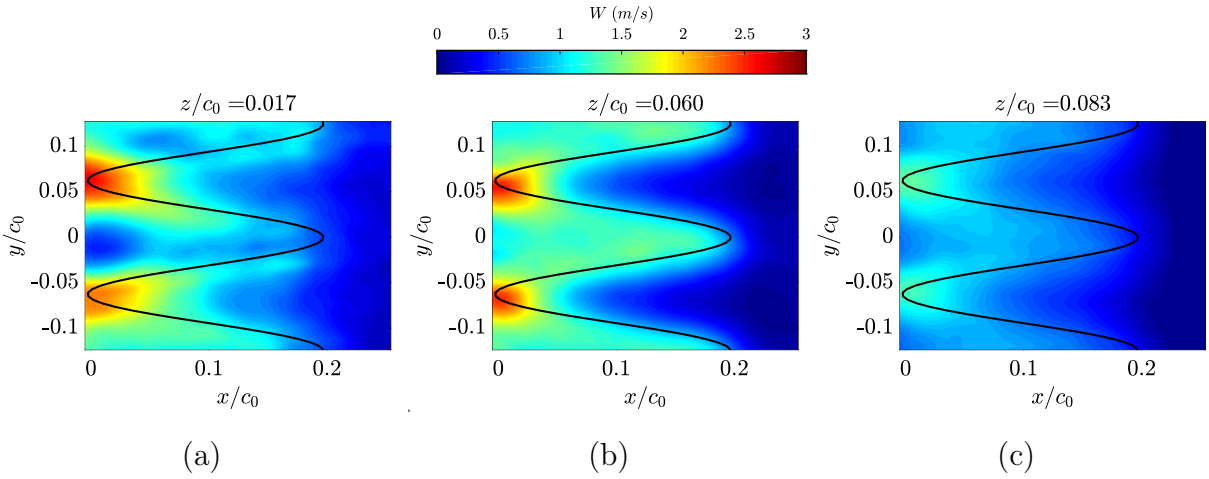

Figure 5.8: Time-averaged velocity component W on planes parallel to the $x-y$ plane for the serrated leading edge, at various z positions. (a): $z/c_0 = 0.017$, (b): $z/c_0 = 0.060$, (c): $z/c_0 = 0.083$. $U_0 = 22$ m/s is the free-stream mean velocity at the LE position ($x/c_0 = 0.2$). Traces of the wavy pattern in the $x-y$ plane as black lines.

Corresponding color map slices of the velocity components for the flat plate with straight leading edge are plotted in Fig. 5.9. Here, the setup 5.3-(b) has been used for performing tomographic measurements capturing both the pressure and the suction side of the flat plate. The norm of the velocity is almost in agreement with the chordwise velocity component for both configurations (Fig. 5.7-(a,b) and Fig. 5.9-(a,b)); this validates the significant contribution of the streamwise component to the total flow direction. The velocity component W in Fig. 5.9-(d) approaches to zero downstream the leading edge. The velocity of the V component (Fig. 5.9-(c)) shows a symmetric and an opposite pattern along the spanwise axis while it is also shown clearly in Fig.5.10-(c). The streamwise velocity component appears an increase approaching the leading edge due to the wall curvature.

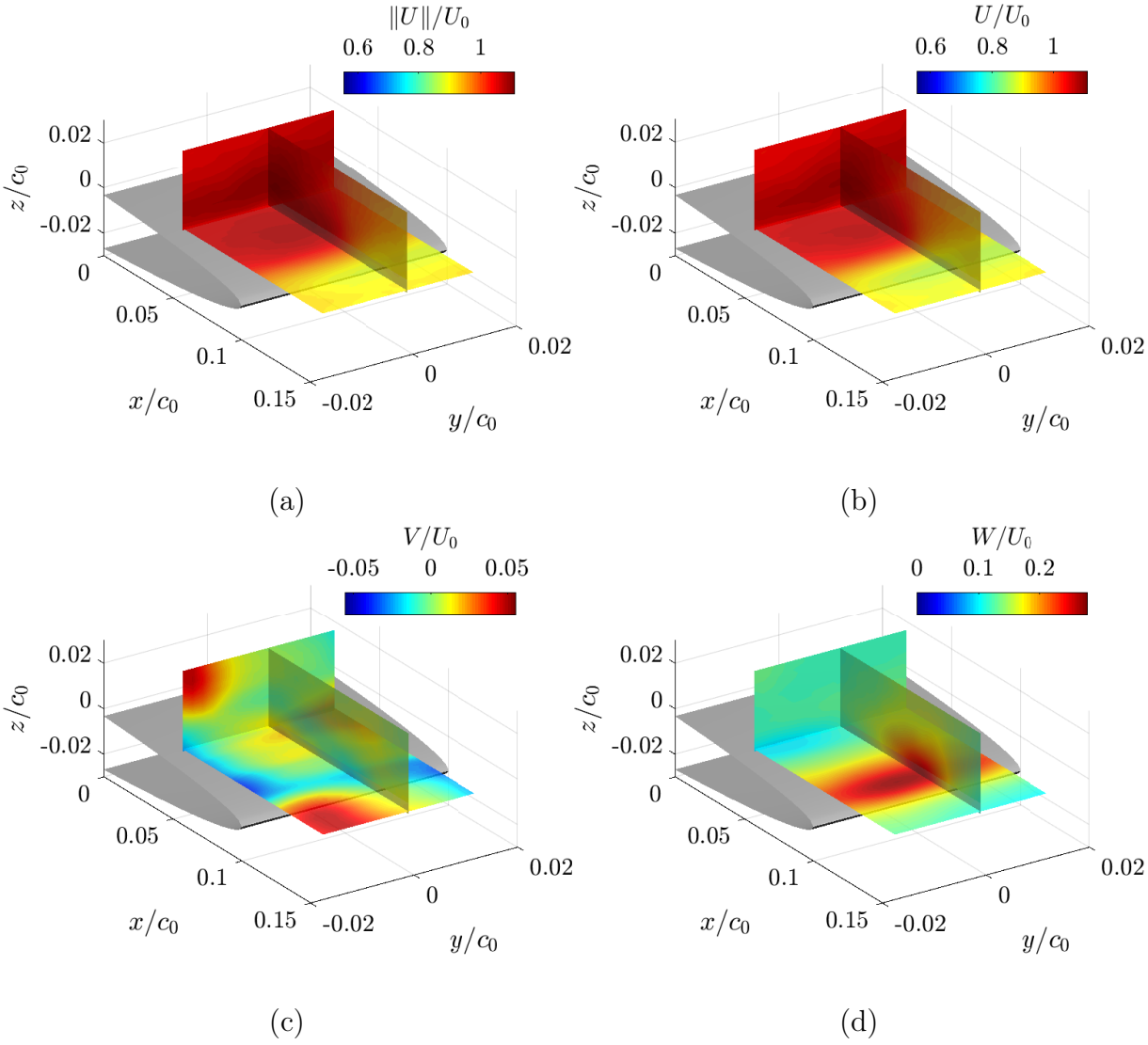

Figure 5.9: Plane views of the dimensionless velocity profile in the interrogation volume, with bottom plane along the span of the flat plate at $z/c_0 = 0.008$. Flow speed $U_0 = 18$ m/s. Baseline flat plate.

Contours of the mean velocity components along the serration tooth and the baseline straight edge, projected in the horizontal $(x - y)$ plane, are shown in Fig. 5.10. Velocity contours in the planes $z/c_0 = 0.077$ and $z/c_0 = 0.052$ correspond to positions outside and very close to the boundary layer, respectively. The streamwise velocity component U in Figs. 5.10-(a) and (c) follows a similar increase approaching the $x/c_0 = 0$ position as it is measured far from the boundary layer. The spatial velocity distribution of the vertical component W for the straight edge features a sudden increase at the position of the leading edge $(x/c_0 = 0.1)$ whereas the gradient of this component for the serrated edge is much lower, with smooth variations (subplots (a) and (b)). Fig. 5.10-(a,b) shows the flow topology which coincides with Avallone *et al.* [17] results for the trailing edge serration regarding the spanwise component. Similar velocity patterns are induced in both axes x and y.

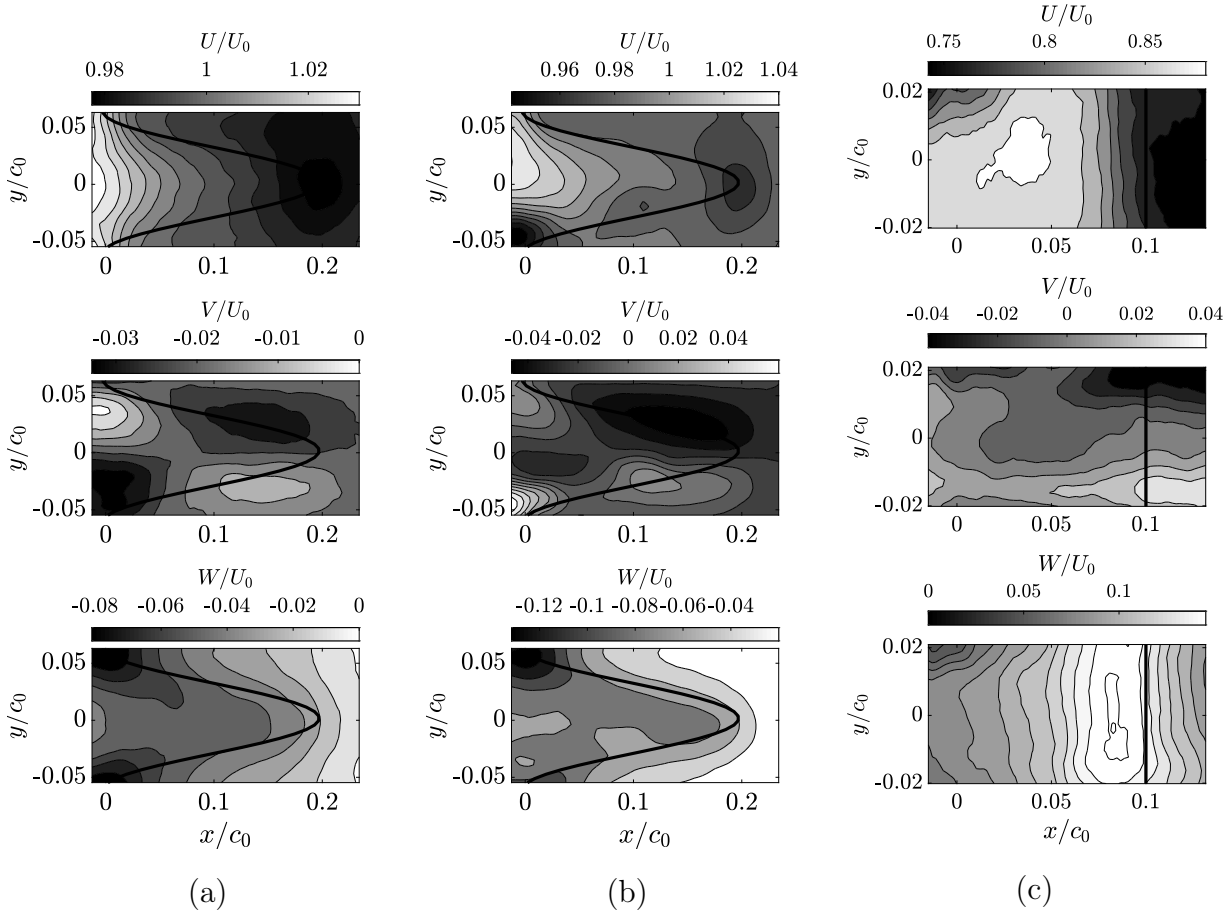

Figure 5.10: Distributions of time-averaged velocity components U, V, W along a tooth and corresponding baseline case at leading edge, in the $(x-y)$ plane. (a): $z/c_0 = 0.077$ and (b): $z/c_0 = 0.052$. Traces of the wavy serration pattern as black lines in subplots (a) and (b). (c): straight edge result for $z/c_0 = 0.007$; projection of the straight line on the $x-y$ plane. $U_0 = 22$ m/s is the free-stream mean velocity at the LE position ($x/c_0 = 0.2$).

5.4 Boundary Layers Characterization

Fig. 5.12-(a) shows the boundary layer profiles of all the velocity components for the baseline and the serrated case, measured by the tomographic PIV. The points of extractions for the BL are shown in Fig. 5.11. The velocity profiles of the baseline case are plotted at the position of the LE and upstream over nearly one wavelength. Considering Kim *et al.* [75] findings that the dominant noise sources on a serrated leading edge are located at the valleys, here the velocity components at the serration valley positions are compared to the corresponding components at the baseline leading edge position. Figures 5.12 and 5.19 show respectively the mean velocity components and the turbulent intensity (standard deviation) of the vertical velocity component in different positions above the LE teeth.

The streamwise component (Fig. 5.12-(a)) seems to decelerate approaching the root and have a minimum at the tooth center as it is confirmed with the color maps (Fig. 5.7-(b)). This agrees with the velocity contour ($z/c_0 = 0.052$, Fig. 5.10-(b)) where the plane closer to the wall features a decrease compared to the other plane ($z/c_0 = 0.077$, Fig. 5.10-(a)).

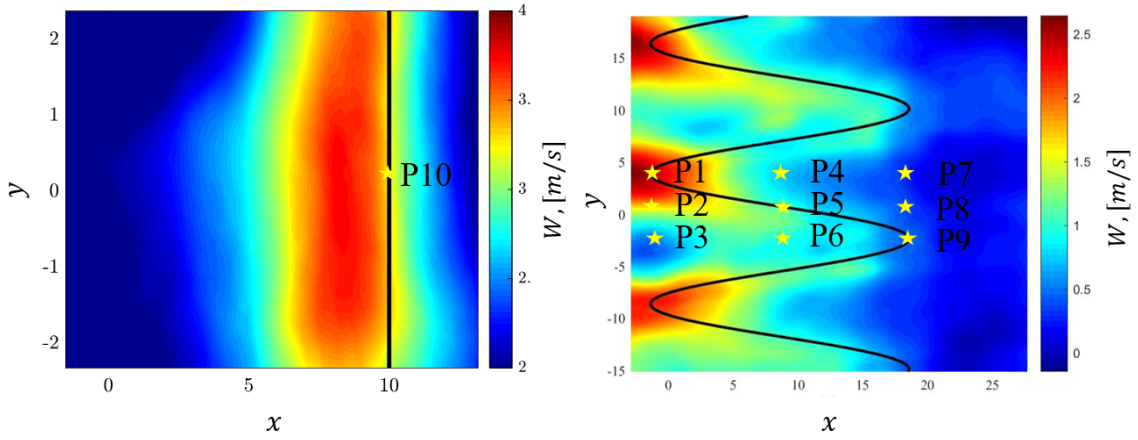

Figure 5.11: Maps of the normal velocity component. Positions of the boundary layers extraction of the baseline (left) and the serrated leading edge (right). The positions are listed from 1 to 11 according to the shown locations. Flow direction from right to left.

A comparison of the velocity contours between the serrated flat plate and the NACA12 airfoil (Fig. 5.13) gives additional information for the mean flow topology. NACA12 results have been obtained by RANS computation features as described in Chapter 6. It shows that the streamwise velocity close to the surface of the flat plate behaves in a similar way as with the plane in the middle of the NACA12 airfoil thickness, Appendix A.2. The streamwise velocity decreases approaching the teeth root. On the other hand, the flow above the airfoil leading edge accelerates approaching the teeth root due to the wall curvature for the NACA12. The spanwise component confirms the symmetric patterns along the tooth shown in Fig. 5.10-(a),(b) around the tooth center, as well as for the NACA12 airfoil. The instantaneous velocity of this component contributes significantly to the counter-rotating streamwise vortices produced along the tooth. This motion fits constructively with the maximization of the vertical component W at the root valley. The opposite flow patterns between the peak and the root areas confirm the existence of an upwash and a downwash at these regions respectively linked to the mean streamwise vorticity. Contour maps of the spanwise velocity V and flow motion indications show the vorticity direction and the resulting upwash and downwash trends. A contour plane at the hill position of the tooth indicates the creation of a downwash motion at the valley root. Probably this reversed motion leads to a more complex flow by adding three-dimensional features in it. Eventually, the vertical component presents its highest amplitude at the root valley as shown already in Fig. 5.12-(c).

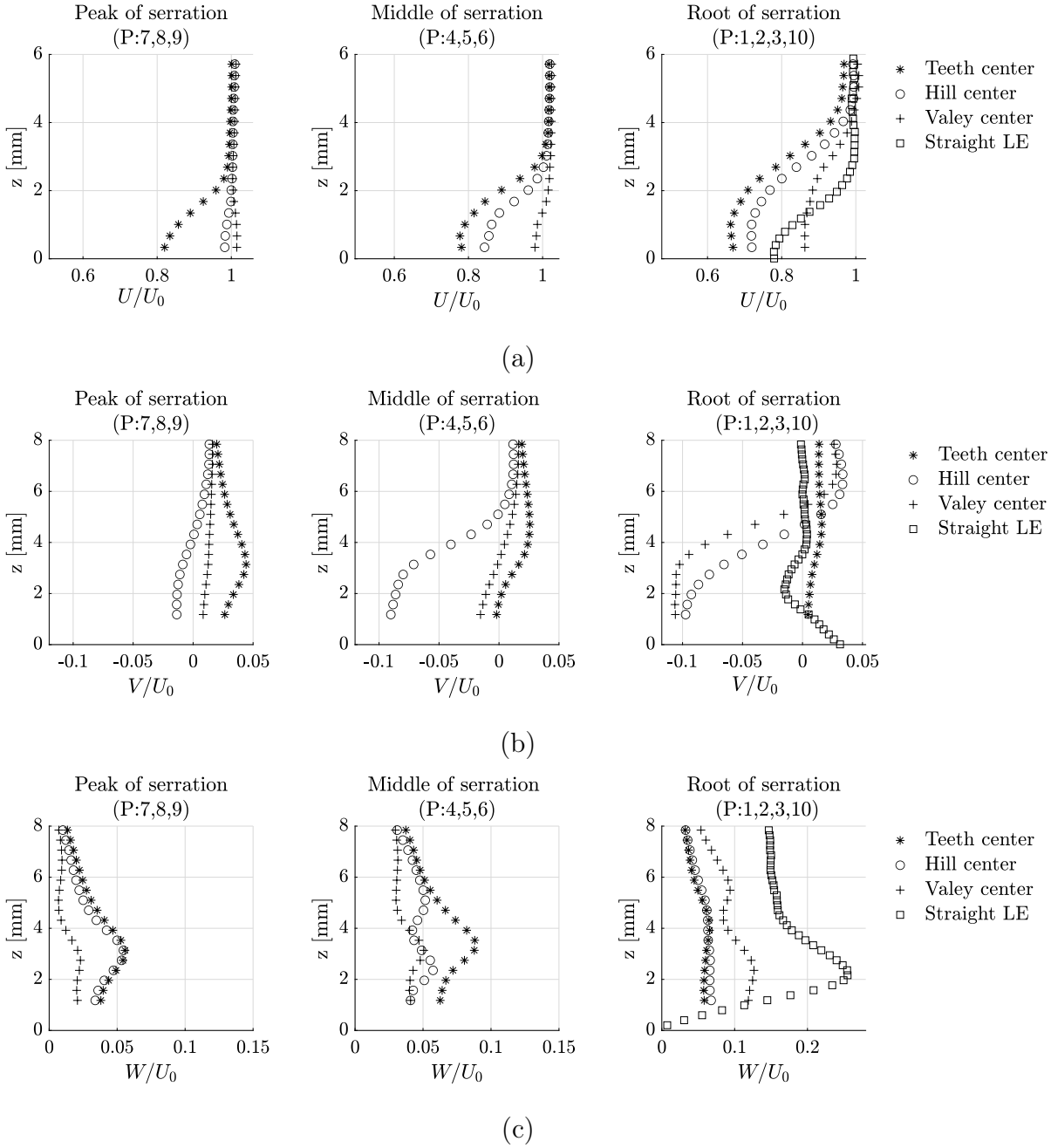

Figure 5.12: Boundary Layer profiles of all the mean velocity components (a) U, (b) V, (c) W in different positions along the LE of the baseline and the serrated cases. $U_0 = 22\,\mathrm{m/s}$ is the free stream velocity.

As mentioned in Section 5.1, stereoscopic measurements on planes vertical to the spanwise direction have been conducted. This leads to additional and more complete exploration of the flow around the leading-edge serrations. Therefore, a good matching from the two setups is required for further comparisons and investigations. Initially, the velocity components between the tomographic and stereoscopic setups are compared for positioning accurately the measured volume at the leading edge. Fig. 5.14 compares the velocity profiles at the position of tooth peak. The agreement of the velocity profiles of the

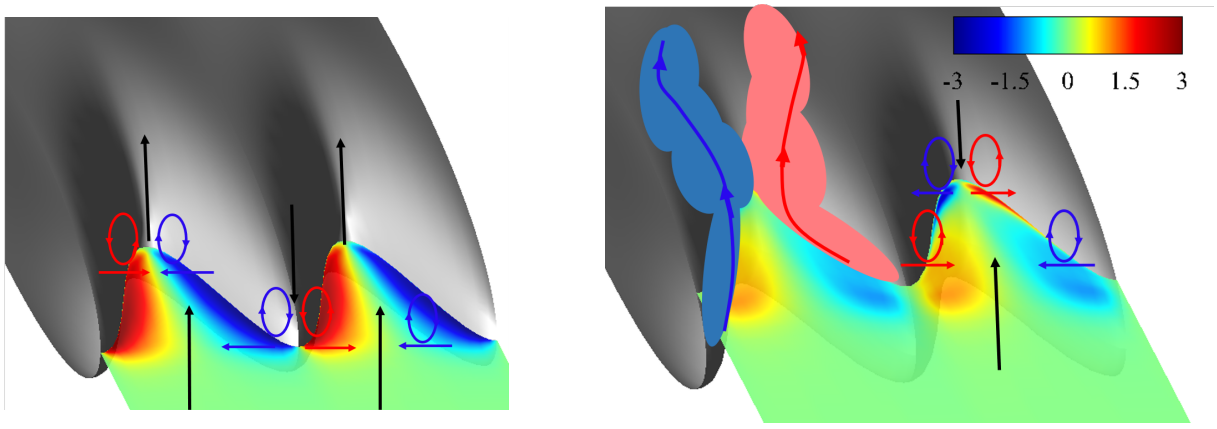

(a) (b)

Figure 5.13: Contour plots of the spanwise velocity component V for a NACA12 airfoil generated with RANS simulations; (a) plane at the center of the airfoil $z/c_0 = 0$ and (b) plane at $z/c_0 = 0.03$. Computational results produced for the optimization study (Chapter 6).

streamwise U and wall-normal W components indicates that the extraction point of the tomographic PIV is located slightly upstream the tooth peak position ($x/c = 0.15$). Both velocity components exhibit some differences for the wall-normal positions beyond 2 mm -(a) and 4 mm -(b). The negative symmetric velocity profile provided by the stereoscopic measurements validates the leading edge upstream conditions in the vicinity of the tooth stagnation point. In addition, the lowest measured position for the tomo-PIV seems to be 0.5 mm far from the wall, as correctly considered above. The distance of 0.5 mm is the information that is lost due to the reflections, thus only numerical simulations and wall pressure probes can give access to this information.

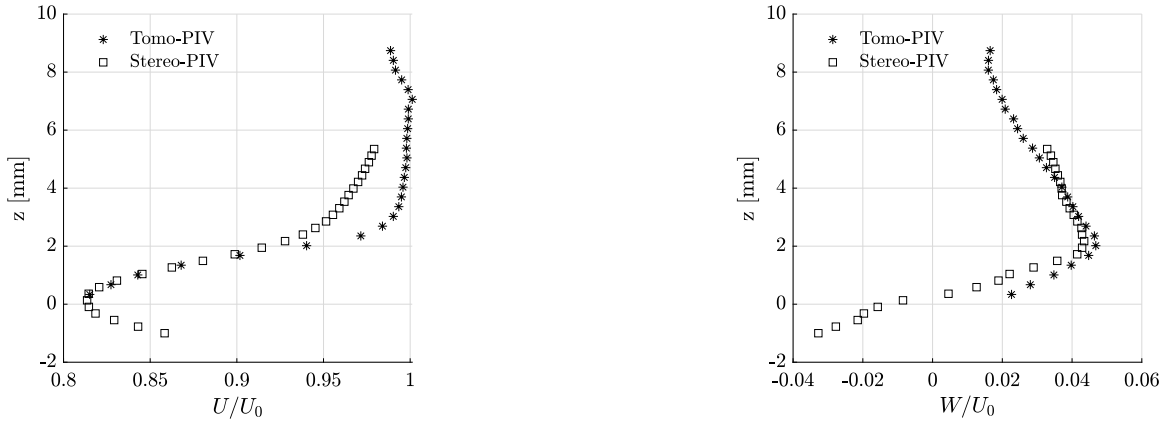

(a) (b)

Figure 5.14: Mean velocity profiles of the components (a) U and (b) W at the tooth peak center extracted by tomographic and stereoscopic measurements. $U_0 = 22\,\mathrm{m/s}$

5.5 Stereoscopic Particle Image Velocimetry Results

Stereoscopic PIV measurements have been performed to describe the turbulent boundary layer profile and the three dimensional integral parameters in a single plane for the serrated flat plate, the serrated airfoil and the corresponding baselines. The calibration procedure was repeated for the second tomographic setup as well as for the stereoscopic and the planar measurements. The calibration plate was held vertically with a movable support at the position of the leading edge. The measured planes (stereoscopic) along the spanwise direction have been recorded at neighbour positions (tooth peak and valley) avoiding additional calibration procedures by using the plate.

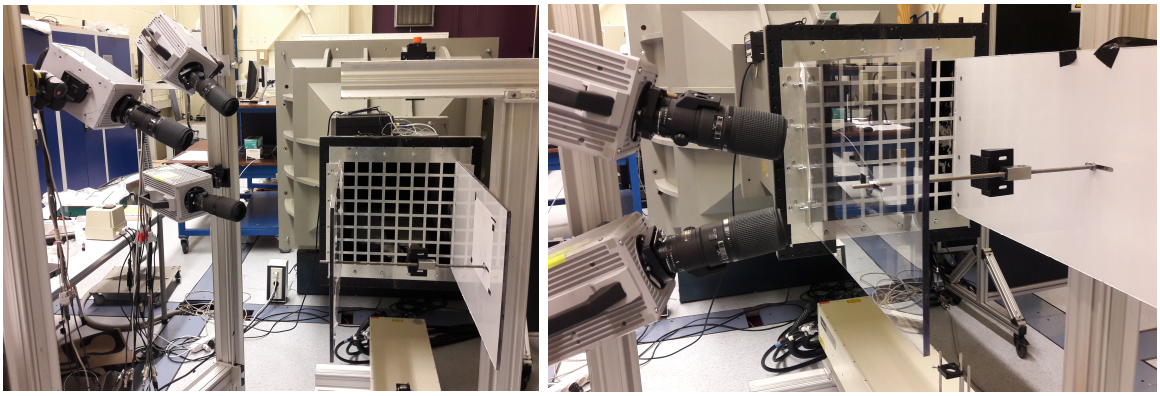

(a) (b)

Figure 5.15: Calibration plate imaging of the second setup for (a) the tomographic and (b) stereoscopic and planar configurations. The calibration plate centered ($x-y$ axis) at the leading-edge position and middle of the airfoil span (z axis) in the absence of the airfoil.

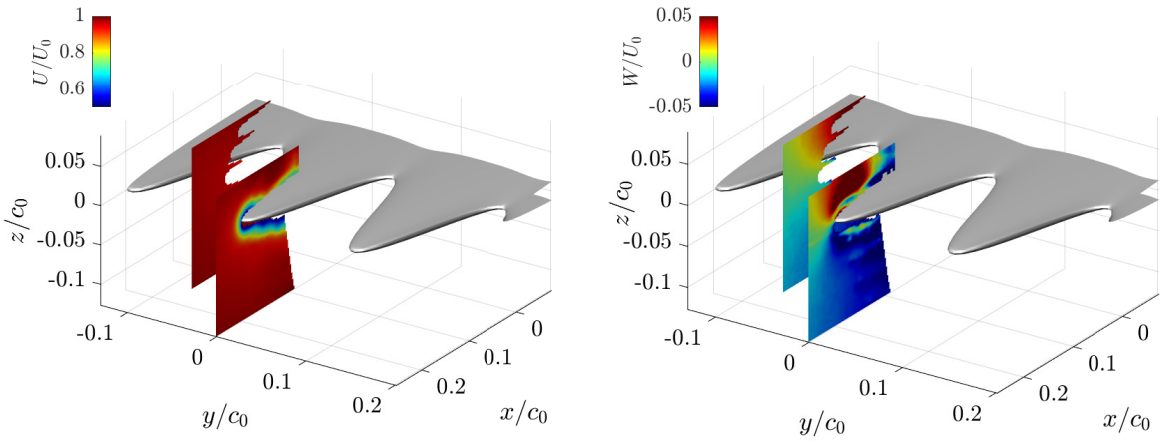

(a) (b)

Figure 5.16: Planes of the streamwise and vertical mean velocity components U-(a) and W-(b) at the peak and valley positions. $U_0 = 22\,\mathrm{m/s}$ is the free stream velocity.

The recorded volume in Fig. 5.16 has a unit thickness and its orientation is similar to the volume in Fig. 5.6. Stereoscopic and planar PIV are plotted to illustrate slices of a flow volume upstream and close to the leading-edge serrations. The origin of the coordinate system is located at the root of the teeth, the x-axis is aligned with the stream-wise direction, the y-axis in the span-wise direction and the z-axis is the direction normal to the flow. The aforementioned planes have been recorded at the peak, hill and the valley of the tooth. The surface in each configuration varies because of the boundaries limitations.

Fig. 5.16 shows contours of the time averaged velocity components U and W at the peak and the valley positions. The vertical component, W, exhibits a symmetric variation in both suction and pressure sides, whereas it is minimized between the two sides. Similar behavior has been observed by Turner & Kim [147] according to the acoustic pressure generated by the WLE-vortex and LE interaction. A zero value is found at the position $z/c_0 = 0$ where is the axis of symmetry for the velocity fluctuation. It is observed a gradual increase of the velocity approaching the LE at the position $x/c_0 = 0.2$. The velocity profile follows the same trend apart from the area close to the peak $z/c_0 = 0$, whereas reaching the peak the velocity gradient is steepest increased.

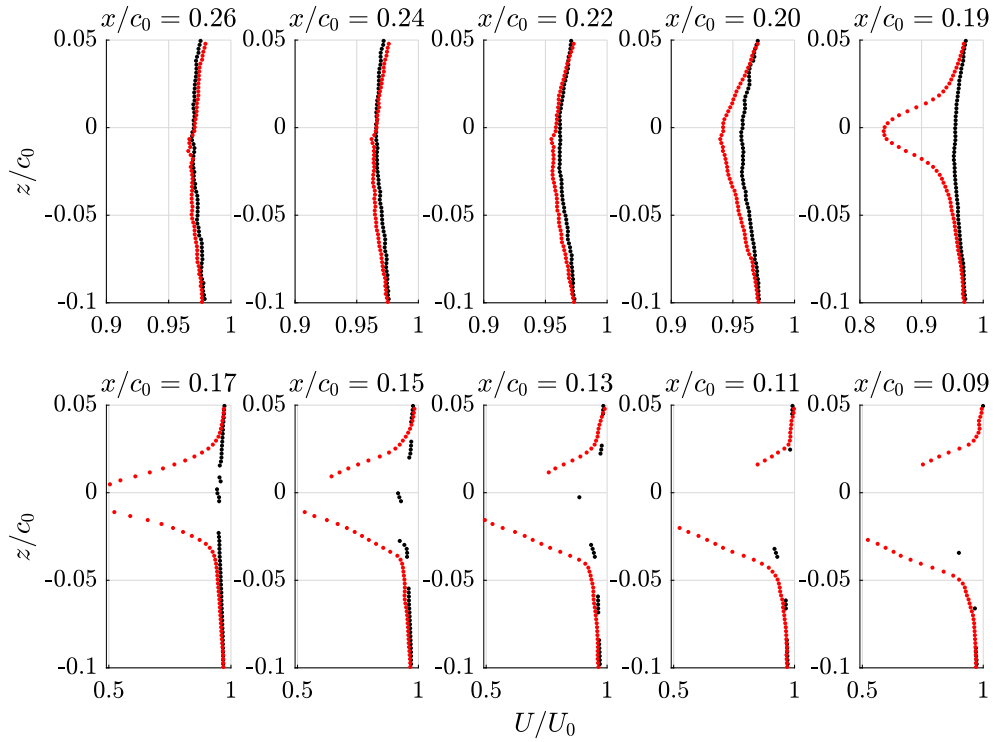

Figure 5.17: Mean velocity profiles of the component U/U_0 at different positions in the chordwise direction. Black points correspond to the valley center and red points to tooth center according to Fig. 5.16-(a).

The steamwise mean velocity profile, U, remains nearly constant upstream the leading edge until the very vicinity where a sudden decrease happens as shown in Fig. 5.16. Its evolution on x-axis is shown better in Fig. 5.17 where the velocity profiles are plotted. These profiles were extracted by the slices in Fig. 5.16-(a), the black and the red dots

correspond to the valley and the tooth peak positions respectively as well as to the same streamwise positions. Velocity values that were recorded very close to the surface are not plotted. A small decrease of the streamwise velocity is observed upstream and are between the teeth whereas the velocity drop to zero at the stagnation point at the tooth peak is clear.

The component W appears to be symmetrical and opposite along the z-axis close to the tooth peak area. Downstream the serration peak a reverse flow zone starts to develop, the boundary layer becomes thicker and the external flow deviates dominantly from the surface of the body. Approaching the volume boundary limits the velocity becomes negative; this is explained by a post-processing artifact. Further analysis of the time-resolved stereoscopic measurement can be achieved in the future for extracting more information from the suction side and the pressure side of the serrated flat plate as well as from the empty spaces between the teeth.

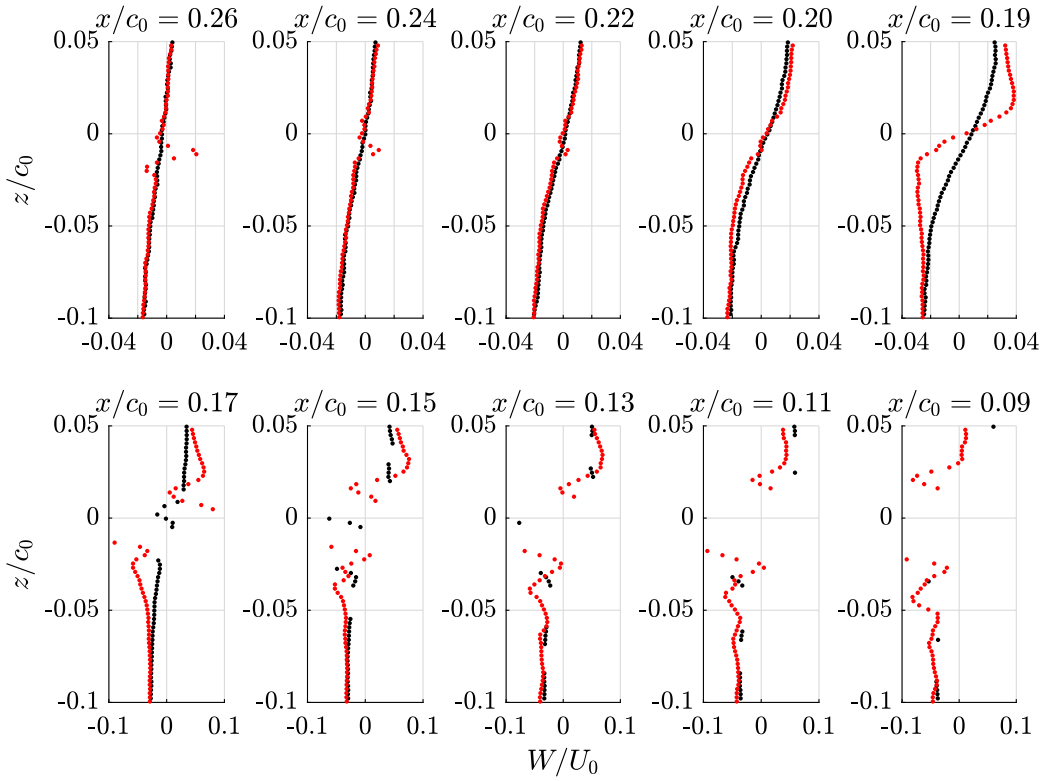

Figure 5.18: Mean velocity profiles of the component W/U_0 at different positions in the chordwise direction. Black points correspond to the valley center and red points to tooth center according to Fig. 5.16-(b).

5.6 Analysis of the Vorticity and Flow Kinematics

The TIN generation mechanism can be related to spectra of velocity statistics as emphasized in Section 2 and Section 4. Particularly, the vertical component (upwash) of the

velocity fluctuations is the input for the TIN generation model according to Amiet's theory which has been proved to capture the main physics of this noise mechanism. Therefore, the standard deviation of the vertical velocity component shown in Figs 5.19 and 5.20 shows the trace of the turbulence interaction as source strength. Regarding the wavy edge, the turbulence strength in Fig 5.19 is obviously located in the valley of the root of the tooth whereas a weaker source is found at the center of the tooth. The reduced level of the vertical velocity disturbances could be explained by a longer measuring distance of about 2 mm compared to the valley. A proper comparison could be the information extracted from the wall pressure statistics. Despite this fact, this reduced level has been also observed by Turner [147] claiming that this stems from the counteracting effect of streamwise vortices. The vertical velocity fluctuations at the root between the teeth are greater than at the straight edge while the flat-plate velocity profile at the root seems to collapse with the tooth center profile (asterisks). Turner [147] observed a doubled amplitude of the vertical velocity disturbances at the valley while he added that the source strength of these two sources remains the same.

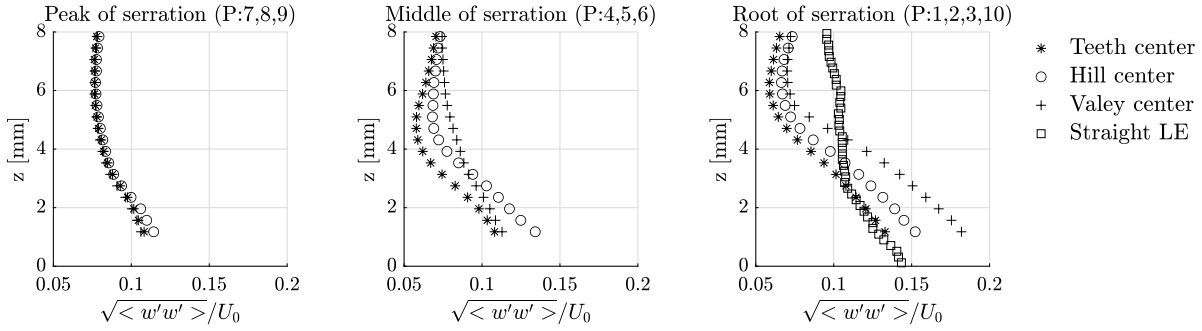

Figure 5.19: Turbulent intensity profiles of the vertical turbulent fluctuations $< w'w' >$ at various positions position along the LE teeth. $U_0 = 22$ m/s is the free stream velocity.

The spatial distribution of the time-averaged velocity fluctuations is presented in Fig. 5.20. The $< u'u' >$ component shows a higher intensity at the valley of the tooth root while a spot of increased intensity is found at the hill, the same for the $< w'w' >$ component. This spot may comes from local morphological discrepancies due to the handmade smoothing procedure; $< v'v' >$ shows high variations at the peak and at the root of the tooth and the $< w'w' >$ agrees with the velocity profiles in Fig. 5.19 where a maximum of the intensity occurs at the root in the empty spaces between the teeth. The vertical velocity statistical component for the straight edge shows an increased intensity approaching the leading edge and finally a drop downstream from it. This flow topology can explain the location of sound generation at the leading edge. Upstream, the turbulence intensity remains of high amplitude, more than 4.5 % of the turbulence measured in free-stream conditions. This makes sense because the obtained information upstream the leading edge is very close to it.

The interaction of impinging vortices with the serrated edge induces vorticity which varies along all the axis while it follows a repeated pattern. The streamwise ω_x and the

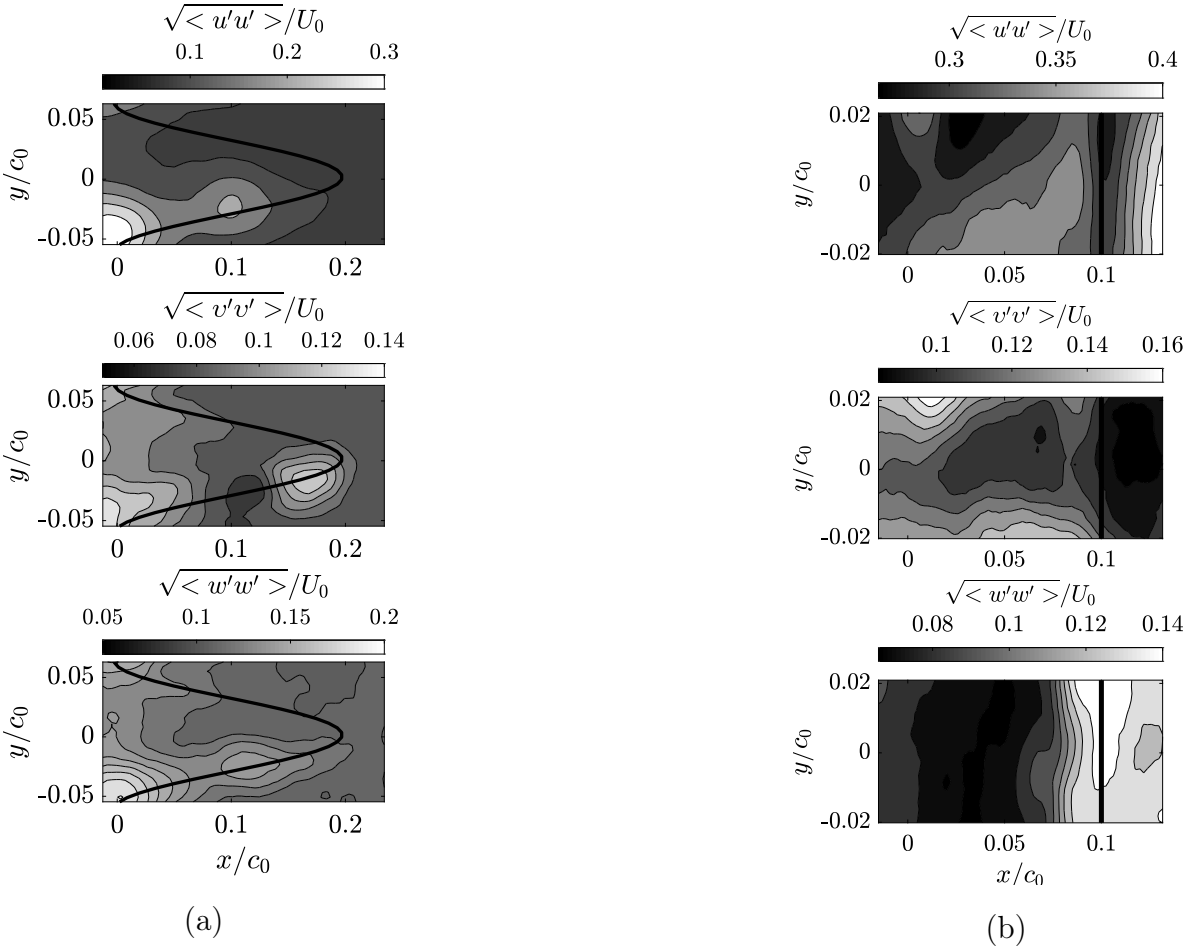

Figure 5.20: Distributions of the time-averaged turbulent-intensity fluctuations $\sqrt{< u'u' >}$, $\sqrt{< v'v' >}$, $\sqrt{< w'w' >}$ along a tooth and corresponding baseline case at leading edge, in the $(x-y)$ plane. (a): $z/c_0 = 0.017$ and (b): $z/c_0 = 0.012$. Traces of the wavy serration pattern and the straight edge as black lines in subplots (a) and (b). $U_0 = 22$ m/s is the free-stream mean velocity at the LE position ($x/c_0 = 0.2$).

spanwise ω_y vorticity components are related primary to the sound generation linked to the vertical disturbances w'. Here, it must be clear that the calculated mean vorticity does not correspond to the sound generation or reduction but is just related to the mean flow topology and maybe provides some hints about the sound source strengths. Fig. 5.21-(a) shows the non-dimensional streamwise mean vorticity $\omega_x c_0/U_0$ in slices in three axes while Fig. 5.21-(b) & (c) show the vortical patterns on $(y-z)$ planes at the peak and root positions. Two pairs of counter-rotating vortices appear around the tooth center at the peak and extend till the root. Vorticity close to the wall seems to be stronger in amplitude at the peak position and tends to weaken approaching the root. Inversely, the second pair of vortices rotate contrary above the primary while they appear to be stronger and more compact at the root. At the root, the pair of vortices is shown to have an upwash direction. Similar streamwise vorticity trend has been observed by Turner [147] but counting for instantaneous vorticity and not the averaged. A minor note at this point

is that the serration geometry might affect in the same way not only the mean flow but also the disturbances. Comparing also the pairs of the vortices at the vicinity of the peak and the valley in Fig 5.21-(a), they present an opposite rotation. An upwash trend appears at the peak and a downwash at the root.

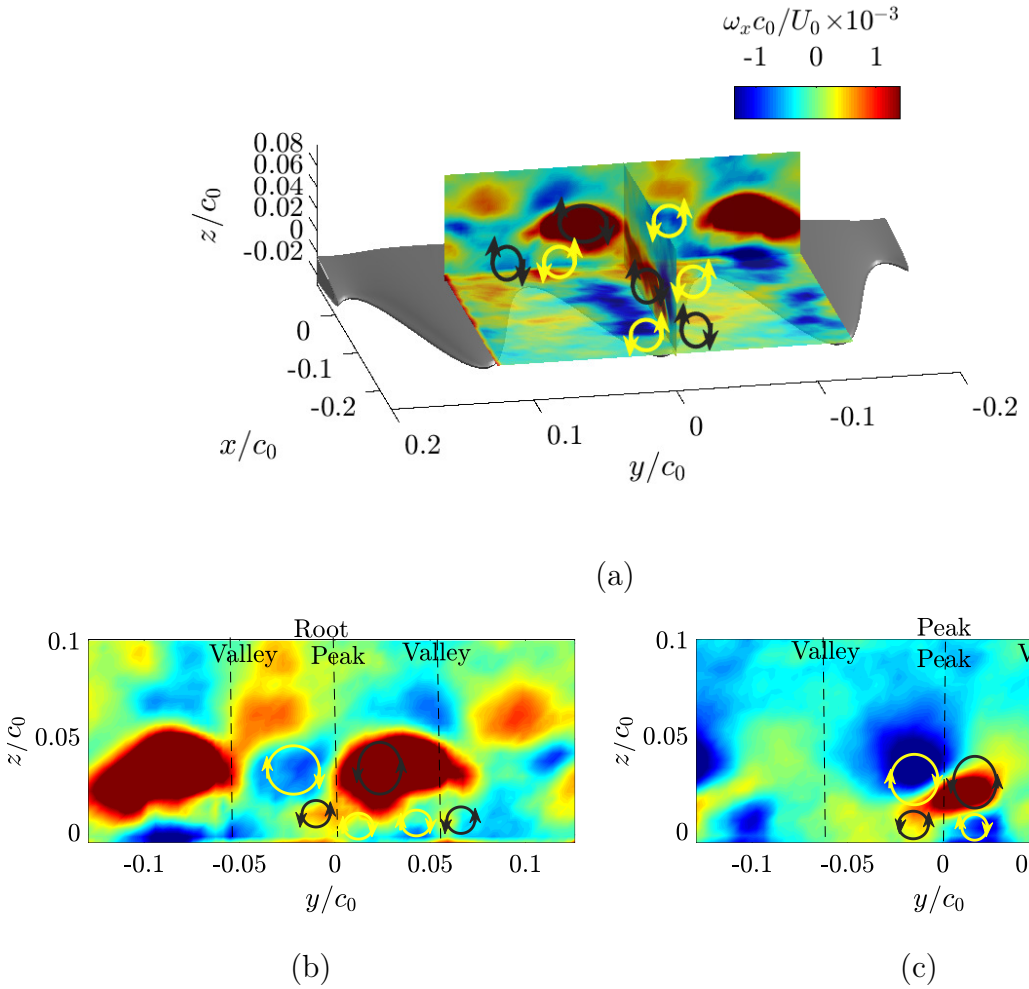

Figure 5.21: Contours of the normalized averaged streamwise vorticity $\omega_x c_0/U_0$; (a) the horizontal plane is located at $z/c_0 = 0.017$ and the vertical spanwise plane at the root of the serrations, (b) plane at the peak ($x/c_0 = -0.2$) and (c) plane at the root ($x/c_0 = 0$). The black and yellow circles correspond to the clockwise and counter-clockwise direction of the averaged vorticity.

Fig. 5.22 shows the spanwise vorticity component ω_y through two different horizontal planes at $z/c_0 = 0.017$ and $z/c_0 = 0.045$. Symmetrical patterns along the span are shown while at the root of the valleys negative values dominate. It is worth mentioning that the peak at $x/c_0 = 0$ encounters vorticity of reduced amplitude both for the streamwise and the spanwise components. Particularly, counter-rotating spanwise vortices appear above the peak position as it is clearly shown at the plane of Fig.5.23-(a). Different planes vertical to the wall illustrate the vorticity variation along the spanwise direction from the tooth center position at $y/c_0 = 0$ till the hill center in both directions $y/c_0 = -0.9$ and $y/c_0 = 0.9$ in Fig.5.23. The vorticity appears diametrically opposed in both x & y

directions and it is of zero amplitude at the center of the valleys. It must be noted that some uncertainties on the exact positioning of the volume of visualization exist due to its experimental and three dimensional nature.

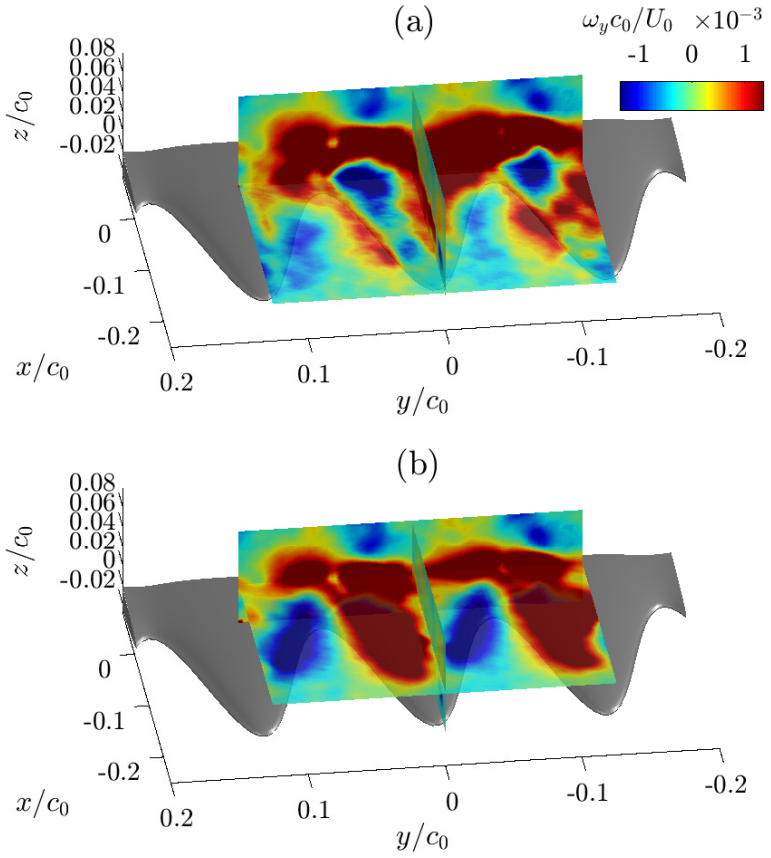

Figure 5.22: Contours of the normalized averaged spanwise vorticity $\omega_y c_0/U_0$; the horizontal plane is located (a) at $z/c_0 = 0.017$ and (b) at $z/c_0 = 0.045$.

Comparing both vorticity components at the peak position $y/c_0 = 0$ it is observed that ω_x contributes constructively to the increase of the vertical velocity component while ω_y acts destructively yielding to cancellation. If it is proved that the vorticity created from the velocity perturbations follows similar trend as the mean vorticity as above then the local cancellation at the peak can be linked to the reduced vertical velocity perturbations. Investigations on the instantaneous vorticity and the spectrum using different techniques such as the two-points correlation and the coherence spectrum could provide information about the source strengths around the tooth. Here, a simple exploration of the instantaneous vorticity after subtracting the mean velocity has been performed.

The instantaneous velocity field and the resulting vorticity are plotted for a single time step. Fig. 5.24-(a) shows two planes of the measured volume colored by the dimensionless instantaneous streamwise and spanwise vorticity. Vectors of the velocity disturbances v' and w' of the streamwise vorticity are shown on the horizontal plane. The u' component is excluded in order to highlight the rotation of the streamwise vortices. The transparency of the planes allows to see the velocity upwash upstream the peak tip, the upwash of the

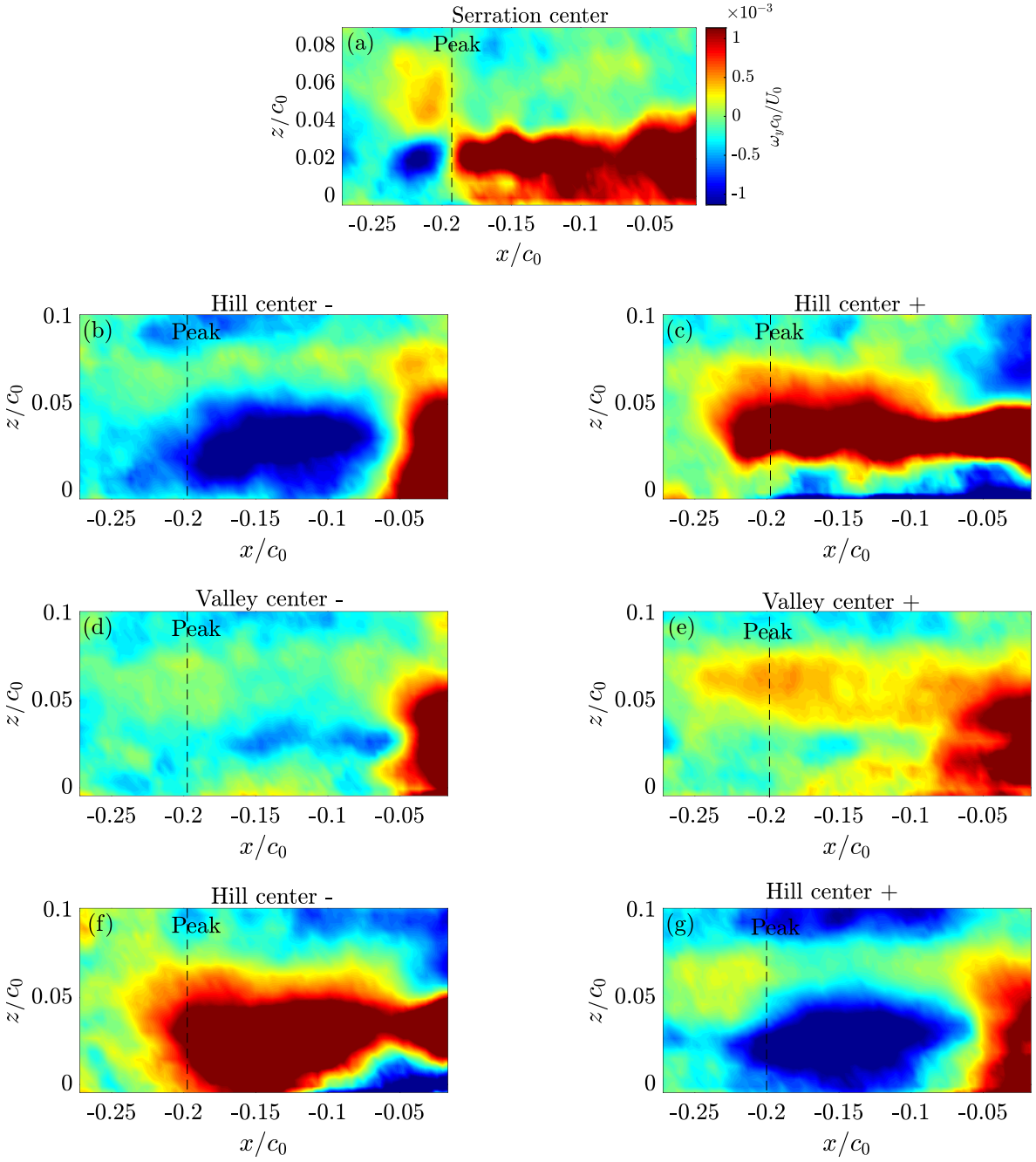

Figure 5.23: Contours of the normalized averaged spanwise vorticity $\omega_y c_0/U_0$ at different xz planes; (a) mid of the tooth at $y/c_0 = 0$, (b,c) hill at $y/c_0 = \pm 0.031$, (d,e) valley at $y/c_0 = \pm 0.063$, (f,g) hill at $y/c_0 = \pm 0.094$.

left side of the tooth ($y+$) and the downwash on the right ($y-$). A side view of the tooth can clearly also visualize the vertical velocity component along the tooth in Fig. 5.24-(b). It is shown that an upwash acts upstream and all along the tooth except for the tip and the root. At the tip, the velocity seems to be quite reduced compared to the downstream part while at the root it becomes zero at the middle of the volume and a strong upwash is found at the bottom plane ($z/c_0 = 0.017$). The reduced amplitude at the tip probably

stems from the interaction between the impinging spanwise vorticity upwash (blue big spot along the vertical plane) with the downwash of counter-rotating streamwise vortices at the tip.

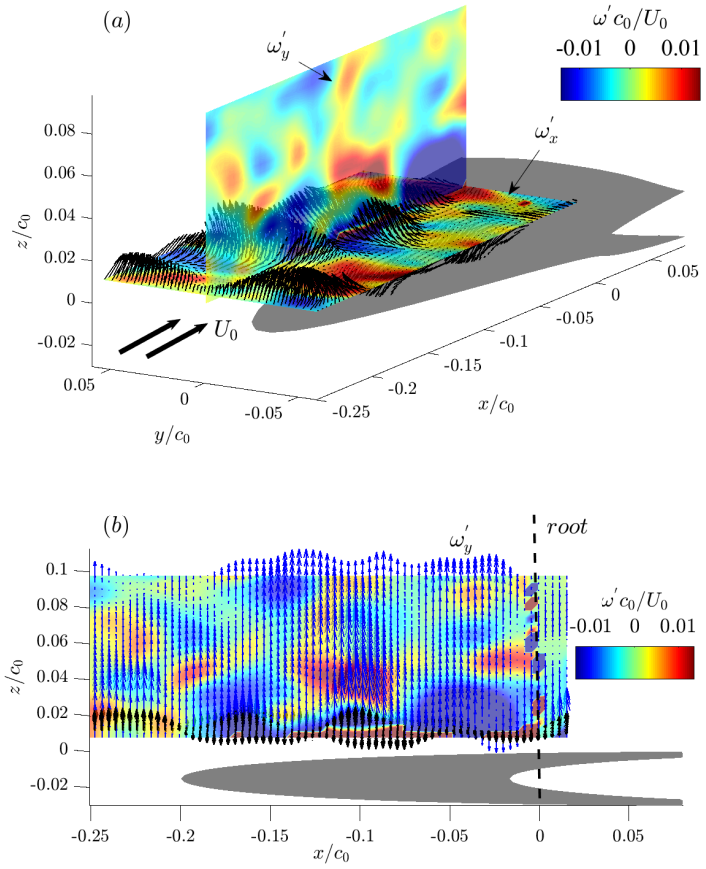

Figure 5.24: Contours of the dimensionless instantaneous vorticity $\omega_x' c_0/U_0$ and $\omega_y' c_0/U_0$ plotted in the horizontal and vertical planes respectively; (a) the horizontal plane is located at $z/c_0 = 0.02$ and (b) the vertical at $y/c_0 = 0$. The black vectors are computed for the v' and w' fluctuations, and the blue vectors for the w' component only.

This mechanism is better shown in Fig. 5.25-(a) where the two vortices are drawn on both sides of the tip closely to the wall. The plotted vectors right above the tip give the positive (red) and negative (blue) rotation at the streamwise direction. Similar vorticity rotation is observed also all along the tooth till the root. Of course, this is taken as an assumption as we can only see a perimeter section of this pair of vortices and not the whole structure. Under this consideration, this pair of vortices yields the generation of horseshoe-like vortex systems emanating from the WLE and be developing downstream the leading edge as described by Turner *et al.* [147] and Vemuri *et al.* [149]. Finally, at the root a pair of the nearby vortices creates an upwash or downwash depending on the upstream pair of vortices. Moreover, pressure evaluation can be estimated using Poisson equation but still the wall pressure information is missing, and that would give misleading results in terms of acoustic signature.

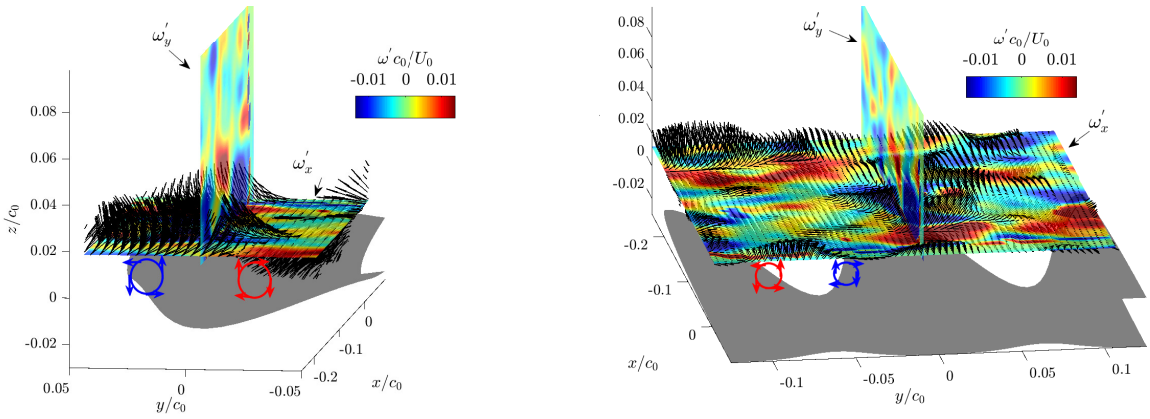

Figure 5.25: Same vorticity contours as in Fig. 5.24. The red and blue circles visualize the counter-rotating streamwise vortices (a) at the tip and (b) at the root (valley) of the tooth. The black vectors of the instantaneous velocity u' and w' show the flow rotation.

5.6.1 Concluding Remarks

Time-resolved tomographic PIV gives an insight into the three-dimensionality of the fluid in the vicinity of the leading edge. Velocity visualization and characterization of the flow motion around the teeth, attest with a first analysis previous observations [75, 32, 147] on the importance of the valley between the teeth as a source of noise generation. An increase of the vertical components of the mean velocity and the turbulent-intensity fluctuations found at the valleys explain this rapid change in direction and blockage of the flow reducing the norm of the velocity locally. Indeed, vertical disturbances are strongly linked with generation of sound according to Amiet's theory and assumptions. Similar flow topology was observed by Avallone *et al.* [17] in the case of trailing-edge serrations. The flow tends to move into the empty spaces between adjacent teeth and to accelerate at their tips. It was observed that the vertical velocity fluctuations at the root between the teeth are

greater than at the straight edge, even double as similarly indicated by Turner [147]. The features of the mean and instantaneous vorticity ω_x and ω_y have been estimated. Mean and instantaneous values agree with Turner's [147] observation on the creation of a pair of secondary vortices along the tooth. This leads to a horseshoe like vortex system downstream the serrations. Additional observation is that the vertical component at the tooth tip seems to be reduced compared to other points along the tooth, probably as a result of the contra-rotating motion of the ω_x and ω_y vorticity components. In the present study, mean and instantaneous values of all computed experimental configurations prove the validity of other similar existing numerical or experimental studies in the literature. Further investigations can be provided in the near future using the remaining part of the obtained experimental data base which is not yet post processed and interpreted. The database will be available for possible validation of numerical simulations.

6 Optimization Strategy for Minimizing the Total Airfoil Noise

Contents

Summary

The main objective in this chapter is to propose a shape optimization strategy in a quite basic context with main criterion the mitigation of the total airfoil noise. Despite the fact that the topic of interest in this thesis is the LEN investigations, the TEN has been also considered as part of this research. Analytical tools described in Section 4 are used to predict the LEN and the TEN for wavy and triangular shapes respectively. The aerodynamic efficiency is also considered a part of the objective functions by the factors C_L^{-1} and C_D. The proposed strategy includes also a description of the optimization algorithm and the numerical tool that are used.

6.1 Introduction

The need for optimal solutions in engineering is becoming more and more crucial in the name of cost and comfort. Therefore, the field of optimization is now an essential element of any brunch of engineering or other fields. In the field of aerodynamics and aeroacoustics, the shape of an airfoil characterizes dominantly its efficiency and its effectiveness by minimizing parameters such as drag and noise. The definition of such a problem can be characterized as a shape optimization problem.

As mentioned before in Section 3.6, the identification and extraction of TEN plays a crucial role for characterizing the LEN reduction behavior. The multiple use of different measurement techniques and noise prediction tools was the consequence of this exploration. Thus, the optimization plan is based on the research of an optimal solution that considers the airfoil as one component in terms of aeroacoustics. Conversely, recent studies focused on the optimization of the LE [23] or the TE [74] parts exclusively delivering a local shape optimization. Here, the definition 'local' describes the region of the applied optimization and not the 'global or local optimization' used for global or local gradient solutions, as described in the science of optimization. Depending the upstream flow conditions and the airfoil behavior, the local shape optimization could give also an optimized solution for the whole airfoil component. This is a function of different parameters depending the application.

This optimization study is part of a secondment taken place in the Parallel CFD & Optimization Unit of the School of Mechanical Engineering of the National Technical University of Athens (NTUA) in the context of the SmartAnswer ITN. Analytical tools for predicting the LE and TE noise as well as an in-house CFD solver have been used for creating a data base of noise predictions and extracting the required inputs respectively. The next sections describe the strategy that was followed and the tools used for this application.

6.2 Problem Definition

A NACA12 airfoil has been considered in this study. The results obtained for this airfoil during this thesis as well as its realistic behavior in terms of aerodynamics are the reasons for choosing it instead of a flat plate or another airfoil. A realistic application can require the inclusion of two criteria namely aerodynamics and acoustics. Therefore, considering an optimization problem, three objective functions are defined for minimization, the $min.C_L^{-1}$ (inverse lift coefficient), the $min.C_D$ (drag coefficient) and the $min.OASPL$ (overall noise emission). For the acoustic part, wavy LE and triangular TE serrations will be introduced in the NACA12 for minimizing the radiated noise. Before introducing the optimization algorithm and its use, a strategy of the estimation of the noise emissions as well as the aerodynamics will be described with a representative flowchart as in Fig. 6.1.

Initially, a set of combinations of the parameterized LE and TE serrations geometry will be defined with the design variables; serration depth h_{LE} and wavelength λ_{LE} as well as for

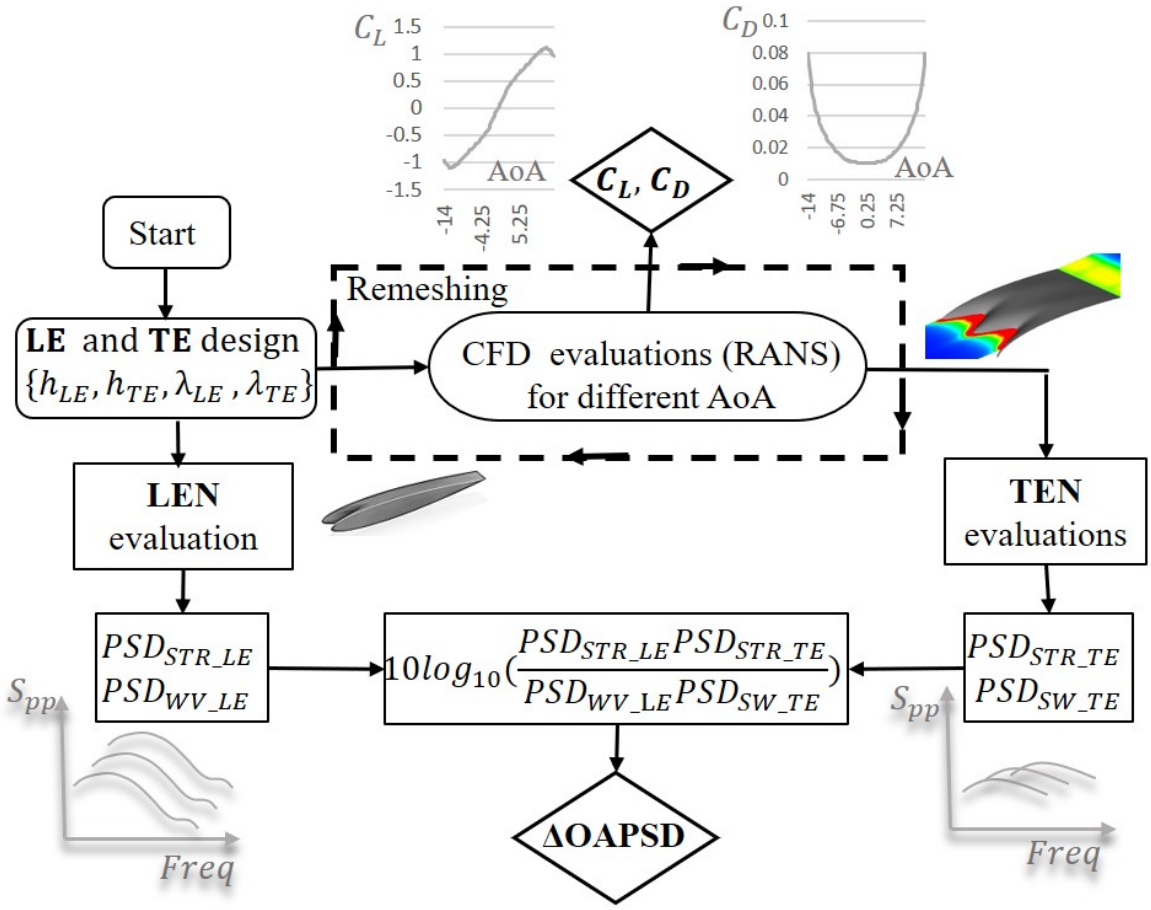

Figure 6.1: The flowchart that defines the objectives functions $OAPSD$, C_L and C_D with the use of analytical noise prediction tools and the CFD solver.

the sawtooth TE serrations, h_{TE}, λ_{TE}. For this set of design variables, the corresponding CFD evaluations are performed for different angles of attack. The required inputs for the TEN prediction will be extracted from the BL at the TE position. The prediction of the total airfoil noise and the corresponding reductions for each design variable is completed by a summation of the PSD stemming from both sources, LEN and TEN. Finally, the lift and drag coefficients are calculated after each simulation.

6.3 Serrated NACA12 Airfoil Designs

The geometry of the serrated NACA12 follows the same definition as in Section 3.7.1. The LE serrations are designed as an oscillatory function around the straight leading-edge line without changing the total airfoil lift area, while the TE serrations are added at the TE as an extention by increasing the chord as shown in Fig.6.2-(a). A different version of the TE serrations geometry could be to maintain the same mean chord and to design serrations like for the LE case. This design would imply vertical cuts in the trailing-

edge wedge, thus bluntness resulting into vortex shedding. Nevertheless, this bluntness could be partially smoothed by modifying the thickness of the airfoil as we did for the LE serrations. Finally, the version with the TE serrations extentions (Fig.6.2-(a)) is proposed for the present study. This design of TE serration is also proposed and it has been studied already by many researchers in the literature wind turbine applications.

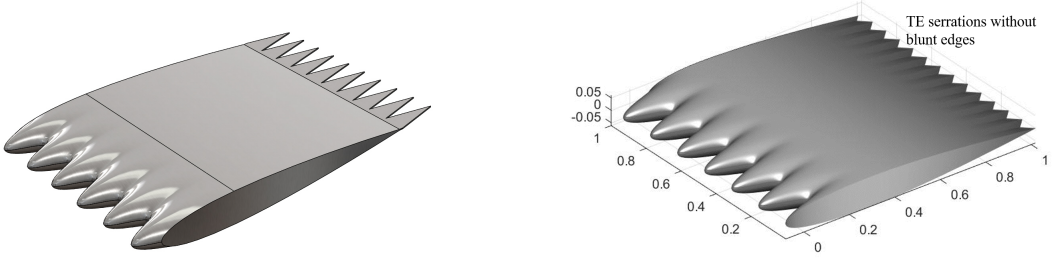

(a) (b)

Figure 6.2: NACA-0012 airfoils with wavy leading edge and triangular trailing-edge serrations as (a) an extension by increasing the airfoil chord and as (b) cuts on the TE maintaining the same averaged chord length.

6.4 Airfoil Noise Prediction Tools

Lyu & Ayton's model [88] for both LE and TE applications have been used for the noise predictions. This model has been already described in Section 4.2 for the leading edge application, thus here only the assumptions made for the model are repeated and further details are mentioned for the use of the trailing-edge model. Now, the coordinate system is transferred at the TE position setting the origin at the straight edge as shown in Fig. 6.3. The assumptions are summarized below:

- The airfoil is considered as a semi-infinite flat plate extended upstream the trailing edge.
- The turbulence is assumed to be frozen inside the boundary layer.
- The flat plate is placed in a uniform incoming flow at zero angle of attack and the hydrodynamic variables ($\tilde{\rho}$, $\tilde{U}$) are assumed constant. The effect of angle of attack will be indirectly accounted for by the associated increased boundary-layer thickness.
- The serrations are periodic in the spanwise direction with spanwise wavelength higher than the spanwise correlation length of the turbulent pressure fluctuations in the boundary layer.

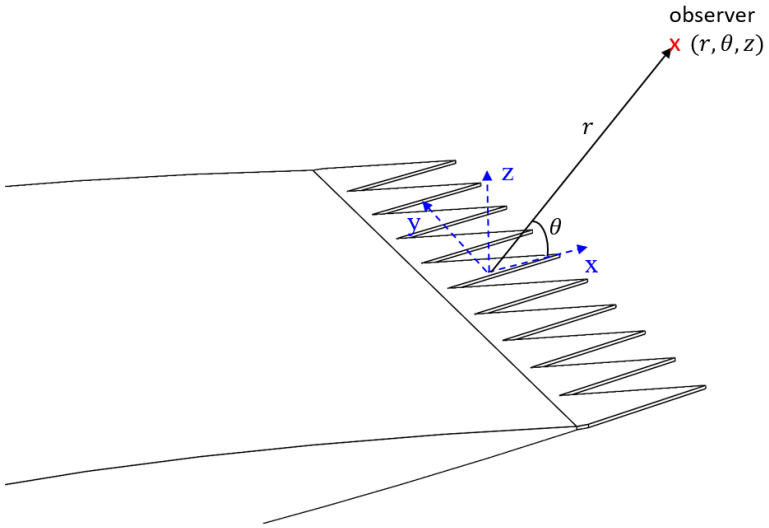

Figure 6.3: Schematic illustration of the axis origin for the trailing edge configuration.

The far-field sound PSD was calculated by making use of the simplified version of the S_{pp} expression with the simple sum of the cut-on modes and is given below:

$$\Psi(r,\theta,z) \sim \frac{\bar{k}}{2\pi r} sin^2\frac{\theta}{2} \frac{(\bar{k}_1+\bar{k})}{(\bar{k}_1-\bar{k}cos\theta)^2} \sum_{n=-\infty}^{\infty} \Pi_0(\omega,k_2)|E_n(-\bar{k}cos\theta)|^2 \tag{6.1}$$

where $k_1 = \omega/\gamma$ and $\bar{k}_1 = (k_1 + (kM - k_1M^2))/\beta$. γ is a constant with a typical value of ($\gamma \approx 0.7$). $\Pi_0(\omega,k_2) = \frac{1}{\pi}\phi_{pp}(\omega)\ell_y(k_2,\omega)$ denotes the wavenumber spectrum of the wall-pressure fluctuations beneath the turbulent boundary layer close to the trailing-edge. The other variables remain the same as for the leading-edge analytical model. Different models exist in the literature for predicting the wall pressure fluctuations such as Amiet [137], Chase-Howe [35, 69], Goody [59] and Rosenberg [131]. The accuracy of these models varies depending on the boundary layer information they use. For example, Rozenberg's model uses a mix of six variables inner and outer ($\delta, \delta^*, \theta_M, U_c, \tau_w, u_\tau$) providing better accuracy compared to Amiet's that uses two variables (δ^*, U_c). Three of the models are presented here and their application is compared in Section 6.4.1.

Schlinker and Amiet [137] proposed an empirical expression making use of the outer variables of a turbulent boundary layer measured by Willmart and Roos [152].

$$\frac{\Phi_{pp}(\omega)}{\rho^2\delta^* U_0^3} = 2.10^{-5}\frac{F(\tilde{\omega})}{2} \tag{6.2}$$

where δ^* is the boundary layer thickness displacement, $F(\tilde{\omega}) = (1 + \tilde{\omega}^2 + 0.217\tilde{\omega} +$

$0.00562\tilde{\omega}^4$) and $\tilde{\omega} \equiv \omega\delta^*/U_0$ with $0.1 \leq \tilde{\omega} \leq 20$.

Rozenberg [131] included the effect of an adverse pressure gradient at his model through Clauser's parameter β_C and Coles' wake velocity deficit parameter Π. The use of inner and outer parameters of the boundary layer leads to a more realistic prediction of the wall pressure spectrum where small and large scales of turbulence are taken into account. The model arised as an extension from Goody's model and is expressed as follows

$$\frac{\Phi_{pp}U_0}{\tau_{max}^2\delta^*} = \frac{\left[2.82\Delta^2(6.13\Delta^{-0.75}+F_1)^{A_1}\right]\left(4.2\dfrac{\Pi}{\Delta}+1\right)St^2}{[4.76St^{0.75}+F1]^{A_1}+(C_3'St)^{A_2}} \tag{6.3}$$

where $St = \omega\delta^*/U$ is the Strouhal number based on the displacement thickness and the parameters $A1$, $A2$, F_1, Δ, β_c, Π, C_3' are given below

$$A_1 = 3.7 + 1.5\beta_c, \qquad A_2 = \min\left(3.19/\sqrt{\mathrm{R_T}}\right) + 4 \approx 7, \qquad \mathrm{F_1} = 4.76\left(\frac{1.4}{\Delta}\right)^{0.75}[0.375\mathrm{A_1} - 1]$$

$$\Delta = \delta/\delta^*, \qquad \beta_C = (\delta^*/\tau_w)(dp/dx), \qquad \Pi = 0.8(\beta_c + 0.5)^{3/4}, \qquad C_3' = 8.8R_T^{-0.57}$$

The ratio of the outer to inner boundary layer time scale is $R_T = (\delta/U)/(\nu/u_\tau^2)$ and the friction velocity is given by $u_\tau = \sqrt{\tau_w/\rho}$ with τ_w the wall-shear stress and (dp/dx) the pressure gradient.

Chase-Howe's model [35, 69] makes use also of mixed boundary layer variables. It is proposed by Howe as an improvement from Chase's physical model

$$\frac{\Phi_{pp}(\omega)U_0}{\tau_w^2\delta^*} = \frac{2\tilde{\omega}^2}{(\tilde{\omega}^2+0.0144)^{3/2}} \tag{6.4}$$

The far-field noise prediction requires the use of the coherence length scale which is determined by Corcos' model as follows

$$\ell_y(k_2,\omega) = \frac{\omega/b_cU_c}{k_2^2+\omega^2/(b_cU_c)^2} \tag{6.5}$$

where $U_c = 0.7U_0$ is the convective velocity and $b = 1.47$ is a constant.

An important detail that was not mentioned in this section is the TIN prediction for the NACA12 airfoils. It is known that the aforementioned analytical models predict the noise for flat plates. Nevertheless, studies on the effect of airfoil thickness for the TIN prediction have been made as mentioned in Section 1.1.2. Roger & Moreau [125] proposed a correction that can be applied on the flat plate noise predictions estimates finally the noise reduction due to thickness effect. Based on previous findings on the reduction due

to thickness effect [100, 117, 107, 108], they concluded that this reduction is proportional to the relative thickness and inversely proportional to the flow speed and the ratio Λ/e. The suggested correction is given below

$$\Delta_{dB} \propto \frac{(e/c)}{(e/c)_{ref}} \frac{f}{U_0} \frac{(\Lambda/e)_{ref}}{(\Lambda/e)} \tag{6.6}$$

where e is the airfoil thickness and the index 'ref' stands for the NACA12 airfoil in Paterson & Amiet's [117] experiment taken as reference.

6.4.1 Models Application and Validation Experiments

In this section, the application of Lyu's & Ayton's model has been used for reconstructing the total airfoil noise. Comparisons have been made with the experimental data obtained in ECL for flat plates and thick airfoils. An example of the model validation is shown below where the spectra of serrated flat plate ($h/c_0 = 0.1$) are compared with Ayton's models for LE and TE serrations with a simple sum of PSD including also the ΔdB corrections for each case. For the TEN prediction, the wall pressure wavenumber spectrum has been modeled with Chase's model, the boundary layer thickness input is obtained from the HWA measurements, see Section 3.9. For LEN prediction, Pao's Gaussian high frequency correction has been applied in the von Kármán spectrum.

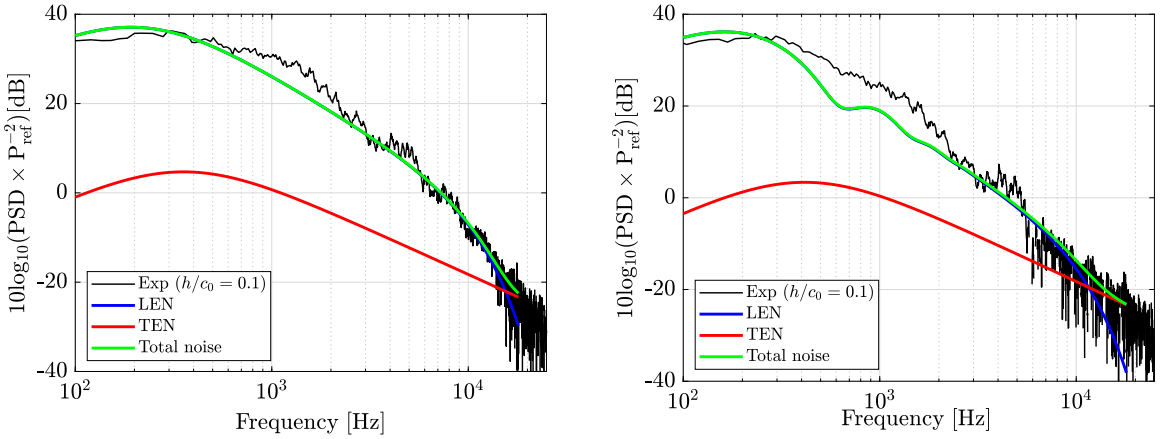

Figure 6.4: Predictions of LE and TE noise using Ayton's model and comparison with the (a) baseline and (b) serrated ($h/c_0 = 0.1$) flat plates.

The agreement of the total airfoil noise with the experiments in Fig. 6.4 for both flat plates is considered good enough for further use in an optimization study, for which realistic relative variations are more important than accurate absolute predictions. The summation of both noise sources captures the total noise for the frequencies at which the leading-edge model was validated successfully in Section 4.2. As already shown by the noise localization technique, the LEN prediction of Lyu & Ayton's model does not fit the real LEN performance beyond 5 kHz where the TEN contaminates the total noise, even if the leading-edge model seems to agree with it. Nevertheless, the noise level and the

general trend are captured successfully and differences with the baseline configuration can be reached for launching the optimization.

6.4.2 Validation of the Numerical Simulation Setup with the Experiments for the NACA-0012 Airfoil

The evaluation of the candidate solutions has been performed with the in-house GPU-enabled CFD solver **PUMA** (**P**arallel Flow-Solver, on **U**nstructured Grids, for **M**ulti-row Analysis & **A**djoint-based optimization) developed by the same group. The flow model consists of the RANS equations for compressible flow and the Spalart–Allmaras turbulence model. 3D models of an airfoil section embedded in a free-stream turbulent flow have been simulated. Specifically, the 3D configuration was conducted for the spanwise extension of one serration wavelength λ with periodic conditions applied at the span end planes. For the spatial discretization of Navier-Stokes and the turbulence model, the vertex–centered variant of the finite volume technique is used on unstructured meshes, consisting of tetrahedra, pyramids, prisms and hexahedra.

The free-stream velocity and the turbulent intensity at the position of the leading edge have been used for the initialization of the numerical simulation. These parameters are related to the turbulent kinetic energy $\bar{K}$ and the dissipation $\bar{\varepsilon}$ according to the following expressions [31].

$$u_{rms}^2 = \frac{2}{3}\bar{K}, \qquad \Lambda \simeq \frac{(2\bar{K}/3)^{3/2}}{\bar{\varepsilon}} \tag{6.7}$$

where $\bar{\varepsilon}$ is related to ω. Therefore, accounting for a free-stream velocity $U_0 = 19.66$ m/s and $u_{rms} = 1.02$ m/s at the leading edge position ($x = 100$ mm downstream the nozzle exit) according to the Fig. 2.9-(b), preliminary results have been obtained and compared to the HWA measurements. A good agreement has been found in both measured positions with the difference that the free-stream velocity at the wake location from the experiment was of 20 m/s and at the leading edge seems to increase locally at 21 m/s. In the simulations, the free-stream velocity was initialized at $U_0 = 19.66$ m/s. Nevertheless, the information we roughly need for estimating the boundary layer thickness or displacement thickness comes to a good agreement with the experiments at the wake position. From this point, few numerical tries could be a lunched for achieving a better 'tuning' of the simulations.

Contours of the mean velocity components (Fig. 6.5) for both NACA12 cases support the validation procedure compared to the PIV results for the flat plates. The vertical to the airfoil velocity component has been presented in two vertical planes (Fig. 6.6). The flow patterns look similar to the serrated flat plate case in Fig. 5.7-d; the positions of the maximum amplitude are located at the valleys while a gradual decrease is evidenced from the peak to the root of the teeth. The only difference is the amplitude that is doubled for the NACA12 compared to the flat plate. RANS simulations give a twofold information in this study, the validation part and a further exploration for the parts that cannot be captured by the PIV measurements.

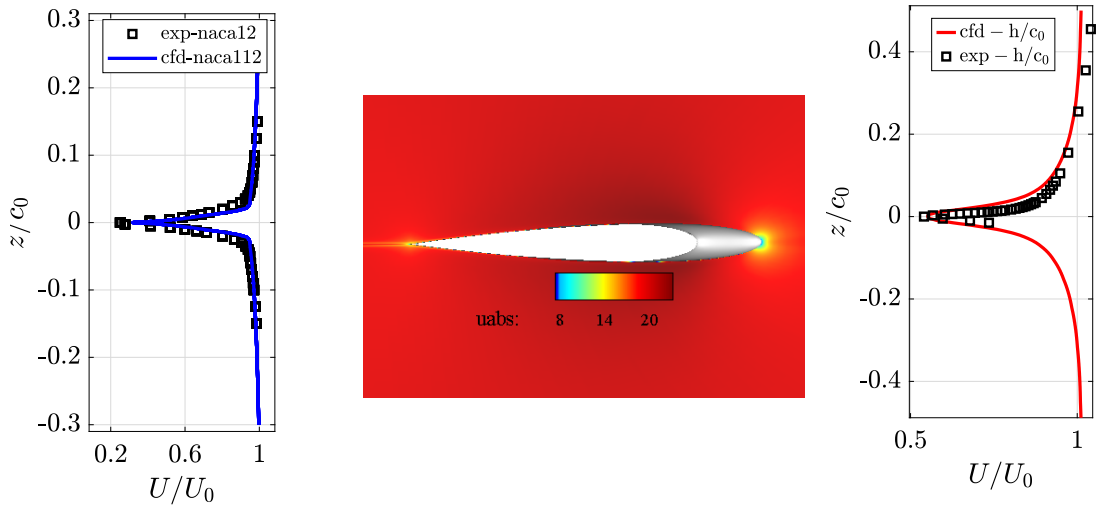

(a) (b)

Figure 6.5: Validation of preliminary RANS computations: the streamwise velocity profile obtained (a) at the near wake of the NACA12 airfoil and (b) in the vicinity of the peak of the leading-edge serrations. The free-stream velocities for each configuration are (a) $U_0 = 20.1$ m/s and (b) $U_0 = 19.5$ m/s.

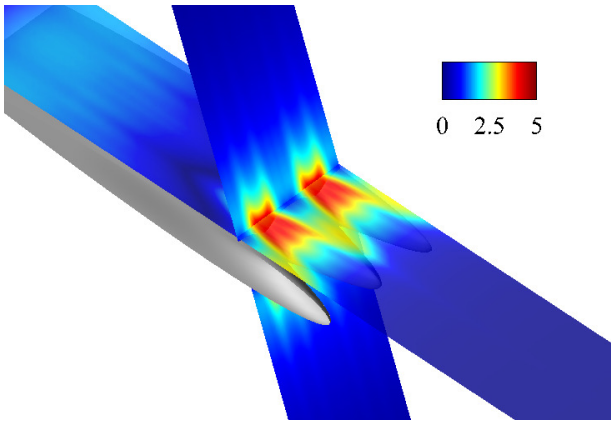

Figure 6.6: Volume slices of the vertical velocity component W of the serrated NACA12. The horizontal plane is located 1 mm above the airfoil surface and the vertical plane at the serration valley. The flow is from bottom right to up left and $U_0 = 20$ m/s.

6.5 Optimization Strategy

A basic representative of stochastic optimization methods that has been chosen for this study is the **evolutionary algorithms** (EA). Its stohastic evolution mechanisms are based on Darwin's theory of evolution.

The definition of an optimization problem is determined with M_0 objective functions to be minimized or maximized, expressed by the objective function vector $\vec{f}$, and M_c constraints ($\vec{c}$) as follows:

$$\begin{aligned} min\vec{f}(\vec{b}) &= (f_1(\vec{b}), ..., f_{M_0}(\vec{b})) \in \mathbb{R}^{M_0} \\ \text{subject to } & \mathrm{c_k}(\tilde{\mathrm{b}}) \leq 0, \mathrm{k} = 1, \mathrm{M_c} \end{aligned} \tag{6.8}$$

where $\vec{b} \in \mathbb{R}^N$ is the vector of design variables with N the number of the design variables. Here, the optimization problem is expressed as a MOO (Multi-Objective Optimization) minimization problem exploited with Pareto dominance technique [156]. A schematic representation of a Pareto front of two objective functions f_1, f_2 corresponding to the $OASPL$ and the C_d is given as an example in Fig 6.7. Individual $\vec{b}_1$ located on the Pareto front dominates all individuals inside the grey area. Multiple Pareto fronts exist in a MOO problem providing different solutions with different optimality.

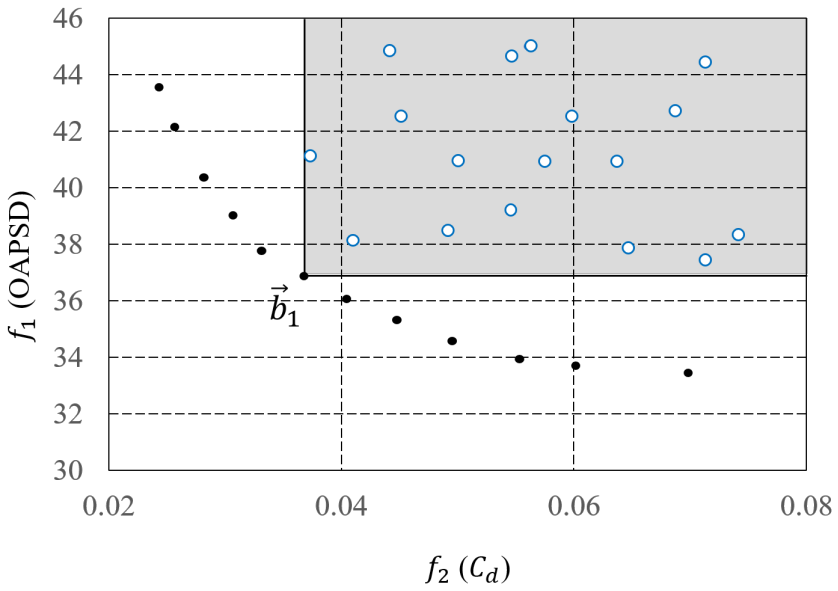

Figure 6.7: Pareto front of a two-objective minimization problem with objective functions f_1, f_2 corresponding to the OAPSD and the Cd. The Pareto optimal individual $\vec{b}_1$ dominates to all individuals (candidate solutions) enclosed in the grey area.

As already discussed in Section 6.2, three objective functions and five design variables are defined for this minimization problem. The PSD will be estimated analytically according to Section 6.4 at all the radiation angles θ in the mid-span plane and finally the minimization of the objective function f_1 can be expressed by a single value in $OAPWL$. The statement of the minimization problem is given below

Find $\mathbf{x} = \{h_{LE}, \lambda_{LE}, h_{TE}, \lambda_{TE}\}$ which minimizes $\boldsymbol{f} = \{OAPWL, C_L^{-1}, C_D\}$

subject to constrains

$$
\begin{aligned}
0 \leq h_{LE} &\leq 0.12c_0 \\
0.5\Lambda \leq \lambda_{LE} &\leq 5\Lambda \\
0 \leq h_{TE} &\leq 0.25c_0 \\
0.08d \leq \lambda_{TE} &\leq 0.5d \\
0^\circ \leq i &\leq 8^\circ
\end{aligned}
\tag{6.9}
$$

to recall that d is the half span, i the angle of attack, c_0 the mean chord and Λ the turbulence integral length scale.

The upper limit of the leading-edge parameters is related to realistic installation, such as space and/or lift requirements. It is obvious that, an airfoil with too long serrations looses its functionality as a lifting surface. Considering the ratio between serration wavelength and turbulence length scale $\lambda_{LE} \approx 4\Lambda$ where noise reduction is maximized [32], the upper limit of λ_{LE} was set a bit higher. For the trailing edge, the upper limits for both parameters were chosen equal to 25% of the chord and the span respectively for being applicable under a realistic scope. The lower limit for the wavelength was decided to be reduced for converging reasons due to very large wavenumbers. The maximum value of the angle of attack was limited to 8° beyond which a reversed cross-flow occurs at the valleys of the TE serrations. A similar criterion has been also considered for the LE serrations for avoiding flow separation close to stall conditions. Regarding the leading-edge noise predictions, the angle of attack does not affect the noise generation significantly according to previous studies. Therefore, no restriction has been imposed for the noise predictions in terms of angle of attack even if the use of the models corresponds to applications with small angles of attack.

The optimization is planned to be launched in an in-house software developed by the PCOpt/NTUA, called **EASY** [72, 70, 53]. It is a generic optimization platform which provides many different optimization algorithms, it includes MAEAs (Metamodel Assisted Evolutionary Algorithms) with different metamodel types and other methods that enhance evolutionary algorithms such as distributed, asynchronous and hierarchical EAs. The reader can find a description of the platform and details of the supported algorithms in Kapsoulis' PhD thesis [71].

6.5.1 Concluding Remarks

The biggest advantages that noise prediction tools provide are the rapid and cheap results. Therefore, their use can be significant for being involved in an iterative procedure like an optimization. In this chapter, an optimization strategy has been proposed to search for optimal solutions in terms of acoustics and aerodynamics. Leading and trailing-edge serrations have been considered for minimizing both sound sources. Lyu & Ayton's model for the trailing edge application has been also described and validated with the present experiments. The optimization plan is based on an evolutionary algorithm using three

objective functions, five constraints and applied on the modified NACA12 airfoil. Two validation simulations (RANS) on a NACA12 baseline and a serrated NACA12 show good agreement with the experimental data. Therefore, the proposed optimization is ready to be operated in the near future. It must be noted that the present study was the matter of a secondment at NTUA in the SmartAnswer project. Application of the optimization strategy would require time-consuming computations which are not compatible with the thesis program. This will be the matter for future work.

7 Turbulence-Impingement Noise of a NACA-12 Airfoil with Porous Inclusions

Contents

Summary

This section reports on experimental investigations on a NACA-0012 airfoil implemented with porous inclusions, embedded in a turbulent flow. The study is aimed at assessing the effect of porosity on turbulence-impingement noise at the leading edge. In order to avoid cross-flow from pressure side to suction side and therefore preserve aerodynamic performances, the airfoil structure includes a rigid skeleton with a center plate, filled with porous material. A smooth surface is ensured by covering the assembly with a wiremesh. Far-field acoustic measurements and near-field microphone-array post-processing are used as complementary techniques to characterize unambiguously the noise reductions in the low-to-medium and medium-to-high frequency ranges, respectively. Wake-velocity profiles are measured to estimate the aerodynamic losses. The observed noise reductions vary between 4 and 6 dB. This makes porosity a promising technique for the noise mitigation of thick airfoils, with potentiality similar to that of leading-edge serrations for fans and other industrial applications.

7.1 Introduction

Regarding the application of porous treatment of airframes surfaces as a noise mitigation strategy, limited studies have been conducted till the now. Hayden and Chanaud [63] proposed foil structures with sound attenuation characteristics, reporting on a considerable reduction of sound power levels for a specific model of airfoil. Experimental studies by Chanaud [33] and Revell *et al.* [120] evidenced significant reductions of fan noise by porous treatments on the blades. Geyer *et al* [50, 52] and Sarradj & Geyer [135, 136] addressed many aspects of porous airfoils, including boundary-layer effects and trailing-edge noise generation/reduction. Their experimental results showed that the overall sound pressure level decreases in the order of a few decibel, but at lower frequencies the reduction is considerable larger and extends 10 dB in some cases. Roger *et al.* [128] also studied TIN reduction by porous treatments, both analytically and experimentally. The modelling based on a panel method combined with a locally-reacting impedance model and the baseline airfoil used for both studies was NACA 0012. The tested porous modification showed a sound reduction up to 5 dB, over a specific range of high frequencies. Also, they described a step-by-step procedure of quantification of the benefit of the reduction techniques by subtracting background and trailing-edge sources.

7.2 Background

The Blade-Vortex-Interaction (BVI) noise radiated from helicopter blades on the present of a porous treatment on the leading edge of an airfoil is studied numerically by Lee [82]. A high-order upwind-biased scheme with a multi-zonal grid system are used to solve unsteady thin-layer Navier-Stokes equations and a turbulent model named Baldwin-Lomax

was modified for considering the transpiration on the surface. The study is focused on velocity and pressure distributions indicating that the leading-edge permeability can cause a destructive effect on the pressure fluctuations locally during BVI reducing the radiating noise strength by $20-30$ % at the vicinity. According to the porous version, the stagnation point appeared to be nearly weaker and increased values of pressure were appeared after the 2 % of the chord compare to the rigid case. He concluded that the strength suppression of the pressure variations at the leading-edge happens because of the mass and momentum exchanges through the surface during the vortex impingement time. That results to weaker in amplitude acoustic waves with the application of the porosity.

Hayden and Chanaud [63] proposed a variety of sound absorbing foil structures (Fig. 7.6-(a)) implemented in fluid flow systems preventing the sound generation as a source by minimizing the flow surface forces at the vicinity. He delivered drawings indicating mock-ups with portions of different degrees of porosity modifying the surface impedance according to the upstream flow conditions. Experimental studies by Chanaud & Muster [34] and Revel [120] *et al.* on the porosity treatment both in stationary and rotating blades have shown significant noise reduction after a proper installation.

Roger *et al.* [128] [126] studied experimentally the TIN using a NACA 0012 profile treated by porous media (Fig. 7.6-(d)). An empirical designed structure with porous cells maintained by a wire-mesh cloth has been tested on acoustics efficiency. The proposed structure goals to dissipate progressively the kinetic energy of the vorticity combining a proper penetration of the flow ensuring a smooth flow path and diffuse efficiently viscous effect in small scales. The porous airfoil mounted in a turbulent flow generated by a grid reached 5 dB noise reductions. The acoustic efficiency is also compared with a serrated NACA 0012 profile where the corresponding noise reduction were up to 10 dB. The effect of the porous airfoil surface has been studied also analytically investigating partially the underlying mechanisms. The response of the porous airfoil is modeled and described by the panel method solving the Laplace equation considering incompressible flow and small perturbation assumption. Non-penetration and impedance boundary conditions have been imposed in the panel method for a porous and a baseline case respectively. The validity of panel method in far-field noise prediction is tested with Amiet's theory for the baseline with an accuracy of 1 dB. The impedance used in the method is defined by the Extended Helmholtz Resonator model, providing an insight into the effect of the impedance curve.

Geyer and Sarradj [50] [52] [135] [136] studied porous airfoils in terms of noise generation/reduction and aerodynamic efficiency in present of clean flow conditions. Five porous airfoils type SD 7003 made by different materials (Fig.7.6-(b)) are measured against a baseline with non-permeable surface. In both studies, the influence characterization of porous material parameters (mainly flow resistivity and porosity) on the modification of the boundary layer characteristics, the aerodynamic performance and the trailing-edge sound were the main objectives. Their work were experimental, they performed acoustic measurements in the far-field using noise localization technique with different beamforming algorithms. Regarding the flow measurements, hot-wire anemometry characterized the flow parameters, like velocity profiles, turbulence intensity, boundary layer thickness and

displacement and wake deficit. The general conclusion is that the porous airfoils present an inferior aerodynamic performance compare to the corresponding baselines (non-porous) and usually significant noise reductions depending the porous material parameters. Precisely, the majority of tested porous airfoils reduced the radiated trailing-edge noise over a large frequency range whereas they increase both the boundary layer thickness and the displacement thickness compare to the non-porous airfoil. In addition, the boundary layer thickness is increased inversely with decreasing the flow resistivities of the porous medium. A difference of the boundary layer thickness between the suction and pressure side is observed and it is possibly resulting by a cross-flow through the porous media. Despite the fact that the porous airfoils had an increased trailing-edge thickness, the trailing-edge noise generated by the bluntness edge, it was not sufficiently detected as a spectral peak predicted by the BPM-model.

After an extensive experimental work by the aforementioned authors, the produced data base was used to build empirical models with symbolic regression analysis that describe the noise generation at porous airfoils [136]. The main objective was to find a well suited relationship between the dependent variable (sound pressure) and a number of independent variables (flow velocity, frequency, airfoil geometry etc.) that expresses turbulence impingement noise and the trailing-edge noise generation. Performing a dimensional analysis, models of different complexity were proposed in function of non-dimensional variables. For the trailing-edge noise, they found a dependency of the sound power on the fifth power of the flow speed and the spectrum is governed by the flow resistivity from the porous medium. Regarding the leading-edge noise power, it is proportional to the square of the turbulence intensity on the fifth to sixth power of the flow speed and the frequency spectrum is driven by the turbulence integral length scale and the flow resistivity.

Recently, Zamponi *et al.* [155] explored the effect of porosity on TIN reduction. This work includes a rod-airfoil configuration and a rigid perforated skeleton of a NACA-0024 profile equipped with melamine foam and covered with a wiremesh (Fig. 7.6-(c)). A recessed edge center plate allows to investigate the compressibility effect of the turbulence impingement on the leading edge and the blockage of the flow between the pressure and the suction side. Hot-wire anemometry and large-eddy simulations results have shown that the proposed porous design allows for a damping of the velocity fluctuations attenuating the upwash component of the root-mean-square of the velocity fluctuations compared to the solid one. It has been also shown that the porosity has an effect mainly on the low-frequency range of the turbulent velocity power spectrum which is also in line with the results of the acoustic beamforming measurements. Zamponi *et al.* [154] has also developed an algorithm based on Rapid Distortion Theory (RDT) modeling the porous treatment as an impedance boundary condition accounting for the Darcy's flow within the body. The model has been validated firstly on a simple case of an impermeable cylinder embedded into a turbulent flow and secondly on their NACA-24 configuration. The results have shown good agreement demonstrating that the present methodology can improve the understanding of the physical mechanisms and be instrumental in designing such passive noise mitigation treatments.

Different porous technologies have been proposed in the literature for mitigating TIN. Some of them are shown below.

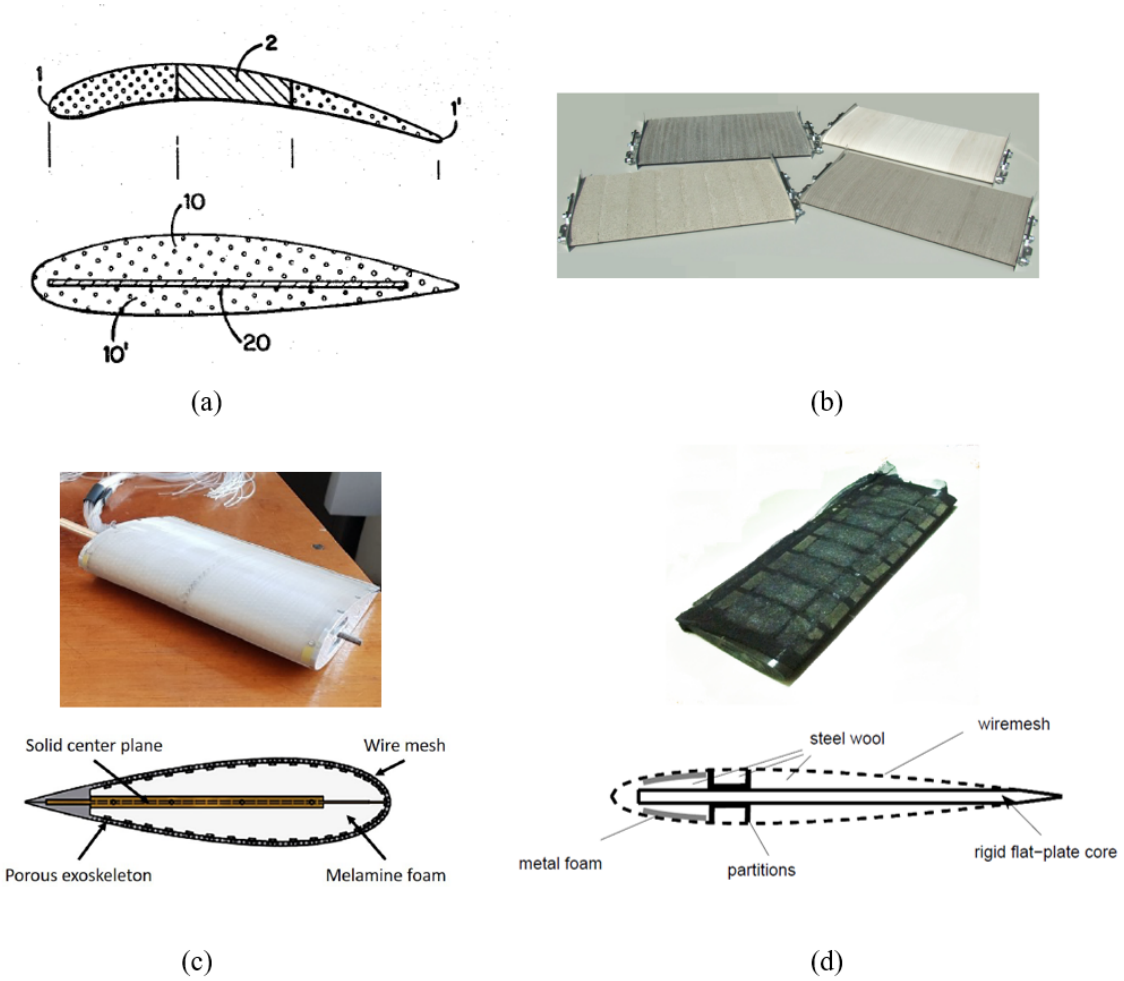

Figure 7.1: Porous airfoils from literature: (a) Hayden and Chanaud [63], (b) Geyer *et al.* [50], (c) Zamponi *et al.* [155, 144], (d) Roger *et al.* [128, 126]

7.2.1 Airfoils Manufacturing

Reducing TIN by means of porosity only makes sense for thick enough airfoils. Therefore the NACA-0012 airfoil has been selected in this part for its well-documented literature. Furthermore the 12% relative thickness is a reasonable order of magnitude of what could be found in some low-speed fan applications. Three different mock-up versions with porous inclusions have been manufactured for investigating the effect on turbulence impingement noise. The structural design of these mock-ups access both to aerodynamic and acoustic investigations. The first two mockups only differ by the extent of the center plate of the skeleton. Indeed the structure of a porous airfoil at leading edge is probably a key factor for TIN reduction. For the version (V1) the plate extends to the very leading edge,

whereas its edge is recessed by 5 mm for the version (V2). The gap is filled with the porous material in the latter. It nearly corresponds to half the turbulence integral length scale of the incident turbulence. The version (V3) has a larger number of smaller grid-structure cells. Its design is motivated by the need to approach the true NACA-0012 airfoil shape as close as possible and to reduce the cloth deformations caused by the pressure gradients over the airfoil surface. Such deformations have been noticed with the other two versions, leading to some deterioration of the aerodynamic performances, essentially in terms of wake thickness and associated losses, as discussed in section 7.5. The skeletons have been manufactured by a 3D printer. The NACA-0012 shape is reproduced by a 3D grid structure of maximum open cell area 8.75 cm^2 and the maximum depth of the hollow volumes is of 5 mm. These volumes are filled with a porous material (Fig. 7.2-(c)) partly maintained by the grid structure. Rigid spanwise stiffeners partition the volume. Apart from mechanical stiffness considerations, they are expected to avoid undesired streamwise mean flow inside the airfoil. Finally, a wiremesh metal cloth of 0.21 mm thickness and of porosity 41 (Ref. 101077) is wrapped and tightened around the airfoil, and sewed on the skeleton, as shown in Fig. 7.2-(d). This ensures the smoothness of the surface and the recovery of the NACA-0012 cross-section profile.

The metal cloth is expected to allow the unsteady flow to partially penetrate inside the material, so that porosity can act for sound absorption or for reduction of the compressibility effect. Complicated mechanisms are believed to take place, on which the inner porosity can act. The main expected one for TIN reduction is the progressive dissipation of the incident kinetic energy in the porous volume, mostly related to the leading edge area. Yet other effects must be kept in mind when interpreting the results. Firstly, the boundary layers developing over the porous airfoil *a priori* differ from those over the baseline airfoil in the same general flow conditions. As a consequence the sources of trailing-edge noise are modified. Secondly, the porous airfoil surface acts as a liner and absorbs sounds of any kind. This includes not only TIN and TEN but also the background noise of the installation and the noise possibly generated by the boundary layers developing over the porous wall. Elucidating the role of these phenomena is a challenging task that this work is aimed at studying partially.

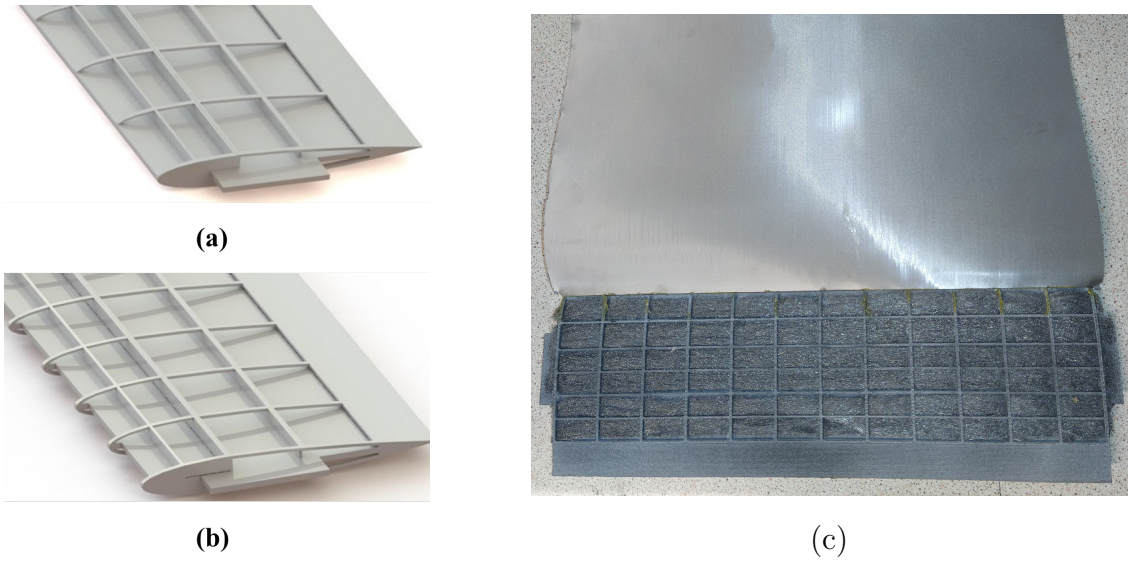

(a)

(b)

(c)

Figure 7.2: Structures of the NACA-0012 airfoils for porosity implementation. Skeletons with full-chord (a) (V1) and recessed edge (b) center plate (V2). (c): porous airfoil (V3) before wrapping by the wiremesh cloth.

7.3 Acoustic Impedance Measurements

Two candidate materials have been selected for the present application, namely melamine foam and metal wool. Melamine foam is an absorbing material of high efficiency and is applied in various acoustic treatments. Metal wool is mostly used in engineering applications where humidity, dust and disturbed flows are present. The absorption coefficient and the acoustic impedance of all samples have been measured with a Kundt's tube according to the two-microphone transfer-function method fully described in ISO 10534-2 and ASTM E 1050. The tube is the Bruel & Kjaer Standing Wave Apparatus Type 4206 [3] for the frequency ranges 50 Hz - 1.6 kHz (large tube) and 500 Hz - 6.4 kHz (small tube), shown in Fig. 7.3. The samples were placed inside a sample holder representative of the porous-airfoil structure. The thickness of each sample is 5 mm and the diameters are 29 and 100 mm. The melamine foam has been tested with and without the wiremesh surface. The final measured samples are made of the supporting structure, the porous material and the wiremesh. Pictures of the samples are shown in Fig. 7.4. The measured absorption coefficients are shown in Fig. 7.5.

The absorption coefficient of a sample of porous material depends on whether it is tested with or without its skeleton structure. It is also strongly modified when the sample is covered by a wiremesh. This is confirmed for the melamine by inspection of Fig. 7.5-(a). Despite its intrinsic high absorption, the melamine foam of 5 mm thickness is poorly efficient. Nevertheless, the absorption coefficient α is doubled after including the structure and the wiremesh. Similar behavior is observed for the metal wool sample, Fig. 7.5-(b). Finally, Fig. 7.5-(b) also indicates that both materials have similar overall performances and are good candidates for the present application.

Though the acoustic effect of a porous treatment might differ from its effect on im-

(a) (b)

Figure 7.3: Setup images of (a) Kundt's large tube of 100 mm diameter, (b) small tube of 29 mm diameter [3].

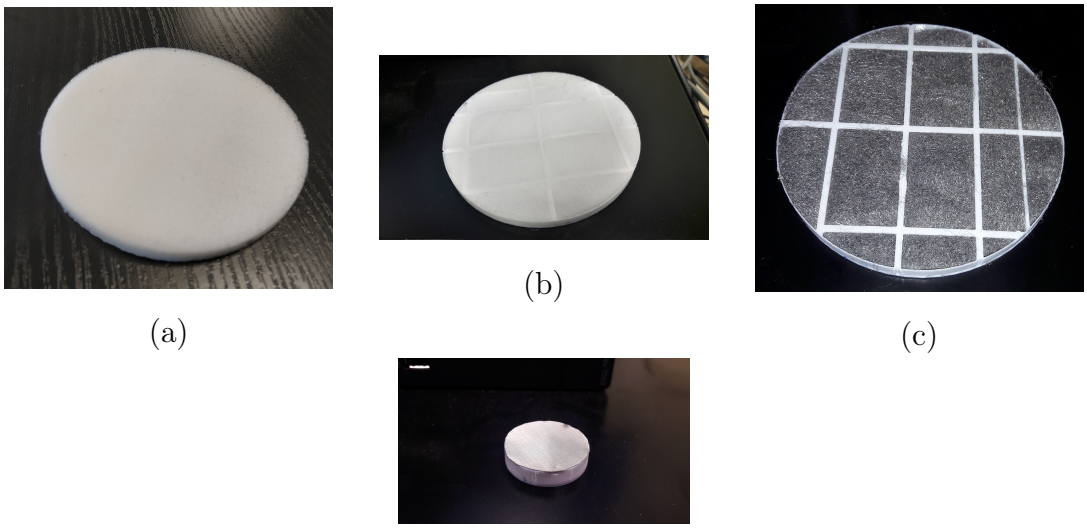

(a) (b) (c)

(d)

Figure 7.4: Pictures of tested samples;(a): melamine foam of 5 mm thickness, (b): melamine foam in the larger frame (for low-frequencies), (c): metal wool in the larger frame, (d): full sample with wiremesh in smaller frame (for high frequencies).

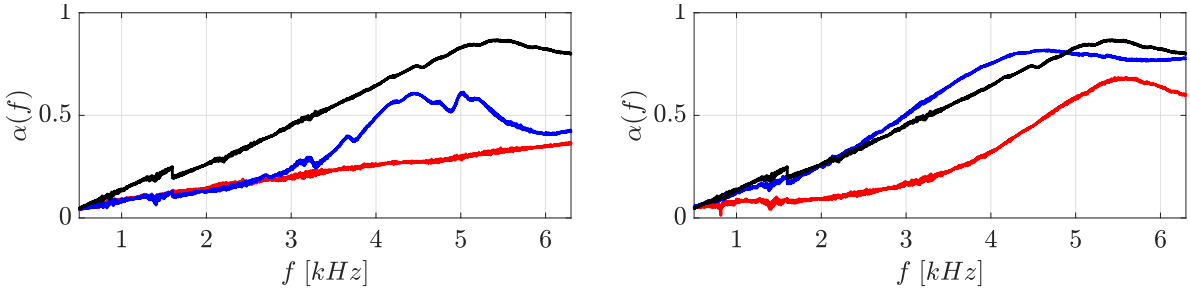

(a) (b)

Figure 7.5: Absorption coefficients of melamine foam and metal wool samples of 5 mm thickness; (a): melamine foam (−−), melamine foam with frame (−−), melamine foam with frame and wiremesh (−−); (b): metal wool with frame (−−), metal wool with frame and wiremesh (−−) and melamine foam with frame and wiremesh (−−).

pinging vortical disturbances, it is guessed that efficient sound absorption in Kundt's tube is a clue of efficient TIN reduction.

7.4 Main Acoustic Results

7.4.1 Far-Field Estimates of TIN Reduction

Noise reductions achieved for all modified airfoils as estimated from far-field measurements give an overview of their acoustic benefits. A comparison of the sound-pressure PSD (Power Spectral Densities) of the baseline and porous airfoils (V1) and (V2) filled with melamine foam is presented in Fig. 7.6-(a). The associated noise-reduction spectra obtained by subtraction in decibels are plotted in Fig. 7.6-(b). The maximum reduction is obtained as about 8 dB for the version (V2) with the recessed edge, whereas the version (V1) with the full-chord center plate achieves a maximum noise reduction of 4 dB only. This confirms that the mechanism of TIN reduction operates essentially in the leading-edge area, and that it requires a full porosity there for maximum effectiveness. A possible concern is that the recessed edge could be detrimental to the lift at non-zero angle of attack, because of the expected induced cross-flow. This point could be the matter for further investigation. The noise reduction is observed beyond 1 kHz and extends up to very high frequencies for the recessed-edge case. It is worth mentioning that the highest noise reduction is achieved between 5 and 6 kHz where the absorption coefficient of the full structure of the melamine foam is maximum in view of Fig. 7.5. However, the reduction is hard to observe in this range because TIN gets lower than the combined TEN and background noise. Furthermore, in view of the quite high-frequency range of observed noise reduction, part of the performance is attributable to the reduction of TEN generation and/or radiation.

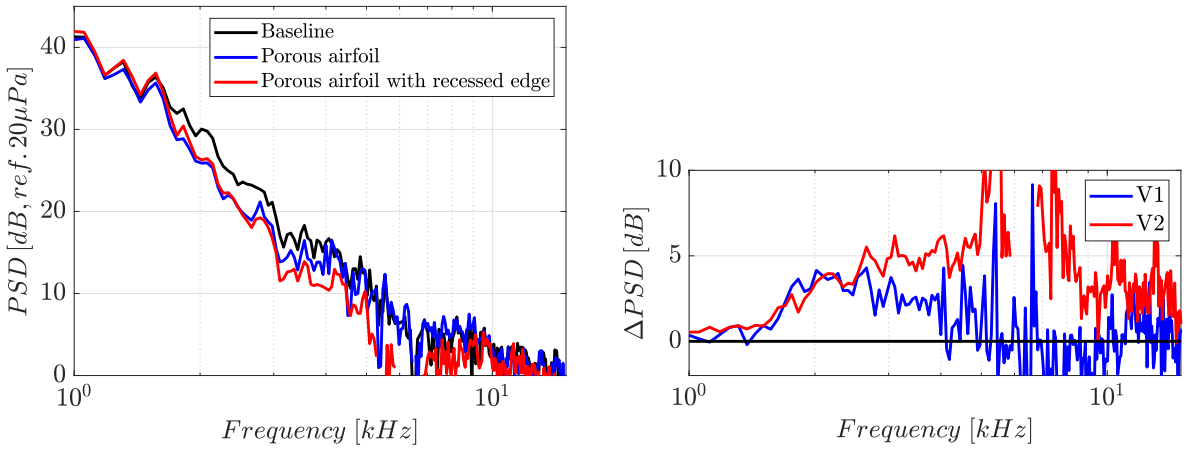

(a) (b)

Figure 7.6: (a): far-field sound spectra at 90° in the mid-span plane. Baseline NACA-0012 (black), porous airfoil (V1) with full-chord plate (blue), porous airfoil (V2) with recessed-edge plate (red). (b) Associated noise-reduction spectra.

7.4.2 Source Localization and Extraction

The far-field microphone measurements presented in section 7.4.1 involve contamination of the higher-frequency range by trailing-edge noise and background noise. A microphone-array technique is used in the present section to extract and separate leading edge and trailing-edge associated sources, for a better assessment of the noise reductions achieved by porosity. A conventional beamforming (CBF) algorithm named CIRA initially developed by ONERA [118] and operated by LMS software is used the recorded sound data. The sound is measured by a spiral Antenna with 81 MEMs microphones placed in a vertical plane parallel to the airfoil at a distance of 0.6 m (black star-shape structure in Fig. 2.3). A detailed description of the algorithm and its applications is given by Bampanis *et al.* [27] and Yakhina *et al.* [153]. The twofold advantage of this technique is the identification of the sources of interest and the extraction of their sound power levels, mainly in a high frequency range where the sources are uncorrelated.

Colormaps in Fig. 7.7-left and Fig. 7.7-right localize efficiently the leading- and trailing-edge noise sources of the baseline airfoil and of the porous airfoil (V2), respectively, for different frequency ranges. Considering a compactness limit of $kc \sim 1$, the two sources can be separated in the range $3-4$ kHz ($kc = 2\pi$), Fig. 7.7-(b), and above. A general observation of these sound power maps is that the source power of leading-edge noise is reduced (when not negligible) for all frequency ranges above 3 kHz. The source power of trailing-edge noise is still dominant beyond 4 kHz. It is also reduced at the highest frequencies. The connection between the structural modifications and their acoustic signatures is supported by the measured absorption coefficient of the melamine foam, Fig. 7.5-(b), indicating an efficient reduction between 5 and 6 kHz. A significant background noise source distribution is localized at the nozzle lips, in all frequency ranges.

The relevant estimate of power-level spectra for each source and its extraction are performed by defining rectangular integration windows on the areas of interest, as shown in Fig. 7.7-(c). The corresponding spectra of leading-edge and trailing-edge sources are shown in Fig. 7.8-(a) for the baseline NACA-0012 and in Fig. 7.8-(b) for the porous airfoil. The total integrated sound power spectrum including the background noise contribution is plotted in black. The leading-edge sound power is plotted in red and that of the trailing-edge in blue, with the aforementioned definition of the rectangular boxes (Fig. 7.7-(c)). This excludes noise sources at the airfoil-support junctions, considered as part of the background noise. The large difference in sound power levels between the total noise and the sum of both TEN and TIN sources confirms the importance of the background noise.

The reduction induced by porosity, again defined by spectral differences in decibels, is plotted in Fig. 7.8-(c). Despite the fact that the reduction of both sources seems promising, in partially overlapping frequency intervals, the total noise reduction only reaches up to $4-5$ dB for medium-range frequencies ($2-3$ kHz) and $1-2$ dB for higher frequencies. Though its estimate exhibits large scatter, the TIN reduction seems to increase with frequency between 1 kHz and 4 kHz. It drops at the highest frequencies. This can be explained by the high-frequency TIN reduction due to the thickness effect, already involved in the response of the baseline airfoil. Unlike what has been found for serrations on thin

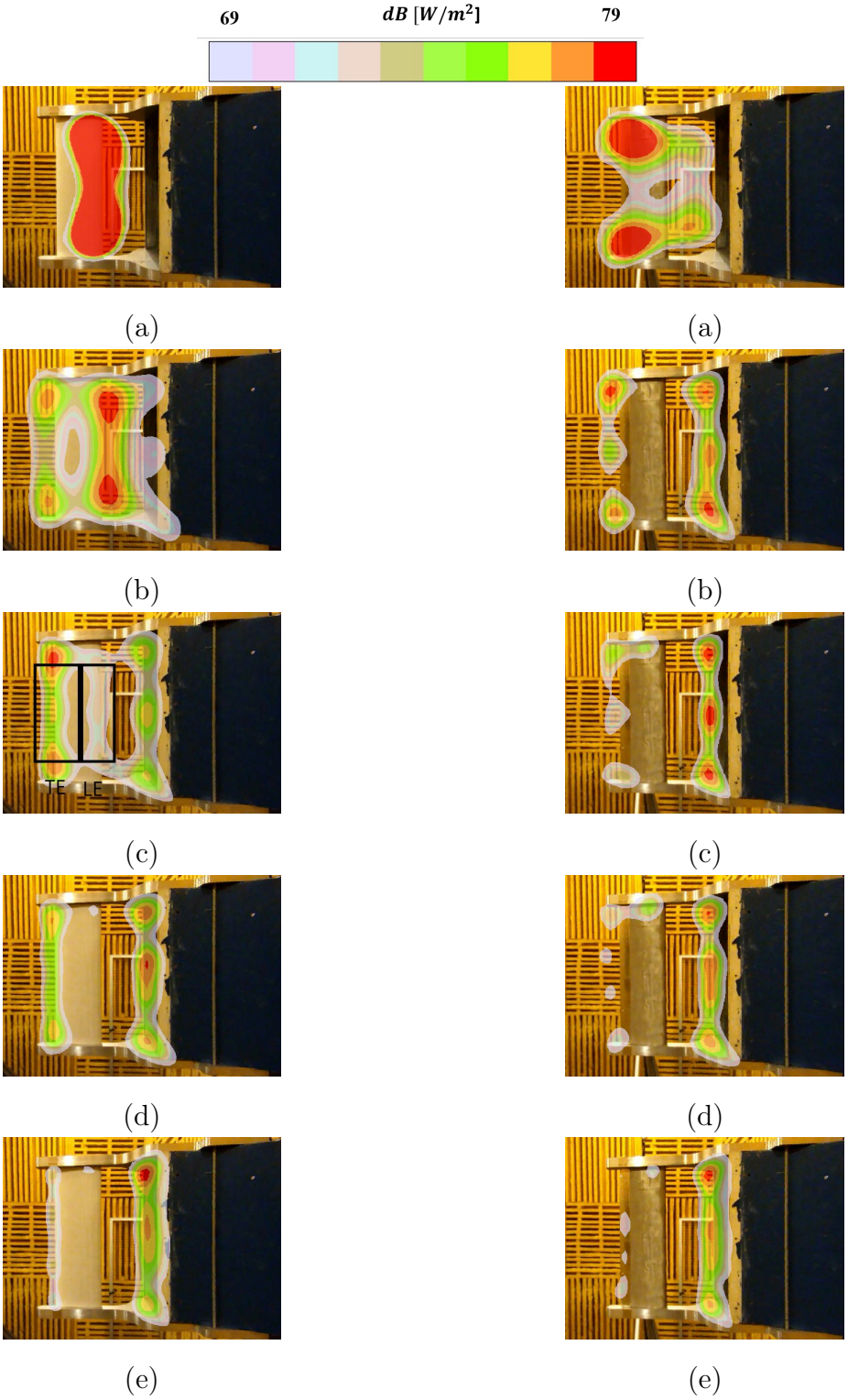

Figure 7.7: Source power color maps corresponding to the baseline NACA-0012 (left column) and the recessed edge (V2) porous airfoil (right column) for various frequency ranges, (a) $2-2.5$ kHz, (b) $3-4$ kHz, (c) $4-5$ kHz, (d) $5-6$ kHz, (e) $10-12$ kHz. $U = 32\,\mathrm{m/s}$. Flow from right to left, nozzle featured by the black area.

plates, porosity on thick airfoils is of poor interest at very high frequencies. The effect on trailing-edge noise is more subtle. TEN is first increased, especially in the range $2-3$ kHz, and then substantially decreased beyond 3 kHz. This reduction seems to be corroborated by the values of the absorption coefficient of the melamine foam, Fig. 7.5-(b). A possible explanation for these trends is that the aforementioned noise increase is due to increased boundary-layer turbulence, whereas the decrease is attributable to sound absorption by the porosity acting as a liner. The noise reduction achieved in the $6-8$ kHz range was unaccessible to far-field, single-microphone measurements because of the background noise issues (see Fig. 7.6).

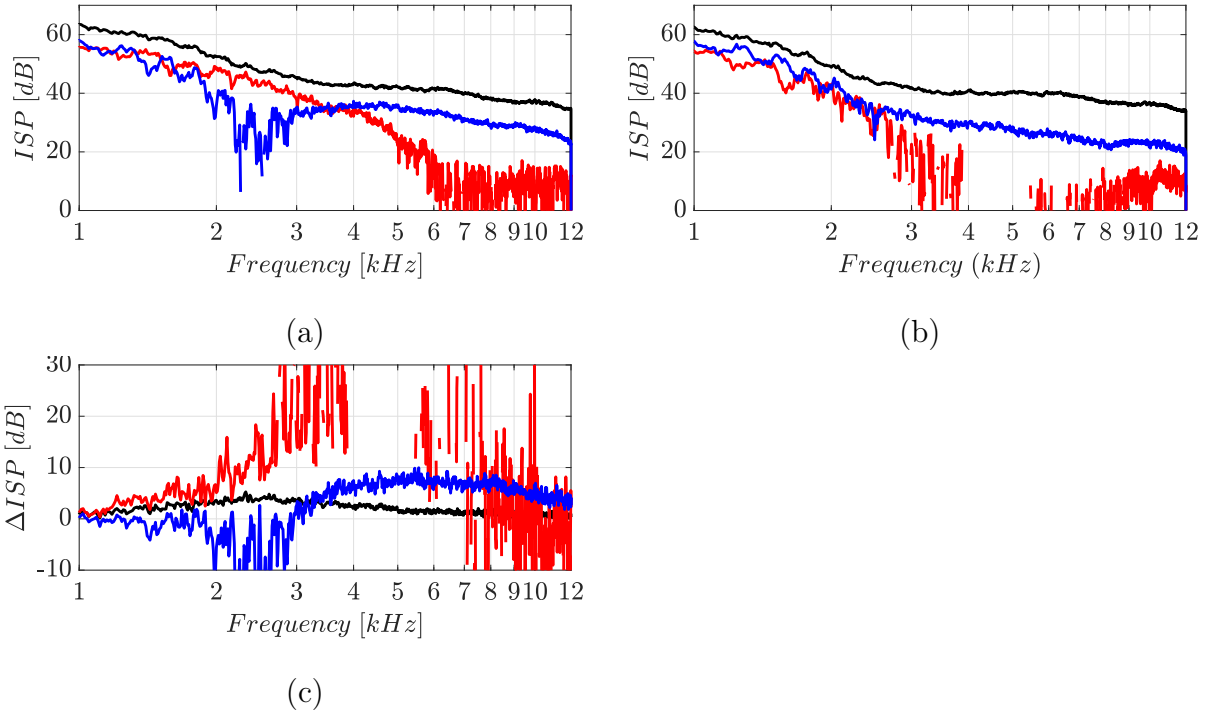

Figure 7.8: Extracted sound power spectra for leading-edge sources (red), trailing-edge sources (blue) and all sources including background noise (black), for the baseline airfoil (a) and the porous airfoil with the recessed edge filled with melamine foam (b). (c): noise reduction spectra for leading edge (red), trailing edge (b), and all (c) sources.

7.5 Airfoil Structure Improvement and Aerodynamic Performances

Near-wake surveys with a traversing total-pressure probe made very close to the trailing edge (not all detailed here) have shown that the porous inclusions described in previous sections substantially increase the thickness of the boundary layers. In addition to the TEN generated at relatively low frequencies, this indicates increased drag and losses that have to be avoided for practical applications. This is why improvements of the manufacturing have been attempted. The preliminary results are presented in this section. The modifications are aimed at ensuring a better fixing of the wiremesh cloth to the grid structure, for better aerodynamic behavior. Indeed difficulties are encountered because the prototype airfoils are handmade in this study. The wide open cells of the structure allow the deformation of the cloth normal to the surface. This drawback has been solved by decreasing the cell width in the streamwise direction and stretching the cloth homogeneously all along the span, leading to the version (V3) shown in Fig. 7.2-(c) to be compared to version (V1).

It is worth noting that aerodynamic and aeroacoustic effects of porosity are linked to the surface roughness and the sound absorption, respectively. A surface with low roughness helps in maintaining the losses and the wake width quite low. Several wiremesh samples have been tested for accessing to these effects, most of them having a surface smooth enough for this purpose. Fig. 7.9 illustrates the absorption coefficient of various samples measured in the Kundt's tube for the high frequency range. All samples are named with the corresponding wiremesh reference number and they have the same underlining structure filled with metal wool. Additionally, a structure sample filled with metal wool without wiremesh (light blue) is reported as reference, leading to a quite low absorption coefficient of about 0.15. Surprisingly, the empty holder without the metal-wool inside incuding the wiremesh on top obtained almost the triple absorption coefficient (WM1) compare to sample WM6. The rest of the complete samples ensured an even better absorption coefficient of about 0.45. An averaged coefficient in the frequency range $1.5 - 6.4\ kHz$ has been calculated as indicator of performance of each sample, to be related to the corresponding wiremesh porosity. Details of the wiremeshes porosity are provided by the manufacturer company Gantois [8] and are given in table Fig. 7.9-(b). The absorption coefficient of each wiremesh sample is also the averaged value for five identical samples using the same wiremesh but different densities of metal wool. This approach is quite empirical. More accurate and controlled processes will be considered in future investigations.

The acoustic results for the porous airfoil (V3) with full-chord center plate are shown in Fig. 7.10. The selected wiremesh is the best performing candidate, with reference No 105365, porosity 39 and average absorption coefficient 0.50 (table in Fig. 7.9-(b)). The preliminary results show a, quite low, maximum noise reduction of 2 dB at mid-to-high frequencies for which the absorption coefficient takes high values. Nevertheless, the reasons for noise reduction are not obvious because the airfoil structure includes many parameters that could contribute to this performance.

The aerodynamic effect of porosity has been estimated from Hot Wire Anemometry

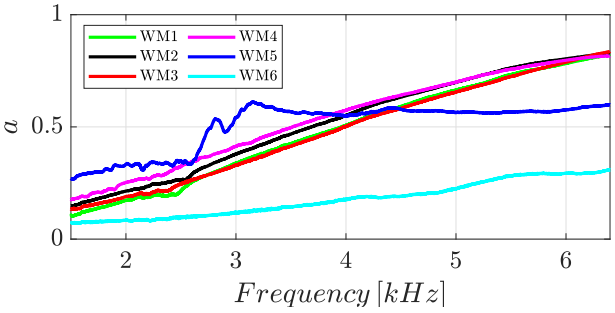

(a)

Reference No	Porosity	Average α
WM1 (101077)	41	0.45
WM2 (101077)	41	0.49
WM3 (101474)	57	0.45
WM4 (105365)	39	0.50
WM5 (102181)	34	0.48
WM6 (no mesh)	–	0.17

(b)

Figure 7.9: (a) Absorption coefficient of various wiremesh samples evaluated with a Kundt's tube for the high frequency range. Only the WM6 sample (light blue) consists of the structure and the metal wool without the wiremesh. (b) Table of the average absorption coefficient as a functionof wiremesh porosity.

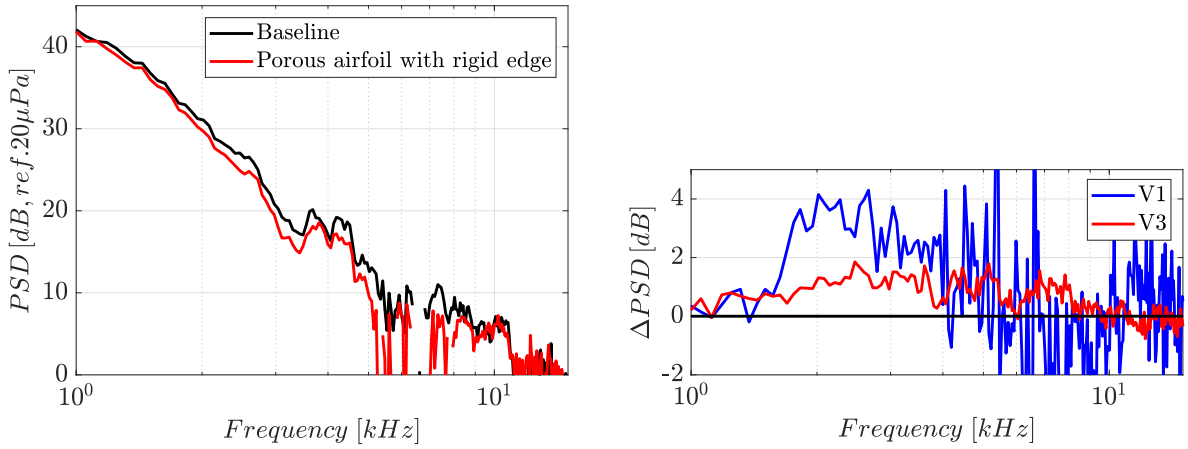

(a) (b)

Figure 7.10: Far-field acoustic spectra of the porous airfoil V3 measured at 90°. (a) Baseline (black) and porous airfoil V3 with the rigid edge (red). (b) Noise reductions comparison between the porous airfoils V1 (blue) and V3 (red) with rigid edges. $U_0 = 32$ m/s.

(HWA) with a traversing single-wire probe, by measuring the velocity deficit in the wake. The estimated distance to the airfoil trailing edge is $\leq$ 1 mm. The baseline and two 'improved' versions of porous airfoils, namely the aforementioned (V3) and a similar architecture (V4) with a recessed-edge center plate, have been tested at 0° AOA. The drag is estimated from the integral momentum theorem by integrating the velocity deficit. The rms and mean-velocity profiles normal to the flow direction are plotted in Fig. 7.11. A slight asymmetry between the two sides of the airfoils is observed. The wake profile is wider for positive values of the reduced coordinate y/c whereas the for negative values it is found very close to the baseline profile. This imbalance is attributed to some surface manufacturing issues. Eventually, the drag coefficients of the porous airfoils with and without the recessed edge exceed that of the baseline by 15% and 14%, respectively. Additional

aerodynamic measurements will be conducted on the same airfoils at different AOA and in different spanwise positions. It is also worth noting that TIN is known as only weakly depending on the angle of attack. This makes the balance of advantages and drawbacks of the porous airfoils an open issue, for which the results in Fig. 7.11 suggest that it is also a matter of airfoil design. Indicative modifications of the lift force as evaluated by observing the deviation of the wind-tunnel jet-flow are also planned as part of the future measurements.

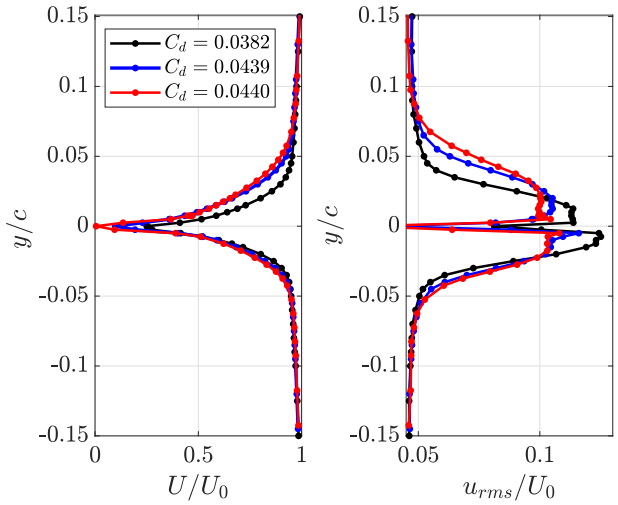

(a)

Figure 7.11: Mean velocity U and RMS velocity u_{rms} profiles for baseline (black), porous airfoil V3 (red) and porous airfoil V4 (blue) measured in the very-near wake with hot-wire probe at $U_0 = 32$ m/s and 0° AOA.

7.6 Concluding Remarks

The present study dedicated to the turbulence-impingement noise of NACA-0012 airfoils with porous inclusions addressed the effects of porosity in terms of noise reduction and aerodynamic performances. Various versions of the porous airfoils with different structure and frame have been tested. The chosen technology involves a rigid skeleton with a center plate, partitioned in volumes filled with porous material, and wrapped in a smooth wiremesh. Furthermore, two options have been assessed, one with a full-chord center plate and one with a recessed-edge center plate. The rounded nose of the airfoil has a rigid part for the former and is completely porous for the latter. A key practical issue is that the manufacturing has to ensure a smooth and regular surface to minimize boundary-layer growth. Two improved porous airfoils with better-controlled wiremesh fixing have shown to keep the aerodynamic losses acceptable. Their acoustic characterization is still in progress.

A microphone-array processing has been used to complement the far-field, single-microphone measurements, allowing to separate the effects of porosity on trailing edge noise and on turbulence-impingement noise, at high frequencies. The major outcomes are summarized below.

- Airfoils with porous inclusions decrease turbulence-impingement noise in a quite wide frequency range from 2 to 18 kHz (for the present tests with airfoil chords of 10 cm and Mach numbers of about 0.1), with frequency-dependent efficiency, unlike other types of porous airfoils reported in the literature that show some noise increase in high frequencies. Yet the reduction drops at higher frequencies because the thickness at leading-edge makes the airfoil poorly respond to turbulence impingement. Maximum reductions of more than 15 dB have been observed in limited frequency ranges.

- Trailing-edge noise is also reduced at high frequencies, whereas it can be increased at low-to-medium frequencies, maybe because of thicker boundary-layer thickness resulting from manufacturing issues. Porosity is believed to act as an acoustic near-field liner in this case.

- Achieved noise reductions are subtantially higher for the recessed-edge center-plate structure, which confirms that the leading-edge area is crucial for the physics of turbulence-impingement noise generation. However, the fully-porous leading edge makes a cross-flow possible, which in turns could be prejudicial to the lift at non-zero angle of attack. This point could be the matter for further investigation.

- The drag coefficient of the baseline NACA-0012 airfoil is increased by about 15% when porosity is installed, with the best achieved hand-made manufacturing. The effect of porosity on the development of boundary layers is another point that should be addressed specifically.

The promising noise reductions observed with the porous airfoils in the present work make this technology a relevant reduction device for various industrial applications where relatively thick airfoils can be used. Many structural and physical parameters are involved, dealing with both the porous material and its embedding structure. Up to that point the presently obtained performances could probably be upgraded by defining an optimization

strategy. Porosity appears as a complementary or alternative action when compared to leading-edge serrations, the latter being logically dedicated to thin airfoils and blades and the former to thicker ones. Its interest is that the geometry of the airfoil does not need to be modified.

7.7 Compared Noise-Reduction Performances of the Tested Airfoils

Part of the conclusions for the present work could be an overview of all the tested airfoils in terms of the efficiency of the implemented noise reduction devices. Therefore, a comparison is made in Fig. 7.12. A new hybrid NACA12 airfoil has been added in this list. This airfoil combines leading-edge serrations and porous inclusions in the main body, as shown in Fig. 7.13. The serrations of this airfoil have the same geometric parameters (λ, h) as the serrated NACA12 and similar skeleton as the porous one.

Having a first look in Fig.7.12-(a), flat plates are obviously the noisiest baseline shapes compare to the thick airfoils that radiate less sound in almost all the frequency range. The serrated flat plate decreases the noise reaching the same level to the NACA12 baseline. This confirms previous studies in the literature that the thickness effect acts as a noise reduction mechanism on the TIN. An additional outcome is that the serrations on flat plates achieve a higher noise reduction for a wide frequency range compared to thick airfoils both with serrations and porosity. A detailed description of the main outcomes are summarized below:

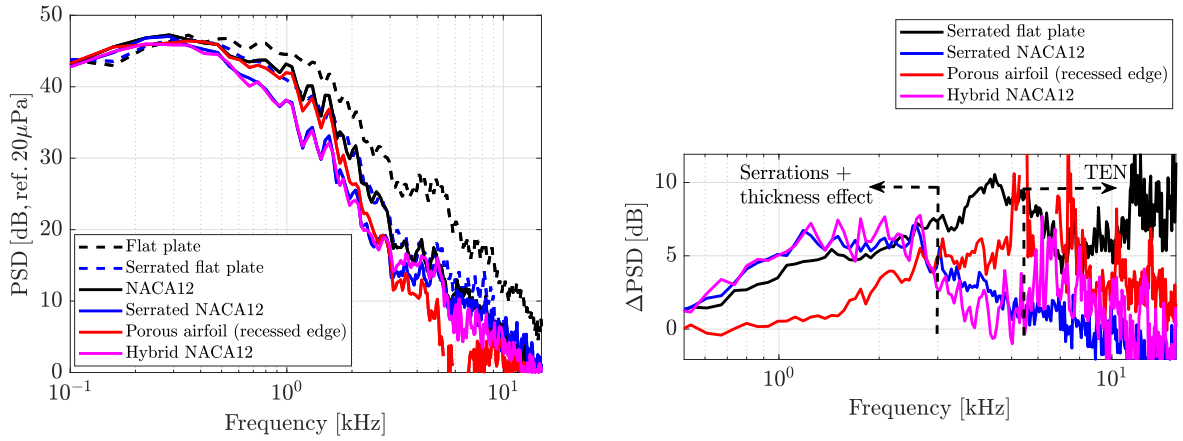

(a) (b)

Figure 7.12: (a) Far-field noise spectra of all tested airfoils and flat plates (b) Noise reductions produced with the corresponding modified NACA12 and flat plates. $U_0 = 32$ m/s at 90°.

- The serrated flat plate decreases TIN till the noise level emitted from the baseline NACA12 and finally collapse almost perfectly with it. At this point, this collapse is

triggering the interest of exploring the noise reduction relation between serrations and thickness effect. It seems to follow the same linear frequency dependence of noise reduction as the expression $10\log_{10}(\mathrm{St_h})$. Similar expressions have been proposed in the literature for predicting inversely the noise radiation from thick airfoils by applying a correction to thin-airfoil acoustic signatures. Probably, both the airfoil thickness and the serration device act in a such way that the gust wavelength interferes destructively similarly with the nose radius of the leading edge and the serration hill. Existing databases in the literature could provide an answer to this question.

- The NACA12 and the hybrid airfoils in Fig. 7.12-(b) present exactly the same noise reduction trend till 3 kHz which almost coincides to the flat plates trend. Beyond this frequency the porosity is beneficial for the hybrid airfoil, probably because it acts as an acoustic liner at high frequencies as mentioned in Section 7.5. Comparing porous and hybrid airfoils, the highest noise reduction occurs at high frequencies beyond 5 kHz for both airfoils. But, the hybrid airfoil presents less efficiency compared to the porous. Probably, the position of the porous inclusions close to the trailing edge reduces the trailing edge noise over 2-3 dB at very high frequencies. Therefore, considering that the TEN is mitigated partially from the porous inclusions of the main body, then the porosity on the leading edge (porous airfoil) acts beneficially between 1 kHz and 4 kHz. A good point for discussion here is poor performance of serrations (NACA-0012) in the range 1.5 kHz and above. A possible scenario could be that the horseshoe vortex (HV) [147] produced downstream the serrations degrades the acoustic performance beyond this frequency. If this is the case, the porous airfoil (without serrations) achieves an increasing NR trend as the HV does not exist. These scenarios raise questions for investigating further the porosity and serrations application in the future.

- An additional outcome of this comparison is to provide candidate solutions for industrial applications in terms of noise minimization, keeping in mind that the noise-reduction devices can degrade the aerodynamic performances by increasing drag, for instance. Therefore, for applications in which high lift and low drag not extremely crucial such as the car cooling fan, cooling or ventilation systems in domestic environments, serrated airfoils or flat plates could be used with an acceptable small aerodynamic penalty, see Table 3.1. For applications where flat plates are used, a thicker baseline airfoil could replace the serrations treatment for reducing the noise. Both provide similar amount of reduction. In these applications, the parameter that usually rejects the use of thick airfoils is the spatial constraint. In many other applications the serrated airfoils seem to be the best candidate because they reduce the low frequency noise which is difficult to mitigate with other techniques (acoustic liners in the installation etc.).

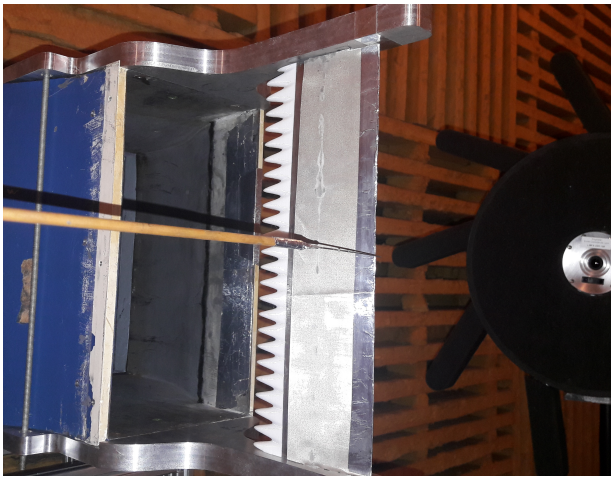

Figure 7.13: Hybrid NACA12 consisting of serrated leading edge ($h/c_0 = 0.1$ and $\lambda/c_0 = 0.12$) and porous main body installed the narrow support plates. A total pressure probe is also installed at the vicinity of the trailing edge.

Conclusions

An experimental study on the turbulence-impingement noise reduction achieved by leading-edge serrations on flat plates and airfoils has been conducted. Previous investigations have been confirmed and completed by using various experimental techniques for the acoustic field and the flow patterns. In particular the effect of serrations has been studied off the mid-span plane, highlighting three-dimensional features. Apart from the reduction of sound levels, the typical directivity of turbulence-impingement noise (TIN) was found the same for both straight and wavy leading edges. This observation differs from the conclusions drawn by a previous study based on theoretical directivity pattern differences.

- TIN reduction can be inferred from differences of far-field sound spectra as long as trailing-edge noise remains of much lower amplitude, which is the case only in a relatively low-to-medium frequency range. An alternative approach resorting to source-power spectra computed from microphone-array measurements has been shown to be more reliable at high frequencies for which turbulence-impingement noise is overwhelmed by trailing-edge noise (TEN). This allows demonstrating reductions of about 14-15 dB with the single-sine serrations that could not be observed from the basic far-field investigation. Source-power spectra deduced from the localization technique have also shown that leading-edge serrations modify trailing-edge noise. TEN is reduced in the medium frequency range and increased in the high-frequency range. This is an additional point regarding the observation that serrations at leading edge decrease airfoil self-noise in high frequencies because of boundary-layer modifications.

- Results of time-resolved tomographic PIV give an insight into the three-dimensionality of the flow in the vicinity of the leading edge. Mean velocity visualization and characterization of the flow motion around the teeth, attest with a first analysis previous observations on the importance of the valley between the teeth as a source of noise. The maximization of the vertical components of the mean velocity at the valleys explains this steep change in direction of motion and blockage of the flow, reducing the norm of the velocity locally. Indeed, vertical disturbances are strongly linked with the generation of sound according to Amiet's theory and assumptions. Further investigations will be made by the authors to address the coherence and the development of the turbulent flow along the serrations.

- Amiet's theory has been successfully compared to the measurements in a complete three-dimensional context for the baseline/straight-edge airfoil and faithfully reproduced the measured noise spectra, both in terms of levels and spectral shape, including the diffraction oscillations occuring when the airfoil chord becomes non compact (Helmholtz number based on the chord $He_c = kc \geq 1$).

- For straight edges, Ayton's model is shown to coincide with Amiet's theory, provided that a correction in the levels is applied, to account for the fact that the model is purely two-dimensional and for an infinite span. The model closely matches the high-frequency (large chord) approximation of Amiet's model and consequently can predict the absolute levels without the oscillations caused by the combined leading-edge and trailing-edge scattering. For serrated edges, Ayton's model can then predict the noise spectra both in terms of levels and shapes for all test cases, without further calibration. The noise reduction levels are much more faithfully predicted than with previous models such as Howe's model. Even though an additional wide peak yields a 5 dB overprediction of the predicted noise reduction around a given frequency, the overall trend follows the empirical linear law found in the present and previous experiments, and so up to a certain frequency after which the predicted levels of noise mitigation become constant. The additional gain observed experimentally (especially after extraction of the leading-edge noise by beamforming) might be attributed to the additional effect of thickness on turbulence-interaction noise not accounted for in the analytical model. Eventhough the present formulation of Ayton's model requires a calibration, its noise gains are already quantitative and can be used to predict the effect of different serration designs. For instance, a first possible development is to apply it as a correction directly on Amiet's model for straight edges. Such a quantitative prediction could then be used in an optimization loop as recently demonstrated by Kholodov and Moreau for trailing-edge noise. A more physically-based improvement of the model could be to use Ayton's pressure jump for the serrated airfoil as a source term for computing a radiation integral as in Amiet's approach. Another possible extension to this model could be the approximate derivation of a trailing-edge back-scattering correction to account for the airfoil finite chord length.

Two versions of porous airfoils have been tested, one with a central rigid frame plate extending over the full chord and another one with a recessed plate at the leading edge. Applying the aforementioned experimental techniques, differences between the two versions have been identified. Some of the findings are summarized below:
- Airfoils with porous cells decrease the noise to some extent in a quite wide frequency range from $2 - 18$ kHz. The noise is minimized till the background noise level in the frequency range of $5 - 7$ kHz. It is worth mentioning that this frequency range corresponds to the maximum absorption coefficient measured in a Kundt's tube on a sample of the porous-cell structure.
-Noise reduction levels between the two versions vary between 4 and 6 dB and in different chord-based Strouhal numbers.
- The drag coefficient was calculated for the baseline and the porous airfoil, giving increases of 15% for the latter. This is attributed to manufacturing issues. Improved cell and cover structures will be tested in further experiments.

A Appendix

A.1 Amiet's Theory for Leading-Edge Noise Prediction

Since the pressure jump is expressed in Chapter 2, the equivalent source distribution along the airfoil will be calculated. The sound radiation of such a source corresponds to the radiation of chordwise and spanwise distributed dipoles which are recognized as dominant in subsonic flows. The sound radiation of a single dipole at an arbitrary frequency [58, 43] is given by Amiet [12] assuming that the receiver is placed in the acoustical far-field:

$$P_1(\boldsymbol{x},\omega;\boldsymbol{x}_0) = \frac{i\omega z F(\boldsymbol{x}_0,\omega)}{4\pi\alpha S_0^2} e^{i\omega\left[t+\frac{M(x-x_0)-S_0}{\alpha\beta^2}+\frac{xx_0+yy_0\beta^2}{\alpha\beta^2 S_0}\right]} \tag{A.1}$$

where $F(x_0,y_0,\omega)e^{i\omega t}\boldsymbol{k}$ is the strength of a point force. The force vector corresponds equally to the pressure difference between the upper and the lower surfaces and coincides to the lift component $\hat{\ell} = \Delta\hat{P}$ perpendicular to the airfoil as it is considered infinitely thin. The corresponding far-field pressure will be resulted by integrating the whole airfoil surface using a double spatial integral.

$$P_1(\boldsymbol{x},\omega) = \int_{-d}^{d}\int_{-b}^{b} \frac{i\omega z \Delta\hat{P}(\boldsymbol{x}_0,\omega)}{4\pi\alpha S_0^2} e^{i\omega\left[t+\frac{M(x-x_0)-S_0}{\alpha\beta^2}+\frac{xx_0+yy_0\beta^2}{\alpha\beta^2 S_0}\right]} dx_0 dy_0 \tag{A.2}$$

The sound power in the far-field will be calculated by defining the cross-Power Spectral Density (PSD) [110]. The pressure jump $\Delta\hat{P}(\boldsymbol{x}_0,\omega)$, as an input parameter, will be linked with the incoming turbulence by introducing statistical quantities. Cross-PSD, the statistical average of two signals, recorded in two different points on the surface, expresses the randomness of the turbulence. The theories of Kirchhoff [80] and Curle [43] are used for linking the far-field sound to the cross-PSD of the surface pressure.

$$S_{QQ}(x_{01},x_{02},y_{01},y_{02},\omega) = \lim_{T\to\infty}\left\{\frac{\pi}{T}E[\Delta\hat{P}_T^*(x_{01},y_{01},\omega)\Delta\hat{P}_T(x_{02},y_{02},\omega)]\right\} \tag{A.3}$$

the expected value of $\Delta\hat{P}_T$ is related to that of the velocity upwash $\hat{w}$ quantity.

The integrated cross-PSD quantity along the whole surface of the airfoil that links the turbulence energy and the far-field sound radiation can be written as

$$S_{pp}(x,y,z,\omega) = \left(\frac{\omega z}{4\pi\alpha S_0^2}\right)^2 \int_{-d}^{d}\int_{-d}^{d}\int_{-b}^{b}\int_{-b}^{b} S_{QQ}(x_1,x_2,\eta,\omega) \\ e^{\frac{i\omega}{\alpha}\left[\beta^{-2}(x_1-x_2)(M-x/S_0)+y\eta/S_0\right]} dx_1 dx_2 dy_{01} dy_{02} \tag{A.4}$$

where $\eta = y_{02} - y_{01}$ is the spanwise separation of the two points on the surface.

The substitution of $\Delta\hat{P}$ in Eq. 4.11 to Eq A.3, gives the cross-PSD quantity by the final expression

$$S_{QQ}(x_1,x_2,y_1,y_2,\omega) = (2\pi\rho_0 b)^2 U \int_{-\infty}^{+\infty} g^*(x_1,K_1,k_2)g(x_2,K_1,k_2)\Phi_{ww}(K_1,k_2)e^{ik_2\eta}dk_2 \tag{A.5}$$

where $\Phi_{ww}(K_1,k_2)$ is the energy spectrum [67] of the incoming turbulence. A more detailed description of the mathematical derivations and definitions is given in the references [12] [37] [31].

Substituting Eq. A.5 in the expression of far-field PSD Eq. A.2, allows the far-field sound radiation to be written as

$$S_{pp}(x,y,z,\omega) = \left(\frac{\omega z}{4\pi\alpha S^2}\right)^2 \int_{-d}^{d}\int_{-d}^{d}\int_{-b}^{b}\int_{-b}^{b} e^{\frac{i\omega}{\alpha}\left[\beta^{-2}(x_1-x_2)(M-x/S)+y\eta/S\right]}(2\pi\rho_0 b)^2 ... \\ \int_{-\infty}^{+\infty} g^*(x_1,K_1,k_2)g(x_2,K_1,k_2)\Phi_{ww}(K_1,k_2)e^{ik_2\eta}dk_2 dx_1 dx_2 dy_{01} dy_{02} \tag{A.6}$$

The next procedure is to define the aeroacoustic transfer function $g(\boldsymbol{x}, K_1, k_2)$ that links the impinging gust to the pressure jump on the airfoil. The analytical solution is a two-fold procedure as proposed by Amiet [12] and is obtained by considering separately the leading and trailing edges contributions using an iterative method called Schwarzschild's [138] technique. Therefore, the same procedure will be used two times; the leading-edge scattering will be expressed by assuming a semi-infinite plate in the downstream direction and a trailing-edge back scattering correction will contribute to the final pressure, accounting in this way for the finite chord length. In detailed, Schwarzschild's procedure is used to solve the convected Helmholtz equation that corresponds to the incoming gust velocity potential (1st iteration) and obtain the pressure correction by the trailing-edge scattering (2nd iteration). The resulting aeroacoustic transfer function $g(\boldsymbol{x}, K_1, k_2)$ is the summation of the two aforementioned contributions, $g = g_1 + g_2$. Assuming an airfoil with an infinite span, the potential that corresponds to the upwash gust $\tilde{w}(k_1, k_2)$ Eq.(4.8) can be factorized as

$$\phi_p(x, y, z, t) = \phi_p'(x, z) e^{i(\omega t + k_1 M/\beta^2 x - k_2 y)} \tag{A.7}$$

The linearized wave equation for the velocity potential in three dimensions leads to the convected Helmholtz equation as

$$\begin{aligned} \left[\nabla^2 - \frac{1}{\alpha^2}\frac{D^2}{Dt^2}\right]\phi_p(x, z, t) = \; & 0 \Rightarrow \\ (1 - M_0^2)\frac{\partial^2 \phi_p}{\partial x^2} + \frac{\partial^2 \phi_p}{\partial y^2} + \frac{\partial^2 \phi_p}{\partial z^2} - 2\frac{M_0}{\alpha}\frac{\partial^2 \phi_p}{\partial t \partial x^2} - \frac{1}{\alpha^2}\frac{\partial^2 \phi_p}{\partial t^2} = \; & 0 \end{aligned} \tag{A.8}$$

and the equation is reduced to the ordinary Helmholtz equation Eq. A.9 by a change of variables.

$$\frac{\partial^2 \phi_p}{\partial \bar{x}^2} + \frac{\partial^2 \phi_p}{\partial \bar{z}^2} + \kappa^2 \phi_p = 0 \tag{A.9}$$

where

$$\bar{x} = \frac{x}{b}\,,\; \bar{y} = \frac{\beta y}{b}\,,\; \bar{z} = \frac{\beta z}{b}\,,\; \kappa^2 = \mu^2 - \frac{\bar{k}_2^2}{\beta^2} \tag{A.10}$$

with

$$\mu = \frac{\bar{k}_1 M}{\beta^2} = \bar{k}_1^* M \text{ and, } \bar{k}_1^* = \frac{\bar{k}_1}{\beta^2} \tag{A.11}$$

The boundary conditions required for the problem solutions are listed below:

1) The velocity potential equals zero upstream the airfoil solid boundary

$$\phi_p(x, y, 0, t) = 0 \qquad x \leq 0 \tag{A.12}$$

2) The hard wall condition states that the velocity normal to the airfoil is zero

$$\frac{\partial \phi_p}{\partial z}(x, y, 0, t) = -w \qquad 0 < x \leq 2b \tag{A.13}$$

3) The Kutta-condition is imposed at the trailing edge where the pressure difference between the suction side and pressure side is zero

$$\frac{D\phi_p}{Dt}(x, y, 0, t) = 0 \qquad x > 2b \tag{A.14}$$

The system in its complete form for the potential ϕ'_p after some derivations is given below in non-dimensional form

$$\frac{\partial^2 \phi'_p}{\partial \bar{x}^2} + \frac{\partial^2 \phi'_p}{\partial \bar{z}^2} + \kappa^2 \phi'_p = 0 \tag{A.15}$$

with the following boundary conditions

$$\phi'_p(\bar{x}, 0) = 0 \qquad \bar{x} \leq 0 \tag{A.16}$$

$$\frac{\partial}{\partial \bar{z}} \phi'_p(\bar{x}, 0) = \frac{-w_0 b}{\beta} e^{-i\bar{k}_1^* \bar{x}} \qquad 0 < \bar{x} \leq 2 \tag{A.17}$$

$$\left(-i\bar{k}_1^* + \frac{\partial}{\partial \bar{z}}\right) \phi'_p(\bar{x}, 0) = 0 \qquad 2 < \bar{x} \tag{A.18}$$

Depending on the values of κ that Eq. A.9 received as an input, the nature of the solution differs. The differential equation is hyperbolic for $\bar{k}_2 < \frac{\bar{k}_1 M}{\beta}$ (supercritical gust) and elliptic for $\bar{k}_2 > \frac{\bar{k}_1 M}{\beta}$ (subcritical gust). For each case, Schwarzschild's procedure is applied two times, called iterations as mentioned before.

At the first iteration, the solution for the potential is obtained for the surface considering the thin airfoil as semi-infinite by removing the trailing edge to infinity downstream. The schematic in Fig. A.1 describes both boundary conditions. The boundary condition upstream the leading-edge wall (Eq. A.16) and the slip condition (Eq. A.17) for the semi-infinite plane are imposed. The final expression for ϕ_p (Eq. A.7) using the solution defined by Eq. A.15 is formulated as

$$\phi_p(x,y,0,t) = -\frac{w_0(1-i)}{\sqrt{k_1^2+k_2^2}} E\left[(\bar{k}_x^* - \kappa)\frac{x}{b}\right] e^{i(U_0 k_1 t - k_1 x - k_2 y)} \tag{A.19}$$

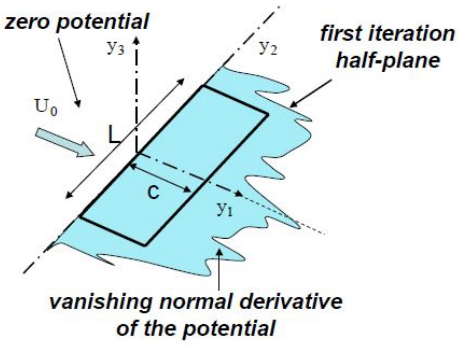

Figure A.1: Leading-edge semi-infinite half-plane

The second iteration (2nd Schwarzschild's application) involves the trailing edge correction to the corresponding boundary condition (Eq. A.13) satisfying also the Kutta-condition (Eq. A.14) at the trailing edge. By this correction, it is considered that the leading edge is removed extending the plate to infinity upstream Fig. A.2. Once determined the velocity potential from the first iteration, the corresponding pressure downstream the leading edge is given by the linerized Bernoulli equation Eq. A.20.

$$\begin{aligned} \frac{\partial \phi_p}{\partial t} + U_0 \frac{\partial \phi_p}{\partial x} + \frac{p_1}{\rho_0} = const \Rightarrow \\ p_1 = -\rho_0 \left(\frac{\partial \phi_p}{\partial t} + U_0 \frac{\partial \phi_p}{\partial x} \right) = -\rho_0 \frac{D\phi_p}{Dt} \end{aligned} \tag{A.20}$$

Using again the linearized wave equation for the pressure p_1 expressed in Eq. A.21, the system solution provides the correction pressure p_2' so that $p' = p_1' + p_2'$ satisfies the kutta condition ($p_1'(\bar{x},0) = 0$, $\bar{x} \geq 2$). The pressure $p(x,y,z,t) = p'(x,z)e^{i(\omega t + \frac{kM}{\beta^2}x - k_2 y)}$ will be the complete pressure solution on the plate surface. So, the differential wave equation is

$$\left.\begin{aligned} \left[\nabla^2 - \frac{1}{\alpha^2}\frac{D^2}{Dt^2}\right] p_1(x,z) = 0 \\ p_1(x,y,z,t) = p_1'(x,z)e^{i(\omega t + \frac{kM}{\beta^2}x - k_2 y)} \end{aligned}\right\} \tag{A.21}$$

The Helmholtz equation for the pressure p_1' is

$$\frac{\partial^2 p_1'}{\partial \bar{x}^2} + \frac{\partial^2 p_1'}{\partial \bar{z}^2} + \kappa^2 p_1' = 0 \tag{A.22}$$

with the following boundary conditions

$$\frac{\partial p_1'}{\partial \bar{z}}(\bar{x}, 0) = 0 \qquad \bar{x} < 2 \tag{A.23}$$

$$p_1'(\bar{x}, 0) = 0 \qquad \bar{x} \geq 2 \tag{A.24}$$

The boundary condition Eq. A.1 will be fulfilled by defining a correction pressure p_2', such that $p' = p_1' + p_2'$.

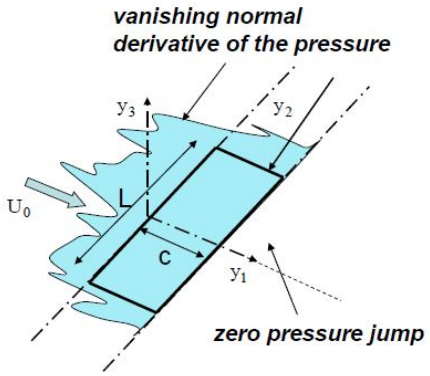

Figure A.2: Trailing-edge semi-infinite half-plane

The system in non-dimensional coordinates for the p'_2 is now re-defined as

$$\frac{\partial^2 p'_2}{\partial \bar{x}^2} + \frac{\partial^2 p'_2}{\partial \bar{z}^2} + \kappa^2 p'_2 = 0 \tag{A.25}$$

with the following boundary conditions

$$\frac{\partial p'_2}{\partial \bar{z}}(\bar{x}, 0) = 0 \qquad \bar{x} < 2 \tag{A.26}$$

$$p'_2(\bar{x}, 0) = -p'_1(\bar{x}, 0) \qquad \bar{x} \geq 2 \tag{A.27}$$

Finally, Schwarzschild's technique will be applied for a second time leading to the final expressions for pressures p_1 and p_2 as below

$$p_1(x, y, 0, t) = \rho_0 w_0 U_0 \frac{e^{-i\pi/4}}{\sqrt{\pi(\bar{k}_1 + \beta^2\kappa)\bar{x}}} e^{i(U_0 k_1 t + (\bar{k}_1^* M^2 - \kappa)\bar{x} - k_2 y)} \tag{A.28}$$

resulting from the solution p'_1 using the expression (A.21)

$$p'_1(x, y, 0, t) = \rho_0 w_0 U_0 \frac{e^{-i\pi/4}}{\sqrt{\pi(\bar{k}_1 + \beta^2\kappa)\bar{x}}} e^{i\kappa\bar{x}} \tag{A.29}$$

and

$$\begin{aligned} p_2(x, y, 0, t) \approx \frac{-\rho_0 w_0 U_0}{\sqrt{2\pi(\bar{k}_1 + \beta^2\kappa)\bar{x}}} e^{i((\bar{k}_1^* M^2 - \kappa)\bar{x} - \pi/4 + \omega t - k_2 y)} \\ \left[1 - (1+i)E^*\left(2\kappa(2-\bar{x})\right)\right] \end{aligned} \tag{A.30}$$

resulting from the solution p'_2 using the expression $p_2(x, y, 0, t) = p'_2(x, 0) e^{i(\omega t + \frac{kM}{\beta^2} x - k_2 y)}$

$$p'_2(\bar{x}, 0) = \rho_0 w_0 U_0 \frac{e^{-i\pi/4} e^{-i\kappa\bar{x}}}{\sqrt{2\pi(\bar{k}_1 + \beta^2\kappa)}} \left[1 - (1+i)E^*\left(2\kappa(2-\bar{x})\right)\right] \tag{A.31}$$

and the final pressure distribution along the plate considering both the leading edge and the trailing edge corrections is

$$p(x, y, 0, t) = p_1(x, y, 0, t) + p_2(x, y, 0, t) \tag{A.32}$$

Expressing the final pressure in Fourier components and substituting it in Eq. 4.7, the transfer function $g(x, K_1, k_2)$ is calculated as below

$$\left.\begin{array}{c} \Delta P = 2p(x, y, 0, t) = 2\pi\rho U_0 w_0 g(x_0, k_1, k_2) e^{i(k_1 U_0 t - k_2 y_0)} \\ p(x, y, 0, t) = p'(x, 0, t) e^{-ik_2 y} \end{array}\right\} \Rightarrow \tag{A.33}$$

$$g(x, K_1, k_2) = \frac{p(x, y, 0, t)e^{ik_1 y}e^{-i\omega t}}{\pi\rho U_0 w_0} \tag{A.34}$$

Therefore, the g functions for the corresponding pressures p_1, p_2 read

$$\begin{aligned} g_1(\bar{x}, k_1, k_2) &= \frac{e^{-i\pi/4}}{\pi\sqrt{\pi(\bar{k}_1 + \beta^2\kappa)(\bar{x}+1)}} e^{-i(\kappa - \bar{k}_1^* M^2)(\bar{x}+1)} \\ g_2(\bar{x}, k_1, k_2) &\approx -\frac{e^{-i\pi/4}}{\pi\sqrt{2\pi(\bar{k}_1 + \beta^2\kappa)}} \left[1 - (1+i)E^*\left(2\kappa(1-\bar{x})\right)\right] e^{-i(\kappa - \bar{k}_1^* M^2)(\bar{x}+1)} \end{aligned} \tag{A.35}$$

Finally, the aeroacoustic transfer function is defined as

$$\mathcal{L}(x, y, z, k_1, k_2) = \int_{-1}^{1} g(\xi, K_1, k_2) e^{-i\mu(M - \frac{x}{S_0})\xi} d\xi \tag{A.36}$$

The same procedure is followed for the case of subcritical gusts ($\bar{k}_2 > \frac{\bar{k}_1 M}{\beta}$).

The final expression for the far-field PSD is given below as a function of the observer's position and frequency, as well as the corresponding $\mathcal{L}$ functions for supercritical and subritical gusts, with $\mathcal{L} = \mathcal{L}_1 + \mathcal{L}_2$.

$$S_{pp}(\boldsymbol{x}, \omega) = \left(\frac{k\,\rho_0\,c\,x_3}{2S_0^2}\right)^2 \pi U_0 d\Phi_{ww}\left(K_1, \frac{kx_2}{S_0}\right) \left|\mathcal{L}\left(x_1, K_1, \frac{kx_2}{S_0}\right)\right|^2 \tag{A.37}$$

A.2 CFD Simulations

The following Figures show the RANS computations performed during the secondment in Athens. The gray area is the wall surface of the NACA-0012 airfoil and the colored planes show the mean velocity components plotted at the leading edge position. The flow is delivered from the right to the left.

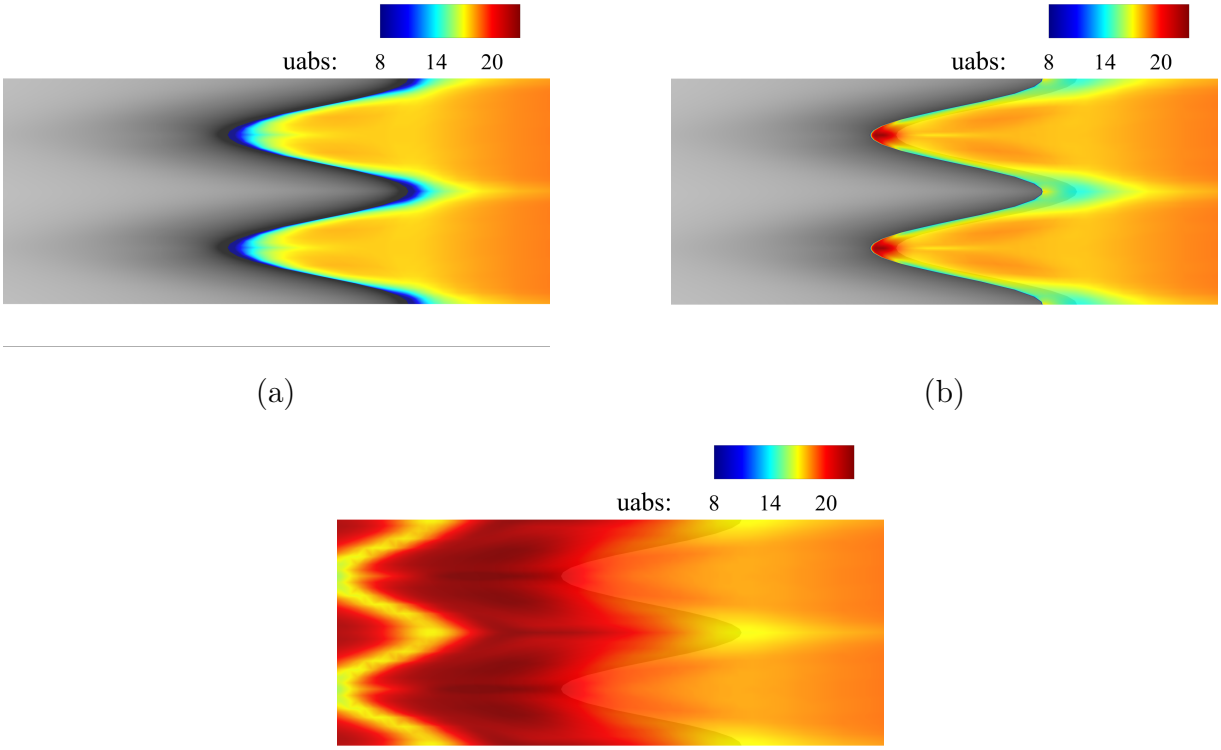

(a) (b)

(c)

Figure A.3: Planar cuts of the streamwise velocity component along the vertical axis (a) $z/c_0 = 0$, (b) $z/c_0 = 0.03$ and (c) $z/c_0 = 0.06$ for the NACA12 airfoil. The free-stream $U_0 = 19.7$ m/s. Obtained by RANS computations.

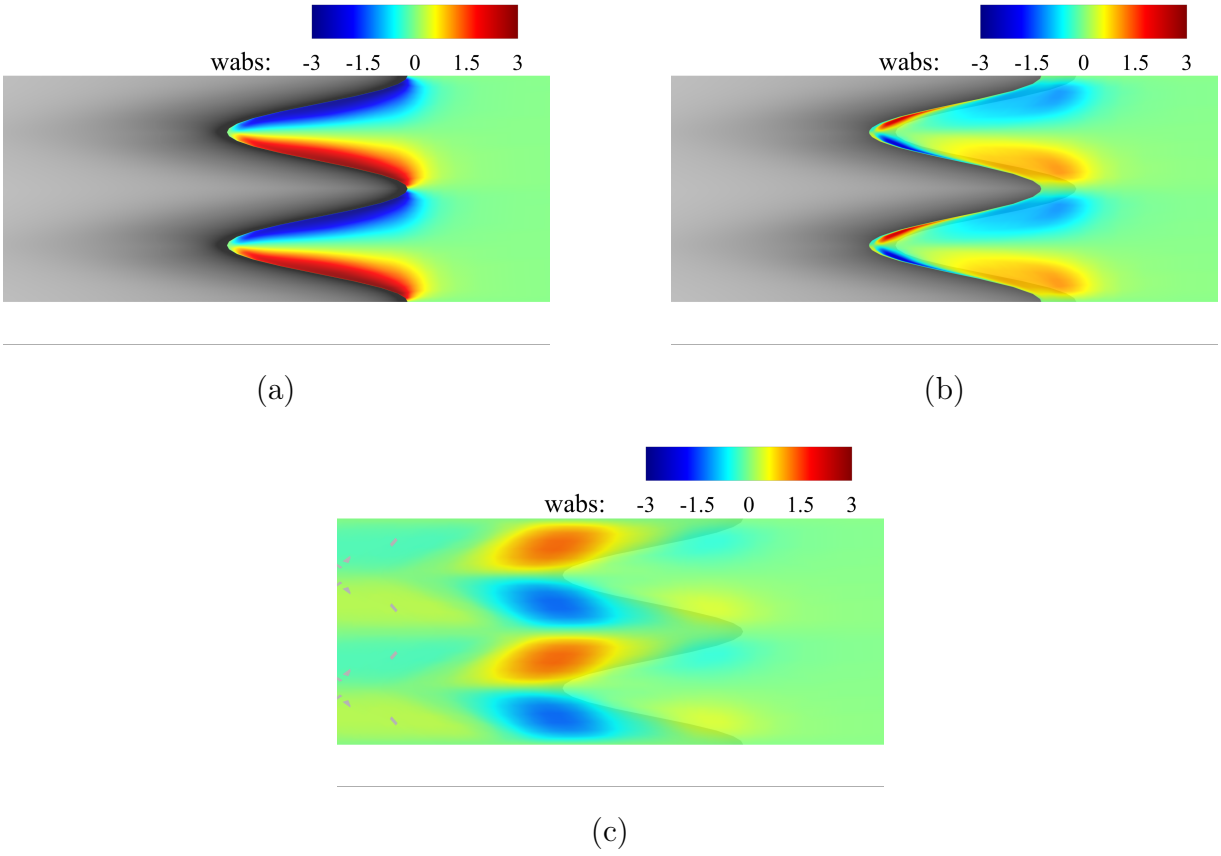

Figure A.4: Planar cuts of the spanwise velocity component along the vertical axis (a) $z/c_0 = 0$, (b) $z/c_0 = 0.03$ and (c) $z/c_0 = 0.06$ for the NACA12 airfoil. The free-stream $U_0 = 19.7$ m/s. Obtained by RANS computations where the spanwise velocity component is referred here as w.

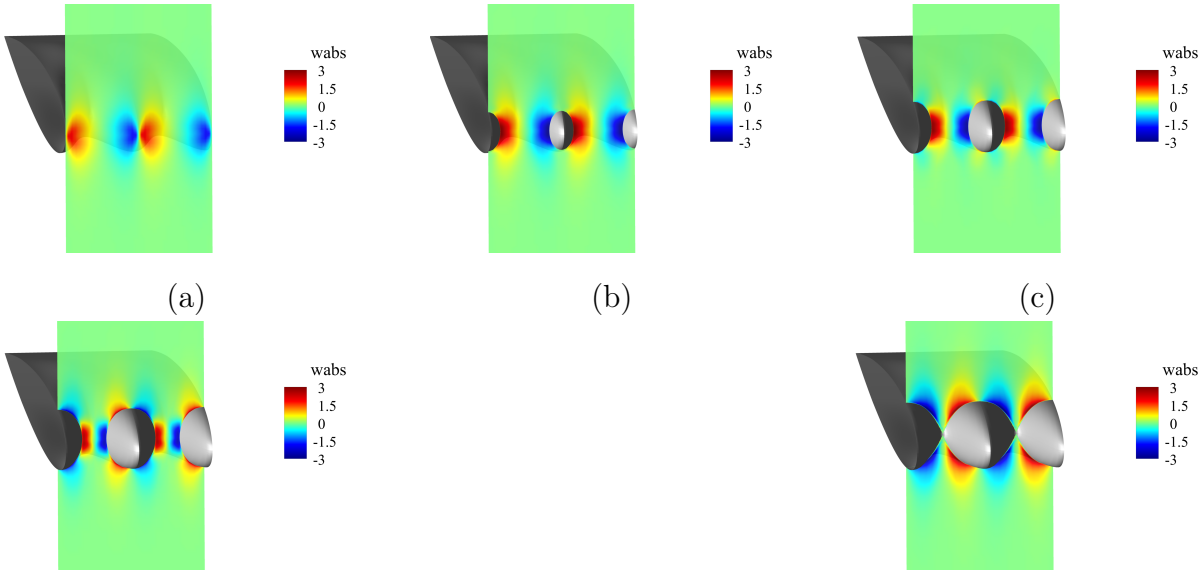

Figure A.5: Planar cuts of the spanwise velocity component plotted at five distances equally distributed along the streamwise axis for the NACA12 airfoil. The free-stream $U_0 = 19.7$ m/s. Obtained by RANS computations where the spanwise velocity component is referred here as w.

Bibliography

[1] World Health Organization 1999. https://www.who.int/docstore/peh/noise/Comnoise-1.pdf, 1999. (Accessed: 20-07-2020).

[2] World Health Organization 2018. https://www.euro.who.int/__data/assets/pdf_file/0008/383921/noise-guidelines-eng.pdf, 2018. (Accessed: 20-07-2020).

[3] Bruel & Kjar. https://www.bksv.com/media/doc/BP1039.pdf, 2020. (09-05-2020).

[4] SmartAnswer. https://www.h2020-smartanswer.eu/, 2020, (Accessed: 20-07-2020).

[5] Flightpath2050. Available at: https://www.cleansky.eu/sites/default/files/documents/acare-sria-citizen.pdf, 2020, (Accessed: 29-07-2020).

[6] Barn Owl. https://en.wikipedia.org/wiki/Barn_owl, Accessed: 10-10-2020.

[7] ExaCorporation. https://ww1.prweb.com/prfiles/2013/05/30/10782200/Denso%20Acoustic%20Fan%20Larger%20w_legend.jpg, Accessed: 20-07-2020.

[8] Gantois. https://www.gantois.com/catalogue/6_catalogue-toile-metallique.pdf, Accessed: 30-09-2002.

[9] DeviantArt. https://www.deviantart.com/treeclimber-stock/art/Pigeon-Wing-02-354936903, Accessed: 31-08-2020.

[10] J. J. Adamczyk. Passage of a swept airfoil through an oblique gust. *Journal of Aircraft*, 11(5):281–287, 1974.

[11] R. K. Amiet. Compressibility effects in unsteady thin-airfoil theory. *AIAA Journal*, 12(2):252–255, 1974.

[12] R. K. Amiet. Acoustic radiation from an airfoil in a turbulent stream. *Journal of Sound and Vibration*, 1975.

[13] R. K. Amiet. High frequency thin-airfoil theory for subsonic flow. *AIAA Journal*, 14(8):1076–1082, 1976.

[14] R. K. Amiet. Noise due to turbulent flow past a trailing edge. *Journal of Sound and Vibration*, 47(3):387–393, 1976.

[15] R. K. Amiet. Refraction of sound by a shear layer. *Journal of Sound and Vibration*, 58(4):467–482, 1978.

[16] H. M. Atassi. The Sears problem for a lifting airfoil revisited—new results. *Journal of Fluid Mechanics*, 141:109–122, 1984.

[17] F. Avallone, S. Pröbsting, and D. Ragni. Three-dimensional flow field over a trailing-edge serration and implications on broadband noise. *Physics of Fluids*, 28(11), 2016.

[18] L. Ayton and C. Paruchuri. Analytical and experimental investigation into the effects of leading-edge radius on gust-aerofoil interaction noise. *Journal of Fluid Mechanics*, 829:780–808, 2017.

[19] L. J. Ayton. An analytic solution for gust-aerofoil interaction noise for plates with leading-edge serrations. In *23rd AIAA/CEAS Aeroacoustics Conference*, page 3492, 2017.

[20] L. J. Ayton and J. W. Kim. An analytic solution for the noise generated by gust–aerofoil interaction for plates with serrated leading edges. *Journal of Fluid Mechanics*, 853:515–536, oct 2018.

[21] L. J. Ayton and C. Paruchuri. Analytic solutions for reduced leading-edge noise aerofoils. *2018 AIAA/CEAS Aeroacoustics Conference*, 2018.

[22] L. J. Ayton and C. Paruchuri. An analytical and experimental investigation of aerofoil-turbulence interaction noise for plates with spanwise-varying leading edges. *Journal of Fluid Mechanics*, 865:137–168, 2019.

[23] L. J. Ayton B. Lyu and C. Paruchuri. On the acoustic optimality of leading-edge serration profiles. *Journal of Sound and Vibration*, 462:114923, 2019.

[24] T. Bachmann, S. Klän, W. Baumgartner, W. Klaas, M.and Schröder, and H. Wagner. Morphometric characterisation of wing feathers of the barn owl Tyto alba pratincola and the pigeon Columba livia. *Frontiers in Zoology*, 4:1–15, 2007.

[25] G. Bampanis and M. Roger. Three-dimensional effects in the reduction of turbulence-impingement noise of aerofoils by wavy leading edges. In *Euronoise*, pages 97–104, 2018.

[26] G. Bampanis, M. Roger, and S. Moreau. On a three-dimensional investigation of airfoil turbulence-impingement noise and its reduction by leading-edge tubercles. *Journal of Sound and Vibration*, page 116635, 2021.

[27] G. Bampanis, M. Roger, D. Ragni, F. Avallone, and C. Teruna. Airfoil-Turbulence Interaction Noise Source Identification and Reduction by Leading-Edge Serrations. *AIAA Conference*, (May):1–18, 2019.

[28] T. Biedermann, N Hintzen, F. Kameier, T. P. Chong, and C. O. Paschereit. On the Transfer of Leading Edge Serrations from Isolated Aerofoil to Ducted Low-Pressure Fan Application. *2018 AIAA/CEAS Aeroacoustics Conference*, 2018.

[29] T. F. Brooks, D. S. Pope, and M. A. Marcolini. Airfoil self-noise and prediction. *NASA Reference Publication*, (1218), 1989.

[30] T.F. Brooks and T.H. Hodgson. Trailing edge noise prediction from measured surface pressures. *Journal of sound and vibration*, 78(1):69–117, 1981.

[31] R. Camussi. *Noise sources in turbulent shear flows: fundamentals and applications*, volume 545. Springer Science & Business Media, 2013.

[32] P. Chaitanya, P. Joseph, S. Narayanan, C. Vanderwel, J. Turner, J. W. Kim, and B. Ganapathisubramani. Performance and mechanism of sinusoidal leading edge serrations for the reduction of turbulence-aerofoil interaction noise. *Journal of Fluid Mechanics*, 818:435–464, 2017.

[33] R. C. Chanaud, N. Kong, and R. B. Sitterding. Experiments on porous blades as a means of reducing fan noise. *International Business Machines Corporatio*, 59(3), 1975.

[34] R. C. Chanaud and D. Muster. Aerodynamic noise from motor vehicles. *The Journal of the Acoustical Society of America*, 58(1):31–38, 1975.

[35] D. M. Chase. Modeling the wavevector-frequency spectrum of turbulent boundary layer wall pressure. *Journal of sound and Vibration*, 70(1):29–67, 1980.

[36] J. Christophe. *Application of hybrid methods to high frequency aeroacoustics*. PhD thesis, Université Libre de Bruxelles, 2011.

[37] J. Christophe. Application of Hybrid Methods To High Frequency Aeroacoustics. *Journal of Chemical Information and Modeling*, 53(9):1689–1699, 2013.

[38] B. Chu and L. S. G. Kovásznay. Non-linear interactions in a viscous heat-conducting compressible gas. *Journal of Fluid Mechanics*, 3(5):494–514, 1958.

[39] V. Clair, C. Polacsek, T. L. Garrec, and G. Reboul. CAA methodology to simulate turbulence-airfoil noise. *AIAA Conference*, (June):4–6, 2012.

[40] V. Clair, C. Polacsek, T. Le Garrec, G. Reboul, M. Gruber, and P. Joseph. Experimental and Numerical Investigation of Turbulence-Airfoil Noise Reduction Using Wavy Edges. *AIAA Journal*, 51(11):2695–2713, 2013.

[41] I. A. Clark, W. N. Alexander, W. Devenport, S. Glegg, J. W. Jaworski, C. Daly, and N. Peake. Bioinspired trailing-edge noise control. *AIAA Journal*, 55(3):740–754, 2017.

[42] F. G. Collins. Boundary-layer control on wings using sound and leading-edge serrations. *Aiaa Journal*, 19(2):129–130, 1981.

[43] N. Curl. The Influence of Solid Boundaries upon Aerodynamic Sound. *Proceedings of the Royal Society A: Mathematical, Physical and Engineering Sciences*, 231(1187):505–514, 1955.

[44] W. J. Devenport, J. K. Staubs, and S. A. L. Glegg. Sound radiation from real airfoils in turbulence. *Journal of Sound and Vibration*, 329(17):3470–3483, 2010.

[45] J. Favier, A. Pinelli, and U. Piomelli. Control of the separated flow around an airfoil using a wavy leading edge inspired by humpback whale flippers. *Comptes Rendus - Mecanique*, 340(1-2):107–114, 2012.

[46] Ffowcs Williams, J. E. and Hawkings, D. L. Sound Generation by Turbulence and Surfaces in Arbitary Motion. *Philosophical Transactions of the Royal Society of London. Serie A, Mathematical and Physical Sciences*, 264(1151):321–342, 1969.

[47] F. E. Fish and G. V. Lauder. Passive and Active Flow Control By Swimming Fishes and Mammals. *Annual Review of Fluid Mechanics*, 38(1):193–224, 2006.

[48] F. E. Fish, P. W. Weber, M. M. Murray, and L. E. Howle. The tubercles on humpback whales' flippers: Application of bio-inspired technology. *Integrative and Comparative Biology*, 51(1):203–213, 2011.

[49] J. Gershfeld. Leading edge noise from thick foils in turbulent flows. *The Journal of the Acoustical Society of America*, 116(3):1416–1426, 2004.

[50] T. Geyer, E. Sarradj, and C. Fritzsche. Porous airfoils: noise reduction and boundary layer effects. *AIAA 2009-3392*, 10(2):11–38, 2009.

[51] T. Geyer, E. Sarradj, and C. Fritzsche. Measuring owl flight noise. *INTERNOISE 2014 - 43rd International Congress on Noise Control Engineering: Improving the World Through Noise Control*, 1904(3):1–16, 2014.

[52] T. F. Geyer and E. Sarradj. Trailing Edge Noise of Partially Porous Airfoils. *20th AIAA/CEAS Aeroacoustics Conference*, (June):1–18, 2014.

[53] A.P. Giotis. *Application of evolutionary algorithms, computational intelligence and advanced computational fluid dynamics techniques to the optimizationinverse design of turbomachinery cascades, using parallel processing.* PhD thesis, National Technical University of Athens, 2003.

[54] H. Glauert. *The force and moment on an oscillating aerofoil.* HM Stationery Office, 1929.

[55] S. Glegg and W. Devenport. *Aeroacoustics of low Mach number flows: fundamentals, analysis, and measurement.* Academic Press, 2017.

[56] S. A. Glegg and W. Devenport. Unsteady loading on an airfoil of arbitrary thickness. *Journal of Sound and Vibration*, 319(3-5):1252–1270, 2009.

[57] S. A. Glegg and W. J. Devenport. Panel methods for airfoils in turbulent flow. *Journal of Sound and Vibration*, 329(18):3709–3720, 2010.

[58] M. E. Goldstein and H. Atassi. A complete second-order theory for the unsteady flow about an airfoil due to a periodic gust. *Journal of Fluid Mechanics*, 74(4):741–765, 1976.

[59] M. Goody. Empirical spectral model of surface pressure fluctuations. *AIAA journal*, 42(9):1788–1794, 2004.

[60] S. Grace. Unsteady blade pressure-the bvi model vs. the gust model. In *7th AIAA/CEAS Aeroacoustics Conference and Exhibit*, page 2209, 2001.

[61] J. M. R. Graham. Similarity rules for thin aerofoils in non-stationary subsonic flows. *Journal of Fluid Mechanics*, 43(4):753–766, 1970.

[62] R. R. Graham. The silent flight of owls. *The Aeronautical Journal*, 38(286):837–843, 1934.

[63] R. Hayden and R. Chanaud. Foil structures with reduced sound generation, 1974.

[64] M. Hazewinkel. *Encyclopaedia of mathematics: Supplement*, volume 1. Springer Science & Business Media, 1997.

[65] A. S. Hersh and R. E. Hayden. Aerodynamic sound radiation from lifting surfaces with and without leading-edge serrations. 1971.

[66] A. S. Hersh, P. T. Soderman, and R. E. Hayden. Investigation of Acoustic Effects of Leading-Edge Serrations on Airfoils. *Journal of Aircraft*, 11(4):197–202, 1974.

[67] J O Hinze. Turbulence McGraw-Hill Book Company. *Inc., New York, NY*, page 488, 1959.

[68] JH Horlock. Fluctuating lift forces on aerofoils moving through transverse and chordwise gusts. 1968.

[69] M. S. Howe. *Acoustics of fluid-structure interactions*. Cambridge university press, 1998.

[70] I.C. Kampolis. *Parallel, multilevel algorithms for the aerodynamic optimization in turbomachines.* PhD thesis, National Technical University of Athens, 2009.

[71] D. H. Kapsoulis. *Low-Cost Metamodel-Assisted Evolutionary-Algorithms with Application in Shape Optimization in Fluid Dynamics*. PhD thesis, National Technical University of Athens, 2019.

[72] M.K. Karakasis. *Hierarchical, distributed evolutionary algorithms and computational intelligence in aerodynamic shape optimization, on multiprocessing systems.* PhD thesis, National Technical University of Athens, 2006.

[73] Th. Von Karman. The fundamentals of the statistical theory of turbulence. *Journal of the Aeronautical Sciences*, 4(4):131–138, 1937.

[74] P. Kholodov and S. Moreau. Optimization of serrations for broadband trailing-edge noise reduction using an analytical model. In *25th AIAA/CEAS Aeroacoustics Conference*, page 2655, 2019.

[75] J. W. Kim, S. Haeri, and P. F. Joseph. On the reduction of aerofoil-turbulence interaction noise associated with wavy leading edges. *Journal of Fluid Mechanics*, 792:526–552, 2016.

[76] S. Klan, T. Bachmann, M. Klaas, H. Wagner, and W. Schröder. Experimental analysis of the flow field over a novel owl based airfoil. In *Animal Locomotion*, pages 413–427. Springer, 2010.

[77] R. A. Kroeger, H. D. Grushka, and T. C. Helvey. Low speed aerodynamics for ultra-quiet flight. Technical report, Tennessee univ space inst, 1972.

[78] K. Kucukcoskun, J. Christophe, C. Schram, and M. Tournour. Broadband scattering of the turbulence-interaction noise of a stationary airfoil: experimental validation of a semi-analytical model. *International Journal of Aeroacoustics*, 12(1-2):83–102, 2013.

[79] H. G. Küssner. Das zweidimensionale Problem der beliebig bewegten Tragfläche unter Berücksichtigung von Partialbewegungen der Flüssigkeit. *Luftfahrtforschung*, 17:355–361, 1940.

[80] H. Lamb. *Hydrodynamics*. Cambridge university press, 1993.

[81] A. S. H. Lau, S. Haeri, and J. W. Kim. The effect of wavy leading edges on aerofoil-gust interaction noise. *Journal of Sound and Vibration*, 332(24):6234–6253, 2013.

[82] S. Lee. Reduction of blade-vortex interaction noise through porous leading edge. *AIAA journal*, 32(3):480–488, 1994.

[83] M. J. Lighthill. On sound generated aerodynamically I. General theory. pages 564–587, 1951.

[84] G. Lilley. A study of the silent flight of the owl. In *4th AIAA/CEAS aeroacoustics conference*, page 2340, 1998.

[85] P. D. Lysak. Unsteady lift of thick airfoils in incompressible turbulent flow. 2011.

[86] P. D. Lysak, D. E. Capone, and M. L. Jonson. Prediction of high frequency gust response with airfoil thickness effects. *Journal of Fluids and Structures*, 39:258–274, 2013.

[87] B. Lyu and L. J. Ayton. Serrated leading-edge and trailing-edge noise prediction models for realistic wavenumber frequency spectra. In *25th AIAA/CEAS Aeroacoustics Conference*, page 2674, 2019.

[88] B. Lyu and L. J. Ayton. Rapid noise prediction models for serrated leading and trailing edges. *Journal of Sound and Vibration*, 469:115136, 2020.

[89] B. Lyu and M. Azarpeyvand. On the noise prediction for serrated leading edges. *Journal of Fluid Mechanics*, 826:205–234, 2017.

[90] C. K. Madnia. *Review of "Fundamentals of Aerodynamics"*, volume 48. 2010.

[91] P. Migliore and S. Oerlemans. Wind tunnel aeroacoustic tests of six airfoils for use on small wind turbines. *J. Sol. Energy Eng.*, 126(4):974–985, 2004.

[92] D. S. Miklosovic, M. M. Murray, and L. E. Howle. Experimental evaluation of sinusoidal leading edges. *Journal of aircraft*, 44(4):1404–1408, 2007.

[93] D. S. Miklosovic, M. M. Murray, L. E. Howle, and F. E. Fish. Leading-edge tubercles delay stall on humpback whale (megaptera novaeangliae) flippers. *Physics of fluids*, 16(5):L39–L42, 2004.

[94] J. W. Miles. Quasi-stationary airfoil theory in subsonic compressible flow. *Quarterly of Applied Mathematics , Vol . 8 , No . 4 (January , 1951), pp . 351-358*, 8(4):351–358, 1951.

[95] P. F. Mish and W. J. Devenport. An experimental investigation of unsteady surface pressure on an airfoil in turbulence—part 1: Effects of mean loading. *Journal of Sound and Vibration*, 296(3):417–446, 2006.

[96] S. Moreau. Turbomachinery noise predictions: present and future. In *Acoustics*, volume 1, pages 92–116. Multidisciplinary Digital Publishing Institute, 2019.

[97] S. Moreau, G. Bampanis, and M. Roger. Analytical and experimental investigation of leading-edge noise reduction on a flat plate with serrations. In *AIAA AVIATION 2020 FORUM*, page 2542, 2020.

[98] S. Moreau and M. Roger. Competing Broadband Noise Mechanisms in Low-Speed Axial Fans. *AIAA Journal*, 45(1):48–57, 2007.

[99] S. Moreau and M. Roger. Back-scattering correction and further extensions of Amiet's trailing-edge noise model. Part II: Application. *Journal of Sound and Vibration*, 323(1-2):397–425, 2009.

[100] S. Moreau, M. Roger, and V. Jurdic. Effect of angle of attack and airfoil shape on turbulence-interaction noise. In *11th AIAA/CEAS aeroacoustics conference*, page 2973, 2005.

[101] S. Moreau, M. Sanjosé, B. Lyu, and L. J. Ayton. Analytical, numerical and experimental investigation of trailing-edge noise reduction on a controlled diffusion airfoil with serrations. In *25th AIAA/CEAS Aeroacoustics Conference*, page 2450, 2019.

[102] P. Moriarty, G. Guidati, and P. Migliore. Prediction of turbulent inflow and trailing-edge noise for wind turbines. In *11th AIAA/CEAS Aeroacoustics Conference*, page 2881, 2005.

[103] M. R. Myers and E. J. Kerschen. Influence of camber on sound generation by airfoils interacting with high-frequency gusts. *Journal of Fluid Mechanics*, 353:221–259, 1997.

[104] S. Narayanan, P. Joseph, S. Haeri, J. W. Kim, C. Paruchuri, and C. Polacsek. Noise reduction studies from the leading edge of serrated flat plates. *20th AIAA/CEAS Aeroacoustics Conference*, (June):1–14, 2014.

[105] S. Narayanan, C. Paruchuri, S. Haeri, P. Joseph, J. W. Kim, and C. Polacsek. Airfoil noise reductions through leading edge serrations. *Physics of Fluids*, 27(2), 2015.

[106] Naumann, N. and Yeh, N. Lift and pressure fluctuations of a cambered airfoil under periodic gusts and applications in turbomachinery. *ASME Pap 72-GT-30 for meeting*, pages 1–10, 1972.

[107] S. Oerlemans and P. Migliore. Aeroacoustic wind tunnel tests of wind turbine airfoils. In *10th AIAA/CEAS Aeroacoustics Conference*, page 3042, 2004.

[108] W. Olsen. Noise generated by impingement of turbulent flow on airfoils of varied chord, cylinders, and other flow obstructions. In *3rd Aeroacoustics Conference*, page 504, 1976.

[109] C. Osborne. Unsteady thin-airfoil theory for subsonic flow. *AIAA Journal*, 11(2):205–209, 1973.

[110] R. Moses P. Stoica et al. Spectral analysis of signals. 2005.

[111] S. Palleja-Cabre, B. J. Tester, J. Astley, and G. Bampanis. Aeroacoustic assessment of the performance of over-tip liners in reducing noise of an aerofoil over a flat surface. In *AIAA AVIATION 2020 FORUM*, page 2608, 2020.

[112] Y. H. Pao. Structure of turbulent velocity and scalar fields at large wavenumbers. *Physics of Fluids*, 8(6):1063–1075, 1965.

[113] C. Paruchuri, J. R. Gill, N. Subramanian, P. Joseph, C. Vanderwel, X. Zhang, and B. Ganapathisubramani. Aerofoil geometry effects on turbulence interaction noise. In *21st AIAA/CEAS Aeroacoustics Conference*, page 2830, 2015.

[114] C. Paruchuri, P. Joseph, S. Narayanan, and J. W. Kim. Aerofoil broadband noise reductions through double-wavelength leading-edge serrations: A new control concept. *Journal of Fluid Mechanics*, 855:131–151, 2018.

[115] C. Paruchuri, S. Narayanan, P. Joseph, and J. W. Kim. Leading edge serration geometries for significantly enhanced leading edge noise reductions. *22nd AIAA/CEAS Aeroacoustics Conference*, (August), 2016.

[116] C. Paruchuri, P. Subramanian, N.and Joseph, C. Vanderwel, J. W. Kim, and B. Ganapathisubramani. Broadband noise reduction through leading edge serrations on realistic aerofoils. *21st AIAA/CEAS Aeroacoustics Conference*, (June):1–29, 2015.

[117] R. Paterson and R. Amiet. Acoustic radiation and surface pressure characteristics of an airfoil due to incident turbulence. In *3rd Aeroacoustics Conference*, page 571, 1976.

[118] J. F. Piet and G. Elias. Modélisation du champ acoustique incident sur la coiffe d'Ariane 5 par des sources simples. *Tiré à part- Office national d'études et de recherches aerospatiales*, 1994.

[119] D. Ragni, F. Avallone, WCP van der Velden, and D. Casalino. Measurements of near-wall pressure fluctuations for trailing-edge serrations and slits. *Experiments in Fluids*, 60(1):1–22, 2019.

[120] J. D. Revell. Trailing-edge flap noise reduction by porous acoustic treatment. *AIAA-97-1646-CP*, pages 493–505, 1997.

[121] M. Roger. On broadband jet-ring interaction noise and aerofoil turbulence-interaction noise predictions. *Journal of Fluid Mechanics*, 653:337–364, 2010.

[122] M. Roger and A. Carazo. Blade-geometry considerations in analytical gust-airfoil interaction noise models. In *16th AIAA/CEAS Aeroacoustics Conference*, page 3799, 2010.

[123] M. Roger and S. Moreau. Trailing Edge Noise Measurments and Prediction for Subsonic Loaded Fan Blades. *Aiaa 2002-2460*, (June), 2002.

[124] M. Roger and S. Moreau. Back-scattering correction and further extensions of amiet's trailing-edge noise model. part 1: theory. *Journal of Sound and vibration*, 286(3):477–506, 2005.

[125] M. Roger and S. Moreau. Extensions and limitations of analytical airfoil broadband noise models. *International Journal of Aeroacoustics*, 9(3):273–305, 2010.

[126] M. Roger and S. Moreau. Airfoil Turbulence-Impingement Noise Reduction by Porosity or Wavy Leading-Edge Cut : Experimental Investigations. *Inter-Noise 2016*, (2):6006–6015, 2016.

[127] M. Roger, S. Moreau, and M. Wang. An analytical model for predicting airfoil self-noise using wall-pressure statistics. *Annual Research Briefs 2002*, (1970):405–414, 2002.

[128] M. Roger, C. Schram, and L. De Santana. Reduction of Airfoil Turbulence-Impingement Noise by Means of Leading-Edge Serrations and/or Porous Material. *19th AIAA/CEAS Aeroacoustics Conference*, pages 1–20, 2013.

[129] M. Roger and S. Serafini. Interaction Noise from a Thin Annulus in a Circular Jet. *11th AIAA/CEAS Aeroacoustics Conference*, (AIAA 2005-2958):23–25, 2005.

[130] N. Rostamzadeh, R. M. Kelso, B. B. Dally, and K. L. Hansen. The effect of undulating leading-edge modifications on NACA 0021 airfoil characteristics. *Physics of Fluids*, 25(11), 2013.

[131] Y. Rozenberg, G. Robert, and S. Moreau. Wall-pressure spectral model including the adverse pressure gradient effects. *AIAA journal*, 50(10):2168–2179, 2012.

[132] M. Sanjose, D. Lallier-Daniels, and S. Moreau. Aeroacoustic analysis of a low-subsonic axial fan. In *Turbo Expo: Power for Land, Sea, and Air*, volume 56628, page V001T09A015. American Society of Mechanical Engineers, 2015.

[133] L. D. Santana, J. Christophe, C. Schram, and W. Desmet. A rapid distortion theory modified turbulence spectra for semi-analytical airfoil noise prediction. *Journal of Sound and Vibration*, 383:349–363, 2016.

[134] L. De Santana, C. Schram, and W. Desmet. Panel method for turbulence-airfoil interaction noise prediction. In *18th AIAA/CEAS Aeroacoustics Conference (33rd AIAA Aeroacoustics Conference)*, page 2073, 2012.

[135] E. Sarradj and T. Geyer. Noise Generation by Porous Airfoils. *13th AIAA/CEAS Aeroacoustics Conference (28th AIAA Aeroacoustics Conference)*, 2007.

[136] E. Sarradj and T. Geyer. Symbolic regression modeling of noise generation at porous airfoils. *Journal of Sound and Vibration*, 333(14):3189–3202, 2014.

[137] R. Schlinker and R. Amiet. Helicopter rotor trailing edge noise. In *7th Aeroacoustics Conference*, page 2001, 1981.

[138] K. Schwarzschild. Schwarzchild Method. *Mathematische Annalen*, 55(1):177–247, 1891.

[139] W. R. Sears. *A systematic presentation of the theory of thin airfoils in non-uniform motion.* PhD thesis, California Institute of Technology, 1938.

[140] W. R. Sears. Some aspects of non-stationary airfoil theory and its applications. *Journal of the Aeronautical Sciences*, 8(3):104–108, 1941.

[141] Soderman, P. T. Aerodynamic effects of leading-edge serrations on a two dimensional airfoil. *National aeronautics and space administration, TM X-2643*, 1972.

[142] Soderman, P. T. Leading edge serrations which reduce the noise of low-speed rotors. *National aeronautics and space administration, TN D-7371*, 1973.

[143] Christopher KW Tam and Hongbin Ju. Aerofoil tones at moderate reynolds number. *Journal of Fluid Mechanics*, 690:536, 2012.

[144] S. Tamaro, R. Zamponi, D. Ragni, C. Teruna, and C. Schram. Experimental investigation of turbulent coherent structures interacting with a porous airfoil. *Experiments in Fluids*, 62:94, April 2021.

[145] G. I. Taylor, J. W. Maccoll, and W. F. Durand. Aerodynamic theory. *Julius Springer, Berlin*, 3:209, 1935.

[146] C. T. Tsai. Effect of airfoil thickness on high-frequency gust interaction noise. 1992.

[147] J. M. Turner and J. W. Kim. Aeroacoustic source mechanisms of a wavy leading edge undergoing vortical disturbances. *Journal of Fluid Mechanics*, 811:582–611, 2017.

[148] J. van Bladel, U.S. Atomic Energy Commission., and Midwestern Universities Research Association. *On Helmholtz's theorem in finite regions.* Number 32 leaves in {MURA} ({Series});440. Midwestern Universities Research Association, Madison, W., 1958.

[149] SH S. Vemuri, X. Liu, B. Zang, and M. Azarpeyvand. Leading-edge serrations for noise control from tandem airfoil configuration. In *25th AIAA/CEAS Aeroacoustics Conference*, page 2556, 2019.

[150] T. von Kármán and W.R. Sears. Airfoil theory for non-uniform motion. *Journal of the Aeronautical Sciences*, 5(10):379–390, 1938.

[151] Y. Wang, W. Hu, and S. Zhang. Performance of the bio-inspired leading edge protuberances on a static wing and a pitching wing. *Journal of hydrodynamics*, 26(6):912–920, 2014.

[152] W. W. Willmarth and F. W. Roos. Resolution and structure of the wall pressure field beneath a turbulent boundary layer. *Journal of Fluid Mechanics*, 22(1):81–94, 1965.

[153] G. R. Yakhina, M. Roger, A. Finez, S. Bouley, V. Baron, S. Moreau, and J. Giez. Localization of swept free-tip airfoil noise sources by microphone array processing. *AIAA Journal*, 58(8):3414–3425, 2020.

[154] R. Zamponi, S. Moreau, and C. Schram. Rapid distortion theory of turbulent flow around a porous cylinder. *Journal of Fluid Mechanics*, 915:A27, May 2021.

[155] R. Zamponi, S. Satcunanathan, S. Moreau, D. Ragni, M. Meinke, W. Schröder, and C. Schram. On the role of turbulence distortion on leading-edge noise reduction by means of porosity. *Journal of Sound and Vibration*, 485:115561, October 2020.

[156] E. Zitzler, K. Deb, and L. Thiele. Comparison of multiobjective evolutionary algorithms: Empirical results. *Evolutionary computation*, 8(2):173–195, 2000.

dernière page de la thèse

AUTORISATION DE SOUTENANCE

Vu les dispositions de l'arrêté du 25 mai 2016,

Vu la demande du directeur de thèse

Monsieur M. ROGER

et les rapports de

M. Y. GERVAIS
Professeur - Université de Poitiers

et de

M. M. AZARPEYVAND
Professeur - University of Bristol

Monsieur BAMPANIS Georgios

est autorisé à soutenir une thèse pour l'obtention du grade de **DOCTEUR**

Ecole doctorale Mécanique, Energétique, Génie Civil et Acoustique

Fait à Ecully, le 15 janvier 2021

P/Le directeur de l'E.C.L.
Le directeur des Etudes

Grégory VIAL